Politecnico di Torino

ScuDo
Scuola di Dottorato ~ Doctoral School
WHAT YOU ARE, TAKES YOU FAR

Doctoral dissertation
Doctoral program in Physics (37^{th} cycle)

Measurement of quantum numbers balance and fluctuations with ALICE at the LHC

Mario Ciacco

* * * * * *

Supervisors
Prof. Stefania Bufalino, Supervisor
Prof. Massimo Masera, Co-supervisor

Doctoral Examination Committee
Dr. Urs Achim Wiedemann, CERN
Dr. Vincenzo Vagnoni, INFN Sezione di Bologna

Politecnico di Torino, 2025

Declaration

I hereby declare that the contents and organisation of this dissertation constitute my own original work and does not compromise in any way the rights of third parties, including those relating to the security of personal data.

. . . . . .

Mario Ciacco

Turin, 2025

* This dissertation is presented in partial fulfillment of the requirements for Ph.D. degree in the Graduate School of Politecnico di Torino (ScuDo).

Abstract

The goal of high-energy nuclear physics is to characterise the phase diagram of QCD. From calculations on the lattice, it is predicted that a crossover phase transition takes place for baryon-number symmetric matter at a temperature $T_c \approx 155$ MeV. This process determines the transition from conventional nuclear matter to a more exotic deconfined partonic phase, known as quark-gluon plasma (QGP). This phase, present in the early universe about 1 μs after the Big Bang, can be recreated in the laboratory via high-energy heavy-ion collisions at the CERN Large Hadron Collider (LHC), where energy densities as high as $O(10\ \mathrm{GeV/fm^{-3}})$ are achieved. The ALICE detector at the LHC is designed to investigate the deconfined QCD phase produced in such collisions.

As quarks and gluons cannot be directly observed, the ALICE detector is used to measure hadronic probes carrying information on the QGP evolution. Consequently, for these studies it is crucial to understand the hadronisation mechanism, by which the fundamental QCD degrees of freedom recombine into hadrons. From a theoretical perspective, different models are available to describe the hadronisation process, most notably, the statistical hadronisation model (SHM) and the string fragmentation model.

The particle-antiparticle balance in the production of hadrons at the LHC is affected by the initial conditions of the collisions through the baryon number stopping, consisting of the transport of a baryon number excess from the colliding ions to the midrapidity regions where hadron production is measured. In addition, the different underlying hadronisation mechanisms provide a different implementation of quantum number conservation in the hadronisation process, implying a different rapidity correlation range among the conserved quantum numbers. This Thesis addresses both of these topics through the extraction of chemical potentials in Pb–Pb collisions at $\sqrt{s_{\mathrm{NN}}} = 5.02$ TeV and via measurements of event-

by-event hadron-multiplicity fluctuations in pp, p–Pb, and Pb–Pb collisions at $\sqrt{s_{\rm NN}} = 5.02$ TeV. These measurements rely on the selection of pure samples of a wide array of light-flavour hadrons: this is achieved with the excellent tracking and particle identification capabilities of the ALICE detector.

The chemical potentials, regulating the conservation of quantum numbers in the grand canonical version of the SHM, are extracted from measurements of antiparticle-to-particle yield ratios of hadrons and light nuclei. The latter, along with protons, are sensitive probes of the baryon asymmetry of the hadron system formed in the collisions. This measurement includes also charged pions and omega baryons, which probe the balancing of electric charge and strangeness, respectively. The results obtained for the baryon number and electric charge chemical potentials are compatible with zero independently of the collision centrality, showing with unprecedented uncertainty that a baryon-number free and electrically neutral system is formed in Pb–Pb collisions at the LHC. These findings, which provide precise constraint for quantum-number transport models in the TeV energy scale, are published in Physical Review Letters [1].

Event-by-event hadron multiplicity fluctuations give insights into the hadronisation mechanisms. In this Thesis, the measurements of normalised second order cumulant of the net-$\Xi^{\pm}$ number and the Pearson correlation coefficient between the net-$\Xi^{\pm}$ and net-$\mathrm{K}^{\pm}$ numbers are presented. This study, relying on the selection of pure kaon and Ξ samples also using machine learning techniques, is carried out in Pb–Pb collisions and, for the first time ever, also in pp and p–Pb collisions. The results indicate that the strange-antistrange correlation observed in data is weaker than predicted by string fragmentation, regulated by a conservation volume for strangeness extending over about 3 units of rapidity. Additionally, the data suggest the existence of a significant same-sign strangeness correlation, as predicted by the SHM in the canonical ensemble approach. The obtained results are published in Physical Review Letters [2]. Finally, the Pearson correlation between the antideuteron and the net-Λ numbers is determined in Pb–Pb collisions at $\sqrt{s_{\rm NN}} = 5.02$ TeV. The results of this analysis, approved as an official public result of the ALICE Collaboration, indicate that a large conservation volume determines the conservation of quantum numbers also in the processes underlying nuclear formation.

Contents

Chapter 1

High energy nuclear physics

High Energy Nuclear Physics (HENP) investigates the properties of strongly-interacting systems characterised by extreme energy density and/or temperatures. In this chapter, the fundamental concepts of HENP are discussed, from both a theoretical and an observational perspective.

1.1 Quantum chromodynamics

The quantum field theory of strong interactions, known as Quantum Chromodynamics (QCD) [3–6], is one of the building blocks of the Standard Model of particle physics [7]. The Lagrangian density of QCD, which is described as a local non-abelian gauge theory [8] invariant under SU(3) transformations, can be written as:

$$\mathcal{L} = -\frac{1}{4} G^a_{\mu\nu} G^{\mu\nu}_a + \sum_f \bar{q}^i_f \left(i \not{D}_{ij} - m_f \delta_{ij} \right) q^j_f, \tag{1.1}$$

where the slashed notation indicates the contraction with the Dirac's matrices. The first term in Eq. (1.1), expressed in terms of the gauge-field strength tensor,

$$G^a_{\mu\nu} = \partial_\mu A^a_\nu - \partial_\nu A^a_\mu + g_s f^a{}_{bc} A^b_\mu A^c_\nu, \tag{1.2}$$

with $a = 1, \ldots 8$, entails the free propagation and self-interaction of the gauge field of QCD, whose quanta are called *gluons*. The quantity g_s is the QCD strong coupling, while f_{abc} are the structure constants of SU(3). The second term in Eq. (1.1) takes into account both the free propagation of matter fields, whose quanta are called *quarks*, and their interaction with the gluon field. Each quark field is characterised by both a colour index, $i = 1, 2, 3$, and a flavour index,

$f = u, d, s, c, b, t$. Different flavours are associated with different quark masses, m_f. The interaction between matter and gauge fields is included in Eq. (1.1) by means of the second term in the covariant derivative:

$$(D_\mu)_{ij} = \partial_\mu \delta_{ij} - i g_s \left(\frac{\lambda^a}{2}\right)_{ij} A^a_\mu. \tag{1.3}$$

The interaction is regulated by the eight generators of the fundamental representation of SU(3), expressed in terms of the 3×3 Gell-Mann matrices λ^a. QCD interactions are flavour-diagonal, but enable colour exchange between quarks.

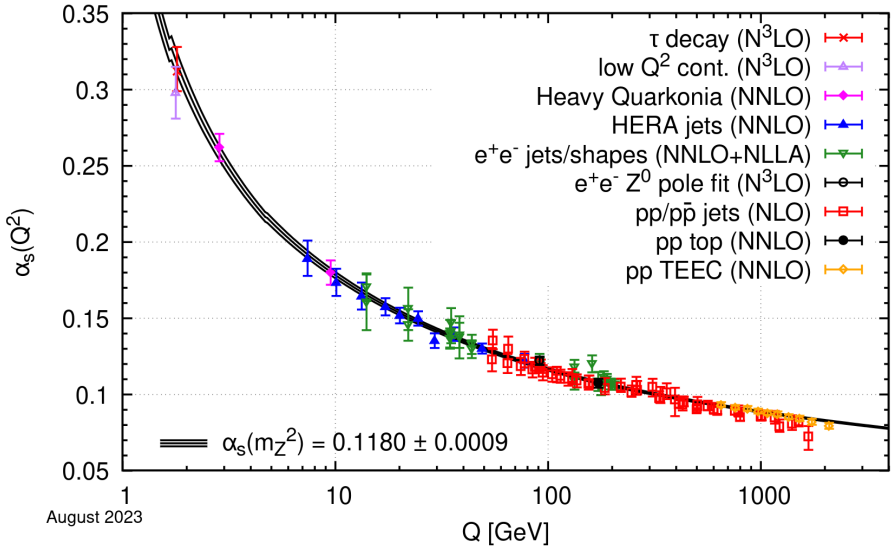

Figure 1.1: Measurements of the QCD coupling $\alpha_s(Q^2)$ as a function of the energy scale Q, in various collision systems and via different processes. The orders of QCD perturbation theory are reported in brackets. The numerical value of α_s at the Z pole is also reported [9].

Perturbation theory can be employed to compute the amplitude of QCD processes via the power-series expansion of the amplitude itself in either g_s or, similarly, $\alpha_s = g_s^2/4\pi$, assuming $g_s \ll 1$. The gluon self-interactions are responsible for the anti-screening of the colour charge, which results in the evolution of α_s with respect to the negative square of the exchanged momentum, $Q^2 = -q^2$. The resulting dependence is written as:

$$\alpha_s\left(Q^2\right) = \frac{\alpha_s\left(\mu^2\right)}{1 + \frac{\alpha_s\left(\mu^2\right)}{12\pi}\left(33 - 2n_f\right)\log\left(Q^2/\mu^2\right)} \tag{1.4}$$

where μ^2 is an arbitrary renormalisation scale and $n_f = 6$ is the number of known flavours.

The predicted dependence of α_s with Q^2 has been tested with numerous experimental measurements, as shown in Fig. 1.1 [9]. The value of $\alpha_s(Q^2)$ approaches zero for $Q^2 \gg 1$ GeV^2. This regime, known as *asymptotic freedom*, is characterised by weaker interactions among quark and gluons, hence justifying the applicability of perturbation theory. On the contrary, in the $Q^2 \ll 1$ GeV^2 range, the coupling rises above unity, implying the loss of predictability for the perturbative expansion. These conditions determine the so-called *confinement* of quarks and gluons inside colour-neutral hadrons.

1.2 Quark-gluon plasma

As a consequence of the running of α_s with the energy scale, the properties of strongly-interacting matter cannot be fully derived within the framework of perturbation theory. Instead, the non-perturbative regime of QCD is investigated via lattice QCD [10, 11], which is a numerical approach based on the discretisation of the Euclidean space-time defined through a Wick rotation, $t \to i\tau$. Using the path-integral formalism, the grand partition function of QCD is built starting from the Lagrangian density of Eq. (1.1). The properties of strongly-interacting systems are determined from this partition function, interpreted in a statistical-mechanical sense, as well as from its derivatives. One of the major results of lattice QCD is the prediction of a phase transition between the confined hadronic phase and a deconfined phase, commonly referred to as quark gluon plasma (QGP), in analogy with the electromagnetic plasma [12].

In a baryon-number-symmetric system, this phase transition is expected to be a crossover with a pseudo-critical temperature $T_c \approx 155$ MeV [13]. As shown in Fig. 1.2, the pressure, energy and entropy densities scaled by powers of the temperatures are characterised by a smooth evolution across the pseudo-critical temperature region. It is worth noting that these quantities, which determine the QCD equation of state, are consistent with those expected for an ideal gas of hadrons and resonances below T_c. Another prediction of lattice QCD is that the spontaneously-broken chiral symmetry of QCD is restored in the phase transition. This is quantified in terms of the chiral condensate, $\langle\bar{\psi}\psi\rangle$, which is expected to reach zero values in the deconfined phase.

The applicability of lattice QCD calculation is limited to net-baryon-number den-

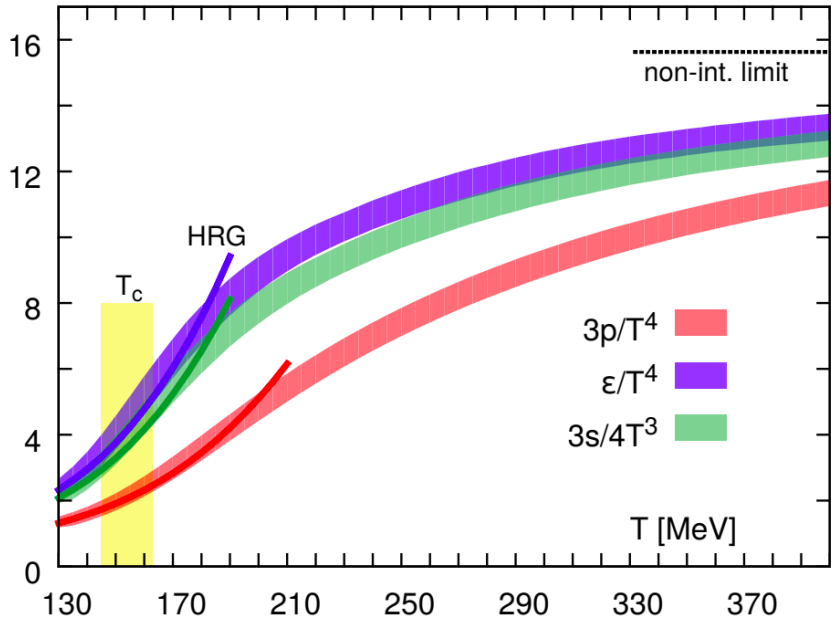

Figure 1.2: Pressure p, energy density ϵ, and entropy density s, normalised to powers of the temperature T, as a function of the temperature in LQCD at zero net-baryon-number density. A comparison with the Hadron Resonance Gas (HRG) model is also shown at lower temperatures [13].

sity, or equivalently, chemical potential μ, close to zero, due to numerical instabilities. As described in Ref. [14], beyond this range calculations rely on: Taylor expansion extrapolation of the lattice results around $\mu = 0$; effective models of QCD; the holographic principle. In all cases, a rich structure of the QCD phase diagram is predicted: a schematic representation in the (μ, T) plane is shown in Fig. 1.3. The crossover transition band is expected to extend also to $\mu > 0$ up to a critical end point, above which a first-order phase transition is expected. The theoretical search of the QCD critical point location has been recently fuelled by the experimental high-order net-proton number fluctuation measurements obtained by the STAR Collaboration at the Relativistic Heavy Ion Colider (RHIC) [15].

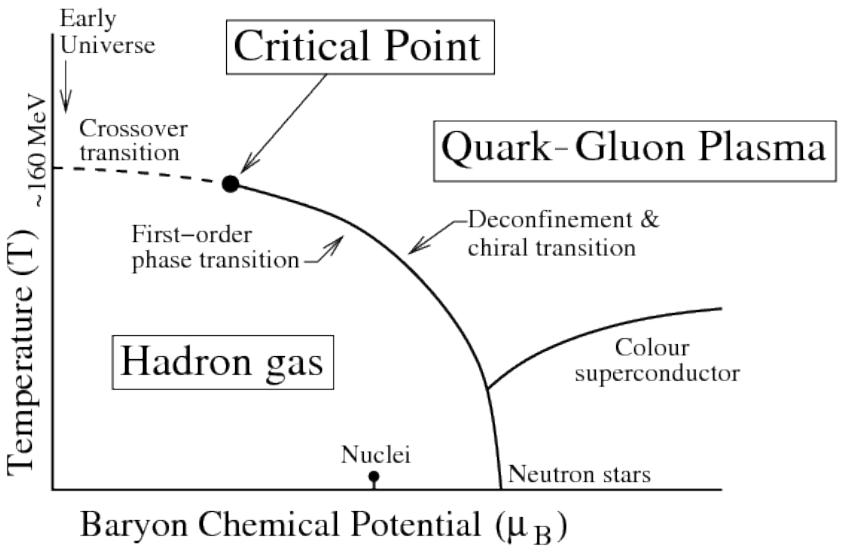

Figure 1.3: Schematic representation of the expected QCD phase diagram [16].

1.3 Heavy-ion collisions

The QCD phase transition is investigated experimentally via high-energy heavy-ion collisions. In such processes, a large energy density (> 1 GeV/fm^3) is deposited over a volume greater than that of a nucleon (~ 1 fm^3) for a relatively long time interval ($> 10^{-23}$ s). The accelerator facilities able to deliver such collisions are the LHC at CERN and the RHIC at the Brookhaven National Laboratory (BNL). Lower energy processes are also studied at the CERN Super Proton Syncrotron (SPS) and at the RHIC in the beam energy scan (BES). Future facilities for low-energy heavy-ion physics include FAIR at GSI and NICA at JINR.

1.3.1 Geometry of the collision

Unlike processes involving point-like elementary particles, the observables measured in heavy-ion collisions are incluenced by the geometry of the collision. This includes both the distribution of nucleons inside the ions and the relative position of the ions when the interactions occur. A widely used approach to describe the collision geometry is the Glauber model [17], which is based on the hypothesis that nuclear collisions can be treated as an incoherent superposition of nucleon-nucleon collisions. The trajectories of the interacting protons and neutrons, treated as independent indistinguishable elementary particles, are assumed to be unperturbed by the interaction, according to the so-called optical limit.

In this approach, all the computed observables are determined as a function of the impact parameter $\vec{b}$, which is defined as the projection onto the plane perpendicular to the beam direction of the vector connecting the centres of the colliding ions. In Fig. 1.4 the collision geometry is schematically shown: A and B indicate the mass numbers of the target and projectile ions, respectively. The probability to

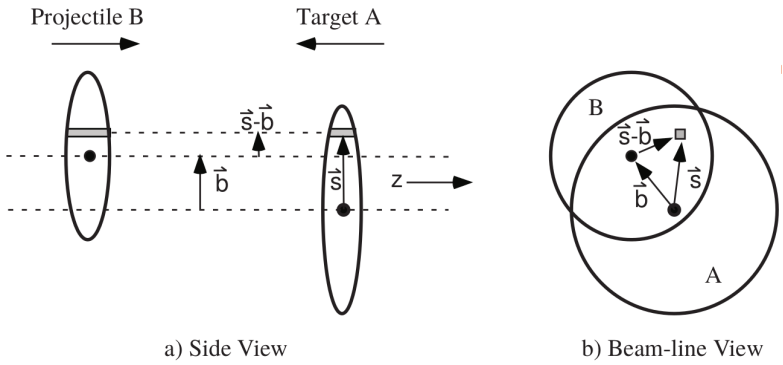

Figure 1.4: Schematic representation of the longitudinal and transverse geometry of an ion-ion collision. The impact parameter vector is labelled as $\vec{b}$ [17].

find a nucleon inside the nucleus A at the $\vec{s}$ coordinates in the transverse plane is determined by the nuclear thickness function:

$$T_A(\vec{s}) = \int \rho_A(\vec{s}, z_A) \mathrm{d}z_A, \tag{1.5}$$

where $\rho_A(\vec{s}, z_A)$ is the normalised nuclear density. The product of the thickness functions of A and B determines the nucleon overlap probability per unit area. This quantity is integrated to compute the nuclear overlap function

$$T_{AB}(\vec{b}) = \int T_A(\vec{s}) T_B(\vec{s} - \vec{b}) \mathrm{d}^2 s. \tag{1.6}$$

The probability of n binomially distributed nucleon-nucleon interactions is determined as:

$$P(n, \vec{b}) = \frac{(AB)!}{n!(AB-n)!} \left[T_{AB}(\vec{b}) \sigma_{\mathrm{inel}}^{\mathrm{NN}} \right]^n \left[1 - T_{AB}(\vec{b}) \sigma_{\mathrm{inel}}^{\mathrm{NN}} \right]^{AB-n}, \tag{1.7}$$

where $\sigma_{\mathrm{inel}}^{\mathrm{NN}}$ is the nucleon-nucleon interaction cross section. The differential nucleus-nucleus interaction cross section is finally obtained as the probability of having at

least one nucleon-nucleon interaction:

$$\frac{\mathrm{d}^2\sigma_{\mathrm{inel}}^{A+B}}{\mathrm{d}b^2} \equiv \sum_{n=1}^{AB} P\left(n, \vec{b}\right) = 1 - \left[1 - T_{AB}(\vec{b})\sigma_{\mathrm{inel}}^{\mathrm{NN}}\right]^{AB}. \tag{1.8}$$

In Eq. (1.8), only the magnitude of the impact parameter vector b is considered assuming nuclei are spherically symmetric. The total interaction cross section is then given by the integral of Eq. (1.8) over all possible values of b:

$$\sigma_{\mathrm{inel}}^{A+B} = \int_0^\infty 2\pi b \mathrm{d}b \left\{1 - \left[1 - T_{AB}(\vec{b})\sigma_{\mathrm{inel}}^{\mathrm{NN}}\right]^{AB}\right\} \tag{1.9}$$

From an experimental point of view, nuclear collisions are classified according to their centrality, i.e. to the degree of overlap between the colliding nuclei. Centrality classes are defined as percentiles of the cross section reported in Eq. (1.9), which is experimentally correlated to observable quantities such as the particle multiplicities.

1.3.2 Space-time evolution of a heavy-ion collision

The particle system formed in heavy-ion collisions at the LHC evolves through multiple steps, as it is shown schematically in Fig. 1.5 [18]. The approaching

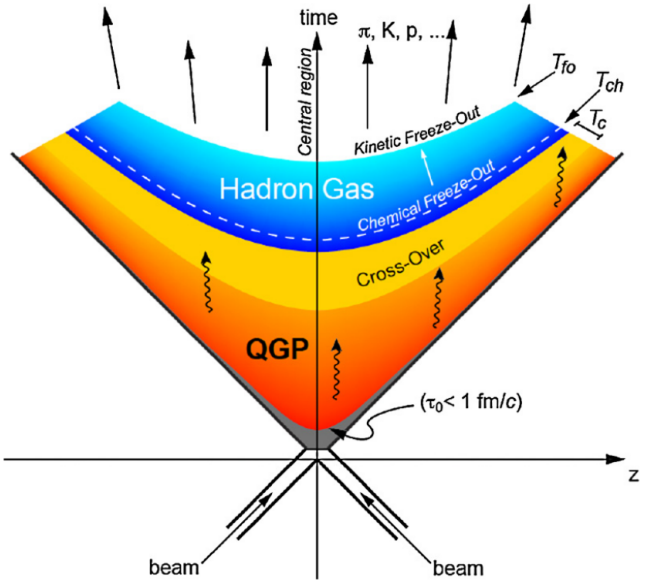

Figure 1.5: Space-time diagram showing the space-time evolution of an ion-ion collision [18].

ion beams move at about the speed of light ($\gamma \approx 2700$ at the LHC) before the collision takes place at $t = z = 0$. The overlap time of the Lorentz-contracted colliding nuclei is extremely short: in Pb–Pb collisions at the LHC, $t_{\text{overlap}} \approx 0.005$ fm/c.

The collision is followed by a pre-equilibrium phase (shown in grey in Fig. 1.5) in which secondary quanta are produced. An estimate of their formation time is obtained with the uncertainty relation, $\Delta E \cdot \Delta t \approx \hbar$, where ΔE is determined by the mean transverse mass of the system, $\langle m_{\text{T}} \rangle$, extracted from measurements of particle multiplicities in heavy-ion collision experiments. This calculation yields $\tau_{\text{form}} \approx 0.1$ fm/c at the LHC. Secondary quanta keep interacting until thermal equilibrium is reached at $\tau_0 \approx 1$ fm/c. At this stage, the energy density of the system is $\epsilon \approx 15$ GeV/fm^3: under these conditions, it is expected that deconfined partonic matter is present in the system. The QGP drop formed in this way expands under the pressure gradients originating between the centre of the system and the vacuum surrounding it. As a result of this expansion, the temperature of the system decreases until the pseudo-critical temperature, T_c, is reached, determining the transition from the deconfined to the hadronic phase.

Due to the system expansion and cooling, the inelastic interactions within the hadronic phase cease, hence fixing the hadron-chemical composition of the system. This process, called chemical freeze-out, takes place at a temperature T_{ch}. The T_{ch} value extracted from experimental measurements of hadron yields [19] is close to the lattice QCD estimates of T_c: this suggests that the chemical freeze-out occurs right after the phase transition. On the other hand, the hadrons undergo elastic interactions until $T_{fo} \approx 120$ MeV [20, 21] is reached, resulting in the so-called kinetic freeze-out. The subsequent evolution is characterised by a free-streaming expansion of the system, where the kinematic properties of hadrons are also fixed.

1.4 Probing the QGP

The system created in heavy-ion collisions can be characterised by a set of observables classified according to the momentum transferred in the formation process of the measured probes. Different momentum scales are related to different stages of the system evolution, as indicated by the relation $t \sim 1/Q^2$.

1.4.1 Hard probes

The earliest QGP probes are produced in hard processes, where $Q \gg 1$ GeV/c. They include both high-momentum hadrons and heavy-flavour particles. Due to their early production, these probes cross the system throughout its full evolution.

High-Momentum Hadrons

In the Glauber picture, the production cross section of high-momentum hadrons is expected to be proportional by the average number of binary nucleon-nucleon collisions, $\langle N_{coll} \rangle$, to the cross section of the analogous process in nucleon-nucleon interactions. Under the model assumptions, the nuclear modification factor, expressed as:

$$R_{\mathrm{AA}}(p_{\mathrm{T}}) = \frac{1}{\langle N_{coll} \rangle} \frac{\mathrm{d}N_{\mathrm{AA}}/\mathrm{d}p_{\mathrm{T}}}{\mathrm{d}N_{\mathrm{NN}}/\mathrm{d}p_{\mathrm{T}}}, \tag{1.10}$$

is equal to unity for hadrons of high transverse momentum, p_{T}. Experimentally, deviations from unity unity are observed [22, 23]. A comparison between the measurements of R_{AA} for light-flavoured charged hadrons both in p–Pb and in Pb–Pb collisions is shown in Fig. 1.6, taken from reference [22].

For low-p_{T} particles it is observed that $R_{\mathrm{AA}} < 1$. This is interpreted as an effect of the scaling of the soft-particle production rate with the number of nucleons that participate in the collision. This quantity is determined by the impact parameter of the collision, which is smaller than the total number of binary nucleon-nucleon interactions [24].

In p–Pb collisions, where no phase transition is expected to occur, an increase of R_{pPb} above unity is observed at $p_{\mathrm{T}} \approx 2 - 3$ GeV/c. This effect, known as Cronin enhancement [25], stems from the increase of parton momenta before fragmentation due to their multiple scatterings inside the target nucleus. Thus, it results from the structure of the colliding ions rather than from the interaction with a thermalised partonic phase. As such, the Cronin effect is classified as a cold nuclear matter effect, similarly to the modification of parton distribution functions (PDFs) inside nuclei [24]. In heavy-ion collisions, the measured R_{AA} is lower than unity for $p_{\mathrm{T}} > 3$ GeV/c, reaching a minimum at $p_{\mathrm{T}} \approx 7$ GeV/c. This is interpreted as the result of the energy loss of partons inside the medium formed in such collisions. In the presence of a deconfined partonic phase, the partons may loose energy both by elastic scatterings in the QGP and via the gluon radiation mechanism, also known as *gluonstrahlung*.

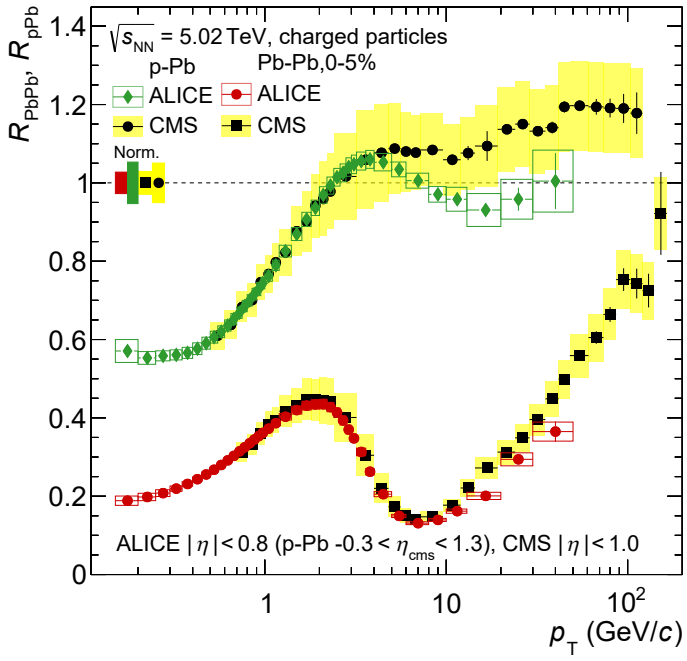

Figure 1.6: R_{AA} of charged hadrons in p-Pb and Pb-Pb collisions at $\sqrt{s_{\mathrm{NN}}} = 5.02$ TeV measured by the ALICE Collaboration [23]. The ALICE measurements are compared with the results obtained by the CMS Collaboration.

Similar R_{AA} measurements are carried out for heavy-flavour hadrons, i.e., hadrons containing c and/or b quarks. The main difference with respect to light-flavour hadrons is that c and b quarks are produced exclusively in hard processes, as their masses are larger than 1 GeV/c^2. Consequently, energy loss effects can be observed also at very low p_{T} in this case. Moreover, the R_{AA} of charm and beauty hadrons is more sensitive to the medium properties, such as the density of gluons, compared to the R_{AA} of light-flavoured hadrons. An example of these measurement is described in Ref. [26].

The energy loss in the medium is characterised also through jets, which are highly-collimated streams of particles arising from the fragmentation of highly energetic partons. In the vacuum, pairs of jets with opposite total transverse momenta form as a result of the hadronisation of high-momentum $q\bar{q}$ pairs. This process can be altered in the presence of a colour-deconfined medium. If the $q\bar{q}$ is produced close to the surface of the system, the outward-pointing parton hadronises in the vacuum,

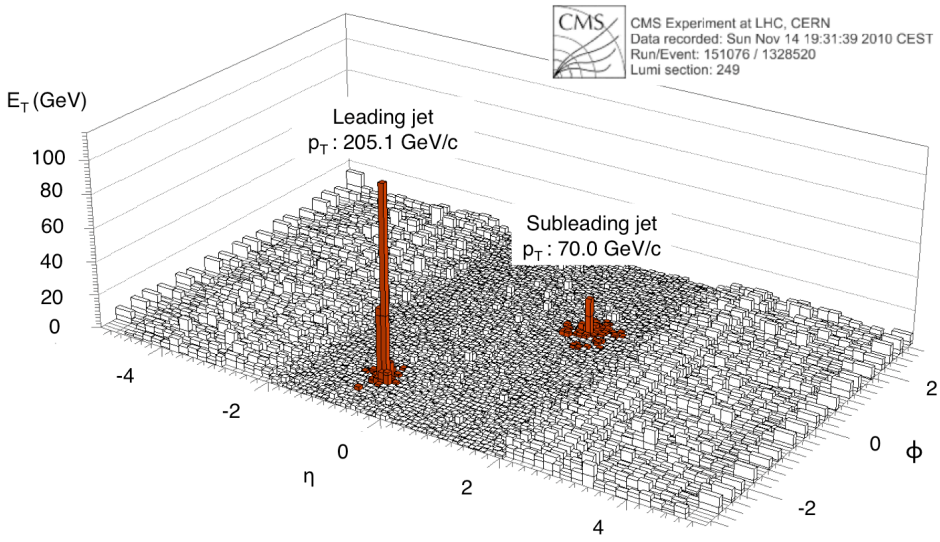

Figure 1.7: Dijet imbalance in a single Pb-Pb collision at $\sqrt{s_{\mathrm{NN}}} = 2.76$ TeV observed at the LHC by the CMS collaboration. The tranverse-energy deposit in the electromagnetic calorimeter is reported on the vertical axis [27].

while the particles emitted by the inwards-pointing one loose energy via strong interactions with the medium. These processes affect the angular correlations between reconstructed high-momentum particles, resulting in the observation of dijets with strongly suppressed subleading components. In Fig. 1.7, an example of a Pb–Pb event recorded by the CMS Collaboration exhibiting dijet imbalance is shown [27]. The (η, ϕ) distribution of the transverse energy, E_{T}, in the CMS electromagnetic calorimeter exhibits an asymmetric double-peak structure. Such a structure is determined by the emission of a pair of anticollinear jets in the event. The lower-E_{T} peak corresponds to the jet that interacted with the medium, causing the redistribution of the initial energy over a wider solid angle.

Quarkonia

A modification of the production of quarkonium states, i.e., bound states of heavy-flavoured $q\bar{q}$ pairs, is predicted inside a colour-deconfined medium [28]. In this environment, the attractive component of the QCD potential is screened by the free colour charge, resulting in a similar phenomenon as the Debye screening inside electromagnetic plasmas. A characteristic length scale evolving with the temperature, called Debye length λ_D, quantifies the minimum length scale at which the QCD potential is screened. In the analysis of quarkonium states, the screening of the potential determines the dissociation of the bound state, resulting in the

suppression of its observed prodiction rate. Suppression effects are measured for both charmonium (J/ψ, ψ', χ_c, ...) and bottomonium (Υ, Υ', Υ'', ...) states in heavy-ion collisions. The suppression of bottomonium states up to Υ'' has been

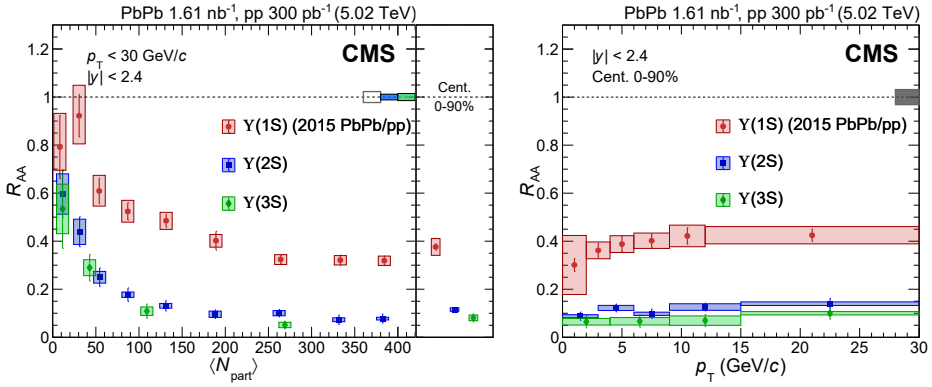

Figure 1.8: R_{AA} of bottomonium states as a function of centrality (left) and in intervals of p_{T} (right) obtained from pp and Pb–Pb collision data recorded at $\sqrt{s_{\mathrm{NN}}} = 5.02$ TeV [29].

measured by the CMS Collaboration at the LHC [29]. The results, shown in Fig. 1.8, indicate a sequential suppression across the $b\bar{b}$ spectrum.

Another effect observed at the LHC is the enhancement of charmonium production with respect to the sequential suppression induced by the Debye screening in the deconfined phase. This phenomenon is understood as an effect of the recombination of the thermalised charm-anticharm quark pairs existing in the deconfined phase [30].

1.4.2 Soft probes

The bulk of the particles emitted in a heavy-ion collision is formed by soft hadrons, which are mainly emitted in the latest stages of the system evolution. In the space-time evolution picture described in Section 1.3.2, these probes are produced after the formation of the deconfined phase.

Hadron multiplicities and momentum spectra

In the most head-on heavy-ion collisions at extreme energies, tens of thousands of particles are emitted. The average abundances of the different produced hadron species are fixed at chemical freeze-out. Among the observed species, light hadrons such as $\pi^{\pm}$ and $\mathrm{K}^{\pm}$ mesons, as well as (anti)protons[1] are the most abundant [20].

[1]The notation "(anti)particle" is a contraction for "particle and antiparticle".

More massive hadrons, such as Λ, Ξ and Ω hyperons, along with light (anti)nuclei, are produced with exponentially suppressed rates for increasing masses. The hadron-chemical composition of the system is employed to characterise the chemical freeze-out, e.g., by determining $T_{\rm ch}$. The experimental data of the yields of light hadrons can be interpreted within the statistical hadronisation model (SHM), as described in detail in Chapter 2.

On the other hand, the $p_{\rm T}$-differential hadron yields carry the information on the multiparticle dynamical correlations arising from the collective expansion of the system. In the absence of collective system dynamics, the $p_{\rm T}$ spectra can be modelled via particle emission from a static thermalised source, resulting in a simple exponential scaling with the transverse mass, $\mathrm{d}N/\mathrm{d}p_{\rm T} \propto \exp(-m_{\rm T}/T_{\rm slope})$. In heavy-ion collisions, a violation of the $m_{\rm T}$-scaling is observed. Specifically, it is observed that the value of $T_{\rm slope}$ depends on the particle mass for $p_{\rm T} < m$:

$$T_{\rm slope} = T_{fo} + \frac{1}{2} m \langle v_{\rm T} \rangle^2. \tag{1.11}$$

T_{fo} is the thermal freeze-out temperature of the system, while $\langle v_{\rm T} \rangle$ is the average transverse velocity of expansion of the system surface at the instant of thermal freeze-out. Consequently, the observed spectra arise from the superposition of a thermal motion and an ordered collective motion. The correlation between velocity and position within the system is known as flow. The effects of radial flow, corresponding to the average transverse flow, can be modelled via the Blast-Wave model [31]. The main hypothesis of the model is that the system is composed of locally equilibrated thermal sources which are boosted in the collision rest frame. A more realistic description can be obtained via full fledged relativistic hydrodynamics calculations. The predictability of hydrodynamics is tested by comparing model calculations and experimental data: as an example, the comparison carried out for $\pi^{\pm}$, $\mathrm{K}^{\pm}$, and (anti)proton spectra is shwon in Fig. 1.9 [20]. The results shown are obtained in semicentral collisions, i.e., with a partial transverse overlap between the colliding ions. Overall, the various hydrodynamic models reported in the legend of Fig. 1.9 describe the data within a $\sim 20\%$ accuracy for $p_{\rm T} < 2$ GeV/c. Except for the EPOS [32] calculations, where the system is described as a hydrodynamically-expanding core surrounded by a non-thermalised corona, the purely hydrodynamical models exhibit deviations from the experimental data at higher $p_{\rm T}$. This feature, which is more prominent in more peripheral collisions, can be understood as the onset of a non-thermal component in the

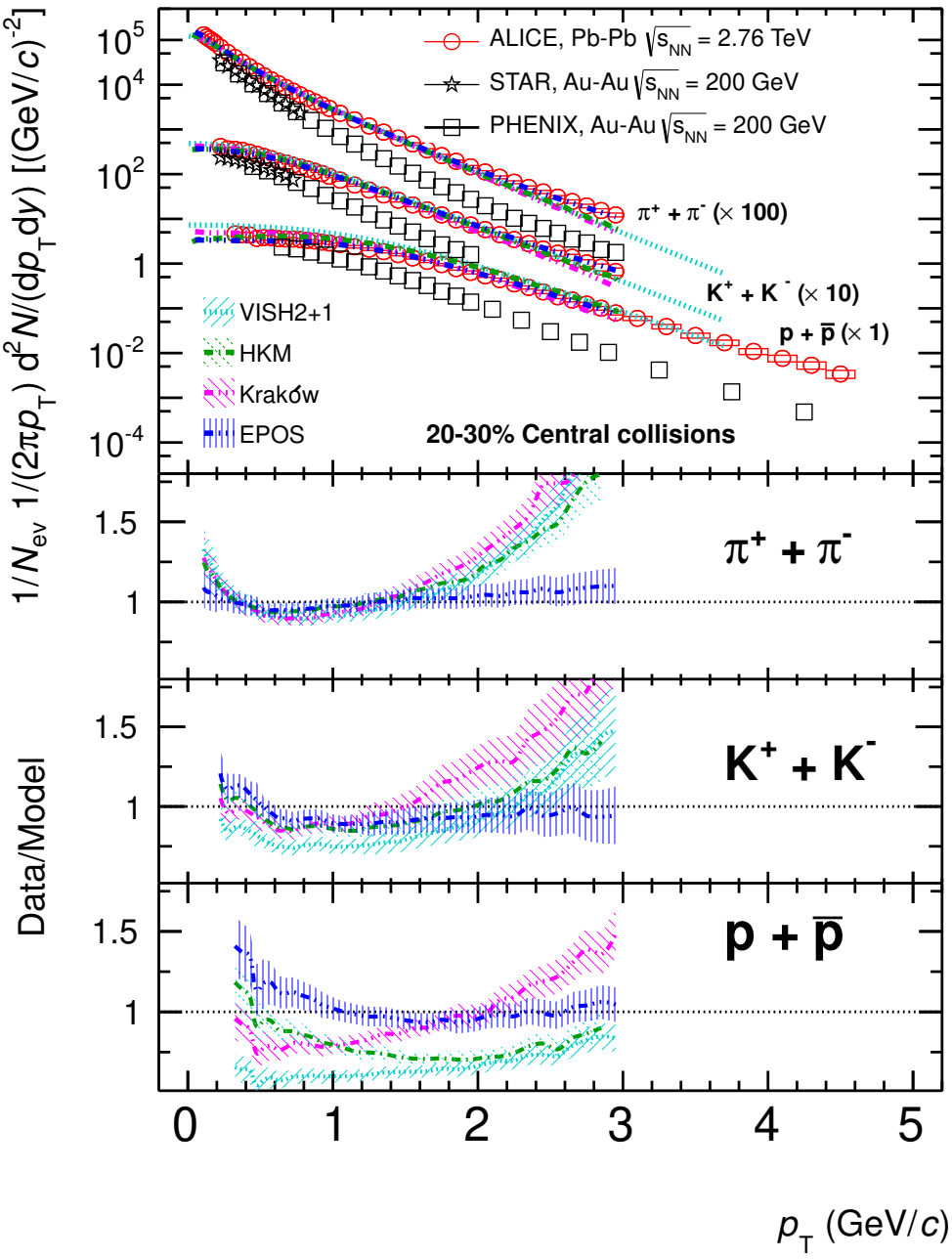

Figure 1.9: p_{T} spectra of charged pions, kaons and (anti)protons measured in Pb-Pb collisions at $\sqrt{s_{\mathrm{NN}}} = 2.76$ TeV by the ALICE Collaboration at the LHC, and in Au-Au collisions at $\sqrt{s_{\mathrm{NN}}} = 200$ GeV by the PHENIX and STAR Collaborations at the RHIC. The experimental data are compared with different hydrodynamics models [20].

hard-particle production [20].

Anisotropic Flow

The collective system expansion is also analysed as function of the azimuthal angle, φ. Anisotropies in the φ distributions of the produced hadrons are related to the initial system anisotropy, regulated by the collision geometry. In semicentral collisions, where the colliding ions overlap only partially, an almond-shaped fireball is formed, as shown in Fig. 1.10. The plane defined by the impact parameter vector

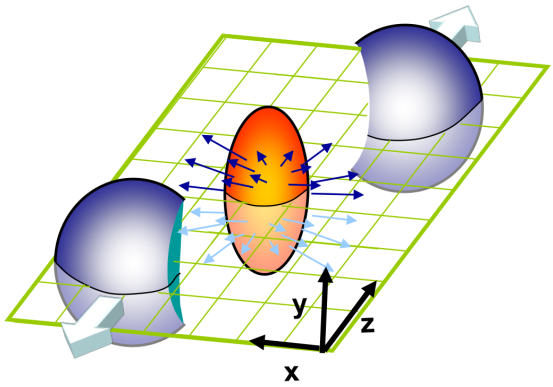

Figure 1.10: Schematic representation of the formation of an anisotropic fireball in a semicentral heavy-ion collision.

$\vec{b}$ and the direction of the colliding ions is called reaction plane. Its projection in the transverse plane is identified by the direction Ψ. The system anisotropy implies that larger pressure gradients are present along the reaction plane, as this would optimize the restoration of isotropy conditions. The imbalance of pressure gradients determines a modification of the azimuthal distribution of particles. The modifications of the azimuthal distributions are quantified by the Fourier coefficients, v_n, resulting from the expansion of the azimuth-differential yields:

$$\frac{\mathrm{d}N}{\mathrm{d}(\phi - \Psi)} = \frac{N}{2\pi}\left\{1 + \sum_{n=1}^{\infty} 2v_n \cos[n(\phi - \Psi)]\right\}. \tag{1.12}$$

Specifically, the v_n coefficients quantify the strength of different anisotropy patterns. For instance, the v_2 coefficient, called elliptic flow, quantifies the amount of elliptic distorsion of the emitted particle momentum distribution.

The interactions occurring at partonic level in the first instants after the collision drive the the initial geometric anisotropy. This, in turn, determines the momen-

tum anisotropies observed in the experiments. For this reason, anisotropic flow measurements are used to extract physical quantities related to interactions inside the QGP: for instance, both the shear viscosity, η, and the thermalisation time scale of QGP are determined from flow measurements [33]. The obtained results indicate that the QGP hydrodynamics resembles that of a perfect fluid, though residual interactions cannot be neglected in this system. Indeed, the flow harmonics observed both at the RHIC and at the LHC agree with hydrodynamic calculations assuming an early-thermalised strongly-coupled QGP [33–35]

Chapter 2

Light-flavour hadron production in hadronic and heavy-ion collisions

The observables measured in this Thesis probe one of the most fundamental aspects of the hadron production process, namely, the conservation of quantum numbers. Specifically, the precise measurement of the antimatter-to-matter imbalance in heavy-ion collisions (Chapter 5) provides insights into the the baryon-quantum-number transport from the initial colliding nuclei to the final state system. This measurement, besides being interesting per se, is also the corner stone to carry out measurements of the fluctuation of particle yields on a collision-by-collision basis (Chapter 6). The event-by-event observables are sensitive to how the quantum numbers carried by hadrons are correlated. This directly stems from the properties of quantum number conservation in the underlying hadronisation mechanism.

The hadronisation process determines the transition from the elementary degrees of freedom of QCD, i.e. quarks and gluons, to hadrons. This process involves the non-perturbative and multi-body dynamics of quarks and gluons, hence it cannot be solved exactly from first principles. In this chapter, two of the major phenomenological models of hadronisation, namely, statistical hadronisation and Lund string fragmentation, are presented. A few experimental tests, relevant for the topics discussed in this Thesis, are then discussed.

2.1 Particle production models

2.1.1 Statistical hadronisation

The statistical hadronisation model (SHM) [36–38] provides a comprehensive description of hadron yields from small to large colliding systems by assuming that the detected hadrons are emitted by a system in chemical and thermal equilibrium at the instant of chemical freeze-out. The equilibration hypothesis is justified *a posteriori* by the successful model-to-data comparison for multiple observables [39–44]. The system is treated by means of statistical mechanics as an ideal gas of hadrons and resonances (HRG). By including resonances in the chemical composition of the system, the effect of interactions among hadrons is partially taken into account. A theoretical argument supporting the ideal HRG hypothesis is that its equation of states matches that extracted from lattice QCD in the vicinity of the pseudocritical temperature: in this sense, the HRG SHM can be viewed as a low-energy effective theory of QCD.

In the SHM, the fundamental quantity used to compute the average hadron yields and their higher order moments is the partition function of the system, Z. The specific functional form of Z depends on the statistical ensemble considered [45]. The hadron yields measured at midrapidity in high-energy heavy-ion collisions are described within a 10% accuracy across several orders of magnitude using the grand canonical ensemble (GCE) treatment of the SHM. This result is due to the limited effect of global quantum-number conservation when measuring within a limited acceptance only a subset of all produced particles. For hadron yields in smaller colliding systems, such as pp, p–Pb, and peripheral Pb–Pb collisions, as well as for the higher-order fluctuations of hadron abundances both in small and large colliding systems, the corrections due to global quantum number conservation are increasingly more relevant [46]. In these cases, a canonical ensemble (CE) treatment of the HRG is required, where quantum numbers are conserved exactly over part of the system volume.

Grand canonical ensemble

The GCE partition function is defined as:

$$Z^{GC}(T, V, \vec{\mu}) = \mathrm{Tr}\left[e^{-(H-\sum_i \mu_{Q_i} Q_i)/T}\right], \tag{2.1}$$

where T, V, and $\vec{\mu}$ are the chemical freeze-out temperature, the system volume, and the chemical potential vector, respectively. The latter is defined as $\vec{\mu} =$

(μ_B, μ_Q, μ_S), in terms of the chemical potentials, μ_{Q_i}, associated to the quantum numbers, Q_i, conserved on average in a light-flavour hadron system, namely, the baryon number, B, the electric charge, Q, and strangeness, S [47, 48]. The operator H is the Hamiltonian of the HRG. The logarithm of Eq. (2.1) can be expanded in terms of the partition functions, Z_i, associated with each of the i hadron species present in the system, as:

$$\ln Z(T, V, \vec{\mu}) = \sum_i \ln Z_i(T, V, \vec{\mu}) \tag{2.2}$$

In the macroscopic limit, assuming that the system is isotropic, the term $\ln Z_i$ can be expressed as:

$$\ln Z_i(T, V, \vec{\mu}) = \frac{V g_i}{2\pi^2} \int_0^\infty \pm p^2 \mathrm{d}p \ln[1 \pm \lambda_i \exp(-\epsilon_i/T)], \tag{2.3}$$

where g_i is the spin-degeneracy factor, p the particle momentum, $\epsilon_i = \sqrt{p^2 + m_i^2}$ the particle energy, computed with the particle mass, m_i. The quantity λ_i, also labelled as *fugacity*, is computed as:

$$\lambda_i(T, \vec{\mu}) = \exp\left(\frac{B_i\mu_B + Q_i\mu_Q + S_i\mu_S}{T}\right), \tag{2.4}$$

where B_i, Q_i, and S_i are the quantum numbers of the i-th hadron species. By Taylor-expanding the logarithm and computing the momentum integral in Eq. (2.3), the following relation is obtained:

$$\ln Z_i(T, V, \vec{\mu}) = \frac{VTg_i}{2\pi^2} \sum_{k=1}^{\infty} \frac{(\pm 1)^{k+1}}{k^2} \lambda_i^k m_i^2 K_2\left(\frac{km_i}{T}\right), \tag{2.5}$$

where K_2 is the Bessel function of second kind. The average particle abundance, $\langle N_i \rangle$, is computed by taking the derivative of the partition function with respect to the chemical potential of the i-th species, $\mu_i = B_i\mu_B + Q_i\mu_Q + S_i\mu_S$:

$$\langle N_i \rangle(T, V, \vec{\mu}) = \frac{\partial}{\partial \mu_i} T \ln Z_i(T, V, \vec{\mu}) = \frac{VTg_i}{2\pi^2} \sum_{k=1}^{\infty} \frac{(\pm 1)^{k+1}}{k} \lambda_i^k m_i^2 K_2\left(\frac{km_i}{T}\right). \tag{2.6}$$

The particle yield thus obtained is further corrected by the feed-down contributions due to heavier resonance decays. The total corrected yield is then obtained

as:

$$\langle N_i \rangle (T, V, \vec{\mu}) = \langle N_i \rangle^{th} (T, V, \vec{\mu}) + \sum_j \Gamma_{j \to i} \langle N_j \rangle^{th} (T, V, \vec{\mu}), \tag{2.7}$$

where $\langle N_i \rangle^{th}$ indicates the thermal yields, obtained via Eq. (2.6), and $\Gamma_{j \to i}$ is the decay branching fraction of resonance j to the species i. Additional effects can be included in the GCE SHM partition function, such as the short-range repulsion of hadrons via a hard-core van der Waals approach [49], as well as a realistic modelling of the width of resonances through either a Breit-Wigner description of the invariant-mass shapes or directly applying the measured phase shifts [50]. The parameterisation of these corrections relies on the known properties of the measured hadron spectrum.

The thermal parameters of the model, T, V, and $\vec{\mu}$, are extracted by comparing the model calculations with the experimental data of hadron yields. The number of degrees of freedom can be reduced by requiring the conservation of quantum numbers from the intitial system of colliding ions to the final state HRG. Specifically, the conservation of B, Q, and S implies the following relations:

$$V \sum_i n_i B_i = B_{\mathrm{S}}, \quad V \sum_i n_i Q_i = Q_{\mathrm{S}}, \quad V \sum_i n_i S_i = 0, \tag{2.8}$$

where B_S and Q_S denote the fraction of baryon quantum number and electric charge transported from the colliding ions to the midrapidity region. The effect of quantum number transport in the SHM analysis is described more in detail in Section 2.2.1. Either all or a subset of these conditions can be exploited to constrain the model parameters as a function of the remaining degrees of freedom, depending on the hadron species used in the model-to-data comparison. By requiring all of the conditions in Eq. (2.8), the only free parameters left in the GCE SHM are T, μ_B, and V.

Canonical ensemble

In the CE treatment of the SHM, the quantum numbers B, Q, and S, are conserved exactly over a correlation volume, V_c. Consequently, the total quantum numbers of the system are set to fixed values. The functional form of the partition function is obtained by considering that each of the quantum numbers conserved in the

HRG are associated to Abelian symmetries:

$$Z(B,Q,S) = \int_{-\pi}^{\pi} \frac{\mathrm{d}\phi_B}{2\pi} \int_{-\pi}^{\pi} \frac{\mathrm{d}\phi_Q}{2\pi} \int_{-\pi}^{\pi} \frac{\mathrm{d}\phi_S}{2\pi} e^{-i(B\phi_B+Q\phi_Q+S\phi_S)} \times \exp\left[\sum_j \sum_{n=1}^{\infty} z_j^n e^{in(B_j\phi_B+Q_j\phi_Q+S_j\phi_S)}\right], \tag{2.9}$$

where the index j runs over all of the species present in the HRG, while the index n takes into account the quantum statistics. The partition functions, z_j^n, associated to the single particles, are computed as:

$$z_j^n = (\pm 1)^{n-1} V_c \int \mathrm{d}m \rho_j(m) g_j \frac{m^2 T}{2\pi^2 n^2} K_2(nm/T), \tag{2.10}$$

where the mass integration weighted by the mass distribution, $\rho_j(m)$, is introduced to extend the definition to finite-width resonances.

Similarly to the GCE treatment, the hadron yields are determined in the CE SHM starting from the derivatives of the partition function, Eq. (2.9). The average abundance of the j-th species is computed as:

$$\langle N_j \rangle = \sum_{n=1}^{\infty} \frac{Z(B - nB_j, Q - nQj, S - nS_j)}{Z(B,Q,S)} \, n z_j^n \tag{2.11}$$

These thermal yields can be further corrected using Eq. (2.7) to add the resonance feed-down component.

The canonical conservation of quantum numbers affects the hadron yields computed in small collision systems, where the multiplicity of particles carrying the conserved quantum numbers is smaller. In addition, the charge conservation affects the higher-order fluctuations of the conserved quantum number. In principle, no fluctuation is expected when analysing the full system, as quantum numbers are conserved exactly over its extension. However, experimental observations are usually limited to a finite fraction of the available phase space due to the finite acceptance of the detectors: in this case, the observed balance of charges may fluctuate on an event-by-event basis. These effects can be modelled through the subensemble acceptance method (SAM) [51], which provides an analytical treatment of the finite acceptance effect by assuming that the detected particles are produced in a fixed fraction, α, of the total system volume. In the simple case

of one conserved charge, e.g., the baryon number B, the partition function of the system is determined by:

$$Z(T,V,B) = \sum_{B_1} Z(T,V_1,B_1)Z(T,V_2,B-B_1), \tag{2.12}$$

where the subvolume $V_1 = \alpha V$ and its complementary, $V_2 = (1-\alpha)V$, are assumed to be larger than the baryon-number correlation length, ξ, i.e., $V_1, V_2 \gg \xi^3$. In this approach, the probability $P(B_1)$ to find B_1 baryons in the subvolume V_1 scales as the product of the partition functions of the two subsystems:

$$P(B_1) \propto Z(T,V_1,B_1)Z(T,V_2,B-B_1) \tag{2.13}$$

The baryon number fluctuations in the subvolume V_1 can be quantified by the cumulants, $\kappa_n[B_1]$, of order n. The cumulants are defined as the coefficients of the Taylor expansion of the generating function $G_{B_1}(t) \equiv \ln\langle\exp(tB_1)\rangle$:

$$\kappa_n[B_1] \equiv \left.\frac{\partial G_{B_1}(t)}{\partial t^n}\right|_{t=0} \tag{2.14}$$

In the thermodynamic limit, the cumulants obtained with the SAM are proven to be related to the GCE susceptibility of the total baryon number, $\chi_n^B = \partial^n \hat{p}/\partial \hat{\mu}_B^n$, where $\hat{p} \equiv p/T^4$ is the reduced thermodynamic pressure and $\hat{\mu}_B \equiv \mu_B/T$ the reduced baryon chemical potential [51, 52]. The volume fraction, α, also enters these relations. For instance, the ratio between the second-order and first-order cumulants, corresponding to the scaled variance, is determined by:

$$\frac{\kappa_2[B_1]}{\kappa_1[B_1]} = (1-\alpha)\frac{\chi_2^B}{\chi_1^B} \tag{2.15}$$

From Eq. (2.15), it is observed that the scaled variance approaches the GCE susceptibilities only in the limit $\alpha \to 0$, while the limit $\alpha \to 1$ yields $\kappa_2[B_1]/\kappa_1[B_1] \to 0$, as expected from the exact conservation of baryon number over the full volume. The SAM can be extended also to the case of multiple conserved charges, which is foreseen by the HRG model [53]. In addition to the analytical treatment, the static subvolume assumption can be also implemented numerically through a Monte Carlo (MC) procedure [54].

Besides the SAM, alternative approaches are available to describe the effect of the

canonical quantum number conservation on higher-order moments of conserved quantum numbers measured in a limited acceptance. Recently, a new method has been proposed to reproduce the rapidity correlations among hadron multiplicities caused by the quantum number conservation, as described in Ref. [55]. This novel approach enables to describe the quantum-number correlations by means of a rapidity correlation length parameter, $\Delta y_{\rm corr}$. As such, it differs from the SAM, where charge conservation effects are imposed by fixing a subvolume of the system within a box approximation. The simple case of Gaussian rapidity distributions is solved analytically by writing the covariance matrix Σ of the joint rapidity distribution of hadrons via the Cholesky factorisation. Using this decomposition, the Σ matrix is expressed as the product of the lower-triangular matrix L with its transpose:

$$\Sigma = \begin{pmatrix} \sigma_{x_1}^2 & \rho\sigma_{x_1}\sigma_{x_2} \\ \rho\sigma_{x_1}\sigma_{x_2} & \sigma_{x_2}^2 \end{pmatrix} = LL^T, \text{ where } L = \begin{pmatrix} \sigma_{x_1} & 0 \\ \rho\sigma_{x_2} & \sqrt{1-\rho^2}\sigma_{x_2} \end{pmatrix}. \quad (2.16)$$

The L matrix is used in Monte Carlo simulations to generate rapidity-correlated hadron multiplicities starting from uncorrelated Gaussian-distributed random numbers. The rapidity correlation length is related to the covariance matrix parameters. Assuming $\sigma_{x_1} = \sigma_{x_2} = \sigma$, as for the case of (anti)baryons at the LHC, $\Delta y_{\rm corr}$ is determined by:

$$\Delta y_{\rm corr} = 4\sigma\sqrt{1-\rho}. \quad (2.17)$$

In the general case of arbitrary rapidity distributions, the correlations among quantum numbers are introduced through a numerical procedure based on the Metropolis algorithm. At present, this approach has been successfully applied solely to the case of a single conserved quantum number, e.g., the baryon number. Due to this limitation, in this Thesis only the numerical implementation of the SAM is used to compare model calculations and experimental data.

2.1.2 Lund string fragmentation

The Lund string fragmentation model [56] provides a QCD-inspired description of the hadronisation process. This model, initially proposed to describe the jet fragmentation process in e^+e^- collisions, was subsequently extended to the more complex hadronic and hevay-ion collisions. Currently, it is employed in some of the most widespread MC event generators used in high-energy particle and nuclear physics, namely, PYTHIA [57], also in the ANAGANTYR[58] version for heavy-ion collisions, and HIJING [59].

The main hypothesis of the model is that the colour field between a quark and an antiquark is contained in a flux tube, also referred to as colour string, characterised by a Cornell-like potential [60] containing a linarly increasing term for large quark-antiquark distances. Due to the initial kinematics of the quark and antiquarks, the inter-pair distance can increase resulting in an increase of the potential energy stored by the string. This may eventually lead to the breaking of the colour string with the subsequent creation of a new quark-antiquark pair at the ends of the broken flux tube. This process is schematically shown for 1-dimensional strings in a space-time diagram, (x, t), in Fig. 2.1.

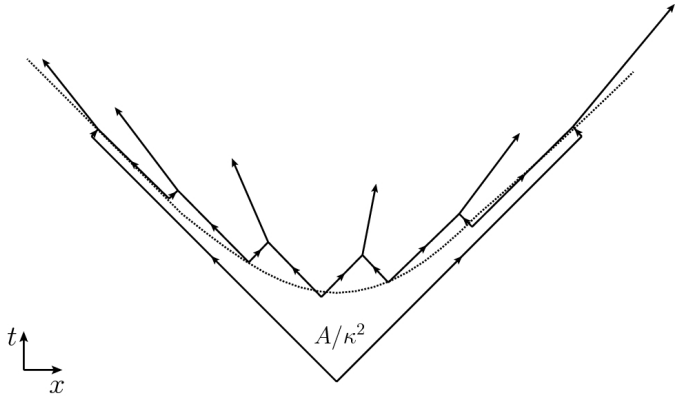

Figure 2.1: Space-time diagram of the string fragmentation process for 1-dimensional strings connecting massless quarks [57]. The outgoing mesons formed in the string fragmentation are represented by arrows. The area, A, of the space-time surface spanned by the propagating strings determines the string breaking probability, as $\mathcal{P} \propto \exp(-A/\kappa^2)$. Due to the causality conditions, the string fragmentation vertices lie on the hyperbola shown with a dashed line.

The creation of a $q\bar{q}$ pair with quark mass m and transverse momentum $p_\perp$ can be treated quantum-mechanically as a tunneling process. The tunneling probability is computed via the semiclassical approximation as [57]:

$$\frac{1}{\kappa}\frac{\mathrm{d}\mathcal{P}}{\mathrm{d}^2 p_\perp} \propto \exp(-\pi m_\perp^2/\kappa) = \exp(-\pi m^2/\kappa)\exp(-\pi p_\perp^2/\kappa), \tag{2.18}$$

where $m_\perp = \sqrt{m^2 + p_\perp^2}$ is the transverse mass of the (anti)quark and $\kappa \approx 1\,\mathrm{GeV/fm}$ is the string tension parameter. The relation of Eq. (2.18) naturally introduces the quark flavour in the model through the quark mass parameter. However, as this quantity cannot be uniquely defined, the relative suppression of flavour is

taken as an external input parameter tuned on experimental observations, e.g., data collected at LEP.

In its simplest form, this mechanism is suited to describe the production of light-flavour mesons from the sequential breaking of a colour string. The gluon radiation processes can be also included in the model by describing gluons as kinks of the strings, in a similar way as obtained in the large colour number, N_c, limit of QCD. In the simple string-fragmentation picture, the production of baryons is determined by two mechanisms. On the one hand, diquark-antidiquark pairs can be produced in the string breaking, leading to the formation of a baryon-antibaryon pair. On the other, baryons can be created through the so-called popcorn mechanism. In this process, a $q\bar{q}$ pair is first produced as a vacuum fluctuation on the string, without breaking it. The string is subsequently broken by the formation of a new $q\bar{q}$ pair, in a similar process as for the meson production.

In recent years, the simple string fragmentation picture has been expanded with additional mechanisms to describe multiple experimental observations. These processes are implemented in the PYTHIA 8 [57] MC event generator. Specifically, interactions among the strings are introduced to model the high-colour-density environment formed in high-multiplicity hadronic collisions. These interaction mechanisms include both the string shoving process [61] and the colour rope hadronisation [62]. The former model takes into account the interactions originating from the repulsive forces between neighbouring strings; the latter describes the formation of overlapping string topologies, called ropes, where the enhanced string tension leads to an enhanced production of heavier flavours, specifically, strangeness.

In the string fragmentation model, the starting colour configuration for the hadronisation process is determined by matching the final-state partons carrying specific colours with those carrying the relative anticolours. The treatment of colour configurations beyond the leading colour connections is required in hadronic collisions, where more complex colour configuration arise due to the multiparton environment. In the PYTHIA 8 event generator, this is carried out via different colour reconnection (CR) mechanisms. The state-of-the-art implementation of CR [63], based on the SU(3) colour algebra, entails the formation of Y-shaped three-string topologies, called junctions, carrying baryon number [64]. The junction formation is responsible for an enhanced production of baryons compared to the baseline provided by both the diquark formation and the popcorn process. This mechanism is

required to describe the baryon-to-meson yield ratios measured in high-multiplicity pp collisions at the LHC [63].

2.2 Experimental tests of hadronisation models

Using the phenomenological models described in Section 2.1, it is possible to obtain expectations for the observables measured in high-energy nuclear physics experiments. The model calculations are compared to the experimental data both to verify the hadronisation mechanism assumed in the model and to constrain the free parameters of the model. In the following, a set of model-to-data comparisons addressing both points are shown. These works represent the state-of-the-art phenomenological understanding of the available experimental results. The main open questions explored in this Thesis are highlighted in the discussion.

2.2.1 Heavy-ion collisions and grand-canonical statistical hadronisation

The GCE SHM offers a comprehensive approach to compute the yields of light-flavour hadrons produced at midrapidity in heavy-ion collisions. As mentioned in Section 2.1.1, the free parameters of the model are extracted by determining the configuration that better describes the measurements. The validity of the statistical-mechanical approach is also tested by the degree of matching between the model calculation and the experimental data.

The comparison between the SHM calculations, obtained with four independent codes [19, 54, 65, 66], and the light-flavour hadron yields measured by the ALICE Collaboration in the 10% most central Pb–Pb collisions at $\sqrt{s_{\rm NN}} = 2.76$ TeV is shown in Fig. 2.2. The experimental measurements include the average integrated yields of light flavour hadrons detected by the ALICE apparatus: the light charged mesons, $\pi^{\pm}$ and $\rm K^{\pm}$; the neutral mesons, $\rm K^0_S$ and ϕ; (multi)strange and non-strange baryons, ($\bar{\rm p}$)p, ($\bar{\Lambda}$)Λ, ($\bar{\Xi}^+$)Ξ^-, and ($\bar{\Omega}^+$)Ω^-; the light (hyper)nuclei, deuteron ($\bar{\rm d}$)d, helium-3 ($^3\overline{\rm He}$)^{3}He, hypertriton ($^3_{\bar{\Lambda}}\overline{\rm H}$)$^3_{\Lambda}$H (a bound state of a proton, a neutron, and a Λ hyperon), and helium-4 ($^4\overline{\rm He}$)^{4}He. The yields of the charge conjugated states are determined separately when present.

The GCE SHM implementations reported in Fig. 2.2 include: the THERMUS package [65], based on the CERN ROOT framework [68]; the SHARE model [66], written in FORTRAN; the GSI-Heidelberg model [19, 50]; the open-source THERMAL-FIST software [54]. These computer programs allow us to carry out GCE SHM calculations of hadron yields including the effects of resonance feed-down. The input

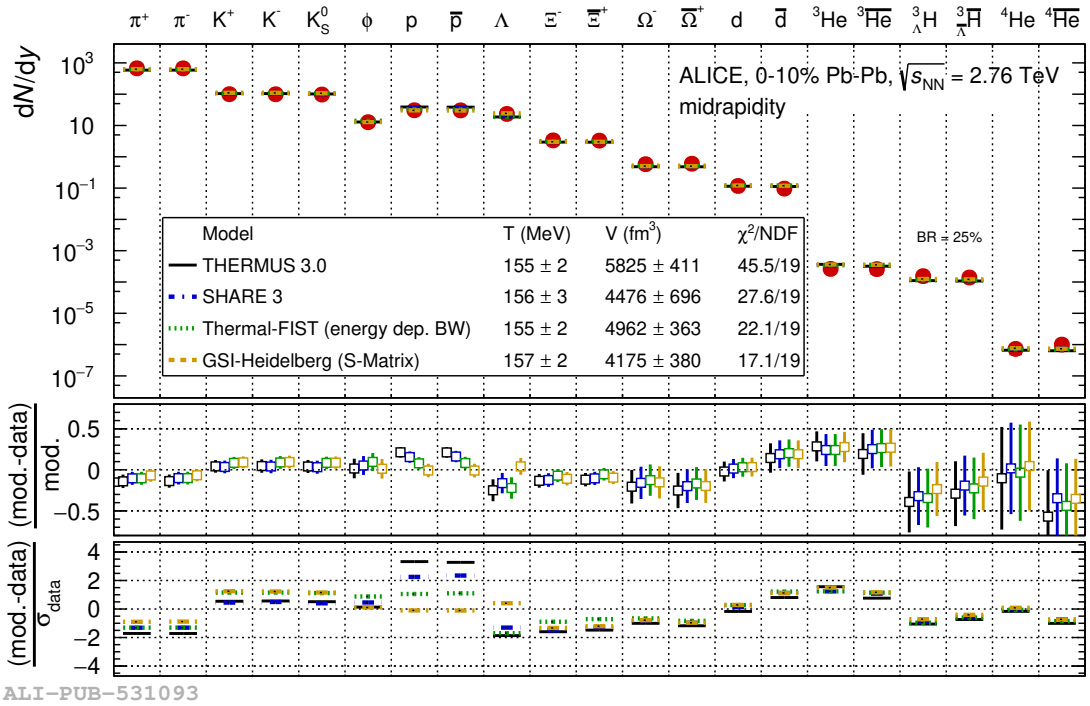

Figure 2.2: Comparison between the GCE SHM expectations and the ALICE Collaboration measurements of hadron yields at midrapidity in the 10% most central Pb–Pb collisions at $\sqrt{s_{\rm NN}} = 2.76$ TeV [67]. The goodness of fit is quantified both globally via the χ^2/NDF reported in the legend and locally through the pull and $n\sigma$ computed for each species. The latter quantities are shown in the two lower panels of the figure.

parameters of these models are both the HRG thermal parameters and the list of considered resonance decays, based on the measured hadron spectrum reported by the Particle Data Group [9]. The THERMUS and THERMAL-FIST packages also include both the description of hard-core hadronic repulsion via an excluded volume approach and the treatment of resonance widths via Breit-Wigner parameterisations, while the GSI-Heidelberg model introduces resonance widths via the phase-shift formalism described in Ref. [50].

The measured yields span across 10^9 orders of magnitude, going from the most abundant light mesons to the rarely produced nuclei. In the nuclei sector, a yield reduction factor of 10^{-3} is observed for each added nucleon. These general properties are well described by the GCE SHM, where an approximate exponential dependence of the yield on the mass is expected, $\mathrm{d}N/\mathrm{d}y \propto \exp(-m/T)$. This approximate relation is derived from the asymptotic expansion of Bessel functions for $m/T \gg 1$. The thermal parameters extracted from the fit of the hadron yields are reported in the legend of Fig. 2.2. The results obtained with the different implementations of the GCE SHM show that the chemical freeze-out temperature is $T \approx 155$ MeV. This value is close to the pseudo-critical temperature of the crossover transition between the confined and deconfined phases as extracted from lattice QCD.

Chemical potentials and baryon number stopping

In the GCE SHM, the chemical potentials determine the average balance of quantum numbers at midrapidity in the collision. This is verified by computing the multiplicity of particles and antiparticles for a given species via Eq. (2.6). The only difference between the charge conjugated states is the sign of the quantum numbers in the fugacity factor, Eq. (2.4), hence the yields of particles and antiparticles are exactly balanced only if $\vec{\mu} = \vec{0}$. For example, the baryon chemical potential, μ_B, which drives the net-baryon number distribution in the midrapidity region, regulates the average balance of baryon number at midrapidity. Consequently, the chemical potentials extracted by comparing the experimental results with the predictions of the SHM provide a global characterisation of the average balance between the matter and antimatter produced at midrapidity in collisions.

The main source of the imbalance between the matter and antimatter in heavy-ion collisions is the transport of quantum numbers from the colliding nuclei to the midrapidity region due to the interactions between the incoming ions. Different phenomenological models are used to describe this phenomenon, mainly

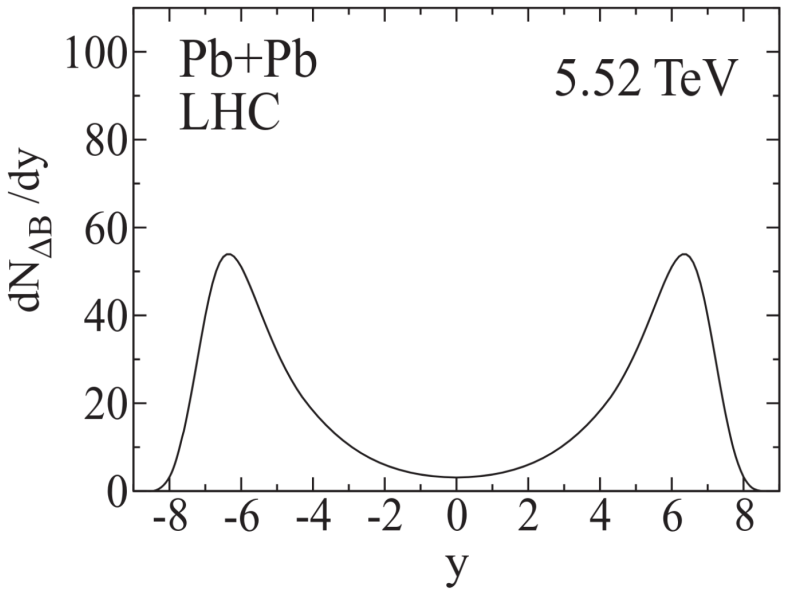

Figure 2.3: Rapidity-differential net-baryon yield predicted for Pb–Pb collisions at $\sqrt{s_{\mathrm{NN}}} = 5.52$ TeV [69].

focusing on baryon number transport, which is also referred to as *baryon number stopping*. In the colour glass condensate model (CGC), the gluons emitted by static colour sources, corresponding to the quarks inside the ions the are experiencing the effects of time dilation, transfer energy to the midrapidity region. Using the CGC, the rapidity-differential net-baryon yield was predicted for Pb–Pb collisions at $\sqrt{s_{\mathrm{NN}}} = 5.52$ TeV before the start of data taking with Pb beams at the LHC [69]. These predictions are shown in Fig. 2.3. It can be observed that the distribution is peaked at $y \approx \pm 6$, implying a rapidity loss from the colliding beams to the beam remnant of $\Delta y \approx 2$. In addition, the net-baryon density expected at midrapidity is suppressed compared to the forward and backward regions: this effect is enhanced in the multi-TeV regime of the LHC compared to lower-energy facilities, where the initial rapidity gap between the incoming ions is reduced. Other baryon number stopping models rely on the colour string picture: they include the diquark breaking model [70] and the baryon junction model [71], both of which have been introduced in Section 2.1.2. The latter mechanism is implemented in the HIJING/B$\bar{\mathrm{B}}$ model [71]. The predictions for baryon number stopping at the LHC obtained with different baryon transport models were summarised in Reference [72]. An alternative approach, explored in a more recent work, describes baryon number stopping in a fully statistical-mechanical picture

as a non-equilibrium transport problem [73].

Over the past decades, the baryon chemical potential has been determined from the heavy-ion experimental data collected by various Collaborations at different accelerator facilities [19, 50, 74–114]. The availability of datasamples collected with different collision systems and centre-of-mass energies enables the collision-energy scan of μ_B and hence of the baryon number stopping effects. The results obtained with the GSI-Heidelberg model [19, 111, 115] using data collected at the AGS, SPS, RHIC, and LHC, are shown in Fig. 2.4. The energy scan of the chemical freeze-out temperature is also shown. The results show a decreasing trend of μ_B for increasing energies, while the chemical freeze-out temperature, denoted as $T_{\rm cf}$, increases for increasing collision energies. In addition, $T_{\rm cf}$ saturates to values close to 155 MeV for $\sqrt{s_{\rm NN}} \approx 10$ GeV, while μ_B reaches values close to zero only in the TeV scale. For reference, in Au–Au collision at the top RHIC energy, $\sqrt{s_{\rm NN}} = 200$ GeV, the chemical potential is $\mu_B \approx 20$ MeV [114]. This first observation indicates that baryon number stopping effects have a progressively smaller impact on the system formed around midrapidity for increasing energy of the colliding nuclei. The μ_B value extracted from the hadron yields measured by the ALICE Collaboration at the LHC in the 10% most central Pb–Pb collisions at $\sqrt{s_{\rm NN}} = 2.76$ TeV is $\mu_B = 0.7 \pm 3.8$ MeV [19, 50]. This value, compatible with zero within uncertainties, suggests that a balance between matter and antimatter is achieved at midrapidity in central Pb–Pb collision. However, this result is affected by a large uncertainty: the main reason is the lack of a proper treatment in the SHM-to-data comparison of uncertainties correlated between particles and antiparticles of the same species, as the full covariance matrix of the measurements was not published.

An additional and complementary handle to test baryon number stopping consists of analysing the dependence of μ_B on the centrality of the collision for a fixed value of $\sqrt{s_{\rm NN}}$, as the amount of interactions is driven by the overlap between the colliding ions. This phenomenon was investigated by the STAR Collaboration at the RHIC beam energy scan (BES) I [114]: the obtained results are shown in Fig. 2.5. The SHM parameters were determined by fitting the antiparticle-to-particle yields ratios measured for various hadron species in each centrality interval and for each centre-of-mass energy. In this way, the particle-antiparticle correlated systematic contributions can be easily cancelled out when carrying out the estimation of the thermal model parameters. The μ_B results show an increasing trend for increasing average number of participating nucleons, $\langle N_{\rm part} \rangle$, across the

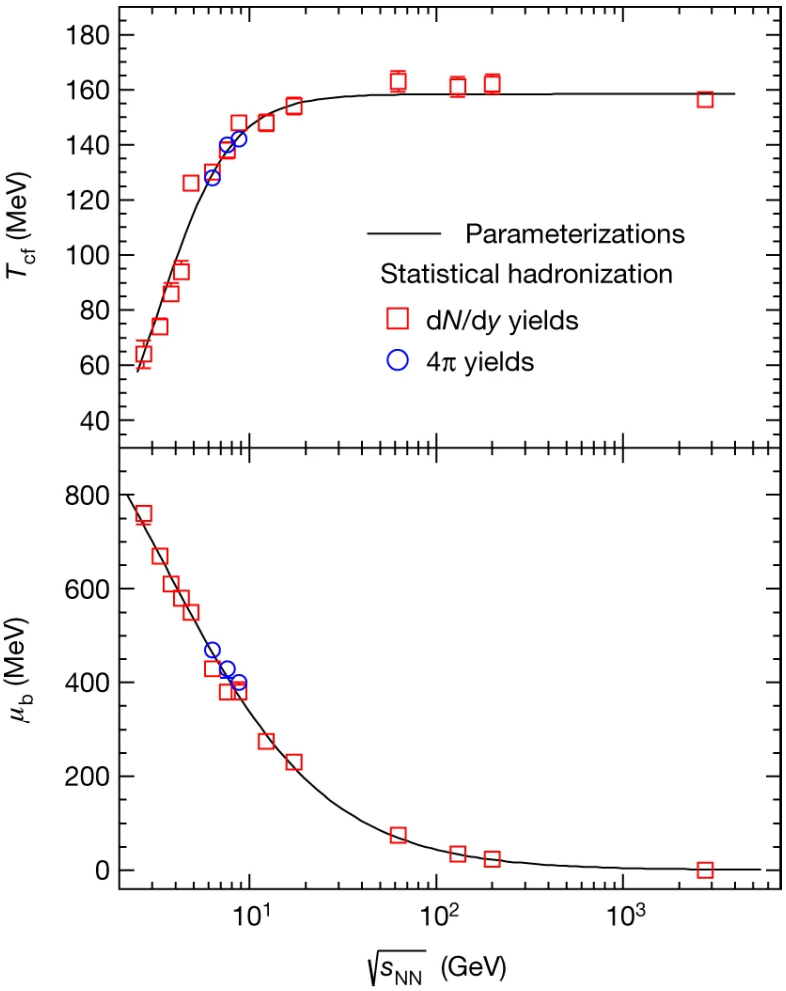

Figure 2.4: Chemical freeze out temperature, T_{cf}, and baryon chemical potential, μ_{b}, extracted from hadron yield and yield ratios measured at the AGS, SPS, RHIC, and LHC, as a function of the centre-of-mass energy, $\sqrt{s_{\mathrm{NN}}}$ [19]. Two phenomenological parameterisations extracted from the data are also shown.

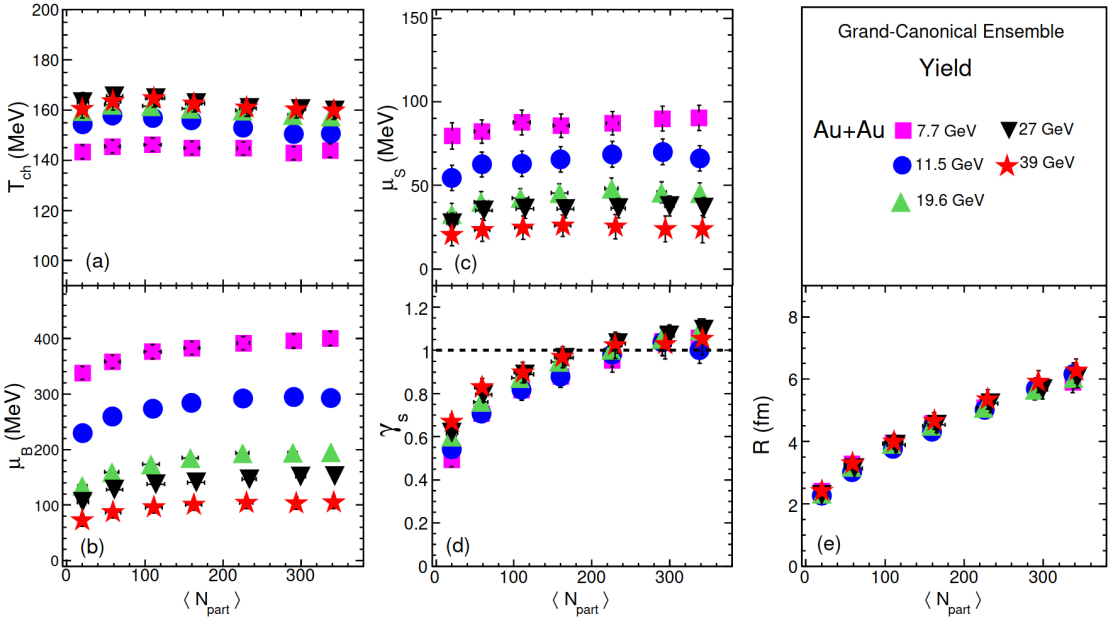

Figure 2.5: GCE SHM parameters extracted as a function of centrality by the STAR Collaboration at the RHIC BES I [114].

centre-of-mass energy range explored in the BES I. This observation suggests that, in the low-energy regime, baryon number stopping has a larger impact on the particle system created in the most central collisions. These effects are analysed for the first time also at the LHC in this Thesis.

2.2.2 Production of light-flavour hadrons across colliding systems

The hadronisation models introduced in Section 2.1 are tested in detail also by analysing the yields of light-flavour hadrons in different colliding systems. In this context, (multi)strange hadrons and light nuclei are among the most studied species. In both cases, different hadronisation mechanisms enable a successful description of the measured yields. As discussed in the following, event-by-event fluctuations of the hadron multiplicities provide a better discrimination among different models, due to their sensitivity to correlations induced by quantum-number conservation effects.

Strange hadrons

The yields of strange hadrons observed in heavy-ion collisions show an enhancement compared to those obtained in e^+e^- interactions [101, 116, 117]. This ex-

perimental observation was initially considered to be a probe of the formation of a deconfined partonic phase [118]. Specifically, it was suggested that the gluon fusion process, $gg \rightarrow s\bar{s}$, which drives the production of (anti)strange quarks in heavy-ion collisions, would be enhanced in a colour-deconfinement regime. More recent studies showed that these effects can be described also in the SHM framework, where no deconfined hypothesis is required [119]. In that case, the CE formulation was used in peripheral collisions, where lower particle multiplicities are achieved, while the GCE formulation is suited to describe central collisions.

The latest experimental results obtained at the LHC for the strange-to-non-strange hadron yield ratios measured in pp [120], p–Pb [121], and Pb–Pb collisions [122] over a large range of average charged particle multiplicity at midrapidity, are shown in Fig. 2.6. These results show a continuous evolution of the yield ratios, with an increasing trend for increasing multiplicity of the collision, with a saturation towards central Pb–Pb collisions. This increase is especially more pronounced for species with a higher strangeness content, such as $\Xi^{\pm}$ and $\Omega^{\pm}$. In Fig. 2.6, the experimental points are compared with the calculations of different phenomenological models. The Monash tune of PYTHIA 8, adjusted to reproduce measurements carried out at e^+e^- accelerators, underpredict the yield ratios observed in pp collisions except for the lowest multiplicity measurement: this is expected, as no enhancement of strangeness yields is observed in e^+e^- reactions. The increasing trend is qualitatively described by EPOS LHC [124], which describes particle emission from a source composed of thermalised *core* and a *corona* dominated by string-breaking processes: the increasing trend is driven by the interplay between the two components of the source, with the corona dominating for smaller multiplicities. A more quantitative description of the experimental results is provided by the DIPSY model [125], which introduces rope hadronisation on top of PYTHIA string breaking implementation. This indicates that, at the level of the average yields, the strangeness enhancement phenomenon can be quantitatively described in a colour string picture. This is also confirmed in more recent works, where also the QCD-based colour reconnection mode is included [126].

An equally satisfactory quantitative description of the yield ratios can be achieved using the CE SHM. In Fig. 2.7, the computations obtained with the THERMAL-FIST model [54] are compared with the measurements obtained by the ALICE Collaboration in different colliding systems [127]. The THERMAL-FIST model contains an additional parameter, γ_s, to describe the undersaturation of the strangeness production which is required to describe the yields of (multi)strange hadrons. This

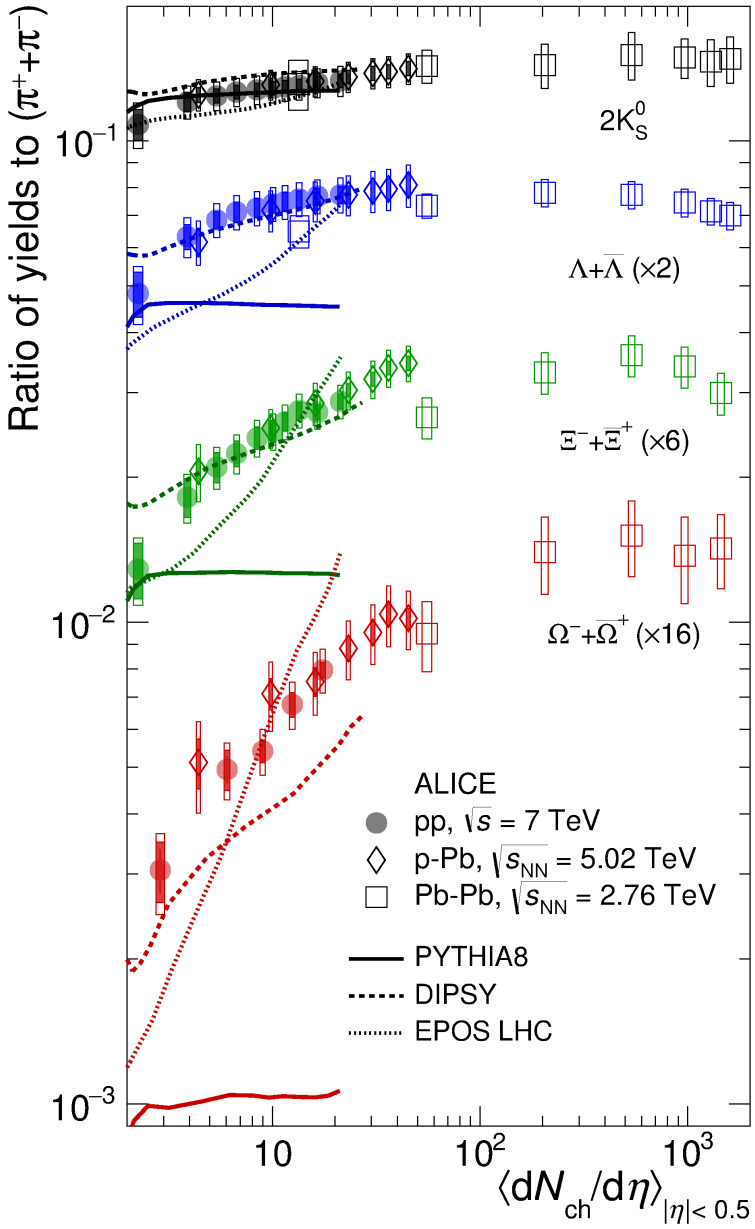

Figure 2.6: Yield ratios of (multi)strange hadron and charged pions measured by the ALICE Collaboration in pp, p–Pb, and Pb–Pb collisions at the LHC [120]. The predictions of PYTHIA 8 Monash [123], EPOS LHC [124], and DIPSY [125] are also shown.

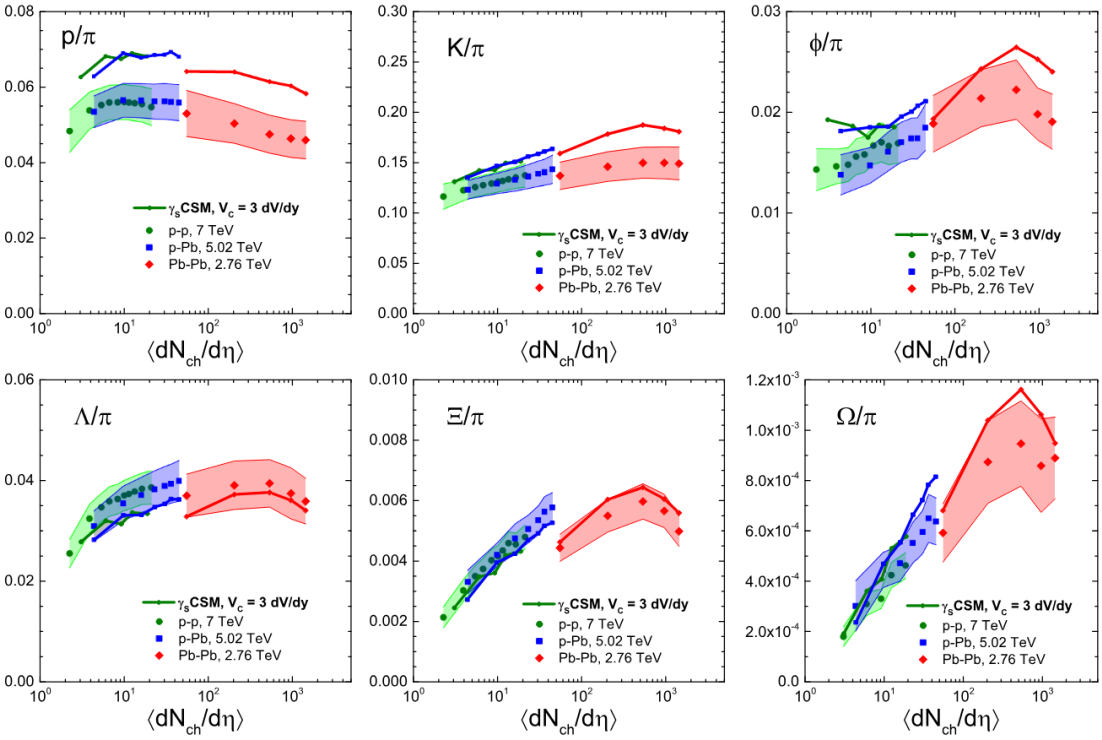

Figure 2.7: Comparison of the yield ratios of light flavour hadrons and charged pions, measured by the ALICE Collaboration in pp, p–Pb, and Pb–Pb collisions, and the results of the THERMAL-FIST model [54, 127]. The correlation volume, V_c, is expressed in terms of the volume per one rapidity unit, $\mathrm{d}V/\mathrm{d}y$.

parameter, which is equal to unity in central Pb–Pb collisions, decreases with decreasing multiplicity, reaching about 0.7 in the low-multiplicity pp collisions. The other thermal parameters, extracted from a fit of the experimental data, also evolve with multiplicity. Alternative implementations of the CE SHM, relying on a different parameterisation of the canonical volume [128], can also describe the multiplicity-evolution of (multi)strange hadron yields without the γ_s parameter.

Light nuclei

In heavy-ion collisions, among the produced hadron species, also light (anti)nuclei and (anti)hypernuclei are observed. These bound states are characterised by binding energies $O(1-10$ MeV) per nucleon, which are smaller by about one order of magnitude than the chemical freeze-out temperature extracted from GCE SHM fits to the hadron yields, including the nuclei ones [19].

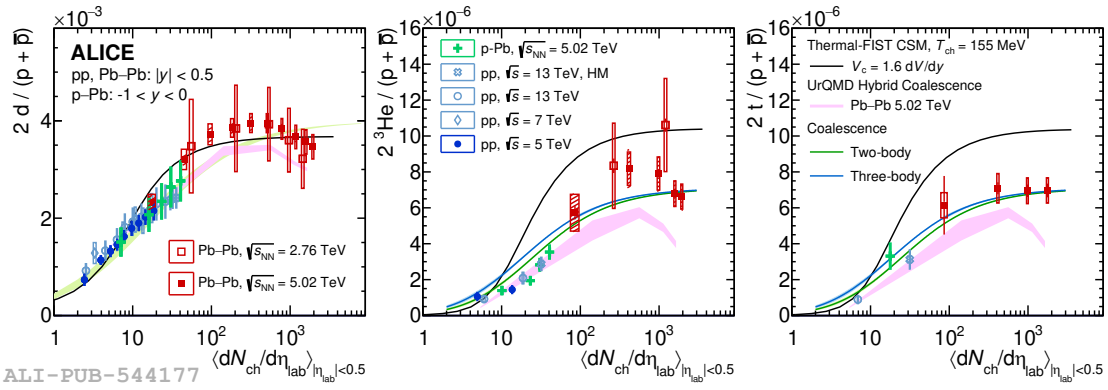

Figure 2.8: Yield ratios between light (anti)nuclei and (anti)protons measured by the ALICE Collaboration in pp, p–Pb, and Pb–Pb collisions, at different centre-of-mass energies. The experimental results are compared with different model predictions.

This observation challenges the statistical-thermal interpretation of nucleosynthesis in heavy-ion collision, where the shallow-bounded nuclear clusters emitted on the chemical freeze-out hypersurface should be equilibrated with the full hadron phase. An alternative description of (anti)nucleosynthesis in the laboratory is given by the coalescence model, which assumes that nuclei are produced by the merging of preformed nucleons close in phase space [129]. The state-of-the-art coalescence calculations [130–132] are based on the Wigner function formalism, which extends the treatment of phase-space distributions to a fully quantum-mechanical picture.

In recent years, the ALICE Collaboration carried out an extensive measurement campaing of (anti)(hyper)nuclei yields across different colliding systems for different centre-of-mass energies of the collision. The most recent measurements of ratios between (anti)nuclei yield and (anti)proton yields are shown in Fig. 2.8, for d, ^{3}He, and ^{3}H. The measured yield ratios show a continuous evolution across the analysed multiplicity range, with an increasing trend from low- to high-multiplicity collisions. This observations suggests that a common production mechanism drives light nuclei production. Both the statistical-hadronisation and coalescence pictures are tested by comparing model predictions and experimental data. The SHM calculations are obtained using the CE treatment to describe the suppression of the yield ratios in low-multiplicity collisions. In this case, the observed trends are the result of the exact conservation of quantum numbers, which has a more sizeable

effect for smaller systems. A similar trend can be also obtained with coalescence calculations, where the multiplicity evolution is caused by the interplay between the size of the nucleon emitting source and the size of the formed nucleus itself. For (anti)deuterons, both models provide a satisfactory description of the experimental data. On the contrary, the yield ratios for heavier nuclei are better described in the coalescence picture, expecially in heavy-ion collisions, where the maximum difference, ≈30%, is observed between the two models. Similar conclusions are also extracted for the hypertriton, ${}^{3}_{\Lambda}\mathrm{H}$ [133]. In this case, the difference between the predictions of the two frameworks are magnified by the shallow binding energy of the system: the separation energy of the Λ hyperon in this hypernucleus is $B_\Lambda = 102 \pm 63(\mathrm{stat.}) \pm 67(\mathrm{syst.})$ keV [134].

Multiplicity fluctuations as a probe of hadronisation

The results shown in Section 2.2.2 show that different hadronisation mechanisms can quantitatively describe experimental data of average yields and yield ratios. Event-by-event observables, such as higher-order fluctuations of the hadron multiplicites, provide a better discrimination among different models. The reason for this is the connection between cumulants of the multiplicity distributions of hadrons carrying certain quantum numbers and the correlation among those quantum numbers. These observables, including the scaled variance defined in Eq. (2.15), as well as other ratios of cumulants, are studied in this Thesis to characterise strange-hadron and light-nuclei production mechanisms. Specifically, it is useful to define a Pearson correlation coefficient, ρ_{AB}, in terms of both the diagonal and off-diagonal second-order cumulants, $\kappa_2(A)$ and $\kappa_{11}(A, B)$, for the species of interest, A and B:

$$\rho_{AB} = \frac{\kappa_{11}(A, B)}{\sqrt{\kappa_2(A)\kappa_2(B)}} \tag{2.19}$$

This coefficient provides a measure of the average linear dependence between the yields observed for both species A and species B. In the present case, the yields of any two different hadron species, identified by a defined set of quantum numbers, are (anti)correlated due to the underlying conservation of quantum numbers through the particle production process. For instance, the conservation of baryon number determines an anticorrelation between the yields of any two baryon species produced in the collisions. The properties of the underlying hadronisation mechanism determine the strength of the correlation that is measured within the experimental acceptance.

As an example of the connection between fluctuation measurements and hadro-

nisation, the Pearson correlation coefficient of the antiproton number and antideuteron number measured by the ALICE Collaboration in Pb–Pb collisions at $\sqrt{s_{\rm NN}}$ = 5.02 TeV is shown in Fig. 2.9 [135]. The results indicate a significant

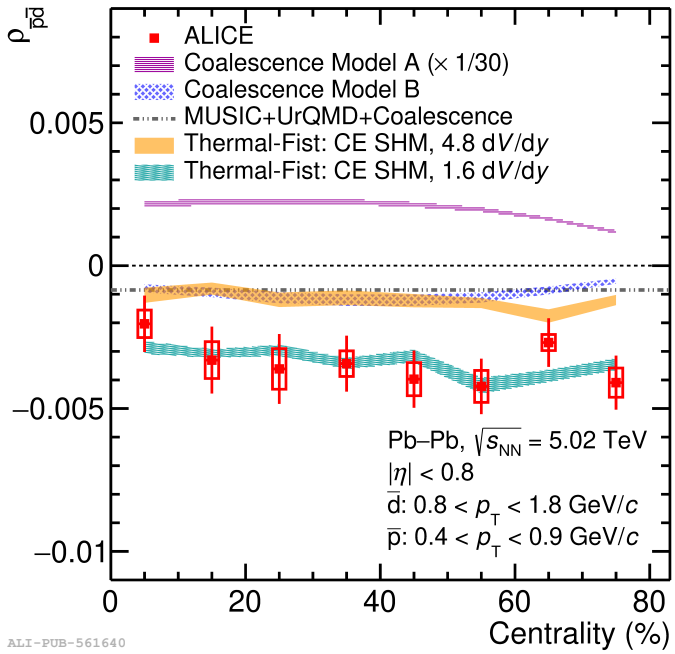

Figure 2.9: Pearson correlation coefficient between the antideuteron number and antiproton number in Pb–Pb collisions, as a function of collision centrality.

anticorrelation between the antideuteorn and antiproton numbers, as a result of the conservation of the baryon quantum number. The experimental results are compared with different model predictions to obtain a quantitative interpretation. Specifically, different versions of coalescence are considered: two of them, models A and B, are simple coalescence implementations assuming either correlated or uncorrelated antinucleon production [136]. In addition, a more refined model is used, including the hydrodynamic system expansion via the MUSIC model [137–139], the evolution of the hadronic phase through UrQMD [140, 141], and finally the nuclear coalescence [142]. Complementary predictions are also obtained with the CE SHM implementation of THERMAL-FIST: two different calculations for different canonical volumes values are shown. Overall, the different models provide contrasting predictions, and not all of the models are able to describe the data quantitatively. Apart from model A, all models predict a negative correlation: in coalescence models, the merging of nucleons imply a short-range anticorrelation between nucleons and the formed nuclei; on the contrary, in the CE SHM, the

anticorrelation arises from the exact baryon number correlation across the full volume. In the SHM case, the conservation volume size determines the strength of the Pearson correlation coefficient: the larger the volume, the smaller the correlation strength. From the model-to-data comparison, the CE SHM model with a small conservation volume, $V_c = 1.6\ \mathrm{d}V/\mathrm{d}y$, is favoured by the data: this parameterisation is also suited to describe the d/p yield ratio in small colliding systems. This result is in contrast with event-by-event measurements exclusively involving (anti)protons [143]: in that case, the fluctuation observables are consistent with a larger conservation volume, $V_c \approx 3\ \mathrm{d}V/\mathrm{d}y$. Potentially, this might indicate that the nuclear formation process introduces an additional correlation on top of nucleon production.

Similar studies can be performed also using (multi)strange hadrons, while being extended also to small colliding systems: this will be described in detail in Chapter 6.

Chapter 3

A Large Ion Collider Experiment

A Large Ion Collider Experiment (ALICE) [144] is one of the four large experiments installed at the CERN Large Hadron Collider (LHC), the most powerful particle accelerator built to date, which operates both with proton and Pb beams. ALICE is specifically designed both to measure QGP probes in heavy-ion and to carry out reference measurements in small systems, such as pp and p–Pb, which serve as a baseline. Its excellent tracking and particle-identification performance are instrumental to carry out the measurements presented in this Thesis. In the following, the description focuses on the apparatus used during the second physics run, Run 2, of the LHC (2015-2018). In addition, the main subdetectors used in the analyses presented in this Thesis are described more in detail.

3.1 The Large Hadron Collider

The CERN accelerator complex is represented schematically in Fig. 3.1. The LHC is the last machine of the accelerator chains, different for protons and Pb ions, which progressively increase the beam energy.

The protons extracted from a ionised hydrogen source are accelerated up to 50 MeV by the LINAC 2. The obtained proton beam is injected in the Proton Synchrotron Booster (PSB), which increases the beam energy up to 1.4 GeV. The beam extracted from the PSB in segments called bunches is then accelerated up to 25 GeV by the Proton Syncrotron (PS). The PS beam is further injected into the Super Proton Synchrotron (SPS), where protons are accelerated up to 450

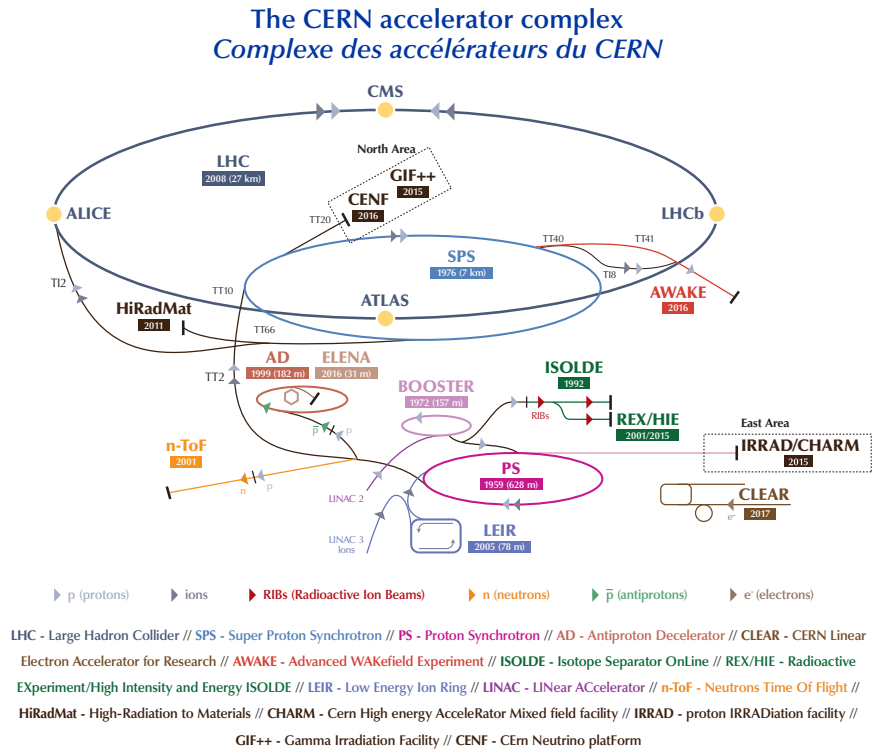

Figure 3.1: Sketch of the CERN accelerator complex [145], including the major experiments.

GeV: this is the injection energy of protons in the LHC [146].

Pb nuclei are ionised in multiple steps starting from the ions emitted by a heated filament of pure ^{208}Pb. Using a microwave cavity, $^{208}Pb^{27+}$ ions are produced: these are subsequently accelerated by the LINAC 3 to 4.2 MeV per nucleon. The beam passes through a carbon foil to strip additional electrons off the ions, resulting in a $^{208}Pb^{54+}$ beam that is injected into the Low Energy Ion Ring (LEIR), where it is first separated into 4 bunches and then accelerated to 72 MeV. The LEIR is then transferred to the PS: from there, the acceleration steps are similar to those described for protons. The final electron-stripping phase is performed before the injection into the SPS using a second thicker foil [147].

In the LHC ring, the beams circulate in opposite directions in separate vacuum chambers, where they are accelerated to the top energy. In the four interaction points surrounded by the ATLAS, ALICE, CMS and LHCb experiments, the beam pipes intersect: in these regions, the beams are further collimated to increase the

rate of collisions. The highest centre-of-mass energies reached during the LHC Run 2 are $\sqrt{s} = 13$ TeV for pp collisions, $\sqrt{s_{\rm NN}} = 8.16$ TeV for p–Pb collisions, and $\sqrt{s_{\rm NN}} = 5.02$ TeV for Pb–Pb ones. The instantaneous luminosity, L, is the machine parameter that determines the rate of physical processes:

$$\frac{{\rm d}N}{{\rm d}t} = L\sigma_{\rm process}, \tag{3.1}$$

where $\sigma_{\rm process}$ is the total cross section of the process of interest. L is determined using the transverse size σ_i of the colliding beams ($i = 1, 2$) measured in van der Meer scans [148] through the equation:

$$L = fN_b\frac{N^2}{2\pi(\sigma_1^2 + \sigma_2^2)}F, \tag{3.2}$$

where f is the relativistic bunch revolution frequency, N_b the number of circulating bunches per beam, N the number of particles per bunch, and F a geometrical reduction factor arising from the crossing angle between the colliding beams. The peak instantaneous luminosity required by ALICE using Pb beams is $L = 10^{27}$ cm^{-2}s^{-1}. The integrated luminosities obtained with proton and Pb beams at the top energies are shown in Fig. 3.2 for different trigger criteria.

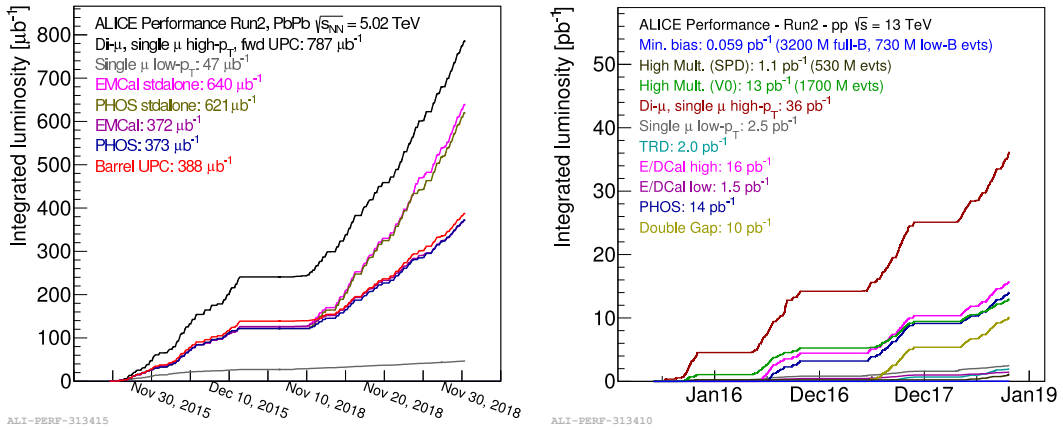

Figure 3.2: Luminosity integrated by the ALICE Collaboration in the LHC Run 2, for Pb–Pb (left) and pp collisions (right) at the top LHC energies.

The nominal position of the collision point, called primary vertex, is the origin of the experiment reference frame. Due to the finite extension of the intersecting beam bunches, the vertex position fluctuates on an event-by-event basis. The dis-

persion of vertices positions is quantified by the standard deviation of the distribution of vertices coordinates, both in the transverse plane and in the beam direction. For ALICE, these parameters are $\sigma_{xy}^{\text{vertex}} \approx 50$ μm and $\sigma_{z}^{\text{vertex}} \approx 5$ cm.

3.2 ALICE

ALICE is the LHC experiment dedicated to the study the strongly interacting matter created in heavy-ion collisions and in high-multiplicity pp and p–Pb collisions [144]. The diversity of probes measured to characterise the system formed in Pb–Pb collisions requires that events are fully reconstructed. Hence, the tracking and particle identification (PID) capabilities of the detector are optimised over a wide p_{T} range, including the low-momentum region. To reach the desired performance in the high-multiplicity environment created in Pb–Pb collisions at the top LHC enery, the ALICE subsystems are designed with high granularity and low material-budget [149, 150].

The ALICE coordinate system is a right-handed orthogonal Cartesian system centered at the nominal interaction point. The x axis lies on the LHC plane and it points the center of the ring, while the y axis is perpendicular to the accelerator plane and upwards oriented. The z axis is then parallel to the beam direction: its orientation is determined by the chirality of the system.

The ALICE setup for Run 2 is shown in Fig. 3.3. The apparatus consists of two main parts: the central barrel and the forward muon arm. Forward- and backward-rapidity detectors are also used both for triggering purposes and to characterise the event multiplicity and geometry.

The central barrel detectors cover the pseudorapidity acceptance $|\eta| < 0.9$. They are located inside a warm resistive solenoid, previously used in the L3 experiment at LEP, which provides a maximum magnetic field $B = 0.5$ T. In such conditions, it is possible to measure transverse momenta down to $p_{\text{T}} = 80$ MeV/c. The innermost central barrel detectors cover the full azimuth. They include the Inner Tracking System (ITS), the Time Projection Chamber (TPC) and the Time-Of-Flight (TOF). The Transition Radiation Detector (TRD), placed between the TPC and the TOF, is mainly used to identify electrons. Additional outer detectors are installed in the central barrel, covering more limited η and ϕ acceptances. They are the High-Momentum Particle Identification Detector (HMPID), used to identify high-momentum hadrons, the ElectroMagnetic Calorimeter (EMCal) and the Photon Spectrometer (PHOS), dedicated to the reconstruction of high p_{T}

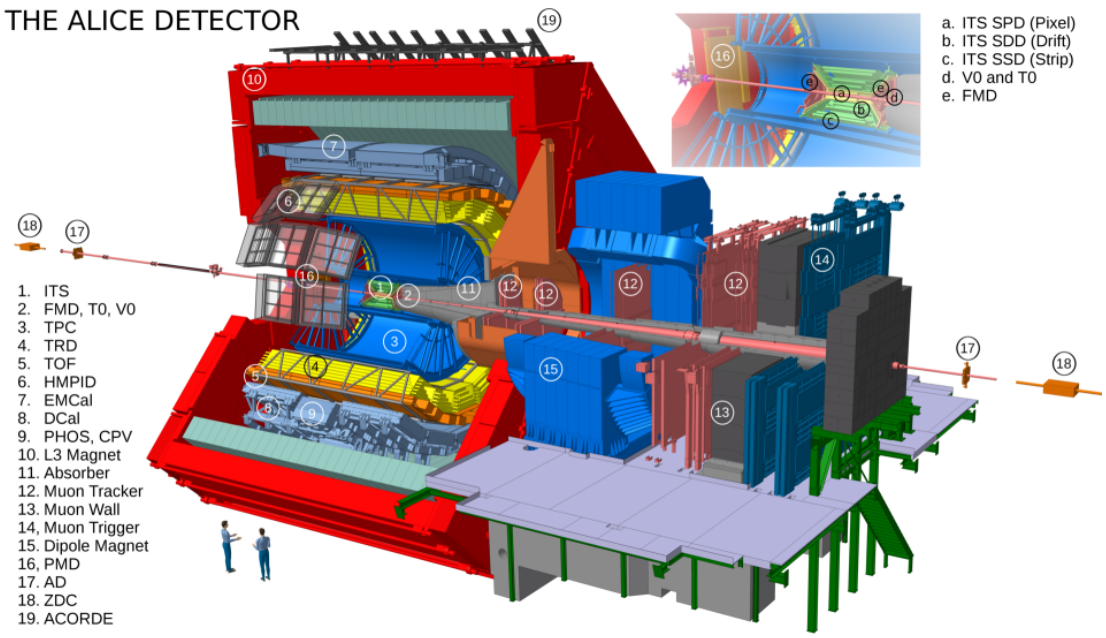

Figure 3.3: A cross section view of the ALICE setup for Run 2. The inset reports a larger view of the Inner Tracking System (ITS), V0 and T0 detectors.

photons and jets, and the Di-Jet Calorimeter (DCal). Cosmic rays events used for detector alignment and calibration are triggered with the ALICE Cosmic Ray DEtector (ACORDE), placed outside the return-yoke of the solenoid.

The forward muon spectrometer is located in the $-4 \leq \eta \leq -2.5$ pseudorapidity region. It includes a set of absorbers and tracking stations, built from Resistive Plate Chambers (RPCs). A dipole magnet is used to bend muon trajectories, enabling the measurements of the particle momentum. The remaining detectors are the Photon Multicplicity Detector (PMD), the Forward Multiplicity Detector (FMD), the Cherenkov T0 detector, the plastic scintillator V0 hodoscope and the Zero Degree Calorimeters (ZDC).

3.2.1 Inner Tracking System

The Inner Tracking System (ITS) [151] is the subdetector installed the closest to the interaction point. The rendering of the geometry of the ITS detector used in the LHC Run 2 is shown in Fig. 3.4. It is a six-layers silicon tracker based on three different technologies: the first two layers are equipped with Silicon Pixel Detectors (SPD), the third and fourth ones are made of Silicon Drift Detectors (SDD), whereas for the last two double-sided Silicon Strip Detectors (SSD) are used. The

detector layout and spatial resolution figures are reported in Table 3.1.

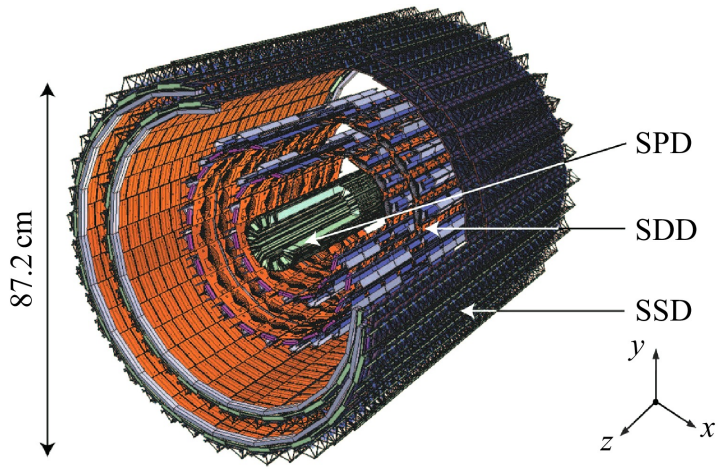

Figure 3.4: The ITS layout during the LHC Run 2.

Table 3.1: Specifications of the three subdetectors of the ALICE ITS.

Parameter	SPD	SDD	SSD
Material budget per layer ($\%X_0$)	1.14 - 1.14	1.13 - 1.26	0.83 - 0.86
Spatial resolution $r\phi$ (μm)	12	35	20
Spatial resolution z (μm)	100	25	830
Two track resolution $r\phi$ (μm)	100	200	300
Two track resolution z (μm)	850	600	2400
Active cell size (μm^2)	50	202	95
Number of readout channels (k)	9835	133	2603

Hybrid-pixel detectors are used for the innermost layers to enhance the detector segmentation close to the interaction point, where the surface track density is the highest. For the outer layers, where a lower granularity is required, different technologies can be used, enabling also the analogue readout of signals. In the SDD, one of the two planar coordinates is determined by the drift time of conduction electrons formed when charged particles cross the sensor. The mean drift velocity, required to determine the drift time, is calibrated using charge injectors implanted in the sensors. In the SSD, strips are implanted on both sides of the sensor with

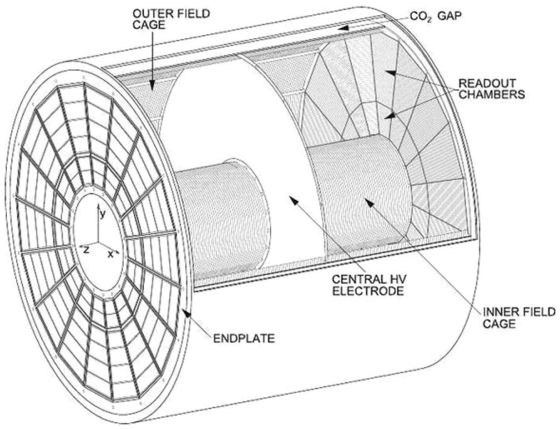

Figure 3.5: Schematic view of the TPC geometry.

tilted orientations to unambiguously determine the planar coordinates of the particle crossing point. As the SDD readout time is intrinsically longer than that of the other layers, it limits the maximum readout frequency of the ITS.

The ITS space-point resolution implies that primary and secondary vertices are reconstructed with a spatial resolution better than 100 μm. Using the ITS as a standalone tracking detector, it is possible to track low-momentum particles down to $p_{\mathrm{T}} = 80$ MeV/c. Besides providing the track space points closest to the primary vertex, the SPD information is used in the early stages of the event reconstruction to extract the first estimate of the primary vertex position. In addition, its signal is also used for triggering purposes. The SPD is read-out digitally as each pixel provides a binary output. On the other hand, for the SDD and SSD an analogue readout is used, hence their signal amplitudes are employed to measure the ionisation energy of the particle in the silicon material: this information is combined with the momentum measurement to identify low-p_{T} hadrons.

3.2.2 Time Projection Chamber

The Time Projection Chamber (TPC) [152] is the main tracker of ALICE. A schematic representation of the detector is shown in Fig. 3.5. The TPC consists of a large cylindrical field cage containing the detector sensitive volume (≈ 90 m^3), which is filled with a Ar-CO_2 gas mixture. A central electrode, kept at a negative voltage of 100 kV, separates the cage into two symmetric sectors. The electrode thickness is only 22 μm to minimise the material budget crossed by tracks in $\eta \approx 0$.

Electron-ion pairs are formed in the TPC gas when it is crossed by a charged particle. The electron clouds drift along the electric field lines toward the endcap readout anodes, which are equipped with position-sensitive detectors to determine the xy position of the clouds. The electron drift time is used to extract the z coordinate of the initial position of the cloud. This measurement requires the calibration of electron drift velocity in the gas: this procedure is carried out using a laser system embedded in the detector. In addition, heat screens are applied on the surfaces of the field cage to achieve a uniform and constant gas temperature: this determines a suppression of temperature-related variations of the electron drift velocity.

The electrons formed by the primary ionisation are multiplied by further ionising the gas in the proximity of the endcap anodes, where a high potential difference is applied. A gating grid, consisting of a plane of wires kept at a positive potential, is installed close to the readout chambers to avoid the backflow of the ions produced in these secondary ionisation processes. Without this device, the build-up of positive charges in the drifting space could determine significant distorsion of the electric field, hence degrading the space-point resolution of the detector. The maximum electron drift time, $t_{\mathrm{drift}} = 88$ μs, poses the major constraint on the maximum event readout frequency of ALICE.

The endplates are equipped with 36 readout chambers each, organised in 18 sectors to cover the full azimuth. The chambers are implemented as Multi Wire Proportional Chambers (MWPC) with cathode pad readout. The pad segmentation into 5.6×10^5 rows ensures the necessary $\mathrm{d}E/\mathrm{d}x$, position and two-track resolution while keeping a low occupancy. Particle tracks are reconstructed with up to 159 3-dimensional space points. By measuring also the charge collected for each point, the energy loss in the gas is measured: this information is combined with the track momentum to identify the particle species.

3.2.3 Time-Of-Flight

The Time-Of-Flight (TOF) detector [153] is used to identify charged particle in the intermediate momentum range, up to $p_{\mathrm{T}} \approx 5$ GeV/c. Its layout is shown in Fig. 3.6. It is based on Multi-gap Resistive Plate Chambers (MRPC) containing 10 gaps of 250 μm thickness, divided in two layers. When crossed by a charged particle, the gas contained in each of the gaps is ionised and the ionisation signal is read out. The thin gas layers ensures a fast detector response: the timing resolution is further reduced by summing the analogue signals collected in each of

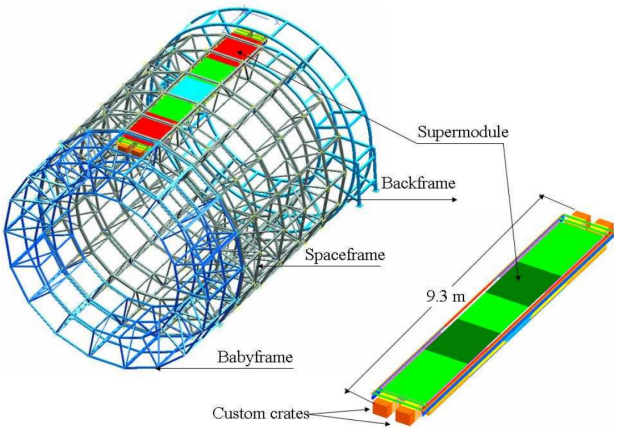

Figure 3.6: Layout of the ALICE TOF detector.

the chambers. The MRPC strips are placed inside the TOF modules, which consist of sealed boxes filled with a gas mixture mainly composed of chlorofluorocarbons. The TOF modules are further arranged in supermodules mounted on a cylindrical support structure, as it is shown in Fig. 3.6.

Using the MRPC technology, the TOF system is characterised by both an intrinsic efficiency $\approx 100\%$ and an intrinsic time resoluction ≈ 40 ps.

The time measurement obtained with the TOF detector is combined with the collision (event) time, t_{event}, to carry out PID. This quantity can be measured either with the T0 detector or with TOF, as it is described in reference [154]. The best estimate of t_{event} is obtained as a weighted average of the two. The total time resolution of TOF is 56 ps in Pb-Pb collisions during Run 2 [155]. The time of flight measurement, along with the track momentum estimate, is used to determine the particle velocity, β, and hence its mass.

3.2.4 V0

The V0 detectors consists of two arrays of plastic scintillator counters (V0A and V0C), located on both sides of ALICE at high pseudorapidity[1]. The V0 signals are used to define trigger conditions for the data acquisition, as well as to reject the interactions between the LHC beam and the residual gas present in the beam pipe. In addition, the V0 signal amplitude is correlated with the charged-particle multiplicity at midrapidity: as such, it is used to construct event multiplicity estimators.

[1]The "A" and "C" sides of ALICE face ATLAS and CMS respectively.

3.2.5 T0

The T0 detector is composed of two arrays of Cherenkov counters, the T0A and T0C. Its main purpose is the determination of the event time with a resolution below 50 ps when the TOF event-time extimate is not available, as it is the case in low multiplicity events. The T0 also provides an online determination of the LHC instantaneous luminosity. In addition, its timing information is used to estimate the primary vertex position along the beam axis with a precision of about 1.5 cm.

3.2.6 Trigger and data acquisition

The output signals of the different trigger detectors are combined with the LHC filling scheme information by the Central Trigger Processor (CTP) [156]. The trigger condition is checked in three sequential levels characterised by an increasing decision time. The level 0 decision is produced in less than 1 μs combining the signals of the SPD, V0, EMCal, PHOS and Muon Trigger, the latter one being part of the forward muon spectrometer. A level 1 condition is determined for the events passing the first one, in about 6.5 μs. Finally, the Level 2 (L2) conditions are issued 100 μs after the collision to include the TPC output signals. The Data Acquisition (DAQ) machines [157] and the High Level Trigger (HLT) [158] process the events passing the L2 selection.

When the data acquisition is triggered, the raw data processed by the front-end electronics are collected through optical connections by the Local Data Concentrators (LDCs) machines. Each of the ALICE subdetectors are connected to one or more LDCs, which further process the raw data to build a subevent. The Global Data Collectors (GDCs) combines the subevents obtained by the LDCs to build a full event. The HLT then carries out a fast event reconstruction to apply further selections. Once the event building is done, the data are transferred to the CERN computing centre for storage.

3.3 ALICE offline analysis

The ALICE offline software is based on ROOT [68], a C++ object-oriented framework designed at CERN for data analysis in experimental High-Energy Physics. The ALICE Collaboration developed an extension of ROOT, named AliRoot, containing C++ classes specialised for the reconstruction and analysis of the collected data. The analysis codes based on ROOT and AliRoot developed by the ALICE analysers are part of the AliPhysics framework. These analysis rountines

are run on the Worldwide LHC Computing Grid (WLCG) [159].

3.3.1 Event reconstruction

The first step of the event reconstruction is the extraction from raw data of the space points, known as clusters, where the particles produced in the collision intersect the detector sensitive volume. Different quantities can be associated to the reconstructed clusters, such as the ionisation energy in TPC and the track time measured with the TOF system.

Primary vertex finding

The position of the primary interaction vertex is first estimated using the space points reconstructed in the first two layers of ITS, the SPD. Track segments, called tracklets, are built by connecting pairs of space points reconstructed in both SPD layers and lying in a limited azimuthal window. The primary vertex is defined by the point minimising the distances from all tracklets. This vertex estimation is employed in the track reconstruction routines. After this process is completed, the vertex finding is run once more, this time using the information of the fully reconstructed tracks. This estimate has a better spatial resolution than the first one, as it can be observed in Fig. 3.7, where the performance of both methods is compared in pp collisions at $\sqrt{s} = 7$ TeV, as a function of the event multiplicity, $\mathrm{d}N/\mathrm{d}y$.

The resolution obtained on the x and y vertex coordinates obtained is improved by a factor larger than 2 when combining the full-track information compared to the early SPD-tracklet estimation. The resolution improves for increasing event multiplicity for both estimators, as the number of either tracklets or full-tracks used in the vertex finding algorithm increases. Specifically, a resolution of about 50 μm is achieved in the highest-multiplicity pp events analysed in Fig. 3.7, where $\mathrm{d}N/\mathrm{d}\eta \approx 40$.

For the measurements carried out in this Thesis, triggered events with pile-up, i.e., where multiple collisions occurred, are rejected. Pile-up is generated by multiple collisions occurring in either the same or different bunch crossings. The vertex finding procedure enables the reconstruction of multiple vertices per event, provided that they are spatially resolved. Other pile-up rejection strategies exploit either the correlation between different multiplicity estimators or track-level requirements, such as the minimum number of space points in the SPD layers [160]. The criteria used in this Thesis are reported in detail in Chapter 4.

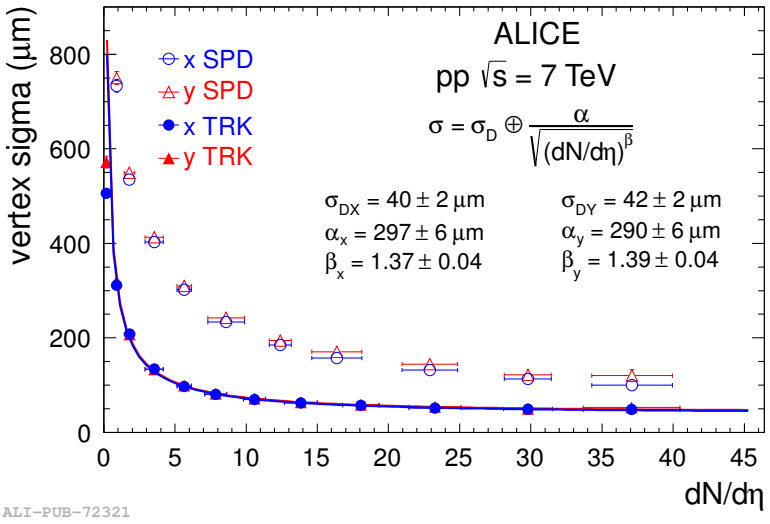

Figure 3.7: Resolution of the primary vertex position reconstructed using both the SPD vertex finder (SPD) and the full-track vertexing (TRK), as a function of the particle multiplicity.

Track reconstruction

The tracks of charged particles are extracted through a kinematic fit of the space points reconstructed in the ALICE subdetectors. In the central barrel, charged particles propagate along helicoidal trajectories that are locally perturbed by both elastic and inelastic interactions in the detector material. Consequently, the fit is carried out with a Kalman filter approach to take into account the perturbation induced by the stochastic interaction processes [161]. The track finding consists of three steps following an inward-outward-inward approach [162]. The first step is seeded by pairs of space points reconstructed in TPC, close to the outer wall of the field cage; the primary vertex position extracted with the SPD algorithm is employed as a constraint. The track fitting then proceeds towards the inner TPC wall by updating the track parameters with the information of additional clusters compatible with the track extrapolation. In this process, the energy loss information associated to the used space points can be combined with the extracted track momentum to obtain a preliminary identification of the particle species. The ITS track finding is started by extrapolating the TPC tracks to the outermost ITS layer: the ITS track fitting is then carried out in a similar way as for the TPC. The track χ^2 is increased by a penalty factor each time compatible clusters are not found. The ITS+TPC tracks stored in the event at the end of the fitting

process are those characterised by the highest goodness-of-fit. A second refit of the ITS+TPC track is carried out in the outward direction. Succesfully refitted tracks are propagated to the TRD, where the track parameters are further updated with the information of compatible TRD tracklets. In this step, the obtained tracks are also extrapolated to the TOF detector to find matches with TOF clusters: at this stage, both the integrated track length and the propagation time under multiple mass hypotheses are determined. The extrapolation to the outer calorimeters and to the HMPID is also carried out in this step.

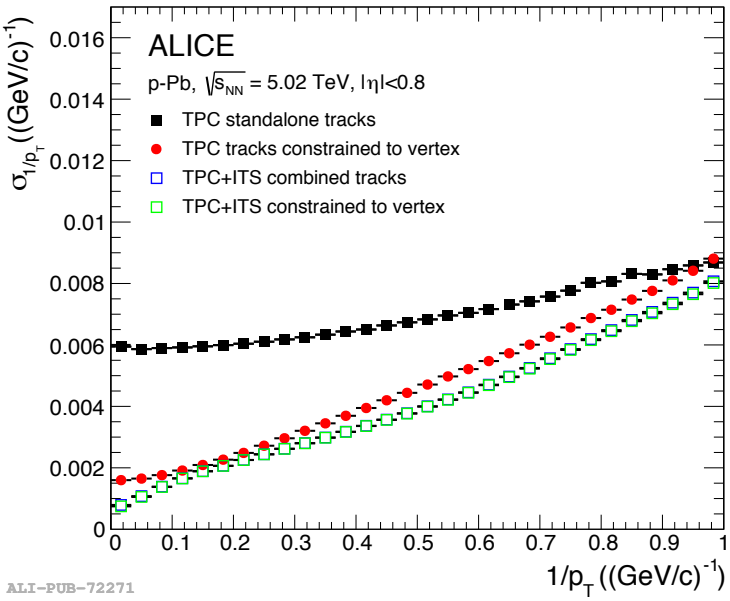

Figure 3.8: Resolution on $1/p_{\mathrm{T}}$ obtained in p–Pb collisions at $\sqrt{s_{\mathrm{NN}}} = 5.02$ TeV for different reconstruction algorithms.

In the last reconstruction steps, the Kalman filter fit is repeated once more using all clusters found in the previous steps. The tracks are inward extrapolated to the innermost ITS layers.

In Fig. 3.8, the inverse transverse momentum resolution, $\sigma_{p_{\mathrm{T}}}$, related to the p_{T} resolution as:

$$\frac{\sigma_{p_{\mathrm{T}}}}{p_{\mathrm{T}}} = \frac{\sigma_{1/p_{\mathrm{T}}}}{1/p_{\mathrm{T}}}, \tag{3.3}$$

is shown for p–Pb collisions at $\sqrt{s_{\mathrm{NN}}} = 5.02$ TeV as a function of $1/p_{\mathrm{T}}$ for track samples obtained in the different steps. The data shown refer to tracks extracted either with TPC space-points only or combining both ITS and TPC clusters, both with and without the constraint of the primary vertex position. For the

TPC standalone tracks, the vertex constraint causes $\sigma_{1/p_{\mathrm{T}}}$ to decrease by a factor of 3 for $1/p_{\mathrm{T}} \approx 0.1$ $(\mathrm{GeV}/c)^{-1}$, i.e. at $p_{\mathrm{T}} = 10$ GeV/c. TPC+ITS tracks are characterised by the best resolution, ≈0.8% at $p_{\mathrm{T}} = 1$ GeV/c, increasing to ≈2% for $p_{\mathrm{T}} = 10$ GeV/c.

Secondary Vertices

The vertices of both photon conversions and displaced weak decays are searched in the event reconstruction. The secondary-vertex finder algorithm used in this Thesis enables the reconstruction of neutral particle decays with decay-product tracks arranged in V-shaped topologies, hence called V^0. The secondary vertices are found using pairs of oppositely-charged tracks: the tracks used are obtained with the aforementioned procedure. The V^0 candidates are stored in the reconstructed event if some loose topological selections are passed. A first set of selection is performed on the Distance of Closest Approach (DCA), i.e. the minimum distance, between the daughter tracks. Additionally, a thershold is applied to the cosine of the pointing angle ($\cos\theta_p$), which is the cosine of the angle formed by the vector sum of the daughter momenta and by the straight line connecting the primary and secondary vertex. These variables are described more in detail in Chapter 4, where also the (tighter) selections used in the offline analysis are reported.

3.3.2 Monte Carlo simulations

The offline analysis of the data collected by the experiment requires the accurate understanding of detector effects, such as the detection and reconstruction efficiencies of the apparatus. This information is extracted using Monte Carlo (MC) simulations, where both the collision process and the interactions of particles with the detector are accurately reproduced. In the first step, the collision dynamics is simulated using dedicated computer programmes called event generators. The input information of event generators include the beam parameters and the cross sections of the physical processes to simulate; the output of the generation is the array of kinematic variables of the particles produced in the collision. In the ALICE offline framework, pp collisions are simulated using the PYTHIA 8 generator [57], while HIJING [59] and EPOS LHC [124] are used to generate Pb–Pb and p–Pb collisions, respectively. The generated particles are then propagated through an accurate geometrical description of the ALICE detector using transport codes. The ALICE offline frameworks supports multiple transport codes through the TVirtualMC interface, namely GEANT 3 [163], GEANT 4 [164], and FLUKA [165]. Simulated raw data are obtained from the MC by reproducing the detector response in the

simulation. These raw data are then processed using the same software employed for the reconstruction of the real data, enabling a direct comparison between the two.

3.4 Particle identification

The different ALICE detectors employs several particle identification (PID) techniques to enable measurements of the various QGP probes. In this Thesis, the PID capabilities of ITS, TPC, and TOF are used to carry out measurements of light-flavour hadrons. Both ITS and TPC provide measurements of the specific ionisation, $\mathrm{d}E/\mathrm{d}x$. On the other hand, the TOF detector is used to determine the time it takes for particles produced in the collision to reach the detector itself. Each of these detector is optimised to carry out the PID of reconstructed tracks in specific transverse momentum regions. In the following, the main methodologies are presented: more details connected to the analyses carried out in this Thesis are reported in Chapter 4.

3.4.1 PID with ITS and TPC

The four outermost ITS layers can be used to measure the specific energy loss of particles in silicon. For tracks with $p_{\mathrm{T}} < 1$ GeV/c, the $\mathrm{d}E/\mathrm{d}x$ resolution is 11%, enabling the rejection of electrons for the identification of hadrons. The specific energy loss in the TPC gas is determined as a truncated mean of the energy deposit measurements associated to each of the track clusters. Using this procedure, the TPC $\mathrm{d}E/\mathrm{d}x$ resolution achieved in pp and Pb–Pb collisions is about 5.5% and 6.5%, respectively.

The $\mathrm{d}E/\mathrm{d}x$ measurements are combined with the track momentum information to carry out PID. These two quantities are related via the Bethe-Bloch formula [166], which can be written in terms of the $\beta\gamma$ relativistic factor as:

$$f(\beta\gamma) = \frac{P_1}{\beta^{P_4}} \left[P_2 - \beta^{P_4} - \ln\left(P_3 + \frac{1}{(\beta\gamma)^{P_4}} \right) \right] \tag{3.4}$$

This parameterisation in terms of the four parameters P_i for $i = 1, 2, 3, 4$ was introduced by the ALEPH collaboration at LEP [167]. This functional form is also used by the ALICE Collaboration. Alternatively, spline parameterisations are also available.

The specific ionisation signal observed both in ITS and in TPC as a function of

momentum and magnetic rigidity[2] of the track, respectively, is shown in Fig. 3.9. At low momenta ($p < 1$ GeV/c) the dominant term of the Bethe-Bloch formula is

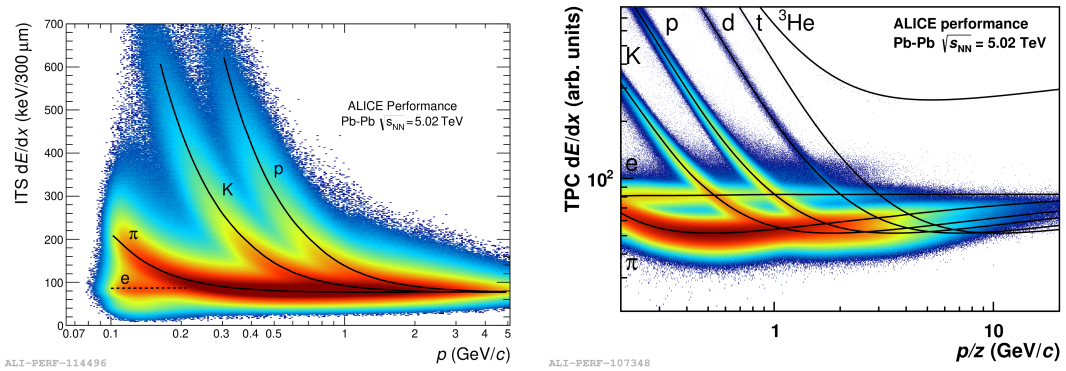

Figure 3.9: ITS (left) and TPC (right) dE/dx signal in Pb-Pb collisions at $\sqrt{s_{\mathrm{NN}}} =$ 5.02 TeV. The response expected for different particle species is also shown with a solid line.

proportional to $1/\beta^2$. In this region, the TPC-based particle identification can be performed on a track-by-track basis, by requiring that the dE/dx signal lies within fiducial regions predicted for each of the species of interest. In the intermediate momentum region, a statistical unfolding of the marginal dE/dx distributions is carried out. The TPC PID can be extended to higher momentum tracks once the Fermi plateau of dE/dx is reached.

For the dE/dx in TPC, the observed ^{3}He signal is well separated from other species up to $p_{\mathrm{T}} = 10$ GeV/c. This effect is due to expected quadratic dependence of dE/dx on the electric charge of the particle.

3.4.2 PID with TOF

The time of flight of a particle is the time interval elapsed between the particle production and the instant it crosses the TOF detector releasing a signal. Using measurable quantities, it is defined as the difference between the TOF time signal t_{TOF} and the event time t_{event}. This quantity is determined with a resolution of about 56 ps for pions having 1.5 GeV/c in Pb-Pb collisions. The particle speed,

[2]The magnetic rigidity p/z is the ratio between the track momentum, p, and the electric charge of the particle, z, measured in units of the proton charge.

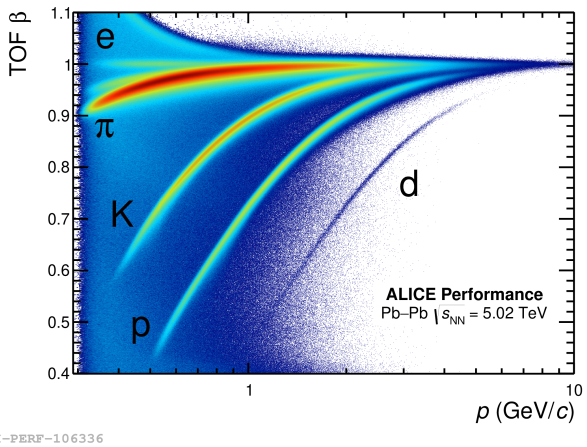

Figure 3.10: Particle speed, β, measured with the TOF in Pb-Pb collisions at $\sqrt{s_{\rm NN}} = 5.02$ TeV.

β, is determined from the time of flight using the following equation:

$$\beta c = \frac{L}{t_{\rm TOF} - t_{\rm event}}, \tag{3.5}$$

where L is the integrated track length computed during tracking. In Fig. 3.10, the particle velocity, β, is shown as a function of the momentum: the expected particle species associated to each of the observed bands is reported in the figure.

Up to $p_{\rm T} \sim 5$ GeV/c, different hadron species are resolved one from the other. Specifically, $z = 1$ hadrons not resolved with the TPC PID information are identified with TOF in the intermediate momentum region.

3.5 Centrality estimation in Pb-Pb collisions

As discussed in Section 1.3.1, the geometry of heavy-ion collisions is regulated by the impact parameter, b. Although the distance between colliding ions cannot be directly measured, the centrality of the collision can be determined using experimental observables related to b in the Glauber Model. Specifically, the energy deposited in the ZDCs and the charged particle multiplicity are used for this purpose [168]. In the literature, events are classified according to centrality classes, which are defined as percentiles of the total hadronic interaction cross section of

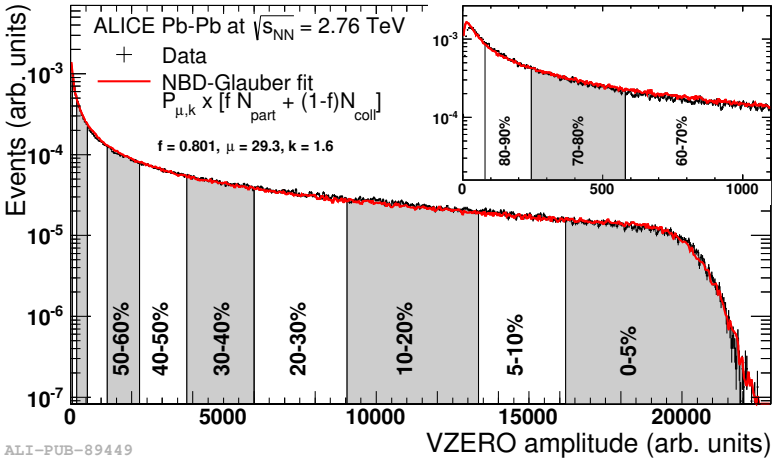

Figure 3.11: Comparison between the measured V0M amplitude distributions and the one expected from a Glauber MC calculation in Pb-Pb collisions at $\sqrt{s_{\mathrm{NN}}} = 5.02$ TeV. Centrality classes are defined as percentiles of the obtained distribution [168].

the colliding nuclei:

$$c(b) = \frac{1}{\sigma_{\mathrm{AA}}} \int_0^b \frac{\mathrm{d}\sigma}{\mathrm{d}b'} \mathrm{d}b', \tag{3.6}$$

where the total cross section, σ_{AA}, is defined as the integral of the differential cross section, $\mathrm{d}\sigma/\mathrm{d}b$, over all possible values of b. Assuming that both the charged particle multiplicity, N_{ch}, and the energy deposit at zero degrees, E_{ZDC}, are monotonically dependent on b, the centrality is determined using two variable substitutions:

$$c \approx \frac{1}{\sigma_{\mathrm{AA}}} \int_{N'_{\mathrm{ch}}}^{\infty} \frac{\mathrm{d}\sigma}{\mathrm{d}N'_{\mathrm{ch}}} \mathrm{d}N'_{\mathrm{ch}} \approx \frac{1}{\sigma_{\mathrm{AA}}} \int_0^{E_{\mathrm{ZDC}}} \frac{\mathrm{d}\sigma}{\mathrm{d}E'_{\mathrm{ZDC}}} \mathrm{d}E'_{\mathrm{ZDC}} \tag{3.7}$$

Under similar assumptions, the interaction cross section can be replaced by the number of events corrected for the trigger efficiency and background contamination. These assumptions break down for the ZDC energy deposit when $c > 50\%$, as the remaining nuclear fragments are deflected outside the ZDC acceptance by the LHC magnets, hence going undetected and biassing the centrality estimate. The resulting ambiguity in centrality determination is solved by correlating the ZDC signal with the energy deposited in a forward electromagnetic calorimeter.

The determination of centrality from the charged particle multiplicity is based on the V0M multiplicity estimator, obtained as the sum of the V0A and V0C signal amplitudes, which is correlated with the multiplicity at midrapidity. The V0M

distribution is fitted with a parameterisation based on a Glauber Monte Carlo model, as it is shown in Fig. 3.11. Centrality classes are defined as percentiles of the integrated V0M amplitude distribution: each of them is associated to an interval of b values. When comparing measurements across colliding systems, the event multiplicity is used as a reference. Hence, in analogy to the Pb–Pb case, multiplicity classes are defined also for pp and p–Pb collisions.

Chapter 4

Analysis methods for the selection of light-flavour hadron candidates

The observables studied in this Thesis are based on the measurement of the yields of particles and antiparticles produced at midrapidity in hadronic and heavy-ion collisions for multiple light-flavour hadron species. These measurements are performed in intervals of either transverse momentum, p_{T}, or proper decay lenght, $ct = ML/p$, where M, L, and p are the mass, decay length, and the momentum of the particle, respectively. The analysed species, ordered by increasing masses, are the charged pion, π^-; charged kaon, K^-; proton, p; the (multi)strange baryons Λ, Ξ^-, and Ω^-; a set of light (hyper)nuclei, namely deuteron, d; helium-3, ^{3}He; triton, ^{3}H; hypertriton, $^3_\Lambda$H, a bound state of a proton, a neutron, and a Λ baryon. Hereafter, the charge conjugate states will be implied in the text unless otherwise specified. The analysis techniques used to identify these hadrons are presented in this chapter. The different hadron species are grouped according to the reconstruction method used. The trajectories of charged particles stable against weak decay over the radial extension of the ALICE spectrometer, $O(5\ \mathrm{m})$, can be reconstructed with tracking algorithms. Conversely, the kinematic properties of shorter-lived particles are obtained by reconstructing their decay vertices starting from tracked charged particles.

4.1 Data samples and event selections

4.1.1 Data samples

The data samples analysed in this Thesis were collected by the ALICE Collaboration during the second data taking run at the CERN LHC, and include different colliding systems: pp, p–Pb, and Pb–Pb. The analysed data samples are summarised in Table 4.1. The hadron species analysed in each of the samples, are also reported.

Table 4.1: Data samples and the corresponding particle species analysed in this Thesis.

System	Year	$\sqrt{s_{\rm NN}}$ (TeV)	B_z (T)	Sel. events	Analysed species
pp	2017	5.02	-0.5	848×10^6	$\rm K^-$, Ξ^-
p–Pb	2016	5.02	$+0.5$	607×10^6	$\rm K^-$, Ξ^-
Pb–Pb	2015	5.02	± 0.5	99×10^6	$\rm K^-$, Ξ^-
Pb–Pb	2018	5.02	± 0.5	272×10^6	all

In all of the presented cases, the centre-of-mass energy per nucleon-nucleon pair is $\sqrt{s_{\rm NN}} = 5.02$ TeV. The different data samples were collected with different polarities of the solenoidal magnetic field, B_z, provided in the ALICE central barrel by the L3 magnet. While the samples of pp and p–Pb collisions were collected with a single polarity, either positive (p–Pb) or negative (pp), both of the samples of Pb–Pb collision data were recorded switching the polarity of the magnetic field in a fraction of the data taking time. This procedure enables the understanding of systematic effects connected to the imperfect knowledge of the magnetic field in the later processing steps. The events analysed in this Thesis are inelastic collisions, for each of the colliding systems employed. The number of events selected in each of the samples with the criteria described in detail below are also reported.

Besides the data collected with the experiment, data samples obtained via detailed Monte Carlo (MC) simulations of both the collision processes and the detector effects are employed in the analysis. The dynamics of the collision, both at the partonic level and in the hadronization phase, is simulated with an event generator program. The event generators used depend on the analysed colliding systems. The Pythia 8 [57] code, with the Monash tune [57, 123], is used to simulate pp collisions, while Epos 3 [32] and Hijing [59] are used to generate p–Pb and Pb–Pb collisions, respectively. The propagation of the final-state particles through

the ALICE detector is simulated using the GEANT 4 [169] transport code. In this simulation step, a detailed model of the ALICE apparatus geometry is used to accurately simulate both the response of the active elements to the passage of particles in the detector and the interactions with the passive elements of the apparatus. In addition, the real data taking conditions affecting the collected data quality, e.g., the misalignement of the detector elements with respect to the ideal geometry and the presence of dead channels in the various ALICE subsystems, are reproduced in the detector model.

The simulation data used in this Thesis are obtained either from *general purpose* MC simulations, where the yield of the particles of interest is the output of the event generator without any further modification, or using *injection* procedures, where additional particles of the species of interest are added on top of those produced by an event generator. To avoid biases in the event reconstruction, the amount of injected particles is limited to a fraction of the total charged particle multiplicity. The number of injected particles and the kinematic distributions sampled in the injection are reported in Table 4.2 for the different analysed species.

Table 4.2: Injection schemes used in this Thesis for the different analysed species. The number of particles injected per event is the same for both particles and antiparticles.

Species	Inj. per event	p_{T} (GeV/c)	y	φ (rad)
p	40	$[0.2, 3.5]$	$[-1, 1]$	$[0, 2\pi]$
Ξ^- (Pb–Pb)	10	$[0.2, 4.0]$	$[-1, 1]$	$[0, 2\pi]$
Ξ^- (pp)	1	$[0, 20]$	$[-0.7, 0.7]$	$[0, 2\pi]$
Ω^-	10	$[0.2, 5.0]$	$[-1, 1]$	$[0, 2\pi]$
d, ^{3}H, ^{3}He	10	$[0, 10]$	$[-1, 1]$	$[0, 2\pi]$
$^3_\Lambda$H	40	$[0, 10]$	$[-1, 1]$	$[0, 2\pi]$

The ranges of the kinematic variables match the ones used for the analysis of yields, to optimise the generation of the simulated samples without disrupting the reconstruction performance. For instance, the number of Ξ^- injected on top of pp events is smaller than that injected in Pb–Pb collisions to avoid biases in the total particle multiplicity of the event, which decreases from Pb–Pb to pp. The kinematic distributions are sampled uniformly in the injection: analysis-specific modulations are applied afterwards to better reproduce the kinematics observed in the data for the species of interest.

4.1.2 Event selection

The analysed inelastic pp, p–Pb, and Pb–Pb events are selected with a set of criteria applied both online during the data taking and offline in the post processing of the collected data.

The online selections include a minimum bias (MB) trigger defined by the coincidence of signals in the V0A and V0C scintillators. In the data sample of Pb–Pb collisions collected in 2018, the acquisition of the 10% most central events and of semicentral events in the 30-50% centrality interval is triggered on top of the MB baseline by comparing the V0 signal amplitude with predefined thresholds.

The offline selections are summarised in Table 4.3.

Table 4.3: Offline event selection criteria.

Event selections
Reject multiple SPD vertices
$\lvert V_z \rvert \leq 10$ cm
$\lvert \Delta V_z \rvert \leq 20\sigma_{\mathrm{TRK}}$, $\lvert \Delta V_z \rvert \leq 10\sigma_{\mathrm{SPD}}$ and $\lvert \Delta V_z \rvert \leq 0.2$ cm

A set of selections is used to reject pile-up events from the analysed sample. In particular, the events with multiple vertices reconstructed with the SPD tracklets, i.e., the track segments obtained by matching pairs of space points in the first two ITS layers, are rejected. In this way, it is possible to reduce the contamination due to pile-up occurring in the same bunches that triggered the data acquisition, as well as the out-of-bunch one, coming from a bunch crossing different from the trigger one. This selection allows us to reject the out-of-bunch contamination from bunch crossings occurring within the SPD readout time window (300 ns) centered around the trigger bunch time. Other selections aimed at rejecting the out-of-bunch contribution outside this time window are applied at the track level.

In addition, the events are required to fulfill a few criteria for the quality of the primary vertex reconstruction. Specifically, the z coordinate of the primary vertex is required to lie inside a 10 cm wide fiducial region around the centre of the ALICE coordinate system. Moreover, an upper threshold of 0.2 cm is applied to the distance between the z coordinates of the vertices, ΔV_z, reconstructed with different algorithms, namely using either the SPD only, V_z^{SPD}, or the fully-reconstructed tracks, V_z^{TRK}. Two additional criteria are defined for ΔV_z in terms of the spatial resolution on V_z reconstructed with either of the two algorithms, σ_{SPD} and σ_{TRK}, respectively.

All of the observables measured in this Thesis are analysed differentially in either the multiplicity or the centrality of the collisions. The multiplicity or centrality estimator used in this Thesis for the pp and Pb–Pb data samples is known as V0M: it consists of the sum of amplitudes of the signals in the V0A and V0C scintillators. For the p–Pb data sample, due to the asymmetry of the colliding system, only the A side one of the V0 system is used. The distributions of the multiplicity and centrality percentiles obtained in the different data samples analysed are shown in Fig. 4.1.

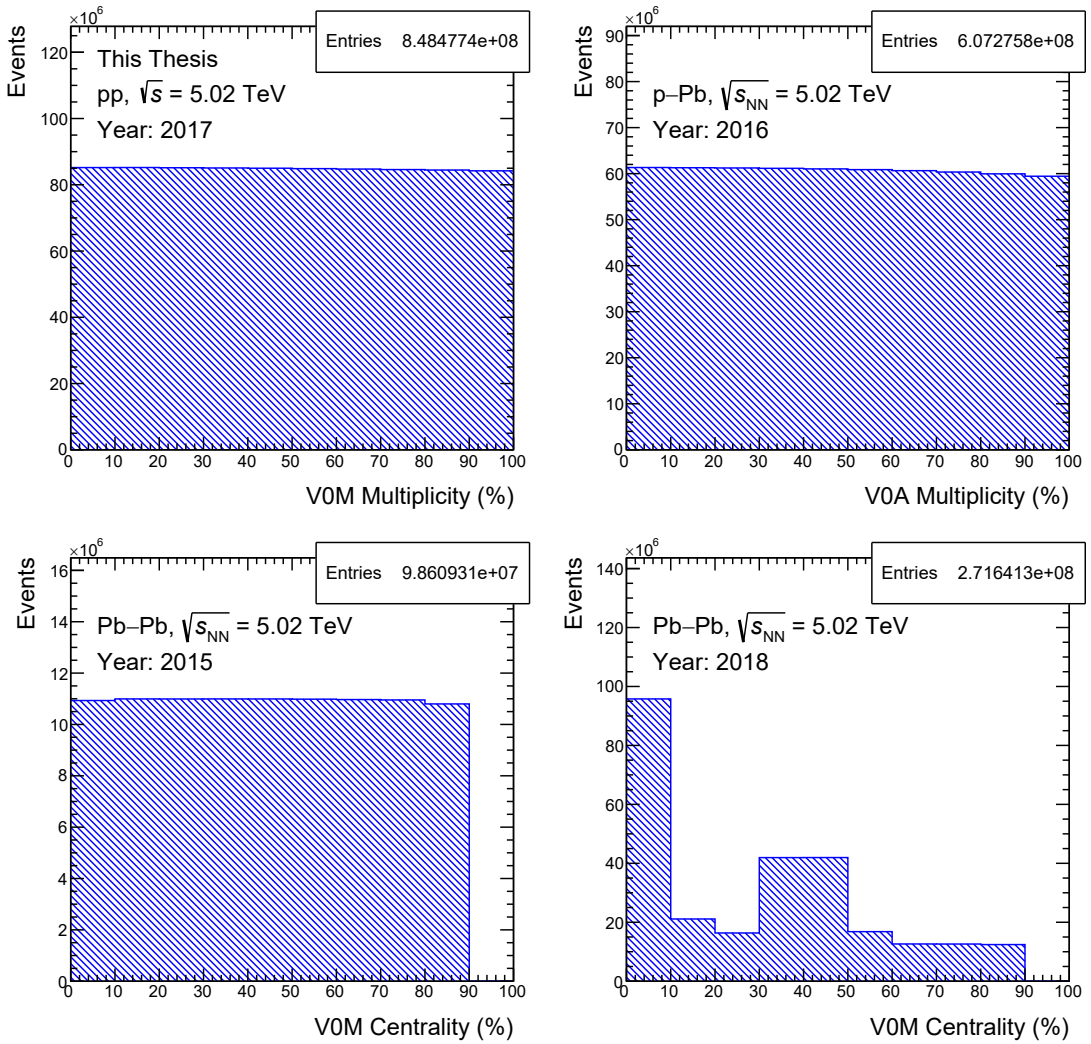

Figure 4.1: Centrality and multiplicity percentile distributions in the data samples analysed in this Thesis.

The central and semicentral trigger selection adopted 2018 result in an enhancement of events selected in the 0-10% and 30-50% centrality intervals, as it is shown in the bottom-right panel of Fig. 4.1

4.2 Hadrons reconstructed by tracking

The charged particles tracked in the ALICE apparatus include π^-, K^-, p, d, ^{3}He, ^{3}H. A schematic representation of the generic candidate topology is shown in Fig. 4.2.

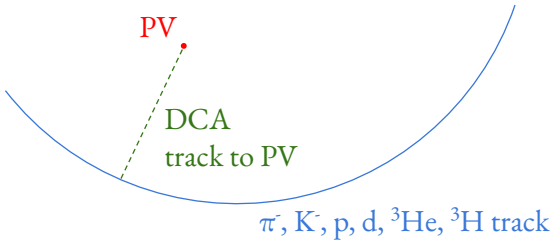

Figure 4.2: Sketch of the topology of tracked candidates. The distance of closest approach (DCA) to the primary vertex (PV) is highlighted in the figure.

The reconstruction quality of the candidate kinematics is further ensured by a set of rectangular selection criteria outlined below. Additionally, the particle identification (PID) information provided by the different ALICE subsystems is used to determine the particle species.

4.2.1 Track selection

The track selection criteria used in this Thesis are reported in Table 4.4.

The analysed tracks are selected in the pseudorapidity region $|\eta| < 0.8$ to exploit the full coverage of the central barrel detectors up to the TOF, avoiding border effects. Only tracks passing the last refitting step both in ITS and TPC are employed in the analysis to obtain the best estimation of the kinematic parameters. It is required that a minimum number of space points, also referred to as *clusters*, are used for the track finding, both in ITS and TPC. The tracks must have at least one associated cluster in the SPD to reject contributions from the residual out-of-bunch pile-up in the selected events. In the Pb–Pb collision data samples, for candidates identified via the specific ionization measurement in the four outermost ITS layers, a minimum of 3 clusters across the SDD and SSD is also required. Only tracks crossing at least 70 out of the 159 readout pad rows of TPC are selected for the analysis. Moreover, it is required that the fraction of crossed TPC rows

Table 4.4: Criteria for the selection of tracks used in this Thesis. Unless otherwise specified, the requirements apply to all analysed data samples for all candidates of each species.

Track selections
$\lvert\eta\rvert < 0.8$
$n_{\mathrm{SPDclusters}} > 0$ and $n_{\mathrm{ITSclusters}} > 1$
$n_{\mathrm{TPCcrossedRows}} \geq 70$
$n_{\mathrm{TPCcrossedRows}}/n_{\mathrm{TPCfindableCls}} > 0.8$
$n_{\mathrm{TPCclusters}} \geq 70$ (≥ 90 for ^{3}He)
$\chi^2/n_{\mathrm{ITSclusters}} < 36$
$\chi^2/n_{\mathrm{TPCclusters}} < 4$ (< 2.5 for the Pb–Pb 2018 data sample)
TPC and ITS refit
Rejection of kink topologies
$\lvert\mathrm{DCA}_z\rvert < 1$ cm
$\lvert\mathrm{DCA}_{xy}\rvert < 0.1$ cm (< 0.12 for p and π^-)
$n_{\mathrm{SDDclusters}} + n_{\mathrm{SSDclusters}} \geq 3$ (Pb–Pb)
(for K^- with $p_{\mathrm{T}} < 0.4$ GeV/c and p with $p_{\mathrm{T}} < 1.2$ GeV/c)

per geometrically findable clusters is larger than 0.8. An upper threshold, tuned differently for the different data-taking periods, is applied to the χ^2 per number of clusters, $\chi^2/n_{\mathrm{clusters}}$, of the kinematic fitting in ITS and TPC. In addition, tracks characterised by a sudden change in curvature along the trajectory are excluded from the track sample. These topologies, called *kinks*, arise from the decay of a charged particle into a charged-neutral pair.

The particles of all the analysed species are produced either in the primary interaction or by secondary processes, such as the decay of heavier unstable states. In addition, non-strange hadrons can be created in the spallation interactions of primary particles with the detector material. Weak decays and spallation processes can be separated from primary interactions by evaluating the displacement of the produced particle from the primary interaction point. Experimentally, this is achieved by measuring the distance of the closest approach (DCA) of the backwards-extrapolated track to the primary vertex (PV). Primary particles are selected by applying upper selection criteria to such distances measured both along the beam direction, DCA_z, and in the transverse plane, DCA_{xy}. More strin-

gent criteria are defined for DCA_{xy} thanks to the better pointing resolution in the transverse plane. For tracks with $p_{\mathrm{T}} = 1$ GeV/c, the pointing resolution along z and in $r\varphi$ is about 170 μm and 60 μm, respectively.

4.2.2 Particle identification

The hadron species associated with the selected tracks are determined either on a track-by-track or on a statistical basis using the particle identification (PID) information provided by different subdetectors. The observables used for PID include the specific ionization, $\mathrm{d}E/\mathrm{d}x$, measured either in the four outermost ITS layers or in the TPC gaseous volume, and the particle velocity, β, measured with the TOF detector. For each of these quantities, a $n\sigma_j$ variable is defined, representing the difference between the measured and the expected value of the observable for a specific momentum value and mass hypothesis, in units of the experimental resolution on the PID observable, σ_j, with $j =$ ITS, TPC, and TOF:

$$n\sigma_i = \frac{(\mathrm{d}E/\mathrm{d}x)_i^{\mathrm{meas}} - (\mathrm{d}E/\mathrm{d}x)_i^{\mathrm{exp}}}{\sigma_i}, \text{ for } i = \text{ITS, TPC} \tag{4.1}$$

$$n\sigma_{\mathrm{TOF}} = \frac{t_{\mathrm{TOF}}^{\mathrm{meas}} - t_{\mathrm{TOF}}^{\mathrm{exp}}}{\sigma_{\mathrm{TOF}}} \tag{4.2}$$

In the analysed data samples, ITS and TPC $\mathrm{d}E/\mathrm{d}x$ resolutions are about 11% and 6%, respectively, while the TOF timing resolution is about 80 ps and 56 ps in the pp and Pb–Pb collisions, respectively. The identification of the candidates is carried out using different detectors in different p_{T} intervals because of the different separation power among the various species. The p_{T} intervals analysed with each detector are summarised in Table 4.5 and they are visualised in Fig. 4.3. Low-p_{T} candidates are identified through the TPC $\mathrm{d}E/\mathrm{d}x$ measurement, while at higher momenta the TOF β information is also required for unitary-charged particles, as they all reach a common minimum $\mathrm{d}E/\mathrm{d}x$. The ^{3}He candidates are identified with TPC throughout the analysed p_{T} range as the $\mathrm{d}E/\mathrm{d}x$ expected for $|z| = 2$ particles is 4 times larger than that of $|z| = 1$ particles with the same $\beta\gamma$. For ^{3}He candidates with $p_{\mathrm{T}} < 5$ GeV/c, the PID hypothesis extracted during the TPC tracking is also required to reduce the contamination of ^{3}H candidates. For the low-p_{T} proton and kaon candidates, the ITS $\mathrm{d}E/\mathrm{d}x$ measurement is used to reject $e^{\pm}$ candidates.

In the measurements presented in this Thesis, the PID of selected tracks is carried

Table 4.5: p_{T} intervals used in this Thesis to carry out the PID of the selected candidates with ITS, TPC, and TOF, for each of the studied mass hypotheses.

Species	Analysed p_{T} (GeV/c)	ITS	TPC	TOF
		p_{T} (GeV/c)		
π^-	[0.7, 1.6]	–	[0.7, 1.6]	[0.7, 1.6]
K^-	[0.2, 1.0]	[0.2, 0.4]	[0.2, 1.0]	[0.4, 1.0]
p	[0.5, 3.0]	[0.5, 1.2]	[0.5, 3.0]	[1.0, 3.0]
d	[0.6, 1.8]	–	[0.6, 1.8]	[1.0, 1.8]
^{3}He	[2.0, 8.0]	–	[2.0, 8.0]	–
^{3}H	[1.6, 3.0]	–	[1.6, 3.0]	[1.6, 3.0]

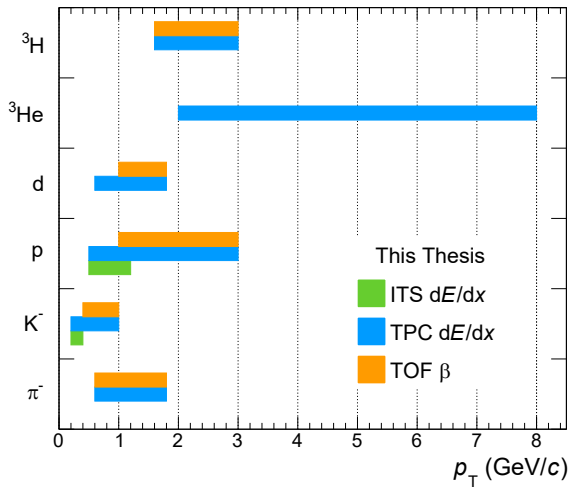

Figure 4.3: PID techniques used in the various analysed intervals of p_{T}, for each of the tracked species studied in this Thesis.

out either on a statistical or on a track-by-track basis, depending on the measured observables. In the statistical approach, for each analysed p_{T} and centrality or multiplicity interval, the $n\sigma$ distribution obtained with the outermost detector is fitted both to extract the yield of the particle of interest and to estimate the background contaminations, due to either other particle species or detector effects, such as the wrong associations of TOF space points to particle tracks. In addition, rectangular selections are applied to the $n\sigma$ quantities estimated candidate-by-candidate with the inner detectors to improve background rejection. The track-by-track PID can be performed when the $n\sigma$ distributions associated with different species are resolved one from each other: the yields are extracted by counting the

number of candidates falling within $n\sigma$ windows set for each of the species of interest. More details on the specific PID selections and fitting procedure are provided in Chapter 5 and Chapter 6.

The calibrations of the PID responses for ITS, TPC, and TOF are centrally computed by the ALICE Collaboration. When a selection is applied on the $n\sigma$ variable, a recalibration procedure is carried out to correct for miscalibration effects resulting in a shift and/or widening of the $n\sigma$ distribution. This procedure consists in determining the mean value, μ_{calib}, and standard deviation, σ_{calib}, of the $n\sigma$ distribution obtained in each of the p_{T} intervals, for each of the analysed hadron species. These parameters are extracted from the $n\sigma$ distributions observed in the data with a fit procedure. The general fit function is defined as the sum of a signal component, modelling the $n\sigma$ distribution of candidates associated with the species of interest, and a background component, describing the contamination effects present in the observed distribution. The signal function S is generally defined as a gaussian core with smoothly-connected exponential tails to describe the non-gaussian shapes of the $n\sigma$ distribution observed in the data:

$$S(x;\mu,\sigma,a,b) \propto \begin{cases} \exp\left[-a\left(\frac{x-\mu}{\sigma}-\frac{a}{2}\right)\right] & \text{if } x \leq \mu - a\sigma \\ \exp\left[-\frac{1}{2}\left(\frac{x-\mu}{\sigma}\right)^2\right] & \text{if } \mu - a\sigma \leq x < \mu + b\sigma \\ \exp\left[-b\left(\frac{x-\mu}{\sigma}-\frac{b}{2}\right)\right] & \text{if } x \geq \mu + b\sigma \end{cases} \tag{4.3}$$

The absolute values of a and b obtained from the fits are approximately $\mathcal{O}(1)$. This implies that the data distribution is described by a gaussian shape within a 1σ region centred around the mean. In the vicinity of the signal peak, the background shape due to residual contamination effects can be generally described by an exponential function. The background effects described by this exponential component are due to either the contamination from other species in the analysed $n\sigma_{\text{ITS,TPC}}$ window, or from wrong matches of tracks to space points in the TOF for the $n\sigma_{\text{TOF}}$ distribution. A few examples of the fits carried out for the recalibration procedure applied to K^- are shown in Fig. 4.4, for $n\sigma_{\text{ITS,TPC,TOF}}$.

The μ and σ parameters extracted with this procedure are used to define a corrected variable, $n\sigma^{\text{corr}}$, as:

$$n\sigma^{\text{corr}} = \frac{n\sigma - \mu_{\text{calib}}}{\sigma_{\text{calib}}}, \tag{4.4}$$

which is then used to define ITS, TPC, and TOF PID selection windows presented in the following.

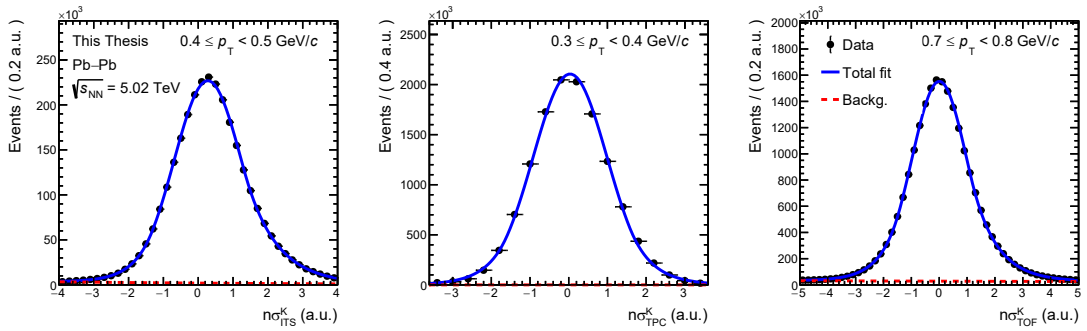

Figure 4.4: Performance of the fitting procedure for the recalibration of ITS (left), TPC (middle), and TOF (right) PID response for K^- candidates, in Pb–Pb collisions.

4.3 Hadrons reconstructed by vertexing

The Λ, Ξ^-, Ω^-, and ${}^3_\Lambda\mathrm{H}$ candidates are identified via their fully-reconstructed decay channels, which are reported in Table 4.6, along with their branching ratios.

Table 4.6: Decay channels analysed for the reconstruction of Λ, Ξ^-, Ω^-, and ${}^3_\Lambda\mathrm{H}$.

Decay channel	Branching ratio (%)
$\Lambda \to \mathrm{p} + \pi^-$	63.9 ± 0.5
$\Xi^- \to \Lambda + \pi^-$	99.887 ± 0.012
$\Omega^- \to \Lambda + \mathrm{K}^-$	67.8 ± 0.7
${}^3_\Lambda\mathrm{H} \to {}^3\mathrm{He} + \pi^-$	25.0 ± 2.3

The analysed decay topologies are subdivided into: two-body decays of Λ and ${}^3_\Lambda\mathrm{H}$ characterised by V-shaped topologies, also called V^0, where the initial hadron decays into a pair of oppositely charged hadrons; cascade decays of Ξ^- and Ω^-, where the initial state decays into a charged hadron, called *bachelor*, and a weakly-unstable particle, which is reconstructed as a V-shaped topology. The two topologies are schematically represented in Fig. 4.5 and Fig. 4.6, respectively.

The algorithm used for the secondary vertex finding starting from reconstructed tracks is described in Chapter Chapter 3. Besides signal candidates associated with real decay vertices, combinatorial background candidates originating from uncorrelated tracks are also found by the algorithm. To enhance the signal-to-background ratio of the samples, a set of rectangular selections is applied to the Λ candidates, while ${}^3_\Lambda\mathrm{H}$, Ξ^-, and Ω^- candidates are selected with a supervised machine learning (ML) approach, enabling a better suppression of combinatorial background at

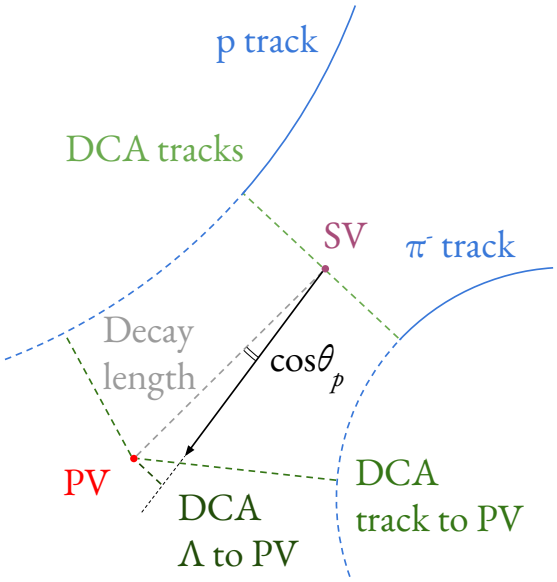

Figure 4.5: Sketch of the two-body decay topology of the Λ baryon. The main topological variablesdescribed in the text are highlighted in the figure.

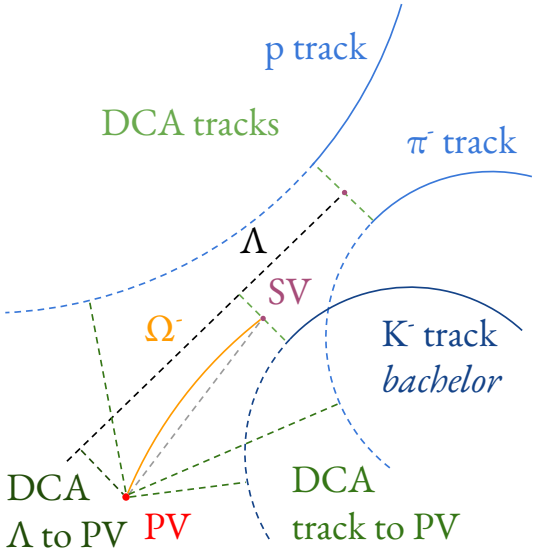

Figure 4.6: and cascade decay topology of the Ω^- baryon.

fixed signal selection efficiency. For cascade topologies, the background component is enhanced compared to the two-body case because of a larger possible combinatorics with three decay products. For the ${}^{3}_{\Lambda}\mathrm{H}$, the large background contamination is due to the large difference, $O(10^8)$, in all collision systems between the yields of

uncorrelated charged pions and pions produced in ${}^{3}_{\Lambda}\mathrm{H}$ decays [133, 170].

4.3.1 Two-body decay topologies: Λ baryon

The criteria for the selection of Λ candidates are defined both for track-level variables of the reconstructed decay products, in analogy to those presented in Section 4.2, and for quantities involving both the tracks and the reconstructed decay vertices. The selections are described in detail below for both kind of variables. In this Thesis, the Λ candidates are analysed differentially in p_{T}, in the range $1 \leq p_{\mathrm{T}} < 4$ GeV/c.

Track selections

The set of track-level selections employed is reported in Table 4.7.

Table 4.7: Track selection criteria applied in the Λ analysis in this Thesis.

Track selections
$n_{\mathrm{TPCclusters}} \geq 100$
$n_{\mathrm{TPCcrossedRows}} \geq 100$
$n_{\mathrm{TPCcrossedRows}}/n_{\mathrm{TPCfindableCls}} > 0.8$
$n_{\mathrm{TPCSharedclusters}} \leq 5$
$\chi^2/n_{\mathrm{ITSclusters}} < 36$
$\chi^2/n_{\mathrm{TPCclusters}} < 4$
TPC refit
at least 1 track has TOF hit or ITS refit
$\lvert\mathrm{DCA}\rvert > 0.1$ cm, $\lvert\mathrm{DCA_{xy}}\rvert > 0.1$ cm
$\lvert n\sigma_{\mathrm{TPC}}\rvert < 4$

The track selections involve the requirement for the number of clusters and crossed rows in TPC to be larger than 100, i.e., more than half of the total number, to reject geometrically overlapping tracks reconstructed with only part of the array of clusters originating from a single particle. In a similar way, tracks having more than 5 associated clusters shared with other tracks are also excluded. To reject the contamination from out-of-bunch pile up, it is required that at least one of the two candidate decay products either has a matched cluster in the TOF detector or was succesfully refitted in ITS in the last kinematic fitting step. To select tracks mostly created in secondary processes, the DCA criteria of the candidate decay products are inverted with respect to those reported in Section 4.2.1, which are

adopted for primary particle candidates. Finally, a 4σ PID selection in TPC is applied to improve the selection of tracks consistent with the mass hypotheses of the Λ decay products.

Vertex selections

The set of selections related to the reconstructed vertex are reported in Table 4.8.

Table 4.8: Vertex selection criteria applied in the Λ analysis in this Thesis.

Vertex selections
$\lvert\eta\rvert < 0.8$ for the Λ candidate and for all tracks
$5 < R_{\Lambda} < 100$ cm
$ct < 40$ cm
$\mathrm{DCA}_{\mathrm{tracks}} < 0.2$ cm
$\mathrm{DCA}_{V^0,\mathrm{PV}} < 0.5$ cm
$\cos\theta_p > 0.997$
$\lvert M(\pi^+ + \pi^-) - M^{\mathrm{PDG}}_{\mathrm{K}^0_{\mathrm{S}}}\rvert > 0.01$ GeV/c^2

The candidates are selected in a window of ct corresponding to the core of the Λ production. The ct is computed as $ct = ML/p$ using the decay length, L, the momentum of the candidate, p, and the nominal mass of the particle under study, i.e., $M^{\mathrm{PDG}}_{\Lambda}$ in this case, as provided by the Particle Data Group (PDG) [9]. As shown in Fig. 4.6, the decay length is obtained assuming a linear trajectory from the primary to the secondary vertex, as:

$$L = \sqrt{(x_{\mathrm{PV}} - x_{\mathrm{SV}})^2 + (y_{\mathrm{PV}} - y_{\mathrm{SV}})^2 + (z_{\mathrm{PV}} - z_{\mathrm{SV}})^2}, \tag{4.5}$$

where $(x, y, z)_{\mathrm{PV}}$ and $(x, y, z)_{\mathrm{SV}}$ are the coordinates of the primary and secondary vertices, respectively. The radius of the reconstructed decay vertex with respect to the nominal interaction point in the transverse plane, is computed as:

$$R = \sqrt{x^2_{\mathrm{SV}} + y^2_{\mathrm{SV}}}, \tag{4.6}$$

is also required to lie in a fiducial range where a good reconstruction quality is achievable.

To reduce the combinatorial background and the feed-down contribution from de-

cays of heavier states, additional selections are applied to the topological variables of the decay, also shown schematically in Fig. 4.6:

1. Distance of closest approach between the decay products, $\mathrm{DCA}_{\mathrm{tracks}}$;
2. Distance of closest approach of the Λ direction of flight, corresponding to the momentum vector of the reconstructed candidate, and the primary vertex, $\mathrm{DCA}_{V^0,\mathrm{PV}}$;
3. Cosine of the ponting angle, $\cos\theta_p$, defined as the angle between the straight line connecting the primary and secondary vertices and the opposite of the momentum vector of the reconstructed candidate.

The distributions of these variables both for signal and background candidates samples obtained with a MC simulation are shown in Fig. 4.7.

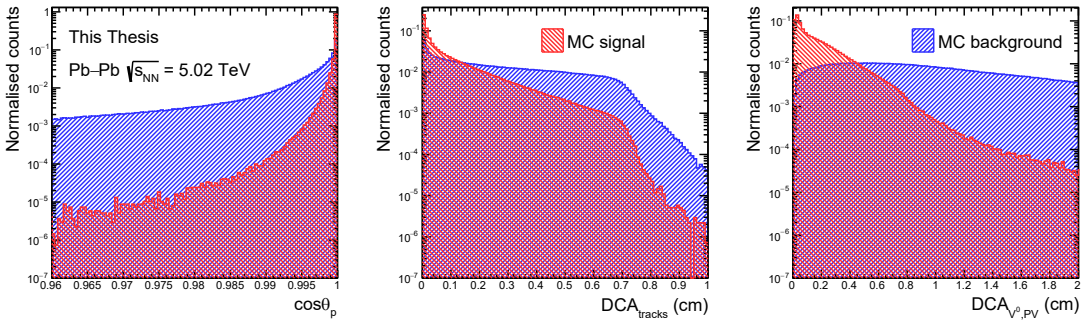

Figure 4.7: Distribution of the topological variables used for the selection of Λ candidates: $\cos\theta_p$ on the left, $\mathrm{DCA}_{\mathrm{track}}$ in the middle, $\mathrm{DCA}_{\Lambda,\mathrm{PV}}$ on the right. The distributions are shown both for signal and background candidates obtained from a MC simulation.

The distributions of these topological variables show significant discrepancies between the signal and background samples. In particular, signal candidates are characterised by a better pointing to the PV than background ones, in terms of both $\cos\theta_p$ and $\mathrm{DCA}_{V^0,\mathrm{PV}}$. Additionally, the two V^0 tracks are geometrically closer, on average, for signal candidates than for background ones. Hence, the selections applied on $\cos\theta_p$, $\mathrm{DCA}_{V^0,\mathrm{PV}}$, and $\mathrm{DCA}_{\mathrm{tracks}}$ provide a powerful handle to reject the combinatorial background in the Λ sample. This is checked by analysing the invariant mass distribution of the selected Λ candidates before and after applying such requirements. For a two-body decay, the invariant mass is computed from the 4-momenta of the decay products determined at the decay vertex, $(E_1, \vec{p}_1)$ and

$(E_2, \vec{p}_2)$, as:

$$M_{1,2} = \sqrt{(E_1 + E_2)^2 - |\vec{p}_1 + \vec{p}_2|^2}. \tag{4.7}$$

As only the momenta of the tracked decay products are measured, their energies are inferred by assuming the mass hypotheses. Hence, it is required to distinguish antiparticles from particles, as the decay products have different masses. This is achieved by determining the Armenteros-Podolanski α variable [171], defined for a V^0 topology as the momentum asymmetry between the two decay products along the direction of flight of the initial particle:

$$\alpha = \frac{p_L^+ - p_L^-}{p_L^+ + p_L^-}, \tag{4.8}$$

where p_L^+ and p_L^- are the projections of the momenta of the positively- and negatively-charged decay products along the direction of the decaying-particle momentum, respectively. From the decay kinematics it is determined that $\alpha > 0$ for Λ, while $\alpha < 0$ for $\bar{\Lambda}$. Hence for the selected Λ candidates, the mass of the proton is assigned to the positively charged track and that of pion to the negatively charged one, and viceversa for $\bar{\Lambda}$. In Fig. 4.8, the distribution of the selected candidates is compared with the one obtained without applying any topological selection related to the reconstructed vertex.

The background rejection performance can be evaluated by determining the purity of the Λ signal in the selected sample of candidates. The purity is defined as:

$$\text{Purity} = \frac{S}{S + B}, \tag{4.9}$$

where S and B are the number of signal and background candidates, respectively. The values of S and B are extracted in a region of interest, centred around the nominal Λ mass, of width $\pm 3\sigma$, with σ the invariant mass resolution observed in the data. The Λ mass reported by the PDG is taken as a reference here, as mass shifts caused by inaccuracies in the momentum measurements are negligible in this context. The background is estimated by integrating in the signal region the extrapolation of an exponential fit to the sidebands of the invariant mass distribution, while the signal counts are extracted as the difference between the total counts in the signal region and the background counts. The sideband candidates are selected requiring that the difference between their invariant mass and the nominal Λ one is larger than 7σ. The purity extracted in this way increases from

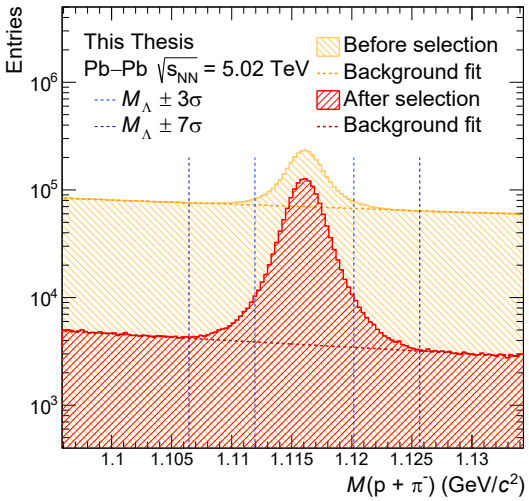

Figure 4.8: Invariant mass distributions of Λ candidates before and after the application of topological selections on the reconstructed vertex. The exponential background fits to the sidebands are shown in dashed lines for the two cases. The vertical lines show the edges of the 3σ and 7σ regions centred around the nominal Λ mass.

about 51% to about 93% with the application of the topological selections.

The Λ candidates are finally selected by comparing their invariant mass with the nominal one. It is possible that a selected candidate is simulataneously consistent with other species by changing the mass hypothesis of the decay products: for the Λ, the largest effect of this kind is caused by the K^0_S meson decaying into a pair of oppositely charged pions, $K^0_S \to \pi^+ + \pi^-$. To reject these candidates, a veto is imposed on the competing invariant mass, computed by assigning the pion mass hypothesis to both decay products.

4.3.2 Two-body decay topologies: $^3_\Lambda$H

The selection of the $^3_\Lambda$H candidates is carried out with a supervised ML approach based on Boosted Decision Trees (BDT). In this Thesis, the BDT implementation provided by the `XGBoost` [172] library is employed. The handling of the ML models and of the data samples is carried out through the `hipe4ml` [173] package, consisting in a series of utilities for ML analyses in heavy-ion physics experiments. In this Thesis, the analysis of $^3_\Lambda$H is carried out differentially in the proper pseudo-decay length of the candidates, ct, in the interval $2 \leq ct < 35$ cm.

BDTs and ML analysis

The BDT is an algorithm commonly used for classification tasks, where signal and background candidates are identified out of a sample containing both components. This is done by computing a score for each of the candidates using a set of input variables, also referred to as *features*. The BDT output score is linked to the probability of the candidate to be signal or background.

The BDT predictions rely on a boosting procedure, where the responses of multiple weak base classifiers are combined to obtain a more discriminative classifier. The base classifiers used in the BDT are decision trees (DT), which consist of a set of binary selections subsequently applied to the input features of the candidates. This process results in a tree structure where the initial data sample, located at the *root* node, is split into either signal- or background-enriched subsamples at each branching point, with the final partitions represented by the *leaves* of the DT. For each candidate fed as input of the DT, a score is computed based on the leaf the candidate under study is assigned to. The scores of the DTs are then weighted to obtain the final BDT prediction.

The selection criteria applied in the single base classifiers, as well as the whole structure of the final boosted classifier, are optimised in a *training* phase using a sample of correctly-classified signal and background candidates, also known as the training sample. During the training, the BDT parameters are progressively modified to minimise the difference, measured by an *objective function*, between the predicted and true class to which the training sample candidates belong. In the `XGBoost` BDT, the objective function also includes a regularisation component to limit the growth of the model during the training. The response of the trained BDT is then validated on a statistically-indipendent data sample constructed in a similar way as the training one, called *testing sample*.

A special set of parameters, called *hyperparameters*, constrain the structure of the classifier: they include the maximum number of base classifiers; the maximum depth of the base classifiers; the learning rate, i.e., the amount of change of the BDT parameters in each iteration of the objective function optimisation; the conditions for adding additional binary splittings to the base classifiers; the conditions for the training set partitioning and sampling during the tree growth. The hyperparameter values used for the ${}^{3}_{\Lambda}\mathrm{H}$ analysis are reported in Table 4.9. The optimal values of these BDT parameters are determined with a Bayesian optimisation algorithm [174]. This optimisation is carried out once for the full training sample and

the obtained hyperparameter configuration is fixed in the model training.

Table 4.9: Hyperparameter values used for the ${}^{3}_{\Lambda}\mathrm{H}$ ML analysis in this Thesis.

XGBoost BDT hyperparameters
max_depth = 13
learning_rate = 0.0982
n_estimators = 181
gamma = 0.4467
min_child_weight = 5.75
subsample = 0.74
colsample_bytree = 0.57

Training sample

The training sample is built out of candidates which are known to be either from real ${}^{3}_{\Lambda}\mathrm{H}$ decays (signal) or from the matching of uncorrelated tracks (background).

To obtain a sample of correctly-tagged ${}^{3}_{\Lambda}\mathrm{H}$ decays, a MC simulation is employed. The sample size of generated ${}^{3}_{\Lambda}\mathrm{H}$ candidates is enhanced with an injection procedure. The underlying Pb–Pb collision is simulated with the HIJING code, while 40 signal particles, both for ${}^{3}_{\Lambda}\mathrm{H}$ and its charge conjugate state, are injected on top of the Pb–Pb event. The kinematics of the injected particles is sampled from uniform distributions of p_{T}, y, and φ, with the ranges $p_{\mathrm{T}} \in [0, 10]$ GeV/c, $y \in [-1, 1]$, and $\varphi \in [0, 2\pi]$. To obtain a signal sample with realistic kinematic properties, the p_{T} distribution of ${}^{3}_{\Lambda}\mathrm{H}$ is modulated with rejection sampling [175]. The reference distribution used in this Thesis is the measured p_{T} spectrum of ${}^{3}\mathrm{He}$ [176]. As of the most recent measurements done by the ALICE collaboration [133], this shape is consistent with the ${}^{3}_{\Lambda}\mathrm{H}$ one within uncertainties, but it is known with better precision due to the higher reconstruction efficiency of ${}^{3}\mathrm{He}$. The p_{T} spectrum shapes in the different analysed centrality intervals are parameterised with the Blast Wave function [177], which provides a good description of p_{T} spectra in heavy-ion collisions.

The background sample is generated with a data-driven procedure. In the selected data sample, the vertex finding algorithm is applied to pairs of tracks with like-sign (LS) electric charge. This procedure enables the production of a large sample of background-only candidates starting from real reconstructed data, also in the signal region of the ${}^{3}_{\Lambda}\mathrm{H}$. The signal region defined in terms of the invari-

ant mass resolution, σ, as the 5σ-wide invariant mass region centered around the nominal ${}^{3}_{\Lambda}\mathrm{H}$ one. The properties of the LS background candidates are checked to be compatible with the real unlike-sign background ones. This is verified by comparing the distributions of the kinematic and topological variables of the LS sample with those of the unlike-sign pairs selected in the sidebands of the invariant mass distribution built for ${}^{3}_{\Lambda}\mathrm{H}$ candidates.

The composition of the obtained training sample is detailed in Table 4.10. The number of candidates reported includes only those that pass the preliminary selections described below.

Table 4.10: Composition of the sample of ${}^{3}_{\Lambda}\mathrm{H}$ candidates used for the BDT training in this Thesis.

Training sample	N_{signal}	$N_{\mathrm{background}}$
${}^{3}_{\Lambda}\mathrm{H}$, Pb–Pb	1.7×10^{6}	3.0×10^{7}

Preliminary selections

A set of preliminary selections is applied to the initial data sample to reduce the sample size for computational reasons and to select only candidates with a good reconstruction quality for the subsequent ML analysis. These selections involve quality criteria applied both on the tracks used in the secondary vertexing and on the properties of the reconstructed vertex itself. The full list of preliminary selections is reported in Table 4.11.

Table 4.11: Preliminary selections applied to the ${}^{3}_{\Lambda}\mathrm{H}$ candidates in this Thesis.

Track selections
$n_{\mathrm{TPCclusters}} > 50$
p_{T} ^{3}He track > 1.2 GeV/c
$\lvert\mathrm{DCA}\rvert < 8$ cm
$\chi^2/n_{\mathrm{TPCclusters}} < 4$
Vertex selections
$\lvert\mathrm{DCA}_{\mathrm{tracks}}\rvert \leq 1.6$ cm
$\cos\theta_p > 0.9$
$0.4 < R < 200$ cm
$2 \leq p_{\mathrm{T}} < 10$ GeV/c

The variables employed for the selections are analogous to those defined in Section 4.2.1 and Section 4.3.1. In this case, large samples both of signal and background candidates are needed in the BDT training: consequently, the applied thresholds are less restrictive than those used to select Λ candidates. Using looser criteria, milder constraints are set also to the phase space of the selected signal and background candidates, avoiding biases in the BDT training due to possible limits in the reproducibility of kinematic and topological variables in the MC simulations used for the training. The background contribution is later suppressed by applying the BDT selections to the data sample.

Training and testing

Separate BDT classifiers are trained for each of the intervals of *ct* used for the extraction of the yields, i.e., [2, 4], [4, 8], [8, 14], [14, 35] cm. As in semicentral collisions the statistical significance of ${}^{3}_{\Lambda}\mathrm{H}$ yields is limited due to the available sample size, a different *ct* binning is applied to improve the yield extraction. Consequently, two additional bins are considered in the training, namely [4, 7], [7, 14] cm.

The BDT input features used both for the training and for the subsequent application of BDT selections on the data are:

- $\cos\theta_p$;
- p_{T} of the ${}^{3}_{\Lambda}\mathrm{H}$ candidate;
- $\mathrm{DCA}_{\mathrm{tracks}}$;
- $|\mathrm{DCA}_{xy,\mathrm{PV}}|$ for both π^- and ${}^3\mathrm{He}$;
- $|\mathrm{DCA}_{\mathrm{PV}}|$ for both π^- and ${}^3\mathrm{He}$;
- $n^{\mathrm{He}}_{\mathrm{TPCclusters}}$ for ${}^3\mathrm{He}$ only;
- $n\sigma_{\mathrm{TPC}}$ for both π^- and ${}^3\mathrm{He}$.

The $n_{\mathrm{TPCclusters}}$ feature is included for the candidate ${}^3\mathrm{He}$ track, as it allows us to discriminate between ${}^3\mathrm{He}$ and ${}^3\mathrm{H}$ candidates. The distributions of the input features are shown in Fig. 4.9, both for background and signal candidates. In addition, the correlation coefficient between all possible pairs of features is studied, both for the signal and for the background sample. The obtained correlation matrices are shown Fig. 4.10.

The differences between the variables of signal and background candidates, as well

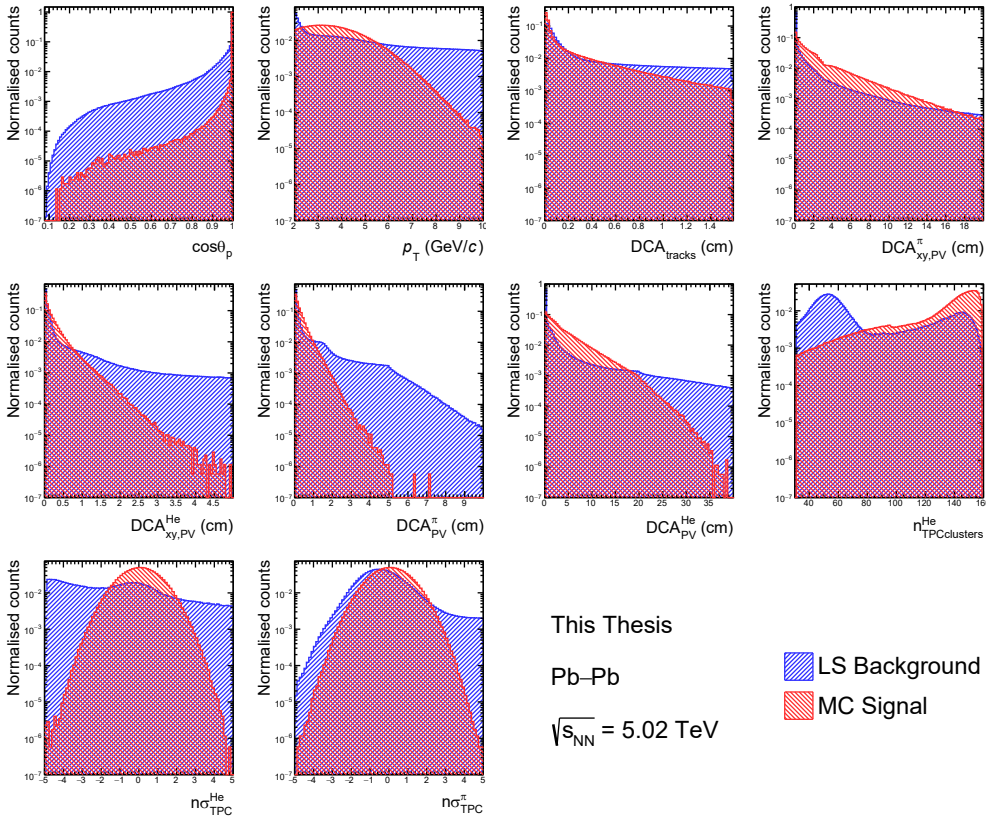

Figure 4.9: Normalised distributions of the BDT input features of both the signal and background ${}^{3}_{\Lambda}\mathrm{H}$ candidates used in this Thesis, for $2 \leq ct < 35$ cm in the 0-90% centrality interval.

as their different linear correlations, are exploited by the classifier to discriminate between the two components.

For the training phase, only half of the training sample is used. The candidates used for the training are uniformly sampled from the training data set; the remaining half is used for the validation of the trained BDTs. The performance of the training is evaluated by comparing the BDT output score distributions obtained in the training and testing samples, both for signal and background candidates. The classification performance is validated separately for matter and antimatter candidates, in the different analysed centrality intervals, as the trained BDT models are applied separately for the two charge-conjugated components in separate centrality ranges in the analysis of real unclassified data. An example of this comparison is shown in the left panel of Fig. 4.11, for the 5% most central collisions and for

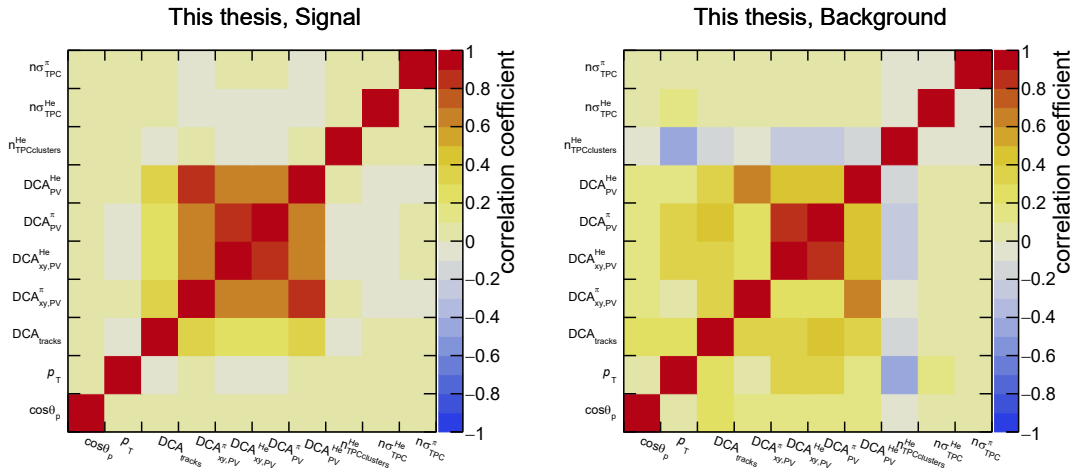

Figure 4.10: Pearson correlation coefficient between all possible pairs of the BDT input features of both the signal and background ${}^{3}_{\Lambda}\mathrm{H}$ candidates used in this Thesis, for $2 \leq ct < 35$ cm in the 0-90% centrality interval.

$2 \leq ct < 4$ cm. The obtained distributions indicate that the model response is con-

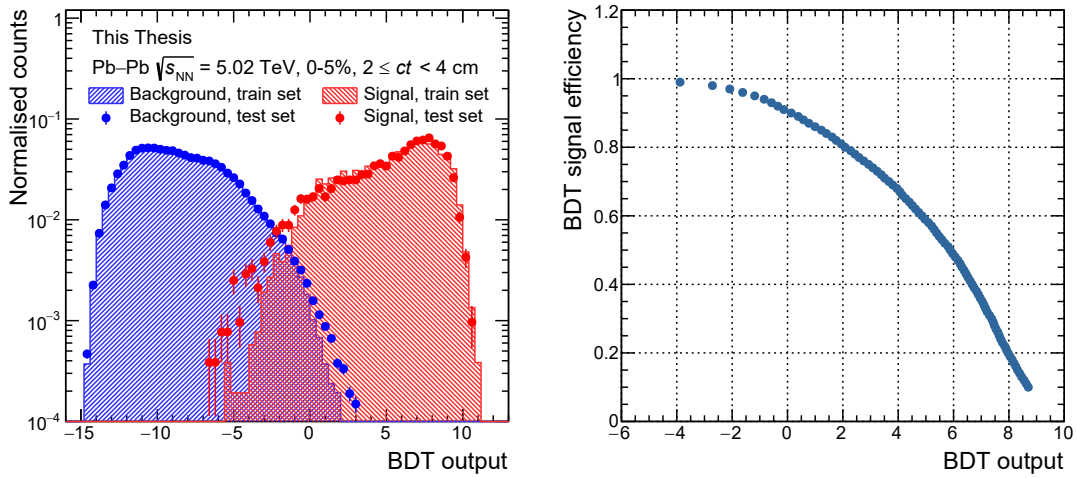

Figure 4.11: Left: BDT output score distribution for the ${}^{3}_{\Lambda}\mathrm{H}$ (excluding ${}^{3}_{\Lambda}\bar{\mathrm{H}}$) candidates in the signal (red) and background (blue) samples, both for the training (shaded area) and testing (filled circles) data samples, for the 5% most central events. Right: BDT signal selection efficiency as a function of the BDT output score.

sistent between the training and testing dataset. This indicates that the trained

classifier is able to reliably generalise its classification output beyond the training examples. A slight difference is observed in the tails of the distributions: this suggests that a small amount of overfitting affects the trained models. However, this does not affect the subsequent processing steps, as all corrections computed from MC simulations, e.g., the signal candidate selection efficiency, rely on using the testing data sample. In this way, any possible classification bias connected to the small discrepancies of the BDT response on the training and testing candidates is avoided.

The signal selection efficiency of a certain BDT output threshold is computed as the fraction of candidates passing the BDT output selection out of the total ones in the testing sample. Consequently, the BDT signal efficiency is monotonically dependent on the BDT output score. To correctly evaluate the BDT selection efficiencies of matter and antimatter candidates, the two components are processed separately at this stage. The BDT signal efficiency as a function of the score is shown in the right panel of Fig. 4.11, for the matter candidates in the 5% most central collisions and for $2 \leq ct < 4$ cm. There, the efficiency values are reported for efficiency steps of 0.01, from 0.1 at large BDT output to 0.99 at small BDT output.

Optimisation of the BDT working point

The BDT selection is performed by selecting only candidates having a BDT signal selection efficiency larger than a certain threshold. The threshold is set to the value maximising the statistical significance of the expected ${}^{3}_{\Lambda}\mathrm{H}$ signal, which is defined as:

$$\text{Significance} = \frac{S}{\sqrt{S+B}}, \tag{4.10}$$

where S and B are the signal and background counts within a 5σ window centered around the nominal ${}^{3}_{\Lambda}\mathrm{H}$ mass. The σ used for this procedure is the resolution of the ${}^{3}_{\Lambda}\mathrm{H}$ invariant mass distribution obtained from MC simulations.

An example of this procedure for the $2 \leq ct < 4$ cm interval in the 0-5% centrality range is shown in Fig. 4.12. The expected ${}^{3}_{\Lambda}\mathrm{H}$ yield is obtained by integrating the measured ${}^{3}\mathrm{He}$ spectra in the analysed interval. To accurately model the expected raw signals, the obtained yields are corrected using the measured ${}^{3}_{\Lambda}\mathrm{H}/{}^{3}\mathrm{He}$ ratio and the branching ratio of the analysed two-body ${}^{3}_{\Lambda}\mathrm{H}$ decay. Additional corrections takes into account the efficiencies of both the preselections and the BDT signal selection. They are computed with MC simulations as the fraction of gener-

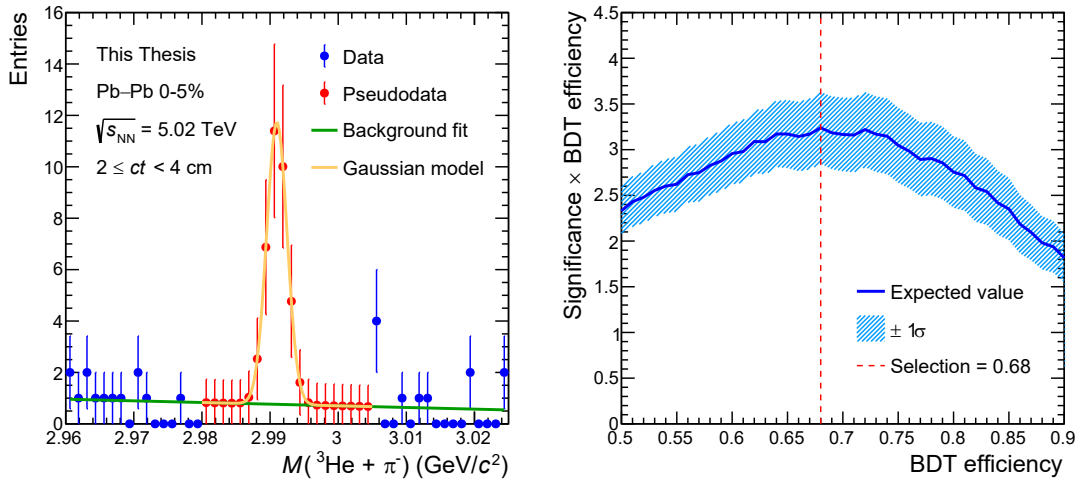

Figure 4.12: Left: fit of the sidebands of the invariant mass obtained from the data for ${}^3_\Lambda$H candidates in the $2 \leq ct < 4$ cm in the 0-5% centrality interval, with a BDT signal selection efficiency of 0.68. The expected ${}^3_\Lambda$H signal is shown with a gaussian shape, which is also sampled to generate the pseudodata reported in the figure. Right: scan of the expected significance in the $2 \leq ct < 4$ cm range and in the 0-5% centrality interval. The central value of the significance and its statistical uncertainty are shown, as well as the threshold set by the optimisation of the significance×BDT signal selection efficiency.

ated ${}^3_\Lambda$H candidates passing the respective selections. The background distribution in the ${}^3_\Lambda$H signal region is modelled with an exponential fit to the sidebands of the invariant mass distribution of the helium-pion pairs observed in the data. The background counts are then obtained from the integral of the fit function extrapolated to the ${}^3_\Lambda$H signal region. This procedure is repeated for each value of the BDT signal efficiency from 0.5 to 0.99, with steps of 0.01. The expected significance is then multiplied by the BDT signal selection efficiency, as a penalty factor for low-efficiency selection criteria characterised by a large background rejection. This optimisation is carried out separately for the charge conjugate candidates, in each of the analysed centrality and ct intervals.

4.3.3 Cascade decay topologies

The Ξ^- and Ω^- candidates are identified with a ML analysis analogous to that applied for the ${}^3_\Lambda$H selection. In this Thesis, the yields of Ξ^- are extracted in intervals of p_{T} while those of Ω^- are studied in intervals of ct. The analysed intervals are $1 \leq p_{\mathrm{T}} < 3$ GeV/c and $1 \leq ct < 10$ cm for Ξ^- and Ω, respectively.

The Ξ^- candidates are selected in the ct interval $ct < 20$ cm, while the Ω^- ones are analysed in the p_{T} range $0.5 \leq p_{\mathrm{T}} < 4.5$ GeV/c.

Training sample

The training sample for the cascade analysis is built with a similar strategy as the one applied for the ${}^{3}_{\Lambda}\mathrm{H}$ analysis: the signal candidates are obtained from MC simulations, while the background sample is obtained with a data-driven procedure.

The MC simulations of pp collisions for Ξ^- and of Pb–Pb collisions for both Ω^- and Ξ^- are carried out using an injection procedure for the multistrange baryons signal. The injection schemes used in both cases are the ones reported in Table 4.2. In both cases, the initially uniform p_{T} distribution is modulated to reproduce the physical shapes observed in the measurements. In the pp sample, the functional form used is a Levy-Tsallis distribution, which is able to describe the measured p_{T} spectra of light-flavour hadrons. The parameterisation of this function is extracted from the p_{T} spectrum of Ξ^- measured by the ALICE Collaboration in pp collisions at $\sqrt{s} = 5.02$ TeV. For the Pb–Pb sample, a Blast-Wave function is used. The parameterisation of the Blast-Wave shape is extracted from the combined fits of the π^-, K^-, and p spectra measured by the ALICE Collaboration in Pb–Pb collisions at $\sqrt{s_{\mathrm{NN}}} = 5.02$ TeV [21]. For the p–Pb simulation used to build the Ξ^- signal sample, no additional injection of signal candidates is applied as the EPOS 3 event generator correctly reproduces the observed yields of multistrange baryons, which are sufficient to obtain the required number of signal candidates for the training.

The background samples for Ξ^- and Ω^- are obtained by selecting in the recorded data the candidates having an invariant mass deviating more than 7σ from the nominal ones, σ being the invariant mass resolution in the data. The invariant mass of the reconstructed candidates is computed with Eq. (4.7), where the decay products are the bachelor track and the reconstructed V^0 decay topology. The energy and momentum vector of the reconstructed V^0s are obtained from the addition of the 4-momenta of the two decay products.

The number of signal and background candidates contained in the training samples for the Ω^- and Ξ^- analysis are reported in Table 4.12.

Table 4.12: Composition of the samples of $\Xi^{\pm}$ and $\Omega^{\pm}$ candidates used in this Thesis to train BDTs.

Training sample	N_{signal}	$N_{\text{background}}$
Ω^-, Pb–Pb	6.8×10^5	2.9×10^6
Ξ^-, Pb–Pb	7.4×10^5	6.8×10^7
Ξ^-, p–Pb	7.7×10^5	1.5×10^6
Ξ^-, pp	1.8×10^6	3.7×10^5

Preliminary selections

The cascade decay topologies of Ξ^- and Ω^- baryons are reconstructed in two steps. First, the decay vertices of the Λ baryons produced by the multistrange baryon decays are reconstructed from pairs of tracks, in the same way as for the candidates described in Section 4.3.1. The reconstructed Λs are then paired with bachelor track candidates to find the multistrange baryon decay vertices. As a result, both the preliminary selection criteria and the BDT input features include variables connected to both of the reconstructed decay vertices.

The list of preliminary selections applied is reported in Table 4.13.

The track selections, here applied both to the V^0 track pair and to the bachelor track, are analogous to those used for the analyses of two-body decay topologies. The threshold applied on the DCA to the PV of the V^0 tracks is larger than that applied in the Λ analysis described in Section 4.3.1, as more displaced V^0s are preferentially selected for the identification of true cascade decays.

The vertex-related selection apply to both of the vertices reconstructed in the cascade decay topologies. Specifically, lower thresholds close to unity are provided for the cosine of the pointing angles computed both for the Ξ^- and Ω^- ($\cos\theta_p$), and for the Λ decay ($\cos\theta_{p,V^0}$). In addition, a lower threshold is applied to the decay radius of both the multistrange decay, R, and the Λ decay, R_{V^0}. Differently from the Λ selection reported in Section 4.3.1, a lower threshold is applied to the $\text{DCA}_{V^0,\text{PV}}$ in this case to reduce the contribution of primary V^0s. Besides the DCA selections concerning the V^0 decay, which are analogous to those described in Section 4.3.1, an additional selection is applied to the distance of closest approach between the bachelor track and the reconstructed Λ, $\text{DCA}_{\text{bachelor},V^0}$.

As the cascade topologies involve three tracks, a possible source of combinatorial background arises from mistaking as the softer decay product of the V^0 the bach-

Table 4.13: Preliminary selections applied in the analysis of reconstructed cascade topologies. The Λ candidate considered for the cascade reconstruction is labelled as V^0.

Track selection
$\chi^2/n_{\mathrm{TPCclusters}} < 4$
$n_{\mathrm{TPCclusters}} \geq 70$
$\lvert\mathrm{DCA}_{\mathrm{bachelor,PV}}\rvert > 0.1$ cm
$\lvert\mathrm{DCA}_{V^0\mathrm{tracks,PV}}\rvert > 0.2$ cm
$\lvert n\sigma_{\mathrm{TPC}}\rvert < 4$
at least 1 daughter has TOF hit or has ITS refit
TPC refit required
Vertex selection
$\lvert\eta\rvert < 0.8$ for the cascade candidate and for all tracks
$R > 1$ cm, $R_{V^0} > 3$ cm
$\mathrm{DCA}_{V^0,\mathrm{PV}} > 0.1$ cm
$\mathrm{DCA}_{V^0\mathrm{tracks}} < 1.2$ cm
$\mathrm{DCA}_{\mathrm{bachelor},V^0} < 1$ cm
$\cos\theta_p > 0.95$, $\cos\theta_{p,V^0} > 0.95$
$\cos\theta_p^{\mathrm{bachBar}} < 0.99995$
$\lvert M_{\mathrm{competing}} - M_{\Omega}^{\mathrm{PDG}}\rvert < 8$ MeV/c^2 for Ξ^- candidates
$\lvert M_{\mathrm{competing}} - M_{\Xi}^{\mathrm{PDG}}\rvert < 10$ MeV/c^2 for Ω^- candidates

elor track itself, which is then paired to the harder baryon produced in that decay. This background source can be rejected by applying a selection on the cosine of the pointing angle of the *bachelor-baryon* pair, $\cos\theta_p^{\mathrm{bachBar}}$: this quantity is indeed closer to unity for the mismatched pairs in the background sample than for the signal candidates.

The candidates obtained with these preliminary selections are identified as either Ξ^- or Ω^- depending on the compatibility between their invariant mass and the one provided by the PDG for both species. As the mass of the decay products, in particular of the bachelor, is an input of the invariant mass computation, a fraction of the candidates identified as Ξ^- might also be compatible with the Ω^- mass hypothesis by exchanging the mass hypothesis of the bachelor from π^- to K^-, and viceversa. To avoid this potential source of contamination, a veto is applied

on the mass of the competing multistrange baryon mass hypothesis: $|M_{\text{competing}} - M_{\Omega}^{\text{PDG}}| < 8$ MeV/c^2 for Ξ^- candidates, $|M_{\text{competing}} - M_{\Xi}^{\text{PDG}}| < 10$ MeV/c^2 for Ω^- candidates.

BDT training and working point

The training of the BDT is carried out in bins of p_{T} and ct for Ξ^- and Ω^-, respectively. The p_{T} intervals employed for Ξ^- are [1.0, 1.5], [1.5, 2.0], [2.0, 2.5], [2.5, 3.0] GeV/c, while the ct intervals used for Ω^- are [1, 2], [2, 3], [3, 4], [4, 5], [5, 10] cm.

The BDT input features used for the ML analysis of cascade topologies are:

- $\text{DCA}_{\text{bachelor,PV}}$;
- the V^0 topological variables, $\text{DCA}_{V^0,\text{PV}}$, $\text{DCA}_{V^0\pi}$, $\text{DCA}_{V^0\text{p}}$, $\text{DCA}_{V^0\text{tracks}}$;
- $\text{DCA}_{\text{bachelor},V^0}$;
- $\cos\theta_p$ and $\cos\theta_{p,V^0}$;
- $n\sigma_{\text{TPC}}^{\text{p}}$.

In Fig. 4.13, the distributions of the features of Ω^- candidates in the training sample, both for the signal and the background components, are shown. Similar results are obtained also for the Ξ^- training sample.

Similarly to the ${}^{3}_{\Lambda}\text{H}$ analysis, the Pearson correlations between all pairs of features are studied. The results obtained for signal and background Ω^- candidates are shown in Fig. 4.14. The hyperparameters of the `XGBoost` BDT implementation used for the Ξ^- and Ω^- classifiers are reported in Table 4.14. Simpler base classifiers are trained in this case to avoid overfitting effects, due to the smaller training sample available. This is ensured by the hyperparameter settings, e.g., the shallow depth of the base decision trees. In this case, the optimisation of the hyperparameters was carried out with a simple grid search.

Out of the full training sample, only half is used to train the BDT classifiers. The other half is used for the validation of the BDT response. The BDT output response distributions of background and signal candidates, both in the training and testing samples, are shown in Fig. 4.15 for the range $2 \leq ct < 3$ GeV/c. Similar results are obtained in the other ct intervals for Ω^- and in p_{T} intervals for the Ξ^-. The trained classifiers show both a good signal-to-background discrimination and a good generalisation performance from the training to the testing data samples.

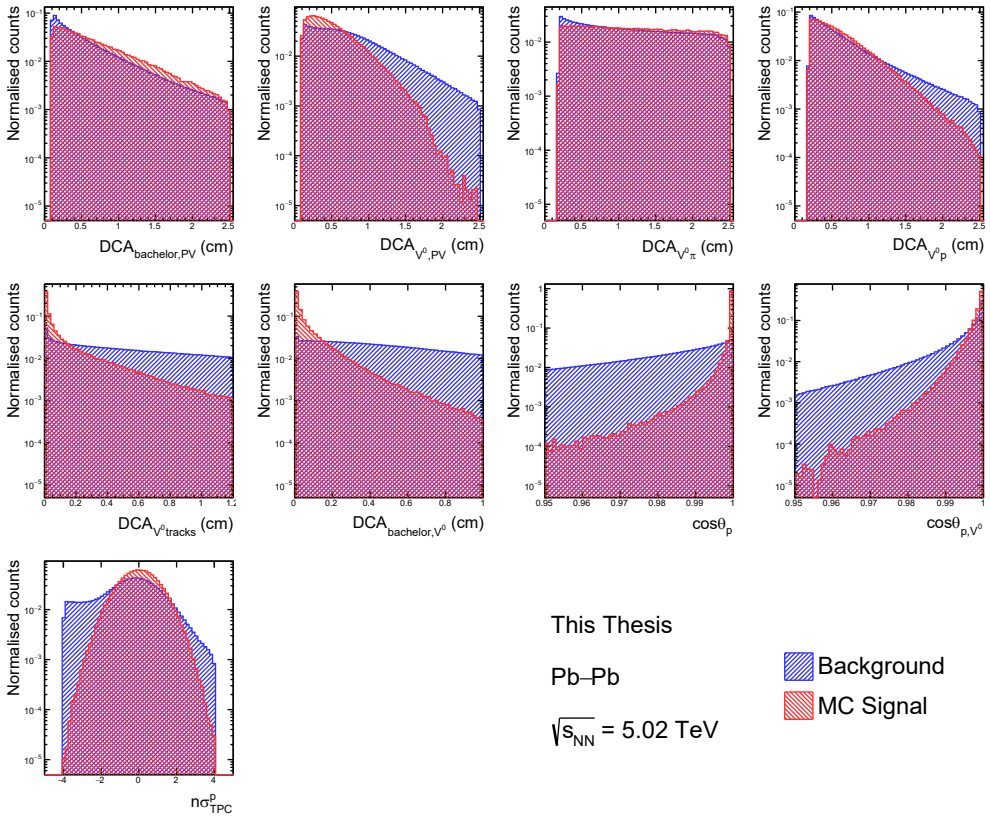

Figure 4.13: Distributions of the BDT input features of both the signal and background Ω^- candidates used in this Thesis, for $0.5 \leq p_{\mathrm{T}} < 4.5$ GeV/c and $1 \leq ct < 10$ cm candidates in the 0-90% centrality interval.

Table 4.14: Hyperparameter values used for the cascade ML analysis in this Thesis.

`XGBoost` BDT hyperparameters
`max_depth = 3`
`learning_rate = 0.05`
`n_estimators = 900` for Ξ^-
`n_estimators = 100` for Ω^-
`gamma = 1.2`
`subsample = 0.8`
`colsample_bytree = 0.7`

The Ξ^- and Ω^- yield in Pb–Pb collisions is about 10^5 and 10^4 times larger than

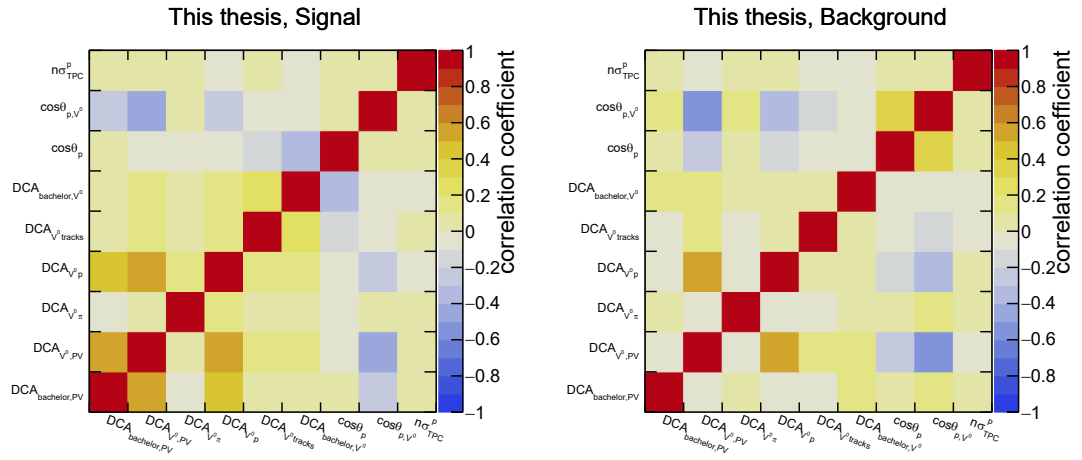

Figure 4.14: Pearson correlation coefficient between all possible pairs of the BDT input features of both the signal and background Ω^- candidates used in this Thesis, for $0.5 \leq p_{\mathrm{T}} < 4.5$ GeV/c and $1 \leq ct < 10$ cm in the 0-90% centrality interval.

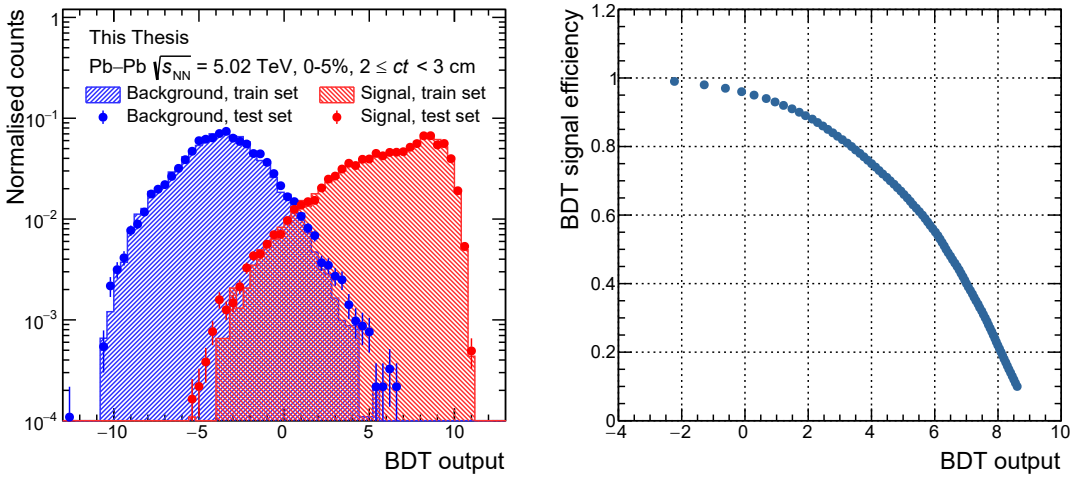

Figure 4.15: Left: BDT output score distribution for the Ω^- candidates in the signal (red) and background (blue) samples, both for the training (shaded area) and testing (filled circles) data samples. Right: BDT signal selection efficiency as a function of the BDT output score.

the ${}^{3}_{\Lambda}\mathrm{H}$ one. Consequently, the selection criteria are less affected by the statistical significance of the extracted signal. However, due to the larger number of candidates analised, the BDT-selected sample is more sensitive to discrepancies

between the MC simulation and the data, due to imperfection in the modelling of detector effects. To reduce the dependence on these effects, the working point of the BDT is set to provide a consistent response between the data and MC. Specifically, the dependency of the extracted signal counts in the data sample on the BDT signal selection efficiency is analysed to determine the region where a linear response is observed. The results obtained for Ω^- candidates in the range $3.0 \leq ct < 3.5$ cm are reported in Fig. 4.16. For the Ω^- analysis, the working point is set to $\epsilon_{\mathrm{BDT}} = 0.5$, for all analysed ct intervals and across centrality. For the Ξ^- analysis, as an additional constraint for the BDT working point, the purity of the extracted signal in the data is required to be at least 0.94. The BDT selection is thus p_{T} dependent in Pb–Pb collisions, ranging from $\epsilon_{\mathrm{BDT}} = 0.3$ at $p_{\mathrm{T}} = 1$ GeV/c to $\epsilon_{\mathrm{BDT}} = 0.5$ at $p_{\mathrm{T}} = 3$ GeV/c, as the residual background contamination decreases at higher p_{T}. In p–Pb and pp collisions, where a lower charged particle multiplicity is created compared to Pb–Pb collisions, the BDT threshold is set to $\epsilon_{\mathrm{BDT}} = 0.6$.

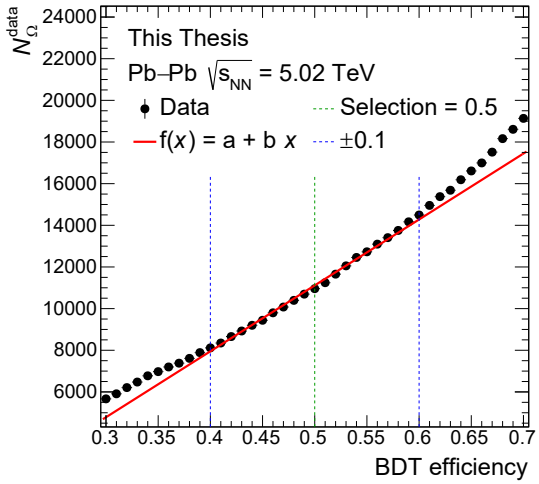

Figure 4.16: Raw yields of Ω^- extracted as a function of the BDT signal selection efficiency, for candidates with $3.0 \leq ct < 3.5$ cm in the 0-5% centrality interval. The data points are compared with a linear fit: the fit range is represented by the blue vertical lines, while the centre of the range, corresponding to the selected threshold, is depicted in green.

Chapter 5

Measurements of chemical potentials in Pb–Pb collisions

In this chapter, the analysis procedure and the final results of the determination of the baryon and eletric-charge chemical potentials, μ_B and μ_Q, from the antiparticle-to-particle yield ratios measured for various hadron species in Pb–Pb collisions at $\sqrt{s_{\rm NN}} = 5.02$ TeV are discussed. The results of this analysis are published in the Physical Review Letters journal [1]. This analysis is based on the full Pb–Pb data sample collected in 2018 by the ALICE Collaboration. The antiparticle-to-particle yield ratios of hadron species are measured differentially, either in $p_{\rm T}$ for tracked species, i.e., π^+, p, ^{3}He, and ^{3}H, or ct for Ω^- and $^3_\Lambda$H, which are reconstructed via their decays. In addition, the analysis is carried out in different centrality intervals, namely 0-5%, 5-10%, 10-30%, 30-50%, 50-90%.

5.1 Analysis strategy

In this Thesis, μ_B and μ_Q are extracted via the combined interpretation of the antiparticle-to-particle yield ratios of π^+, p, Ω^-, ^{3}He, ^{3}H, and $^3_\Lambda$H in the context of the grand canonical (GC) version of the Statistical Hadronisation Model (SHM). These ratios are determined in the midrapidity region $|y| < 0.5$, where the full PID capabilities of the ALICE apparatus can be exploited. The analysed species are selected based on how sensitive their antiparticle-to-particle yield ratios are to the chemical potential values. The approximate relation between the antiparticle-to-particle yield ratios and the chemical potentials can be expressed via the SHM

as [178]:

$$\frac{\bar{h}}{h} \propto \exp\left[-2 \cdot \frac{B_h\mu_B + Q_h\mu_Q + S_h\mu_S}{T_{\rm chem}}\right] \tag{5.1}$$

where $\frac{\bar{h}}{h}$ is the antiparticle-to-particle yield ratios of the hadron spacies h, $T_{\rm chem}$ the chemical freeze-out temperature, and B_h, Q_h, and S_h are the values of the baryon number, electric charge, and strangeness carried by the species h. From Eq. (5.1), it is obtained that the antiparticle-to-particle yield ratios of species characterised by a large baryon-number content are in principle more sensitive to the μ_B value than smaller baryon number ones. However, the experimental precision of the $\bar{h}/h$ measurements also affects how sensitive each species is to the chemical potential values.

The most constraining measurement in the μ_B extraction is provided by the $\bar{\rm p}/{\rm p}$ ratio. Despite carrying $B = 1$, the protons are the most abundantly produced baryons in Pb–Pb collisions: about 40 protons and antiprotons are produced on average in the 5% most central Pb–Pb collisions at the top LHC energy. Consequently, this yield ratio can be measured with minimal statistical uncertainty. The antiparticle-to-particle yield ratios of light nuclei are also suited for this analysis due to their baryon content larger than unity. In this Thesis, all of the detectable $A = 3$ (hyper)nuclei are utilized. The most precisely measured, and hence constraining, antiparticle-to-particle yield ratio in the nuclei sector is the one of ^{3}He, as this nucleus can be identified over a large fraction of its $p_{\rm T}$ production spectrum with a high reconstruction efficiency. Its isospin counterpart, ^{3}H, is included as a test of the isospin dependence of yield ratios. The $^3_\Lambda$H, on the other hand, enables a check also on the strangeness effect in the antimatter-to-matter imbalance of nuclear matter produced in heavy-ion collisions. Deuterons are not included in this measurement, as the measured $\bar{\rm d}/{\rm d}$ ratio is already employed by the ALICE Collaboration to calibrate the antideuteron inelastic cross section used in particle transport codes [179]. Consequently, this information would be used in the measurement of the antiparticle-to-particle yeld ratios themselves through the calculation of the reconstruction efficiency of antideuterons.

A more constraining test of the effect of the strangeness content on these yield ratios is obtained with the measurement of the $\bar{\Omega}^+/\Omega^-$ yield ratio. Compared to the other (multi)strange baryons Λ and Ξ^-, the production of Ω^- is only negligibly affected by decays of heavier states, hence enabling a precise and model-independent determination of its primary yield. Finally, the π^-/π^+ yield ratio is included as

a constraining measurement for the determination of μ_Q, as thousands of charged pions are produced in every central Pb–Pb collision at the LHC, and the only quantum number carried by charged pions is the electric charge.

5.2 Signal extraction

The extraction of the signal, i.e., the number of identified observed candidates, of the tracked species is carried out on a statistical basis by analysing the $n\sigma$ distributions described in Chapter 4. The PID criteria applied in the analysis presented in this Section are reported in Table 5.1.

Table 5.1: PID criteria used in the $\pi^{\pm}$, (anti)proton, (anti)^{3}He, and ^{3}H analyses. The detector used for the PID selection is reported in the second column, while the width of the Region Of Interest (ROI) is reported in the third column. The p_{T} range of each ROI definition is reported in the rightmost column.

Species	Detector	ROI	p_{T} (GeV/c)
(anti)^{3}He	TPC	$[\mu - 3\sigma, \mu + 3\sigma]$	[2.00, 8.00]
(anti)^{3}H	TOF	$[\mu - 3\sigma, \mu + 3\sigma]$	[1.60, 3.00]
(anti)proton	TPC	$[\mu - 3\sigma, \mu + 5\sigma]$	[0.50, 1.00]
(anti)proton	TOF	$[\mu - 8\sigma, \mu + 8\sigma]$	[1.00, 1.55]
		$[\mu - 6\sigma, \mu + 8\sigma]$	[1.55, 2.00]
		$[\mu - 5\sigma, \mu + 9\sigma]$	[2.00, 2.50]
		$[\mu - 3.5\sigma, \mu + 10\sigma]$	[2.50, 2.80]
		$[\mu - 3.5\sigma, \mu + 11\sigma]$	[2.80, 3.00]
$\pi^{\pm}$	TOF	$[\mu - 2\sigma, \mu + 11\sigma]$	[0.70, 1.20]
		$[\mu - 2\sigma, \mu + 9\sigma]$	[1.20, 1.60]

For π^+ and p, the total counts are extracted inside the signal region and the background counts, extracted with a fitting procedure, are subtracted to isolate only the signal counts. The background fitting is carried out in the sidebands of the $n\sigma$ distributions extracted either with TPC, for $p_{\mathrm{T}} < 1$ GeV/c protons, or with TOF, for protons having $p_{\mathrm{T}} > 1$ GeV/c and π^+ in the full p_{T} range analysed. The sideband region is defined by excluding the signal region of interest from the observed $n\sigma$ distribution. For the TPC analysis, the signal region is defined as $[\mu - 3\sigma, \mu + 5\sigma]$. For the TOF PID analysis of protons, due to the contribution of non-gaussian tails in the observed signal shapes, larger signal regions are defined in terms of the $n\sigma$ resolution extracted in the data, specifically $[\mu - 8\sigma, \mu + 8\sigma]$, to exclude signal effects from the sidebands samples. For charged pions, the signal region is defined as an asymmetric interval, $[\mu - 2\sigma, \mu + 11\sigma]$ since a strong asym-

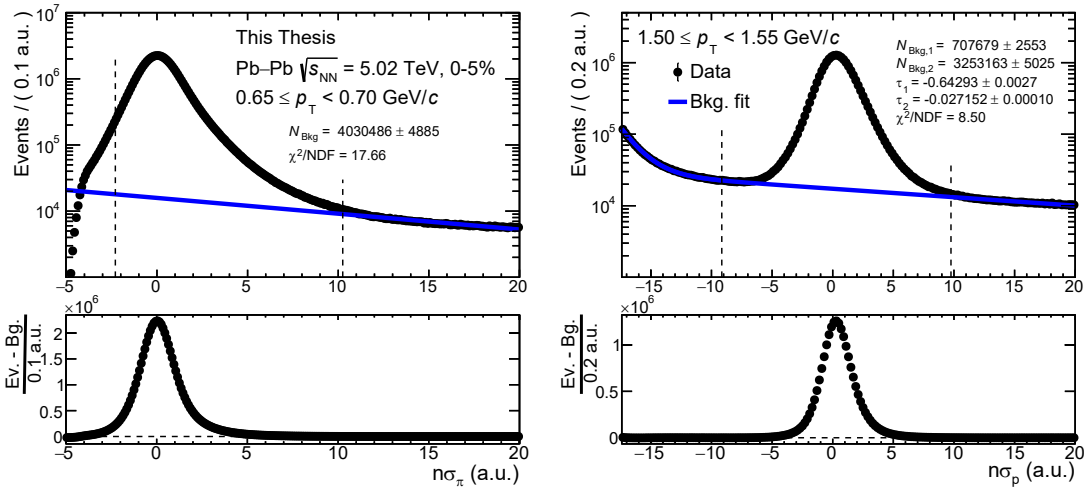

Figure 5.1: Background subtraction performance for π^+ (left) and p (right), in the 5% most central Pb–Pb collisions, for specific p_T bins. The signal regions are delimited in the plot by the pair of vertical lines. The τ parameters are the slopes of the exponential shapes used to model the background components. The background-subtracted distributions are shown in the lower panels.

metry is observed for the signal shapes: the background contribution is fitted only in the right sideband in this case. To optimise the background rejection performance, a moving region of interest is defined for increasing p_T: the intervals used are summarised in Table 5.1. The tight lower limit in the signal region ensures the rejection of mismatches accumulating in the structure observed on the left of the pion signal peak, as shown in the left panel of Fig. 5.1. For the modelling of the background distribution, a simple exponential function is used in the TPC analysis to describe the K^- contamination in the sample of proton candidates, while a double exponential function is used in the TOF analysis to describe both the mismatch contribution and the contamination due to other hadron species. An example of the background subtraction procedure is shown in Fig. 5.1 for both pions (left) and protons (right).

The signal extraction of tracked light nuclei is carried out in a similar way. The background component is extracted from a fit to the $n\sigma$ distributions of either TPC (^{3}He) or TOF (^{3}H), including both the signal and background components. The signal distributions are modelled with gaussian shapes both in TPC and TOF, while the background shapes are modelled as done for the signal extraction of protons. For the ^{3}H signal selection, a tight TPC preselection $|n\sigma| < 2$ is applied

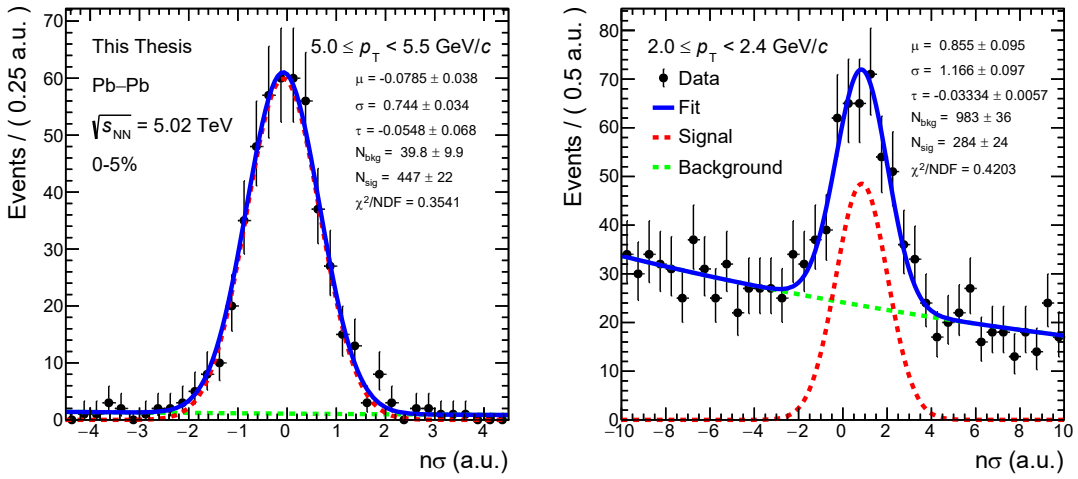

Figure 5.2: Signal extraction fit performance for ^{3}He (left) and ^{3}H (right), in the 5% most central Pb–Pb collisions, for specific p_{T} bins. The signal and background components of the fit are separately shown in the figure. The τ parameter is the slope of the background fit function.

to reduce the ^{3}He contamination. The performance of the fitting procedure is shown in Fig. 5.2. Due to the reduction of statistical significance of the signal at high p_{T} in both semicentral and peripheral events, the p_{T} range analysed for ^{3}He is limited, in terms of upper limit, to 7 GeV/c and 5 GeV/c in the centrality intervals 10-50% and 50-90%, respectively.

For species identified via fully reconstructed decays, the signal is extracted by integrating the measured invariant-mass signal distribution. To disentangle the signal contribution from the residual combinatorial-background contamination, a fit to the invariant mass distribution obtained from the data is carried out. For the hypertriton analysis, the signal shape is obtained through a kernel density estimation (KDE) model [180, 181]. The KDE enables the extraction of a template for the invariant-mass signal distribution obtained from MC simulations, adding also a gaussian smoothening to reduce the effect of statistical fluctuations in the simulations. The only free parameter of the extracted KDE is the mass shift, δm, between the central mass values reconstructed in data and MC. The utilized MC sample contains injected hypertriton particles to enhance the available sample size. For the Ω, the signal shape is described via an extended Crystal Ball function [182], consisting of a gaussian core with smoothly-connected power-law tails. This signal shape enables the description of non-gaussian effects in the tails

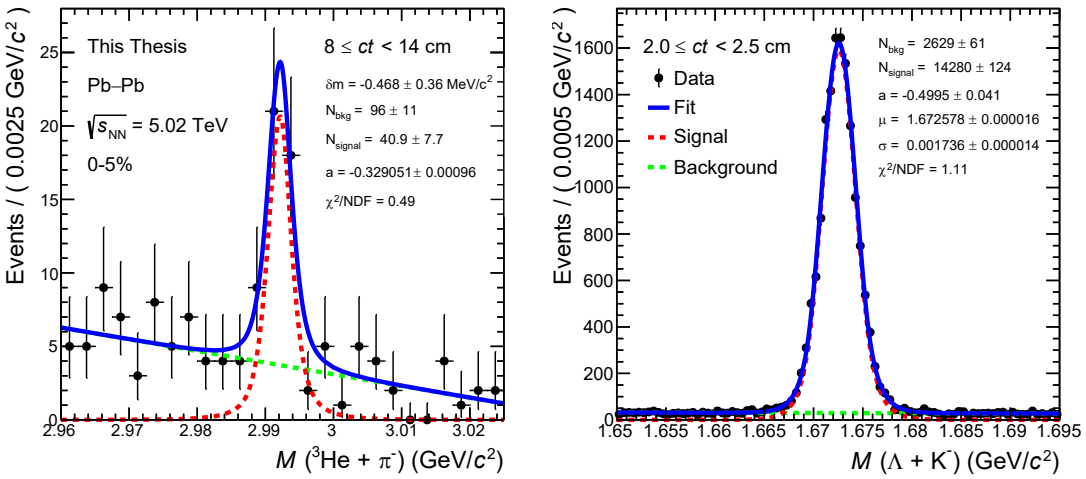

Figure 5.3: Signal extraction fit performance for ${}^{3}_{\Lambda}\mathrm{H}$ (left) and Ω^{-} (right), in the 5% most central Pb–Pb collisions, for specific ct bins. The signal and background components of the fit are separately shown in the figure. The a parameter is the slope of the background fit function.

of the observed invariant mass distributions. In both cases, the distribution of the residual background is modelled through a first degree polynomial. A few examples of the fitting procedure are reported in Fig. 5.3. Similarly to the light nuclei cases, the signals are extracted in narrower ct intervals for semicentral and peripheral events due to the reduction of the available candidate samples. For Ω^{-}, the analysed range is limited to 7 cm in the 50-90% interval; for ${}^{3}_{\Lambda}\mathrm{H}$, the signal is extracted up to 14 cm in the 10-50% centrality interval, while in the 50-90% interval the statistical significance of the extracted signal is negligible over the full ct range.

5.3 Correction factors

The signal counts extracted with the previously described procedure are multiplied by a set of correction factors taking into account effects related to the detection, reconstruction, and candidate selection. Specifically, the reconstruction and candidate selection efficiency, the fraction of primary particles in the samples, and the loss of candidates due to absorption in the detector material are computed for the analysed species. These quantities rely on MC simulated data samples, which are obtained as described in Section 4.1.1.

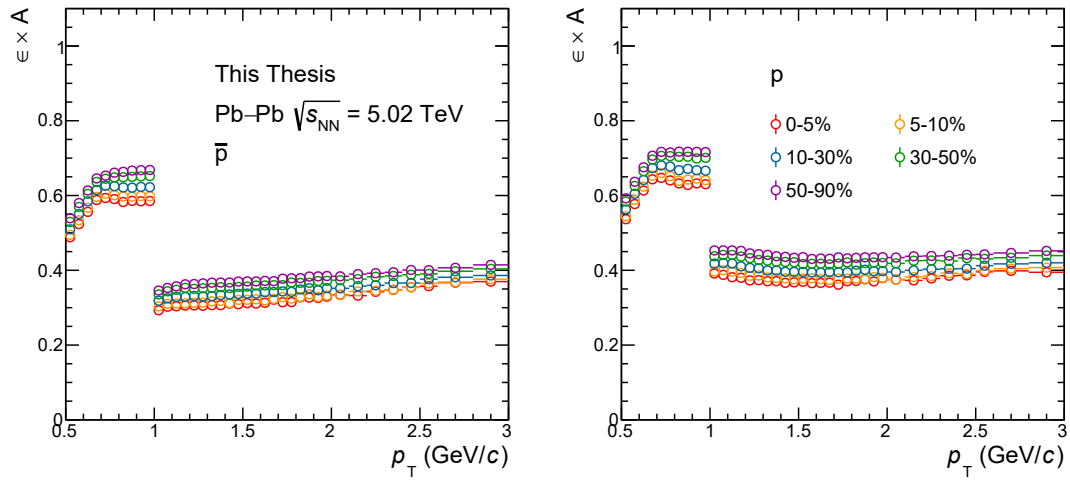

Figure 5.4: Efficiency × acceptance term for $\bar{\mathrm{p}}$ (left) and p (right), in bins of p_{T} for each of the analysed centrality classes.

5.3.1 Efficiency and acceptance

The efficiency, ϵ, of the reconstruction algorithms and of the criteria applied for the candidate selection is computed from MC simulations for each species as the fraction of generated primary particles passing the same criteria applied to the analysed data. The geometrical acceptance of the ALICE central barrel detectors, A is also taken into account in this factor by requiring the same η coverage as the one used in the candidate selection. For the species reconstructed by tracking, where only rectangular selections are applied, the efficiency is computed as:

$$\epsilon \times A = \frac{N_{\mathrm{reco}}(|y| < 0.5, |\eta| < 0.8)}{N_{\mathrm{gen}}(|y| < 0.5)}, \tag{5.2}$$

where N_{reco} and N_{gen} are the number of reconstructed and generated particles, respectively. The $\epsilon \times A$ quantity is determined in each analysed p_{T} bin, separately for the particles and antiparticles, in each of the employed centrality intervals.

As an example, the results obtained for both protons and antiprotons are shown in Fig. 5.4, for each of the analysed centrality intervals. A lower efficiency is observed for the antiparticles with respect to the particles. This reduction is due to the larger inelastic cross section of antimatter in the detector material compared to matter candidates, causing a reduction in the number of reconstructed candidates. Similar differences between antimatter and matter efficiencies are observed for ^{3}He, ^{3}H,

and their charge conjugates. The lower efficiency observed for candidates identified with the TOF detector information, i.e., with $p_{\mathrm{T}} > 1$ GeV/c for (anti)protons, is due to the efficiency of the matching between reconstructed tracks and space points in the TOF. This efficiency, close to 50%, is also affected by the absorption in the TRD detector material, which is located between the TPC and the TOF in the radial direction. The efficiencies are lower in intervals containing more central collisions compared to cases in which peripheral collisions are analysed. This effect is caused by the larger detector occupancy observed in central collisions, causing a degradation in the performance of the tracking algorithms. Similar results are obtained also for the efficiencies of π^+, ^{3}He, and ^{3}H.

For the Ω and ${}^3_\Lambda$H, which are selected with a ML approach, the $\epsilon \times A$ correction is composed of two factors, as reported in Eq. (5.3). The first term takes into account the geometrical acceptance imposed by the $|\eta| < 0.8$ selection, as well as the efficiency of the preliminary selections. The second term is the BDT signal selection efficiency, ϵ_{BDT}: this is uniformly equal to 0.5 across ct and centrality for Ω^-, while for ${}^3_\Lambda$H it is determined in each centrality and ct interval separately for the matter and antimatter components through the optimisation procedure described in Section 4.3.2. The total efficiency is thus computed as:

$$\epsilon \times A = (\epsilon_{\mathrm{prel.}} \times A) \cdot \epsilon_{\mathrm{BDT}} \tag{5.3}$$

As an example, the $\epsilon \times A$ factor obtained for Ω^- and $\overline{\Omega}^+$ are shown in Fig. 5.5. The efficiencies shown in the figure contain also the contribution from the BDT signal selection efficiency. The centrality dependence observed in this case is connected to the evolution of the underlying p_{T} [122], and consequently ct distributions, from central to peripheral collisions within the analysed ct acceptance.

5.3.2 Primary fraction

Out of the selected candidates, only a fraction is produced in the primary interaction. Additional secondary processes, specifically the weak decays of heavier states and the interactions of primary particles in the material of the ALICE apparatus, contribute to particle production. The contribution from secondary processes is partly suppressed via the DCA selections described in Section 4.2. The residual contribution in the selected sample is estimated in this analysis by applying a fitting procedure on the DCA$_{xy}$ distribution observed in data to estimate the fraction of primary particles in the sample. The template fitting is carried out with

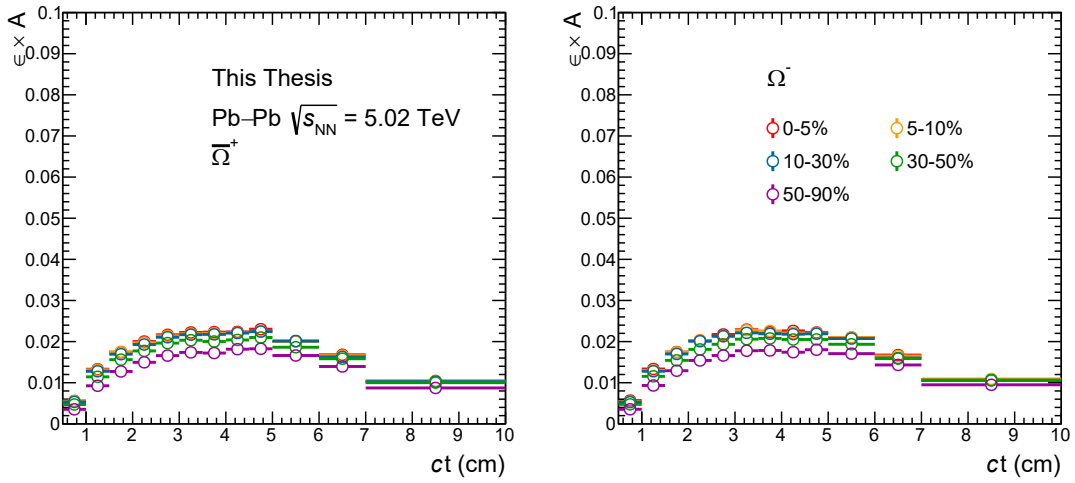

Figure 5.5: Efficiency × acceptance term for $\overline{\Omega}^{+}$ (left) and Ω^{-} (right), in bins of c_{T} for each of the analysed centrality classes.

the `TFractionFitter` class of the ROOT framework. The fitting algorithm is a binned maximum likelihood.

The DCA_{xy} distributions are obtained in the data by applying strict PID criteria to select pure samples of the candidates of interest: two examples for (anti)protons in the 5% most central collisions are shown in Fig. 5.7. The fitting procedure relies on using template distributions extracted from MC simulations for each of the sources contributing to the particle production. The expected DCA_{xy} distribution of primary particles is peaked at zero, as the corresponding tracks point to the primary vertex. The width of the distribution, $O(100\ \mu\mathrm{m})$, represents the pointing resolution of single tracks to the primary vertex.

For secondary tracks produced by interactions of primary particles with the material, a uniform DCA_{xy} distribution is expected because of the lack of correlation between the created particles and the primary vertex position. In reality, a peak is observed at $\mathrm{DCA}_{xy} \sim 0$ for low p_{T} tracks. This effect is due to wrong matchings between real secondary tracks and at least one uncorrelated space point in either of the two SPD layers, resulting in tracks with a better pointing to the primary vertex. In the light nuclei analysis, the template of spallation secondaries is built with simulated secondary deuteron tracks, which are used as proxies of both secondary ^{3}He and secondary ^{3}H to improve the statistical precision of the templates themselves. The transverse momentum of the employed deuteron candidates is

scaled by the electric charge of helions and tritons, as the DCA in the transverse plane depends on the curvature of the analysed tracks.

The distribution of secondary tracks produced in weak decays of light-flavour hadrons is characterised by a decreasing trend for increasing magnitude of the DCA_{xy}. The slope of the expected shape is governed by the hyperon decay lengths, $O(1\ \mathrm{cm} \div 10\ \mathrm{cm})$. However, the distribution is not a simple exponential as a result of the convolution between the decay law with both the kinematics of the decaying particle and the pointing resolution effects. For charged pions, the main feed-down contribution is provided by K^0_S decays, while the production of protons is mainly contaminated by Λ hyperon decays. For light nuclei, the only known feed-down contribution from a weak decay is due to the decay of hypernuclei. This effect is taken into account only for ^{3}He and its charge conjugate, as the effect on ^{3}H is negligible due to the limited size of the available sample. Also for ^{3}He, only a small fraction, $O(5\%)$, of feed-down candidates from $^3_\Lambda$H is expected because of the rarity of the process. Hence, to avoid instabilities in the template fitting procedure, the fraction of helions produced in weak decays of $^3_\Lambda$H is separately estimated using the $^3_\Lambda\mathrm{H}/^3\mathrm{He}$ yield ratio measured by the ALICE Collaboration in Pb–Pb collisions at $\sqrt{s_\mathrm{NN}} = 2.76$ TeV and the feed-down ^{3}He reconstruction efficiency estimated from MC simulations. First, the fraction of reconstructed feed-down ^{3}He, R, is computed using the efficiency factors of ^{3}He from both weak decays, $(\epsilon \times A)_\mathrm{WD}$, and primary interactions, $(\epsilon \times A)_\mathrm{prim}$, along with the branching ratio $\mathrm{BR}(^3_\Lambda\mathrm{H} \to\ ^3\mathrm{He} + \pi^-)$ and the measured yield ratio $(^3_\Lambda\mathrm{H}/^3\mathrm{He})_\mathrm{ALICE}$, as:

$$R = \frac{N^\mathrm{rec}_\mathrm{WD}}{N^\mathrm{rec}_\mathrm{prim}} = \frac{(\epsilon \times A)_\mathrm{WD}}{(\epsilon \times A)_\mathrm{prim}} \cdot \mathrm{BR}(^3_\Lambda\mathrm{H} \to\ ^3\mathrm{He} + \pi^-) \cdot \left(\frac{^3_\Lambda\mathrm{H}}{^3\mathrm{He}}\right)_\mathrm{ALICE} \tag{5.4}$$

The fraction of secondary ^{3}He from weak decays, f_WD, is then obtained as:

$$f_\mathrm{WD} = \frac{R}{R+1} \tag{5.5}$$

The f_WD extracted differentially in p_T in the 5% most central collisions is shown in Fig. 5.6. The obtained fraction is mildly dependent on p_T, with a value $f_\mathrm{WD} \sim 0.05$: similar results are obtained across centrality and also for the charge conjugated states. The statistical uncertainties on the f_WD points are caused by the size of the simulated sample: they are propagated to the final results as p_T-uncorrelated and centrality-uncorrelated sources of systematic uncertainty.

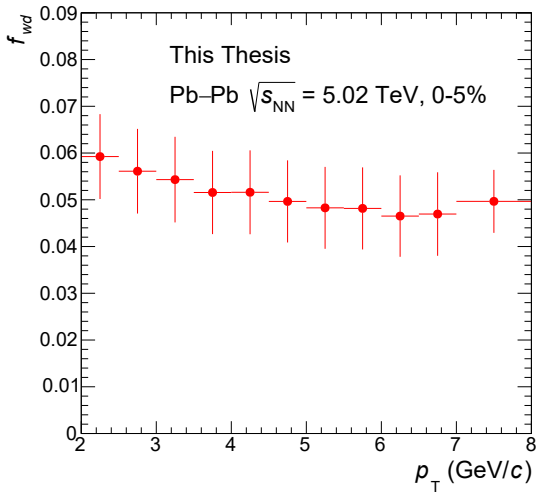

Figure 5.6: Fraction of ^{3}He from two-body decays of hypertriton, ${}^3_\Lambda\mathrm{H} \rightarrow {}^3\mathrm{He}+\pi^-$, in the 0-5% centrality interval.

The f_{WD} fraction is then used to correct the primary fraction extracted with the `TFractionFitter`, f_{TFF} to include the effect of feed down from weak decays:

$$f_{\mathrm{prim}} = f_{\mathrm{prim+WD}}(\mathrm{TFF}) \cdot (1 - f_{\mathrm{WD}}) \tag{5.6}$$

An example of the fitting performance is shown in Fig. 5.7 in a specific p_{T} bin for protons and antiprotons, in the 5% most central Pb–Pb collisions. For the matter component, all of the aforementioned sources contribute to the particle production. On the other hand, for antimatter, no significant contribution of secondary particles produced in spallation interactions is expected due to baryon number conservation in the inelastic interactions with the ALICE material. For charged pions, the templates of secondary tracks both from weak decays of $\mathrm{K}^0_{\mathrm{S}}$ mesons and from interaction in the material are summed before the fitting step. This is done to improve the stability of the template fit procedure, since the material contribution is subdominant.

The fitting procedure is carried out separately for matter and antimatter in each of the analysed p_{T} intervals, separately for each of the centrality classes employed. The fraction of primary particles, f_{prim}, in each of these subsamples is determined as the ratio between the integral of the fitted primary template, N_{prim}, and the total number of candidates, N_{tot}, each of which are computed within the DCA_{xy} window, delimited by the upper threshold $\mathrm{DCA}^{\mathrm{thr}}_{xy}$, used for the candidate selection:

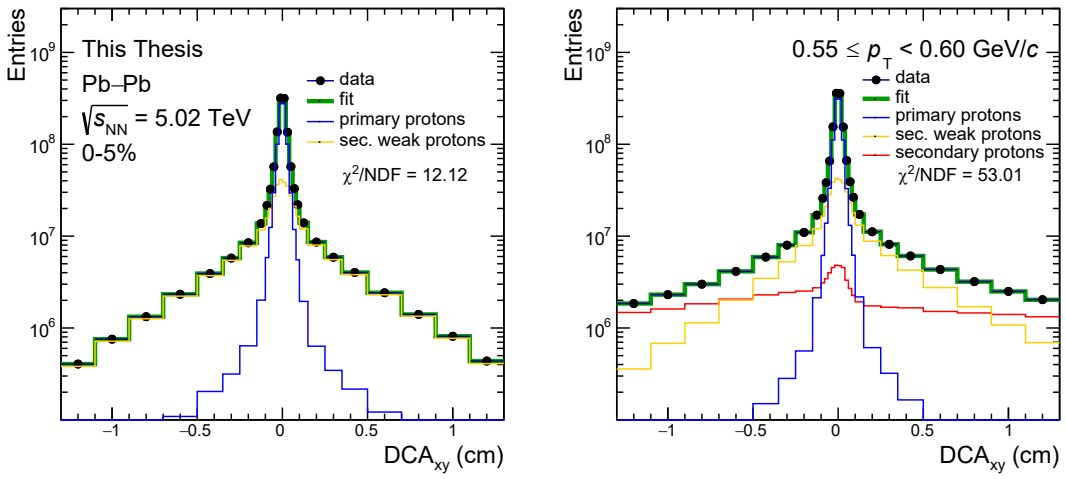

Figure 5.7: Fit of the DCA$_{xy}$ distributions of protons (left) and antiprotons (right) using MC templates, in the 0-5% centrality interval and for $0.55 \leq p_{\mathrm{T}} < 0.60$ GeV/c.

$$f_{\mathrm{prim}} = \frac{N_{\mathrm{prim}}(|\mathrm{DCA}_{xy}| < \mathrm{DCA}_{xy}^{\mathrm{thr}})}{N_{\mathrm{tot}}(|\mathrm{DCA}_{xy}| < \mathrm{DCA}_{xy}^{\mathrm{thr}})} \tag{5.7}$$

As an example, the fraction of primary particles extracted differentially in p_{T} in the 5% most central Pb–Pb collisions is shown in Fig. 5.8 for (anti)protons. A smaller f_{prim} is observed in the low p_{T} region for the matter component because the fraction of secondaries from material exponentially decreases for increasing p_{T}. The centrality dependence observed, connected to the relative charged particle multiplicities, justifies *a posteriori* the extraction of this correction factor separately in each centrality class analysed. The step observed at $p_{\mathrm{T}} = 1$ GeV/c is connected to the matching of tracks to TOF space points.

5.3.3 Inelastic cross-section correction

The accuracy of the efficiency corrections described in Section 5.3.1 relies on the parameterisation of the inelastic cross sections implemented in the GEANT 4 transport code. In recent years, the inelastic cross sections of light antinuclei have been precisely measured by the ALICE Collaboration [183, 184]. However, at present these measurements are not yet adopted to tune the cross sections used in transport codes. To include these additional elements in the measurement, dedicated scaling factors are computed for the $\epsilon \times A$ terms of ^{3}He and ^{3}H. For antiprotons, it was

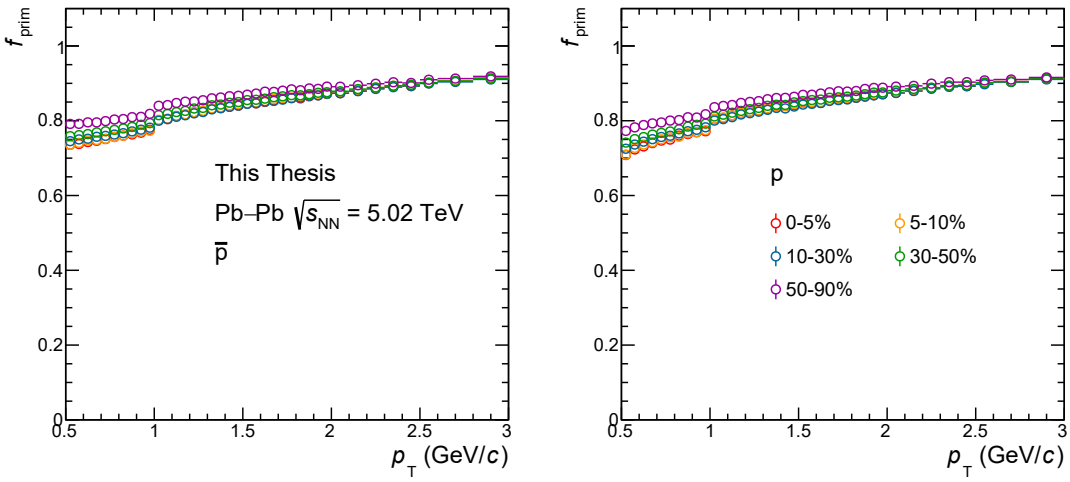

Figure 5.8: Primary fraction of antiprotons (left) and protons (right) in bins of p_{T}, for each of the analysed centrality classes. The discontinuity of the trend around $p_{\mathrm{T}} = 1$ GeV/c is caused by requiring the matching of tracks to TOF clusters for $p_{\mathrm{T}} \geq 1$ GeV/c.

checked that the parameterisation of the inelastic cross section present in GEANT 4 agrees with the inselastic cross section measured by the ALICE Collaboration within experimental uncertainties.

The applied procedure is also derived from previous analyses carried out by the ALICE Collaboration [176]. The transmission efficiency, ϵ_{t}, i.e., the probability that a particle passes through a layer of material without being absorbed, is driven by the inelastic absorption cross section in the material, $\sigma_{\mathrm{I}}(p)$, which is determined as a function of the particle momentum, p. By defining the hadronic interaction length, $\lambda_{\mathrm{I}}(p) = M/[\rho N_A \sigma_{\mathrm{I}}(p)]$, where M and ρ are the molar mass and density of the detector material, respectively, and N_A is the Avogadro number, the transmission efficiency is obtained as:

$$\epsilon_{\mathrm{t}}(p) = \exp[-\Delta x/\lambda_{\mathrm{I}}(p)], \tag{5.8}$$

for a crossed material layer of thickness Δx. In the case of particles interacting with the ALICE apparatus, which is composed of multiple layers of several materials, Eq. (5.8) holds for the effective interaction length determined by the average material elements crossed by the particles. The relative efficiency change, $\Delta\epsilon_{\mathrm{t}}/\epsilon_{\mathrm{t}}$, caused by a variation in the inelastic cross section parameterisation, $\Delta\sigma_{\mathrm{I}}$,

is determined from Eq. (5.8) via the uncertainty propagation as:

$$\frac{\Delta\epsilon_{\rm t}}{\epsilon_{\rm t}} = \frac{\Delta x}{\lambda_{\rm I}} \cdot \left| \frac{\Delta\sigma_{\rm I}}{\sigma_{\rm I}} \right| \tag{5.9}$$

By solving Eq. (5.9), the effective detector thickness, $\Delta x/\lambda_{\rm I}$, is determined as the ratio between $\Delta\epsilon_{\rm t}/\epsilon_{\rm t}$ and $\Delta\sigma_{\rm I}/\sigma_{\rm I}$. The efficiency variation can be extracted differentially in track momentum using two independent MC simulations: in the first one, the default GEANT 4 parameterisation of the inelastic cross sections are used; in the second one, these cross sections are scaled by a known amount, $\Delta\sigma_{\rm I}/\sigma_{\rm I}$, with respect to the nominal ones. Using the effective $\Delta x/\lambda_{\rm I}$ obtained from MC simulations, and by applying once more Eq. (5.9), the efficiency scaling factor, f_σ, is then obtained as:

$$f_\sigma = 1 - \frac{\Delta x}{\lambda_{\rm I}} \cdot \frac{|\sigma_{\rm GEANT4} - \sigma_{\rm data}|}{\sigma_{\rm GEANT4}}, \tag{5.10}$$

where $\sigma_{\rm GEANT4}$ and $\sigma_{\rm data}$ are the cross section values either provided in GEANT 4 or measured by the experiments. This correction factor is computed differentially in momentum and separately for each of the analysed nuclear species.

The $^3\overline{\rm He}$ and $^3\overline{\rm H}$ inelastic cross sections measured by the ALICE Collaboration [183, 184] are employed to compute the efficiency scaling factors using Eq. (5.10). The measured cross sections are fitted with the GEANT 4 parameterisations computed for the average atomic number for the ALICE material up to the TOF detector, i.e. $\langle A \rangle = 31.8$. The fit parameter provides the ratio $\sigma_{\rm data}/\sigma_{\rm GEANT4}$: this quantity is used in Eq. (5.10) to obtain the efficiency scaling factor. A similar procedure is applied for ^{3}He, using a preliminary measurement of the absorption cross section of ^{3}He in the ALICE apparatus. The obtained cross section scaling factors are reported in Table 5.2.

Table 5.2: Cross section scaling factors computed for the analyses presented in this Thesis and extracted from the comparison between the ALICE measurements and the GEANT 4 parameterisations.

Species	$\sigma_{\rm data}/\sigma_{\rm GEANT4}$
^{3}He	0.87 ± 0.06
$^3\overline{\rm He}$	0.83 ± 0.07
$^3\overline{\rm H}$	0.93 ± 0.19

For ^{3}H, the cross section correction factor is obtained multiplying the measured ^{3}He cross section by a rescaling term, extracted in the Glauber geometrical limit.

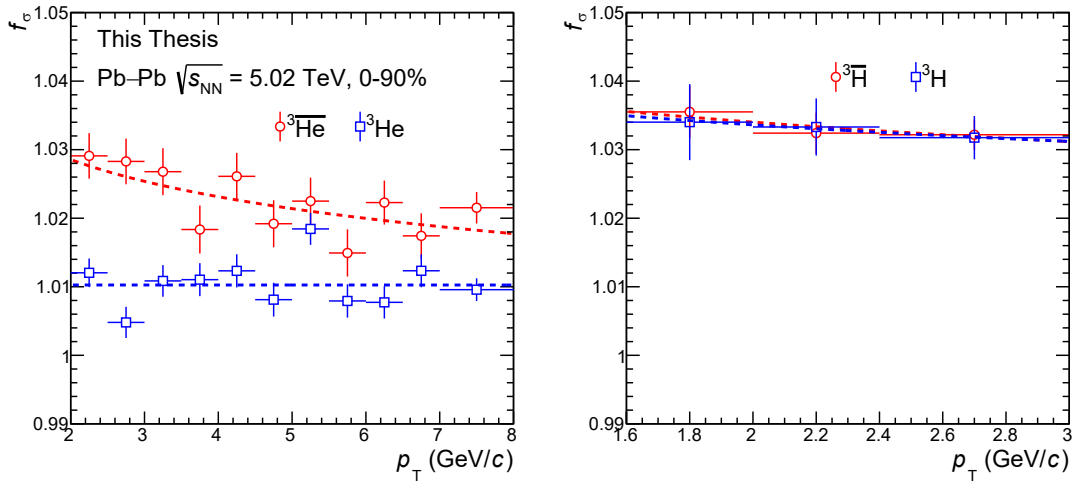

Figure 5.9: Efficiency scaling factors for (anti)^{3}He (left) and (anti)^{3}H (right) in bins of p_{T}, for the 0-90% centrality interval. The power-law fits are shown with dashed lines for both the matter and antimatter components.

In this limit, the ratio between the two cross sections is computed in terms of the radii of the incoming nuclei, denoted as $r(^3\mathrm{H})$ and $r(^3\mathrm{He})$, respectively, and the radius of the ALICE average material element, which can be approximated with silicon [179], $R(\mathrm{Si})$:

$$\frac{\sigma_{\mathrm{I}}^{^3\mathrm{H}}}{\sigma_{\mathrm{I}}^{^3\mathrm{He}}} = \left[\frac{r(^3\mathrm{H}) + R(\mathrm{Si})}{r(^3\mathrm{He}) + R(\mathrm{Si})}\right]^2 = 0.88 \tag{5.11}$$

The efficiency scaling factors obtained in the analysed p_{T} bins are shown in Fig. 5.9. To reduce statistical fluctuations, the data points are fitted with a power law function: the efficiency scaling is then computed from the fit value. The statistical uncertainties on the extracted points, which are connected to the size of the analysed MC sample, are propagated to the final results as uncorrelated systematic uncertainties.

For the $^3_\Lambda$H, a similar efficiency scaling factor is computed via a toy MC procedure. For each trial, a (p_{T}, ct) pair is sampled from the physical p_{T} shape, modelled with a Blast-Wave function, and ct distribution, defined by the free Λ baryon lifetime. The pairs are then accepted with a rejection sampling procedure, using either the nominal or scaled efficiencies. By binning the two samples in the same ct intervals used in the analysis, and by computing the ratio between the number of candidates accepted with either the nominal or the scaled efficiency, the ct-differential scaling

factors are extracted.

5.3.4 Absorption correction for ${}^{3}_{\Lambda}\mathrm{H}$

In this Thesis, ${}^{3}_{\Lambda}\mathrm{H}$ candidates are reconstructed from their charged-mesonic two-body decays. Out of all the produced ${}^{3}_{\Lambda}\mathrm{H}$, a subsample is absorbed in the ALICE detector before the weak decay, causing a loss of signal candidates. The efficiency correction described in Section 5.3.1 does not correctly include this effect as the absorption cross section parameterisation of ${}^{3}_{\Lambda}\mathrm{H}$ present in the GEANT 4 code is underestimated with respect to the state-of-the-art theoretical calculations [185]. A correction factor taking into account the ${}^{3}_{\Lambda}\mathrm{H}$ absorption is then computed using a simulated sample of ${}^{3}\mathrm{He}$ candidates as proxies of ${}^{3}_{\Lambda}\mathrm{H}$. To reproduce the expected absorption of hypertriton, the helion absorption cross section is scaled by a factor 1.5 in the simulation, which allows us to reproduce the expected ${}^{3}_{\Lambda}\mathrm{H}$ cross section [134, 170, 185]. The decay process is simulated by assigning each simulated helion candidate both a pseudo proper decay length, ct, sampled from the decay law of ${}^{3}_{\Lambda}\mathrm{H}$, and proper absorption decay length, l_{abs}, extracted from the distance between the ${}^{3}\mathrm{He}$ production vertex and the position of the first inelastic interaction of the ${}^{3}\mathrm{He}$ with the ALICE detector. The two lengths are then compared, and the candidate is considered as absorbed when $l_{\mathrm{abs}} < ct$. The fraction of absorbed ${}^{3}_{\Lambda}\mathrm{H}$ is then computed as:

$$f_{\mathrm{abs}} = \frac{N_{\mathrm{abs}}}{N_{\mathrm{gen}}}. \tag{5.12}$$

The efficiency is then corrected by a factor obtaiend as $f = 1 - f_{\mathrm{abs}}$. This correction term is computed in each ct interval, for each of the analysed centrality classes. The results obtained in the 0-5% centrality interval are shown in Fig. 5.10. A stronger correction factor is obtained in the antimatter case because of the larger absorption cross section in the material. Similar results are obtained in the other centrality intervals.

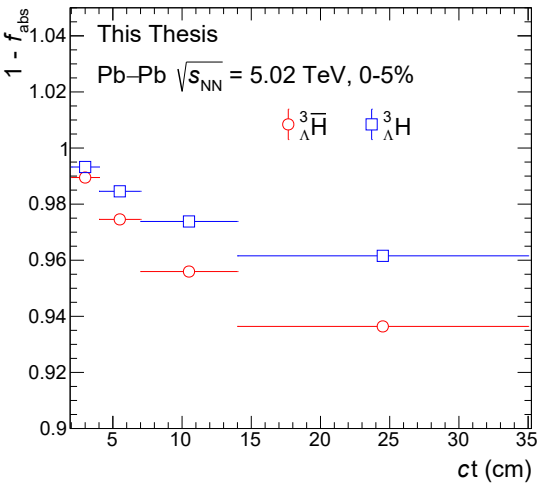

Figure 5.10: Absorption correction factor for (anti)$^3_\Lambda$H in bins of ct, for the 0-5% centrality interval.

5.4 Systematic uncertainties

In this Section, the methods used to estimate the systematic uncertainties related both to the candidate selection procedures and to the subsequent processing of the selected data are presented. The contributions arising from the different identified sources of systematic uncertainty are determined as described in the subsections reported below.

5.4.1 Selection criteria and signal extraction

The candidate selection criteria applied in this Thesis imply the rejection of a certain fraction of reconstructed signal candidates. The resulting signal loss effect is corrected via the $\epsilon \times A$ factor, which is extracted from MC simulations as described in Section 5.3.1. The accuracy of this correction relies on the agreement of the distributions of kinematic, topological, and PID variables between data and MC. Possible data-to-MC discrepancies, caused for example by the mismodelling of detector effects in the simulations, constitute a source of systematic uncertainty in the final results. To assess the effect on the final results of the data-to-MC mismatching at the candidate selection level, the full analysis procedure is repeated multiple times varying the selection criteria with respect to the nominal ones described in Chapter 4. The threshold variations used for the analysis of tracked hadrons are reported in Table 5.3 for π^+ and p, and in Table 5.4 for ^{3}He and ^{3}H.

Table 5.3: Variation of the track selection criteria and signal extraction regions for the π^+ and p analysis.

Variable	Variations
$n_{\mathrm{TPCclusters}}$	59, 64, 69, 74, 79
$\lvert\mathrm{DCA}_z\rvert$ (cm)	0.5, 0.75, 1.0, 1.5, 2.0
$\lvert\mathrm{DCA}_{xy}\rvert$ (cm)	$0.10, 0.11, 0.12, 0.13, 0.14$
$\chi^2_{\mathrm{TPC}}/n_{\mathrm{TPCclusters}}$	$2.00, 2.25, 2.50$
$\lvert n\sigma_{\mathrm{TPC}}\rvert$	3.0, 3.25, 3.5
ROI lower and upper limit (σ_{TOF})	nominal ± 0.5
$n_{\mathrm{SPDclusters}}$ for $(\bar{\mathrm{p}})\mathrm{p}$, $p_{\mathrm{T}} < 1.2$ GeV/c	1, 2
$n_{\mathrm{SDDclusters}} + n_{\mathrm{SSDclusters}}$ for $(\bar{\mathrm{p}})\mathrm{p}$, $p_{\mathrm{T}} < 1.2$ GeV/c	3, 4

Table 5.4: Variation of the track selection criteria for the ^{3}He and ^{3}H analysis.

Variable	Variations
$n_{\mathrm{TPCclusters}}$	$75, 61, \ldots, 105$ for ^{3}He
$n_{\mathrm{TPCclusters}}$	$60, 61, \ldots, 80$ for ^{3}H
$\lvert\mathrm{DCA}_z\rvert$ (cm)	$0.5, 0.6, \ldots, 1.5$
$\lvert\mathrm{DCA}_{xy}\rvert$ (cm)	$0.08, 0.09, 0.10, 0.11, 0.12$
$\chi^2_{\mathrm{TPC}}/n_{\mathrm{TPCclusters}}$	$2.00, 2.25, 2.50$

For the decay topologies selected with BDTs, the variations are applied directly on the BDT output thresholds, as they encode the selections on the various input features. The variations are expressed in terms of the BDT signal selection efficiency, similarly to the thresholds applied in the candidate selection. Variations up to ± 0.1 in efficiency, with respect to the nominal ones, are employed for the estimation of systematic uncertainties.

In addition, the systematic uncertainties related to the the signal extraction step are also determined by varying the default procedure to assess the effect on the final results. For the π and p analysis, the $n\sigma$ window used for the signal extraction is either extended or reduced by $\pm 0.5\sigma$, while for the ^{3}He and ^{3}H analysis the signal is extracted via either the integral of the signal function or by the background subtraction to the total counts in the region of interest $[\mu - 3\sigma, \mu + 3\sigma]$. For the Ω^- and ${}^3_{\Lambda}\mathrm{H}$ analysis, the background fit function is varied between an exponential and a first-order-degree polynomial.

For the analysis of light nuclei and decay topologies, where the uncertainty of the antiparticle-to-particle yield ratio measurements is dominated by the statistical

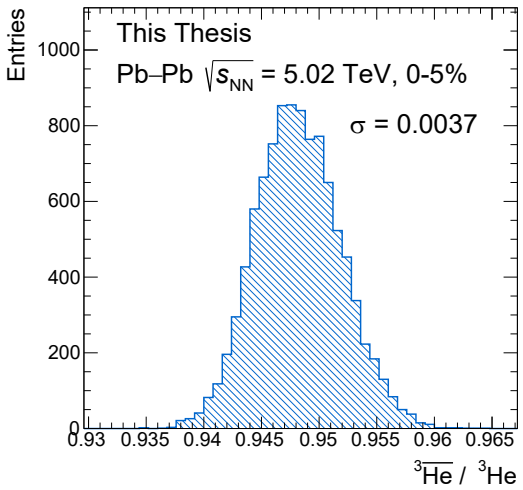

Figure 5.11: Distribution of the p_{T}-averaged $^3\overline{\mathrm{He}}/^3\mathrm{He}$ yield ratios obtained in the multiple trials, for the 5% most central collisions.

component, the systematic uncertainties are determined for the p_{T}-averaged ratios using a multitrial approach. First, multiple combinations of the different variations are defined by uniformly sampling all possible threshold variations: the number of trials is 10^4. The full analysis procedure is then repeated and the uncertainty is evaluated as the standard deviation of the distribution of results obtained in the various trials. This procedure is repeated separately in each of the analysed centrality classes: an example for ^{3}He in the 0-5% centrality interval is shown in Fig. 5.11. The obtained systematic uncertainties are propagated in the evaluation of chemical potentials as centrality-uncorrelated contributions.

For the charged pions and proton analysis, the largest uncertainty contribution is provided by systematic components. The contributions arising from the variation of the thresholds of track variables are separately estimated for each variable as the standard deviations of the results extracted with the different threshold settings. This procedure is carried out separately in each of the analysed p_{T} bins and for each centrality interval. The systematic uncertainties on the integrated antiparticle-to-particle ratios are obtained taking into account both the p_{T}-correlated and p_{T}-uncorrelated components. To estimate the p_{T}-correlated fraction, the difference between the results determined with varied and default threshold settings is computed for each p_{T} bin. The distributions of these residuals are obtained as a function of the threshold values. The Pearson correlation coefficient between the residuals and threshold values is used as the estimate of the correlated fraction.

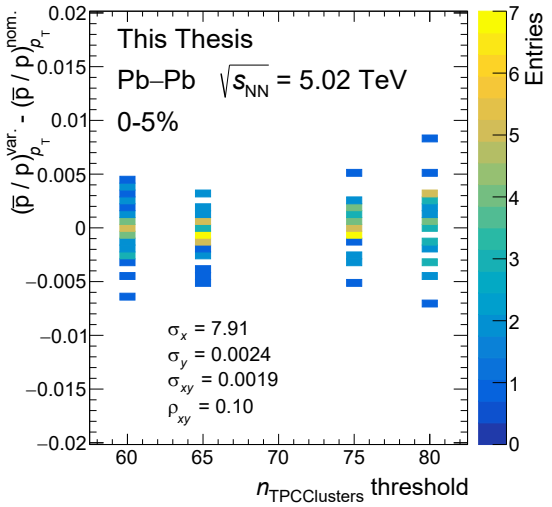

Figure 5.12: Distribution of the p_T-differential difference between the ratios obtained with varied and nominal criteria as a function of the threshold value, for the variation of the $n_{TPCcluster}$ selection, in the centrality interval 0-5%.

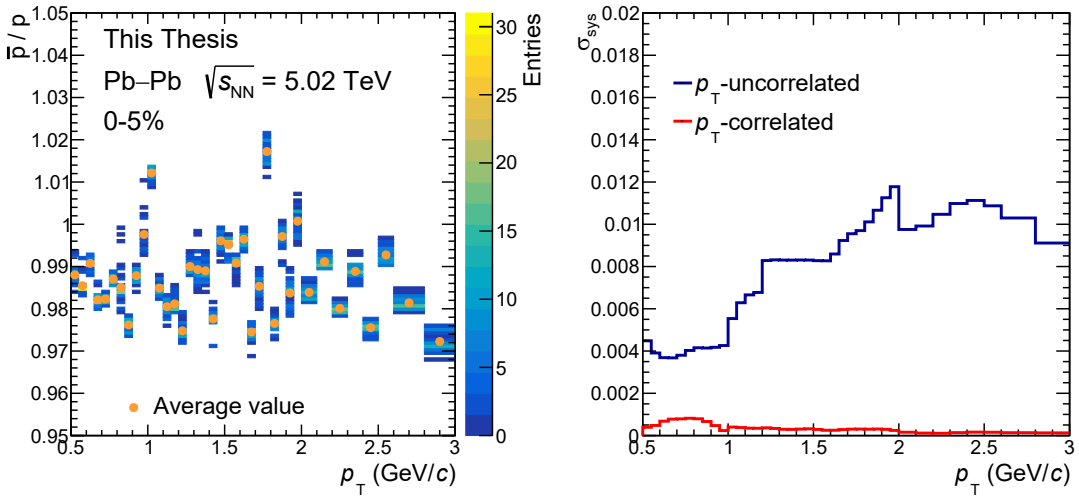

Figure 5.13: Left: distribution of the $\bar{p}/p$ yield ratios obtained with the different variations described in the text. The average values in each p_T bin are also reported. Right: p_T-correlated and -uncorrelated contributions to the systematic uncertainty on the $\bar{p}/p$ yield ratio in the 5% most central collisions.

An example of this procedure for the antiproton-to-proton ratio in the 0-5% centrality interval is shown in Fig. 5.12. The total systematic uncertainty reported for each p_{T} bin is evaluated as the summation in quadrature of the contributions from the different sources. In these analyses, the central values of the antiparticle-to-particle yield ratios are also extracted from the pool of analyses with varied criteria, as the average values of the various results. The results obtained for the systematic analysis of the $\bar{\mathrm{p}}/\mathrm{p}$ ratio is shown in Fig. 5.13.

5.4.2 Statistical uncertainty on $\epsilon \times A$

The size of the MC samples used in this Thesis constitutes a source of statistical uncertainty on the $\epsilon \times A$ correction factors described in Section 5.3.1. As this uncertainty affects the precision of the corrections applied, it is propagated as a source of systematic uncertainty to the final results. This source of uncertainty is p_{T}- and centrality-uncorrelated due to its statistical nature. This contribution is particularly relevant for π^+, p, Ω^-, and their charge-conjugated states, as the simulated samples have sizes smaller or equal than the collected data samples. In these three cases, the uncertainty on the p_{T}-integrated yield ratios is $O(5 \times 10^{-3})$. For the light (hyper)nuclei analysis, where the MC samples have a larger number of candidates than the data ones, this source of uncertainty is negligible according to 2σ Barlow tests [186].

5.4.3 Inelastic cross-sections

The efficiencies estimated through MC simulations are affected by the inelastic cross sections parameterised in the GEANT 4 transport code. Besides the scaling factors described in Section 5.3.3, systematic uncertainties are evaluated to take into account the uncertainties on the measured cross sections [187–199]. First, the experimental uncertainties are combined by fitting the measured cross sections with the parameterisations provided in GEANT 4, similarly to the procedure applied in Section 5.3.3. For the light (anti)nuclei, the results reported in Table 5.2 are used for the estimation of the cross section uncertainty. For ${}^{3}_{\Lambda}\mathrm{H}$, the uncertainty on the ${}^{3}\mathrm{He}$ cross section is used as a proxy, while no uncertainty is assigned to Ω^- for this source as no experimental measurements of hyperon inelastic cross sections are currently available. For pions and protons, a set of measurements of inelastic cross sections for the particles of interest on different targets, covering both the possible materials present in the ALICE detector and the momentum range analysed, are employed [187–199]. Simultaneous fits of the data collected with different targets are carried out. The fit parameter is the scaling factor ap-

plied to the GEANT 4 cross sections for the full set of targets, for each of the species and for the charge-conjugated states separately. The fit results for $\pi^{\pm}$ and ($\bar{\mathrm{p}}$)p are shown in Fig. 5.14.

To propagate the cross-section uncertainties on the antiparticle-to-particle yield ratios, dedicated MC simulations are carried out varying the input inelastic cross sections of GEANT 4 by known scaling factors. The $\epsilon \times A$ terms are then computed using these simulations, as well as their ratios to the $\epsilon \times A$ obtained with the nominal parameterisations. From Eq. (5.8), an exponential dependence of the efficiency ratios from the cross section scaling factor is expected, hence an exponential fit of the obtained efficiency ratios is carried out. As a constraint for the fit, it is required that the efficiency ratio is equal to unity when the cross section parameterisation is the nominal one. Using the curve extracted from the fit, the 1σ uncertainty interval is propagated from the cross section scaling factor to the efficiency scaling factor. In this way, the relative systematic uncertainty on $\epsilon \times A$ is obtained. This procedure is shown in Fig. 5.15 for the (anti)helion case.

The uncertainties extracted with this method are reported in Table 5.5, for all the analysed species. This uncertainty contribution is propagated to the final results as a source of centrality-correlated systematic uncertainty, as it affects all centrality intervals in a coherent way.

Table 5.5: Systematic uncertainties on the efficiency ratios due to the uncertainty on the absorption cross section.

	π^+	π^-	p	$\overline{\mathrm{p}}$	^{3}He	$^3\overline{\mathrm{He}}$	^{3}H	$^3\overline{\mathrm{H}}$
$\sigma(\epsilon^{\mathrm{data}}/\epsilon^{\mathrm{GEANT4}})$	0.003	0.007	0.00017	0.0013	0.005	0.009	0.018	0.11

5.4.4 Material budget

The accuracy of the ALICE detector material budget in the MC simulations affects the correction factors estimated in this Thesis. From photon conversion measurements published by the ALICE Collaboration, an uncertainty of maximum 4.5%, dependent on the transverse radius from the nominal interaction point, is assigned to the material budget coded in the simulations [200]. To estimate the resulting systematic uncertainty on the antiparticle-to-particle yield ratios, two MC samples are produced varying the material budget description by the maximum uncertainty, $\pm$4.5%. The $\epsilon \times A$ factors are computed using these samples and the resulting corrections are applied to the extracted uncorrected yields. The ratios of the efficiencies with varied material budget and the nominal ones are shown

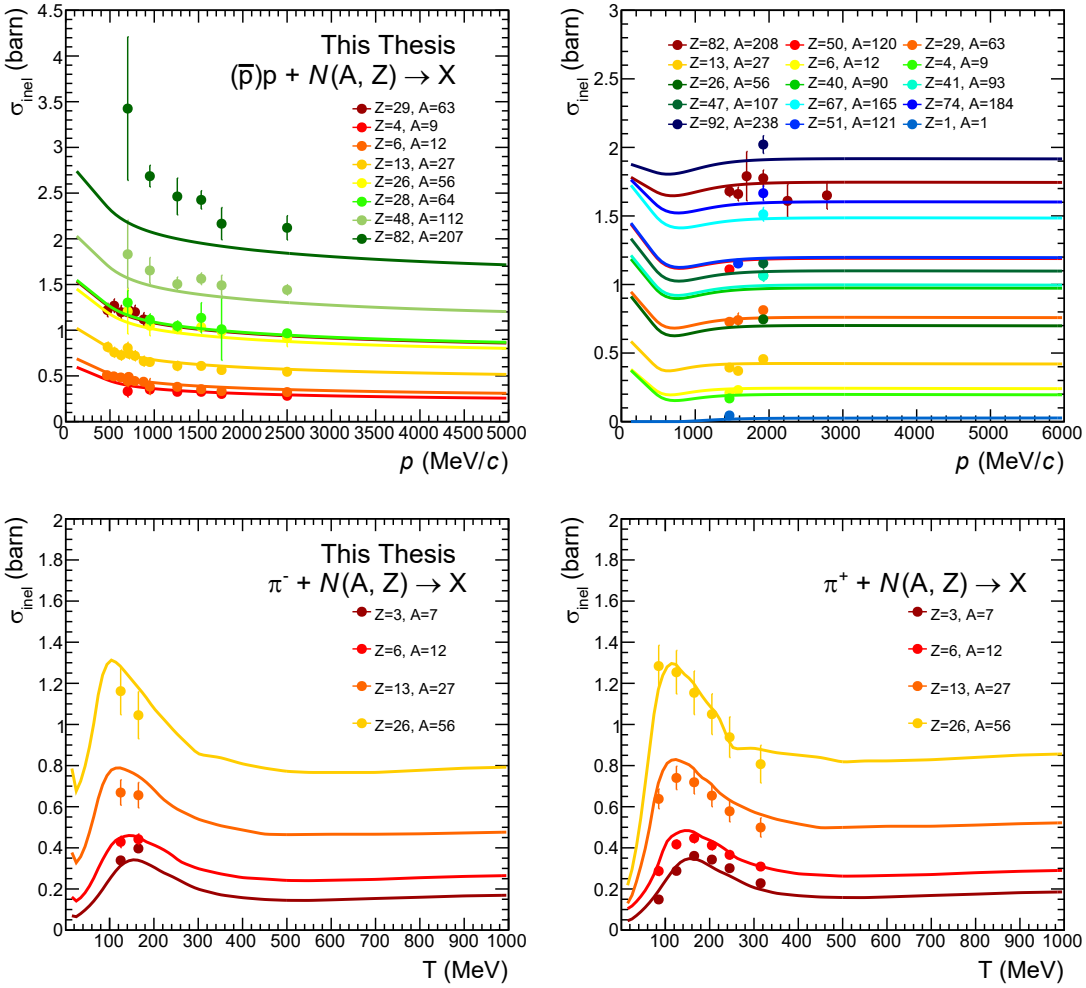

Figure 5.14: Fit of the measured inelastic cross sections, differential in momentum, p, and energy, T, of charged pions (lower panels) and (anti)protons (upper panels) on different target materials. For each species, the data points are fitted with the relative GEANT 4 cross sections, depicted by continuous lines. The GEANT 4 cross sections are multiplyied by a scaling factor which is the free parameter of the simultaneous fit. The error bars depict the total uncertainties on the available measurements.

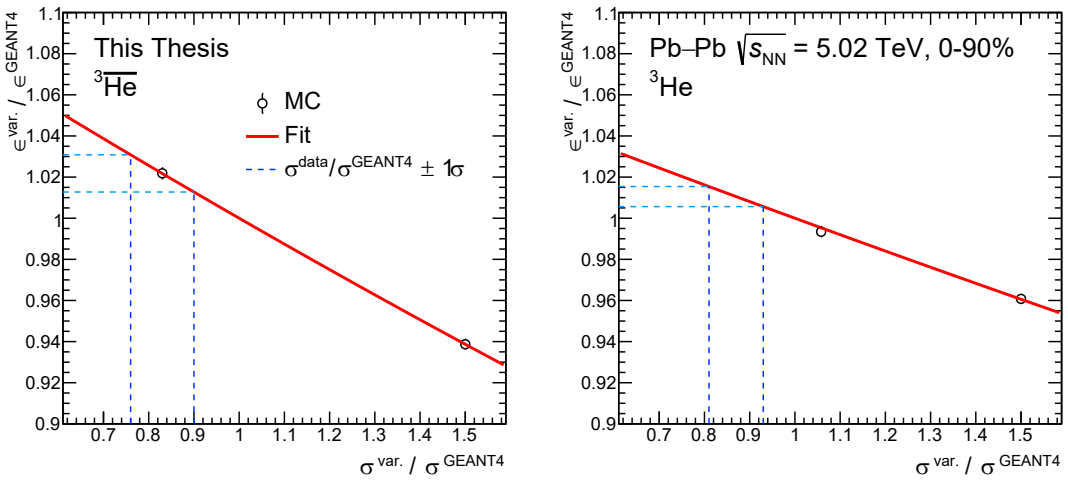

Figure 5.15: Extraction of the systematic uncertainty due to the inelastic cross-section uncertainty for $^3\overline{\text{He}}$ in the left panel and ^{3}He in the right panel.

in Fig. 5.16 for (anti)protons. A larger deviation is observed for the antimatter component for both variations due to the larger inelastic cross section of $\bar{\text{p}}$ in the detector material. Similarly, the deviations decrease for increasing p_{T} because the inelastic cross sections of both matter and antimatter decrease for increasing particle momentum.

The uncertainty on the yield ratios is then computed as half of the difference between the antiparticle-to-particle ratios obtained with the two maximum variations of the material budget description. The resulting uncertainty assigned to charged π and proton ratios is $O(5 \times 10^{-3})$, while for all of the other analysed species the uncertainties are negligible according to a 2σ Barlow test. The material budget uncertainty is propagated to the final results as a centrality-correlated source of systematic uncertainty. The effect of the radius-dependent uncertainty is also assessed by producing an additional MC sample with a material budget variation dependent on the transverse radius. As no significant effect is observed in the final results according to a 2σ Barlow test, no further uncertainty is assigned for to the radius dependence.

5.4.5 Magnetic field polarity

The knowledge of the magnetic field map of the L3 solenoid affects both the data reconstruction and the MC simulations. To assess the degree of the data-to-MC discrepancies due to this effect, a study of the efficiency of the matching of tracks

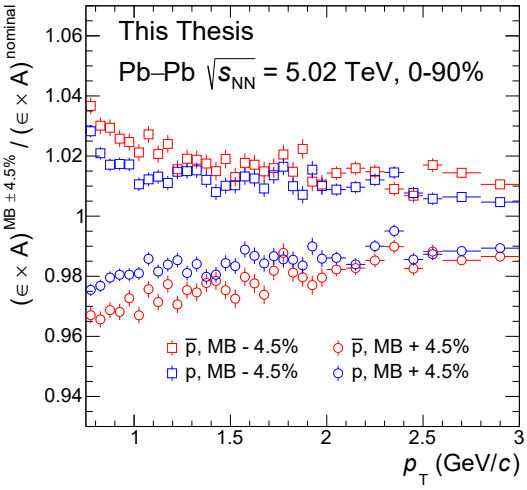

Figure 5.16: Ratio between the $\epsilon \times A$ of ($\bar{\text{p}}$)p obtained with both the modified and the nominal material budget descriptions, in the 0-90% centrality interval.

to TOF space points is carried out using separately the data collected with opposite polarities of the L3 solenoid field. The matching efficiency to the TOF is computed as the fraction of reconstructed tracks that are matched to space points in TOF:

$$\epsilon_{\text{Matching}} = \frac{N_{\text{hasTOF}}}{N_{\text{reco}}} \tag{5.13}$$

Unlike other efficiencies, which rely on the generated-level information only available in MC simulations, $\epsilon_{\text{Matching}}$ is only defined in terms of reconstructed quantities, hence it can be estimated also in the data. In this Thesis, this efficiency is computed for charged pions due to the large sample available: in the MC sample, $\pi^{\pm}$ tracks are selected through the particle-identity information available from the simulation; in the data, a pure sample of $\pi^{\pm}$ tracks is extracted by selecting the candidate decay products of K^0_S decay topologies. The K^0_S sample is obtained both with tight selections on the topological variables of the reconstructed V^0s, as reported in Table 5.6, and by accepting only candidates having an invariant mass compatible with the nominal one, taken from the PDG, within 3σ.

The efficiencies are estimated separately for the two charge states. The negative-to-positive efficiency ratios are then computed and their p_T-average values are determined in each of the analysed centrality intervals. The p_T interval analysed is restricted to the one used in the analysis of the antiparticle-to-particle yield ratios, i.e., $0.7 \leq p_\text{T} < 1.6$ GeV/c. This procedure is repeated in the data samples

Table 5.6: Criteria applied to select K^0_S for the matching efficiency studies.

Vertex selections
$\|\eta\| < 0.8$ for the K^0_S candidate and for all tracks
$3 < R_{K^0_S} < 100$ cm
$DCA_{tracks} < 1$ cm
$DCA_{V^0,PV} < 0.5$ cm
$\cos\theta_p > 0.9995$
$\|M(\pi^+ + \pi^-) - M^{PDG}_{K^0_S}\| < 3\sigma$

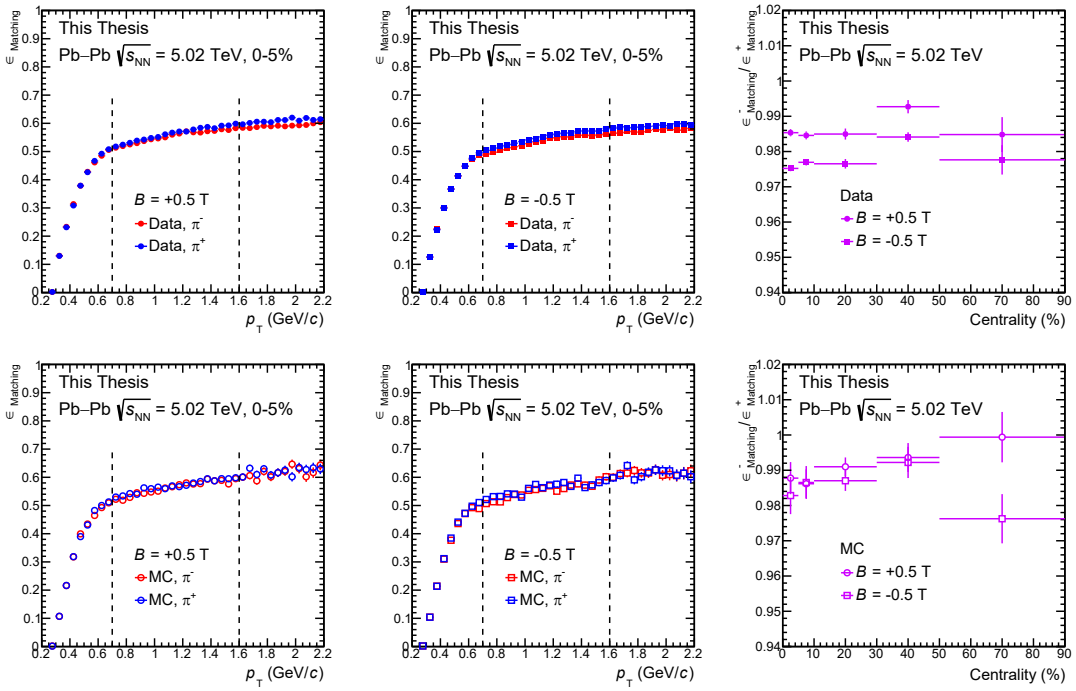

Figure 5.17: Study of the matching efficiency to TOF space points in data (upper panels) and MC (lower panels). The results obtained with positive and negative magnetic-field polarities are shown on the left and in the center, respectively, for the 5% most central collisions. The vertical dashed lines indicate the region where the ratio of the negative-to-positive-pion efficiency ratio is computed. The ratios obtained in the different centrality classes are shown in the right panels.

collected with both positive and negative magnetic field polarities. The results obtained for both polarities, shown in Fig. 5.17, are compared between data and MC. As it is shown in the righmost panel of Fig. 5.17, in the real data a significant discrepancy between the two polarities is observed in central and semicentral col-

lisions. This effect is not reproduced in the MC simulations, where the results are consistent in the two cases within statistical uncertainties. Consequently, the data-to-MC discrepancy is taken into account by including the effects of the L3 polarity inversion as a sources of centrality-correlated systematic uncertainty.

The systematic uncertainty due to the magnetic field polarity is estimated by repeating the full analysis splitting the data and MC samples according to the polarity employed. The results of this procedure are shown in Fig. 5.18 for the 0-5% and 10-30% centrality intervals. The value of the uncertainty is then obtained as half of the difference between the antiparticle-to-particle yield ratio results obtained in the two cases. For pions and protons, where a significant difference between the two periods is observed, an uncertainty of 3×10^{-3} and 2×10^{-3} is assigned to the antiparticle-to-particle yield ratios in the centrality intervals 0-5% and 10-30%, respectively. The results obtained in the 5-10% centrality interval are similar to those of the 0-5% interval: the uncertainty assigned in this range is 3×10^{-3}. For the other centrality intervals and species, no significant difference is observed, hence this source of uncertainty is neglected in those cases.

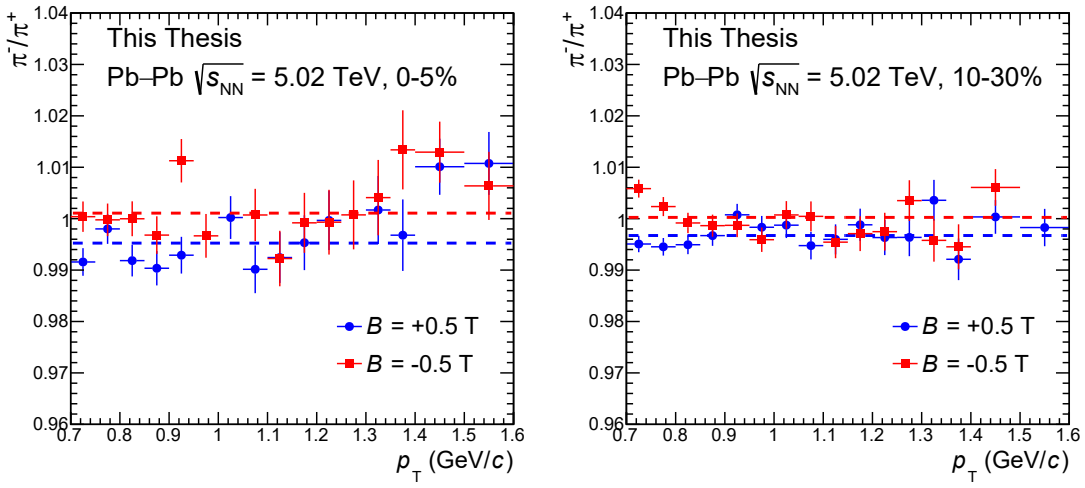

Figure 5.18: Antiparticle-to-particle yield ratios of charged pions obtained with opposite magnetic field polarities, in the 0-5% (left panel) and 10-30% (right panel) centrality intervals. The error bars represent the total p_T- and centrality-uncorrelated uncertainties. The dashed lines show a zero degree polynomial fit to the experimental points.

Table 5.7: Relative systematic uncertainty on the average antiparticle-to-particle ratios due to the different sources considered in the analysis.

Source	$\overline{\Omega}^{+}/\Omega^{-}$	π^{-}/π^{+}	$\overline{\mathrm{p}}/\mathrm{p}$	${}^{3}_{\Lambda}\overline{\mathrm{H}}/{}^{3}_{\Lambda}\mathrm{H}$	${}^{3}\overline{\mathrm{H}}/{}^{3}\mathrm{H}$	${}^{3}\overline{\mathrm{He}}/{}^{3}\mathrm{He}$
Cand. selection	0.5%	0.05%	0.05%	10%	3%	0.5%
MC precision	0.5%	0.1%	0.1%	1%	1%	1%
Material budget	–	0.1%	0.5%	–	–	–
Inel. cross section	–	0.7%	0.5%	1%	10%	1%
B field polarity	–	0.2–0.3%	0.2–0.3%	–	–	–

5.4.6 Summary of the systematic uncertainties

The different contributions to the antiparticle-to-particle yield ratios systematic uncertainty are summarised in Table 5.7, for each of the analysed species. Only the statistically significant contributions to systematic uncertainties, according to Barlow tests, are reported in the table. The MC precision includes all contributions from statistical uncertainties on the applied corrections, i.e., $\epsilon \times A$, f_{prim}, f_{WD}, and f_{σ}, arising from the size of the analysed MC samples.

5.5 Results

The extraction of the final results of both antiparticle-to-particle yield ratios and chemical potentials extracted with fits to statistical-hadronisation models is described below.

5.5.1 Antiparticle-to-particle ratios

The final results for the antiparticle-to-particle yield ratios are obtained by applying the corrections described in Section 5.3 to the raw signals, N_{raw}, extracted with the procedure described in Section 5.2. For tracked species, the p_{T}-differential yield of both particles and antiparticles is obtained as:

$$\frac{\mathrm{d}N}{\mathrm{d}p_{\mathrm{T}}} = \frac{f_{\mathrm{prim}}}{f_{\sigma} \cdot (\epsilon \times A)} \cdot \frac{N_{\mathrm{raw}}}{\Delta p_{\mathrm{T}}}, \tag{5.14}$$

while the ct-differential yields of species reconstructed through their decay topologies are computed as:

$$\frac{\mathrm{d}N}{\mathrm{d}(ct)} = \frac{1}{f_{\sigma} \cdot (1 - f_{\mathrm{abs}}) \cdot (\epsilon \times A)} \cdot \frac{N_{\mathrm{raw}}}{\Delta(ct)}, \tag{5.15}$$

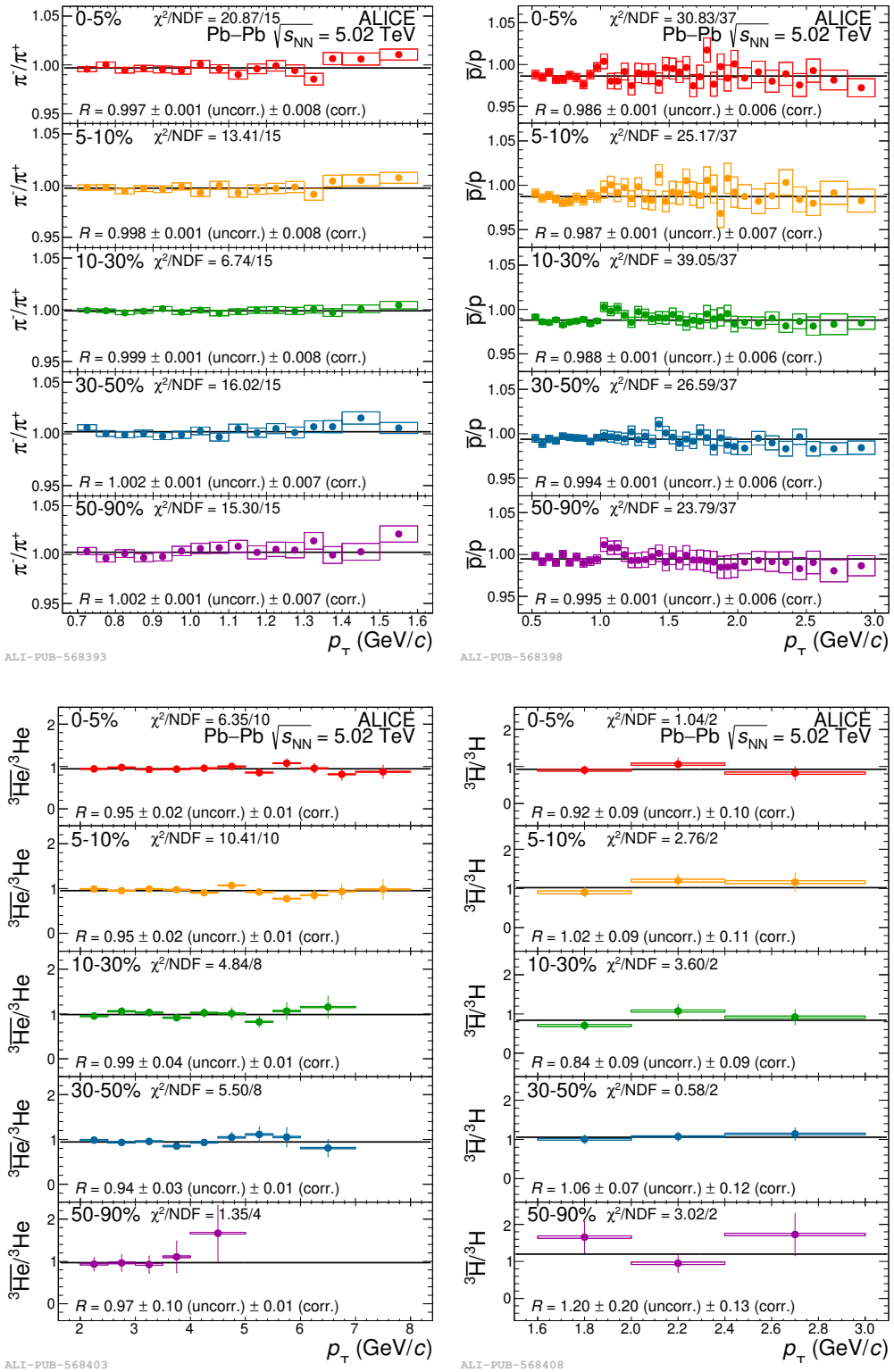

Figure 5.19: p_T-differential antiparticle-to-particle yield ratios of the π, p, ^{3}He, and ^{3}H, for each of the centrality classes used. The statistical uncertainties are shown as error bars, while the uncorrelated systematic uncertainties are shown as boxes. When not visible, the error bars are hidden by the markers. The correlated systematic uncertainties are not shown: they are separately reported in the text. The fits performed with zero degree polynomials are shown in black.

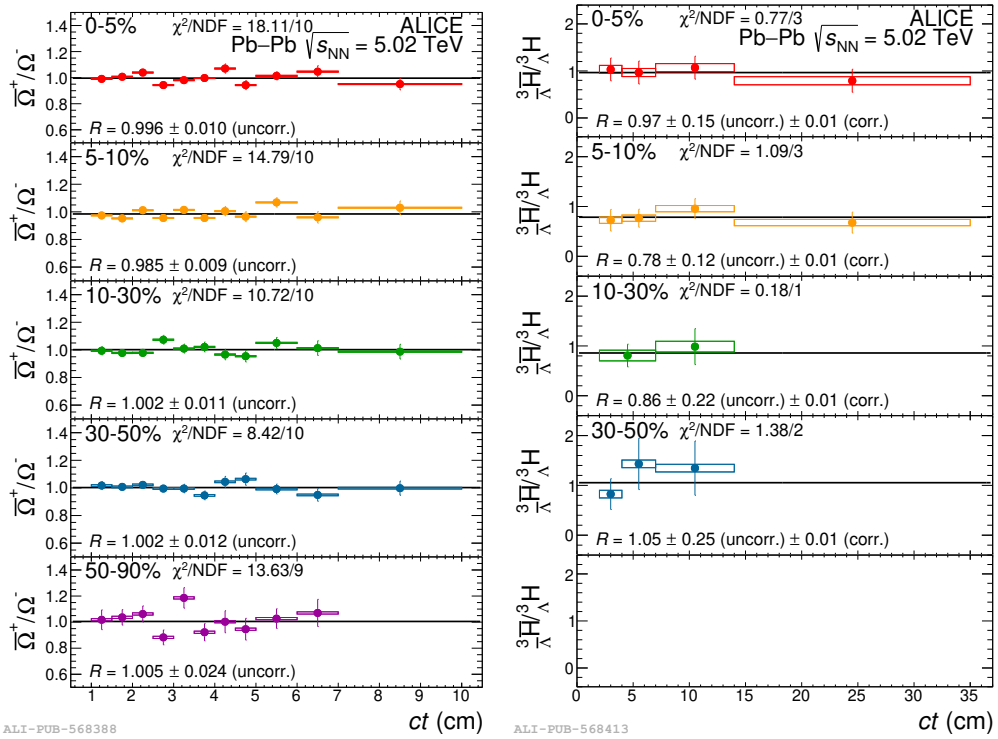

Figure 5.20: *ct*-differential antiparticle-to-particle yield ratios of the Ω and ${}^{3}_{\Lambda}\mathrm{H}$, for each of the centrality classes used. The statistical uncertainties are shown as error bars, while the uncorrelated systematic uncertainties are shown as boxes. When not visible, the error bars are hidden by the markers. The correlated systematic uncertainties are not shown: they are separately reported in the text. The fits performed with zero degree polynomials are shown in black.

All of the quantities appearing in both Eq. (5.14) and Eq. (5.15) are evaluated bin-by-bin. As both the antiparticle and particle yields are determined in coherent p_{T} and ct bins, the bin widths, Δp_{T} and $\Delta(ct)$, cancel out in the ratios. The fully corrected antiparticle-to-particle yield ratios obtained differentially in either p_{T} or ct for each of the analysed species are shown in Fig. 5.20. For the π^-/π^+ and $\bar{\mathrm{p}}/\mathrm{p}$ ratios, the statistical uncertainties are not visualised in the plots, as they are $O(10^{-5})$ in each p_{T} bin.

The obtained data points are fitted with zero degree polynomials to test the evolution of the yield ratios in both p_{T} and ct. The results are shown in Fig. 5.20, along with the χ^2/NDF of the fits. For the fitting procedure, only the statistical uncertainties and either p_{T}- or ct-uncorrelated uncertainties are considered. From this check, no evidence of a p_{T}- and ct-differential dependence of the ratios is observed. Hence, the extracted fit parameters are directly used as estimates of the antiparticle-to-particle yield ratios in the subsequent statistical-model analysis to determine the chemical potentials.

5.5.2 Chemical potentials

The chemical potentials, μ_B and μ_Q, are extracted from the yield ratios determined in Section 5.5.1 by fits of the statistical hadronisation model expectations in each of the analysed centrality classes. The model implementation used in this Thesis is the THERMAL-FIST code [54]. The Grand Canonical (GC) ensemble implementation of the SHM is employed for the fit.

In these fits, the only free parameters are μ_B and μ_Q. The strangeness chemical potential, μ_S, which appears in Eq. (5.1), is fixed in the model by requiring in the HRG composition the strangeness neutrality conditions imposed by the initial state of the collision, i.e., $n_s = n_{\bar{s}}$, where $n_s(n_{\bar{s}})$ is the (anti)strange quark density, respectively. The only other relevant parameter is the chemical freeze-out temperature, T_{chem}, as the volume of the system cancels out when computing yield ratios. The value used in this Thesis, $T_{\mathrm{chem}} = 155 \pm 2$ MeV, was previously determined by fitting, with the SHM coded in THREMAL-FIST, the hadron yields measured by the ALICE Collaboration for several species [67, 201]. The same value is used for all of the analysed centrality intervals, as T_{chem} has a weak dependence on centrality across the 0-90% interval, with variations up to $O(1\%)$ [114, 201–203] that are covered by the experimental uncertainty on the extracted value. The uncertainty on the T_{chem} estimate is propagated to the final results as a centrality-correlated source of systematic uncertainty.

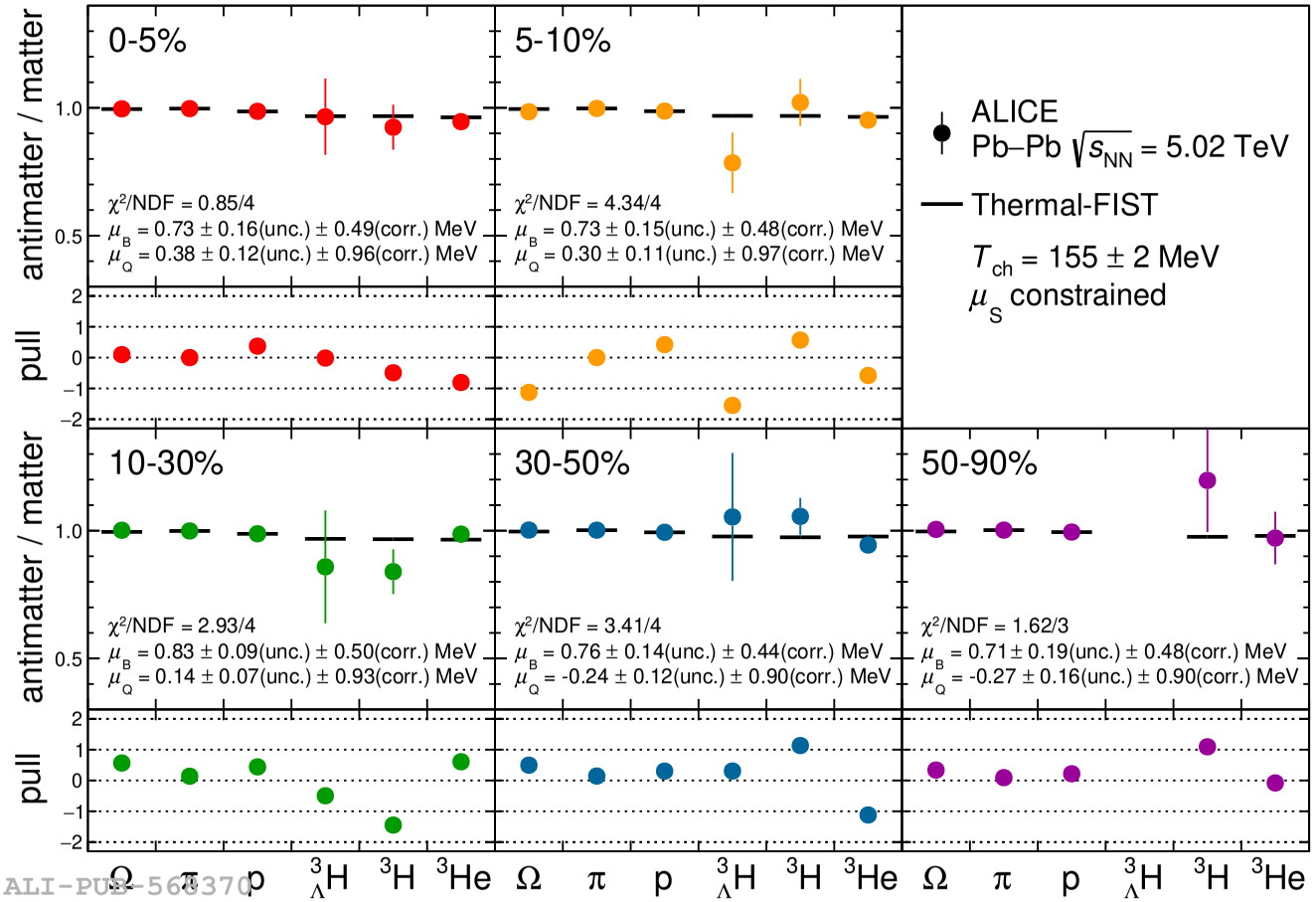

Figure 5.21: Fits of the antiparticle-to-particle yield ratios in each of the analysed centrality intervals. The error bars show the total uncorrelated uncertainty on the data points. The fit results are shown in black, while the fit χ^2 and the extracted μ_B and μ_Q are reported in the text on the plot. In the lower panels, the pulls are shown for each species in each centrality interval.

The antiparticle-to-particle yield ratios measured are affected by the contribution of both strongly- and electromagnetically-decaying resonances, as it cannot be disentangled in the data. This contribution is taken into account in the model by requiring that the computed yields, and hence yield ratios, contain the feed-down from strong and electromagnetic decays. It is verified that this contribution marginally affects the final results, as it affects similarly both particles and antiparticles.

The fit results are shown in Fig. 5.21, while the chemical potentials extracted in each centrality class are summarised in Table 5.8.

Table 5.8: Summary of the values obtained for μ_B and μ_Q at $T_{\rm ch} = 155 \pm 2$ MeV from the fits of antiparticle-to-particle ratios in the 0-5%, 5-10%, 10-30%, 30-50%, and 50-90% centrality classes.

Centrality	μ_B (MeV)	μ_Q (MeV)
0-5%	0.73 ± 0.16(unc.) ± 0.49(corr.)	0.38 ± 0.12(unc.) ± 0.96(corr.)
5-10%	0.73 ± 0.15(unc.) ± 0.48(corr.)	0.30 ± 0.11(unc.) ± 0.97(corr.)
10-30%	0.83 ± 0.09(unc.) ± 0.50(corr.)	0.14 ± 0.07(unc.) ± 0.93(corr.)
30-50%	0.76 ± 0.14(unc.) ± 0.44(corr.)	-0.24 ± 0.12(unc.) ± 0.90(corr.)
50-90%	0.71 ± 0.19(unc.) ± 0.48(corr.)	-0.27 ± 0.16(unc.) ± 0.90(corr.)

In the fitting procedure, only the uncorrelated uncertainties on the yield ratios are employed. The uncertainties correlated both with centrality and particle species are propagated to the final results by repeating two times the SHM fits on the yield ratios. In these two trials, the yield ratios are coherently biased by $\pm 1\sigma_{\rm corr}$, where $\sigma_{\rm corr}$ is the value of the correlated uncertainty on the yield ratio for each species and centrality interval. The correlated uncertainty on μ_B and μ_Q is then extracted as half of the difference between the values extracted in the two trials. In Fig. 5.21, both the reported χ^2/NDF, close to unity, and the pulls of the fits, consistent with zero within 2σ, indicate that the GC SHM well describes the measured yield ratios across the 0-90% centrality range. These results show that the canonical conservation of quantum numbers required in the hadron yield calculations in the most peripheral collisions [127, 128] cancel out in the antiparticle-to-particle yield ratios. Similar conclusions were reached also in previous works [41, 204].

The chemical potentials obtained from the fits are shown in the (μ_B, μ_Q) plane in Fig. 5.22. The centrality-correlated and -uncorrelated uncertainties are separately reported in the plot. The centrality dependence of the extracted chemical potentials is tested by fitting the centrality-differential μ_B and μ_Q measurements

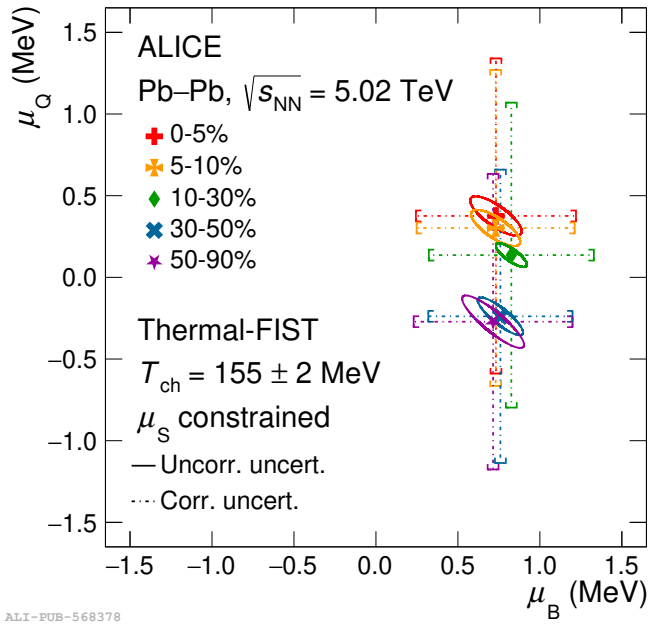

Figure 5.22: Chemical potentials extracted from the SHM fits in each centrality interval. The 1σ contour of the centrality-uncorrelated uncertainties are shown as ellipses. The correlated uncertainties are shown as error bars.

with zero degree polynomials, taking into account the full covariance matrices, V, obtained by as the sum of the covariance matrices of the uncorrelated, V_{uncorr}, and correlated contributions, V_{corr}:

$$V = V_{\text{uncorr}} + V_{\text{corr}} \tag{5.16}$$

The covariance matrices are defined for the μ_B and μ_Q extracted in each centrality class. The diagonal elements of the matrices are obtained as the total variances of the chemical potentials, $V_{ii} = (\sigma_{\text{tot}})_i^2 = (\sigma_{\text{uncorr}})_i^2 + (\sigma_{\text{corr}})_i^2$, where $(\sigma_{\text{corr}})_i$ and $(\sigma_{\text{uncorr}})_i$ are the total centrality-correlated and -uncorrelated uncertainties on the chemical potentials extracted in the i-th centrality class, respectively, for $i \in [1, 5]$. The off-diagonal elements are computed as $V_{ij} = \rho_{ij} \cdot (\sigma_{\text{corr}})_i \cdot (\sigma_{\text{corr}})_j$, ρ_{ij} being the correlation coefficient between the uncertainty sources in the centrality classes i and j, for $i \neq j$. As the analysed centrality-correlated sources of systematic uncertainties are fully correlated with centrality, it is set $\rho_{ij} = 1$ for $i, j \in [1, 5]$. The covariance matrices obtained for both μ_B and μ_Q are shown in Fig. 5.23: only the upper-triangular part is reported as the covariance matrices are symmetric by

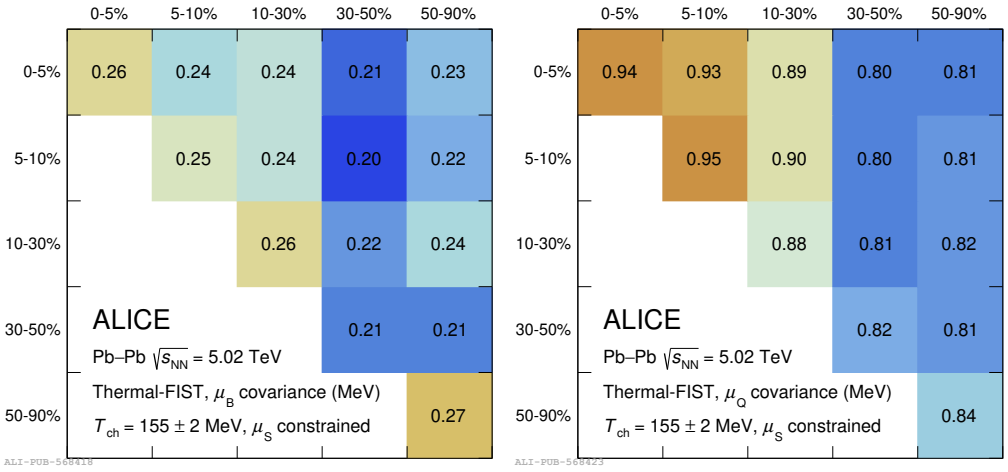

Figure 5.23: Covariance matrices for the centrality-differential μ_B (on the left) and μ_Q (on the right) estimates.

definition.

The χ^2 profiles obtained from the zero-degree-polynomial fits of both μ_B and μ_Q are shown in Fig. 5.24. The fit probabilities in the minima of the two χ^2 profiles, $P(\chi^2 < \chi^2_{\text{min}}; \text{NDF} = 4)$, are 0.97 and 0.64 for μ_B and μ_Q, respectively. Hence, the centrality-differential values of both μ_B and μ_Q do not show any centrality dependence. As a result, the centrality-integrated μ_B and μ_Q can be defined as estimates of chemical potentials: the obtained results are $\mu_B = 0.71 \pm 0.45$ MeV and $\mu_Q = -0.18 \pm 0.90$ MeV. Both chemical potentials are compatible with zero, within 1.6σ and 0.2σ respectively: this implies that the hadronic system created in Pb–Pb collisions at the LHC is on average baryon-number free and electrically neutral. These conditions define the *nuclear transparency* regime, where the quantum number transport from the colliding ions to the midrapidity region is negligible. From the centrality independence of the chemical potentials, it is concluded that this regime is reached throughout the 0-90% centrality range, hence also in the most central collisions, where larger baryon-number stopping effects were observed at lower energy by the STAR Collaboration at the RHIC beam energy scan I [114].

Some cross checks are performed to assess the validity of the extraction of chemical potentials. First, the fit of the antiparticle-to-particle yield ratios is repeated by constraining μ_Q from the initial conditions of the colliding system in a similar way to what is done for μ_S. In this case, the constraint is provided by the charge-to-

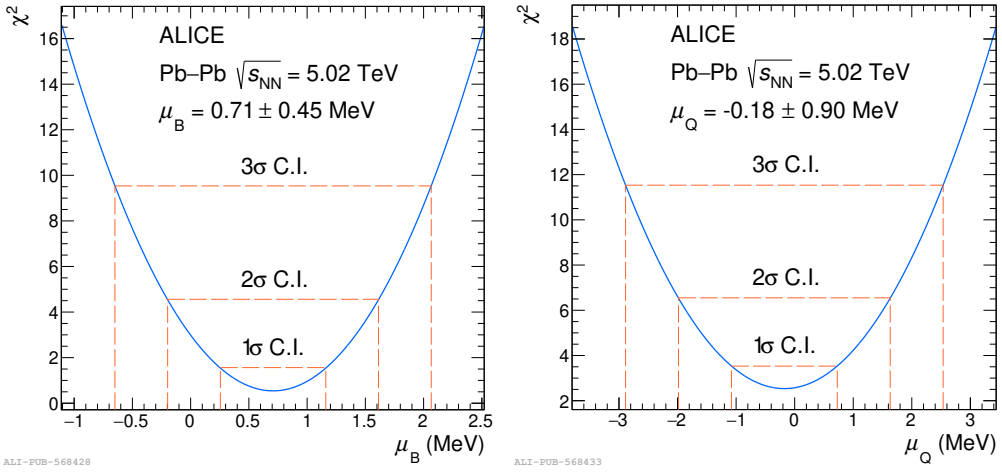

Figure 5.24: χ^2 profiles obtained from the zero-degree-polynomial fit of the centrality-differential μ_B and (on the left) and μ_Q (on the right)values. The 1σ, 2σ, and 3σ confidence intervals (C.I.) are also reported in the figure.

baryon ratio of the colliding ions, i.e., $Z/A \approx 0.4$ for ^{208}Pb. The ratio between the electric-charge and baryon-number densities of the system, $\langle n_Q \rangle / \langle n_B \rangle$, is then required to be equal to the initial Z/A ratio [205]. This condition implies a dependence between μ_Q and μ_B, as both chemical potentials enter the definition of the densities, n_i, through the fugacity factor, $\lambda_i = \exp[(B_i\mu_B + Q_i\mu_Q)/T_{\rm ch}]$. Similar constraints were also applied in previous works, where no direct estimates of μ_Q were provided [41, 50, 111]. For this check, the only fit parameter left in the SHM fit is μ_B. The centrality-integrated value extracted from the fit is compatible within 1σ with the one obtained with μ_Q as additional free parameter. Also in this case, no centrality dependence is observed from the centrality-differential analysis of μ_B. As an additional check, the extraction of μ_B is also carried out with a different implementation of the SHM than THERMAL-FIST. The code used is the GSI-Heidelberg model, which has been extensively used in previous SHM analyses of measured hadron yields and yield ratios [41, 50, 111]. Also in this fit, the μ_S and μ_Q are constrained by the initial state conditions through conservation laws. The chemical freeze-out temperature in this case is set to $T_{\rm chem} = 156.6 \pm 1.7$ MeV [115]. This value was extracted with the same model by fitting hadron yields measured by the ALICE Collaboration in Pb–Pb collisions at $\sqrt{s_{\rm NN}} = 2.76$ TeV. The centrality-integrated baryon chemical potential extracted with the GSI-Heidelberg model is $\mu_B = 0.90 \pm 0.43$ MeV. This result is in agreement with the one extracted with THERMAL-FIST, confirming the validity of the approach across different model

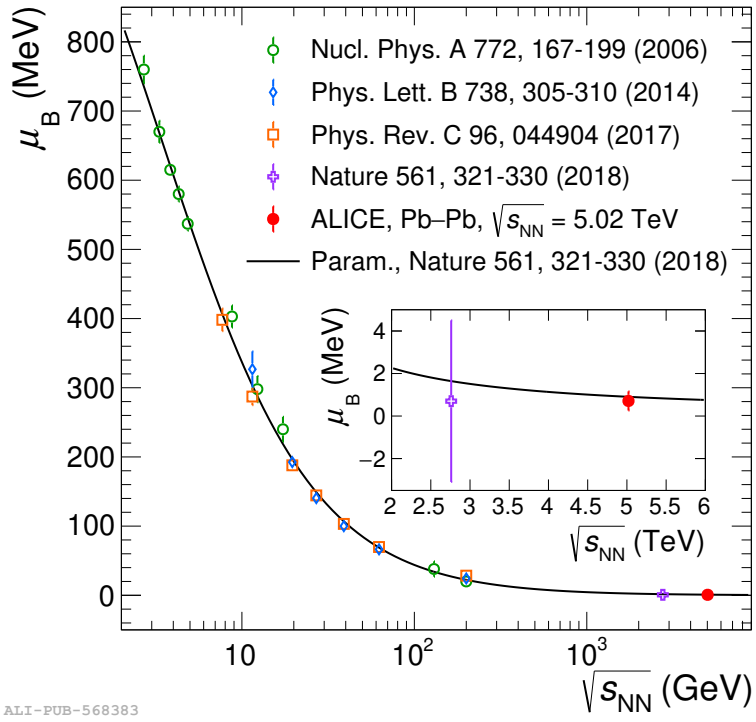

Figure 5.25: Baryon chemical potential, μ_B, extracted as a function of the centre-of-mass energy per nucleon pair, $\sqrt{s_{\rm NN}}$, from the SHM analysis of hadron yields and yield ratios measured in Au–Au and Pb–Pb collisions at the AGS (E802, E866, E877, E895, E896, E917 Collaborations), SPS (NA44, NA49, NA47 Collaborations), RHIC (BRAHMS, PHENIX, STAR Collaboration), and LHC (ALICE Collaboration) facilities [111, 113, 114]. The phenomenological parameterization of $\mu_B(\sqrt{s_{\rm NN}})$ is shown in black [19]. The comparison between the two results obtained at the LHC is shown in the inset of the figure [19]

implementations.

The value of the centrality-integrated baryon-chemical potential obtained in this Thesis is compared with the results obtained in previous works at different collision energies in different facilities, as shown in Fig. 5.25. The results obtained in previous works are determined in either Au–Au or Pb–Pb collisions via SHM fits of either hadron yields or yield ratios, both for the antiparticle-to-particle case and for yield ratios of different species. The extracted values are also compared with a phenomenological parameterisation reported by Reference [19], given by:

$$\mu_B = \frac{a}{1 + 0.288\sqrt{s_{\rm NN}}}, \tag{5.17}$$

with $\sqrt{s_{\rm NN}}$ expressed in GeV and $a = 1307.5$ MeV. The parameters are obtained by fitting the previous estimations of μ_B with the functional form of Eq. (5.17). The result obtained in this Thesis is consistent with the decreasing trend as a function of the collision energy also observed in the previous works. The obtained μ_B is also consistent with the phenomenological parameterisation within 1σ. In addition, the result obtained in this Thesis is compared in detail with the previous estimation of μ_B obtained at the LHC in Pb–Pb collisions at $\sqrt{s_{\rm NN}} = 2.76$ TeV, $\mu_B = 0.7 \pm 3.8$ MeV [50, 115]. The present result is consistent with the previous one within uncertainties, while reducing the uncertainty on the μ_B estimate by a factor ≈ 8.4. The main improvement from the past estimation is connected to the treatment of the uncertainties correlated between particles and antiparticles of the same species. These systematic contributions were not treated separately in the previous work, while in this Thesis they are cancelled out in the antiparticle-to-particle ratios. In addition, the study of yield ratios determines a reduction in the number of fit parameters, as the volume of the system is the same for particles and antiparticles.

Extraction of the net-proton density

The extracted chemical potentials can be used as input parameters to study the phenomenological models of baryon number transport. In the following, μ_B and μ_Q obtained in the 0-5% centrality interval are used to test the predictions of the baryon junction model: the check is based on the work published in Reference [206]. The baryon junction model provides a phenomenological description of the baryon number transport to midrapidity through the formation of non-perturbative three-gluon configuration, called junctions, which carry baryon number [207]

The net-proton density at midrapidity, which is computed starting from the obtained μ_B and μ_Q in the SHM, can be directly compared with the expectations of the baryon junction model. In the baryon junction model, the net-proton density at midrapidity per participant nucleon pair, $2/\langle N_{\rm part}\rangle {\rm d}N_{\rm p-\bar{p}}/{\rm d}y$, is predicted to have an exponential dependence on the deviation of the beam rapidity with respect to the centre-of-mass rapidity, $\delta y = y_{\rm beam} - y_{\rm cm}$:

$$\frac{{\rm d}N_{\rm p-\bar{p}}/{\rm d}y}{\langle N_{\rm part}\rangle/2} = N_B \exp(-\alpha_B \delta y), \tag{5.18}$$

where the parameters $N_B = 1.1 \pm 0.1$ and $\alpha_B = 0.61 \pm 0.03$ are extracted from fits of net-proton yields measured by the STAR Collaboration using the functional form of Eq. (5.18) [206]. At the LHC, where $\delta y \approx 8.6$, it is expected that

$2/\langle N_{\rm part}\rangle {\rm d}N_{\rm p-\bar{p}}/{\rm d}y \approx 5.8 \times 10^{-3}$. Using THREMAL-FIST along with the μ_B and μ_Q values obtained in the 0-5% centrality interval, the extracted value for the same observable is $(3.4 \pm 1.4) \times 10^{-3}$. With the GSI-Heidelberg model and the respective μ_B estimate, the obtained result is $5.9^{+2.2}_{-2.8} \times 10^{-3}$, also in this case for the 0-5% centrality interval. In both calculations, the system volume is set to $V = 5280 \pm 410$ fm^3 [50, 115], while the average number of participant nucleons is set to $\langle N_{\rm part}\rangle = 383.4 \pm 17.8$ [208]. The computation is carried out including the feed-down effects of strong, electromagnetic, and weak decay of heavier states. These two results agree with the baryon junction expectations within the experimental uncertainties.

Chapter 6

Measurements of event-by-event fluctuations of multistrange hadrons and light-nuclei

In this chapter, the measurements of both the normalised second-order cumulant of the net-charged-Ξ number and the Pearson correlation coefficient between the net-charged-kaon number and net-charged-Ξ number are described. The results of this analysis are published in Physical Review Letters [2]. In addition, the measurement of the normalised second-order cumulant of the net-Λ number and of the Pearson correlation coefficient between the net-Λ number and the $\bar{\mathrm{d}}$ number are reported. The results of the analysis have been approved as official public results by the ALICE Collaboration. The analysis involving $\Xi^{\pm}$ and $\mathrm{K}^{\pm}$ is carried out in pp, p–Pb, Pb–Pb collisions with data collected at a centre-of-mass energy $\sqrt{s_{\mathrm{NN}}} = 5.02$ TeV, while the measurements involving $\bar{\mathrm{d}}$ candidates and $(\bar{\Lambda})\Lambda$ are carried out in Pb–Pb collisions at $\sqrt{s_{\mathrm{NN}}} = 5.02$ TeV. In both cases, centrality- or multiplicity-differential measurements are performed.

6.1 Analysis strategy

The analysed hadron species are chosen based on their sensitivity to the hadron production mechanisms studied. To test the strangeness hadronisation mechanisms, $\mathrm{K}^{\pm}$ and $\Xi^{\pm}$ are employed. Using two separate particle species both carrying strangeness, it is possible to probe not only opposite-strangeness-sign correlations but also the same-sign ones, thus enabling a better discrimination among differ-

ent hadronisation models. Specifically, in the string-fragmentation model [56] the strength of same-strangeness-sign correlations is expected to be negligible compared to the opposite-sign ones due to the prevalence of $q\bar{q}$ pair creation in the string breaking over diquark-antidiquark production mechanisms, as discussed in Section 2.1.2. In addition, $\mathrm{K}^{\pm}$ and $\Xi^{\pm}$ are marginally affected by decays of heavier states that could affect the measured correlation strengths via the correlated production in decays.

The study of the processes underlying the formation of light nuclei is carried out using $\bar{\mathrm{d}}$ candidates and Λ baryons. As Λ hyperons are not contained in $\bar{\mathrm{d}}$ candidates, the correlations measured between these two species are insensitive to the baryon number conservation effects induced by the nuclear formation mechanism. The effects of spurious correlations caused by decays are negligible, as in this case the main common feed-down sources are hypernuclei, which are rarely produced compared to both $\bar{\mathrm{d}}$ candidates and Λ baryons. In addition, only $\bar{\mathrm{d}}$ candidates are considered rather than the matter counterpart, as their production is not affected by inelastic interaction of primary particles in the ALICE detector material, as it is also discussed in detail in Section 5.3.2. Finally, similarly to the aforementioned case, both the same-baryon-number and opposite-baryon-number correlations are determined in this Thesis by measuring $\bar{\mathrm{d}}$ and both Λ and $\bar{\Lambda}$ candidates.

The fluctuation observables measured in this Thesis rely on counting the number of identified particles produced in each collision, i.e., on an event-by-event basis, for each of the species of interest. The main requirement for this kind of measurements is the identification of the particle species with high purity ($> 90\%$) within the analysed acceptance to enable the identification of the corresponding candidates in each event. The identification methods described in Chapter 4 allow us to achieve the purity required for all of the species, as it is also shown in detail in the next Section.

6.2 Definition of the observables

The event-by-event observables studied in this Thesis are defined in terms of both single-particle and two-particle cumulants, κ_i and κ_{jk}, respectively, up to the second order. As briefly mentioned in Section 2.1.1, the n-th order cumulants κ_n of the probability density function $f(x)$ of a random variable x are computed starting

from the characteristic function, $\phi(t)$, which is defined as:

$$\phi(t) = \int_{-\infty}^{\infty} e^{itx} f(x) \mathrm{d}t. \tag{6.1}$$

The cumulants correspond to the coefficients of the Maclaurin expansion of the logarithm of $\phi(t)$:

$$\ln \phi(t) = \sum_{n=1}^{\infty} \kappa_n \frac{(it)^n}{n!}. \tag{6.2}$$

The cumulants derive their name from their cumulative properties. Indeed it can be proven that the n-th order cumulant of the sum of m independent random variables $x_1 + x_2 + \cdots + x_m$ is given by:

$$\kappa_n(x_1 + x_2 + \cdots + x_m) = \kappa_n(x_1) + \kappa_n(x_2) + \cdots + \kappa_n(x_m) \tag{6.3}$$

The first order, second order, and mixed cumulants are computed as:

$$\kappa_1(A) = \langle n_A \rangle, \tag{6.4}$$

$$\kappa_2(A) = \langle (n_A - \langle n_A \rangle)^2 \rangle, \tag{6.5}$$

$$\kappa_{11}(A, B) = \langle (n_A - \langle n_A \rangle)(n_B - \langle n_B \rangle) \rangle, \tag{6.6}$$

where A and B are two generic hadron species, n_i is the number of particles of the i-th species produced in each event, and $\langle \cdot \rangle$ is the average over all events. The first order and second order cumulants of Eq. (6.4) and Eq. (6.5) are equivalent to the average and variance of the event-by-event multiplicity distribution of the species A, respectively. Additionally, the two-particle cumulant in Eq. (6.6) corresponds to the covariance of the event-by-event joint multiplicity distribution of species A and B.

Using the correspondence between cumulants and statistical moments, the two-particle cumulants and the second-order cumulants can be combined to define the Pearson correlation coefficient of the joint density of A and B:

$$\rho_{AB} = \frac{\kappa_{11}(A, B)}{\sqrt{\kappa_2(A)\kappa_2(B)}} \tag{6.7}$$

6.2.1 Volume fluctuations

In the event-by-event analyses presented in this Thesis, the observables are measured in multiplicity intervals of finite width. Consequently, the defined intervals contain events characterised by several particle multiplicity values that differ from the reference one, which is the centre of the interval if the multiplicity is uniformly distributed in that interval. This results in additional event-by-event fluctuations on top of those driven by the hadronisation mechanism. These fluctuations are commonly referred to as *volume fluctuations*, as the particle multiplicity produced in each event is related to the initial volume of the system.

The observables measured in this Thesis are defined in terms of net-particle numbers, i.e., the difference between the number of particles, N_A, and antiparticles, $N_{\bar{A}}$ of the species of interest, $\Delta A = N_A - N_{\bar{A}}$. By analysing net-particles instead of particle and antiparticle numbers separately, the effects of volume fluctuations are canceled out, provided that the matter and antimatter produced in the collisions are balanced on average, i.e., $\mu_B \approx 0$. In Pb–Pb collision, this condition is verified via the observation of chemical potentials compatible with zero, as it is shown in Chapter 5 of this Thesis. The same condition is also verified in other colliding systems, via the precise measurement of the $\bar{\mathrm{p}}$/p yield ratio in pp collisions [209, 210], and by determining the antiparticle-to-particle yield ratios of light nuclei in p–Pb collisions [211, 212]: in both cases, the obtained yield ratios are compatible with unity.

The analytical proof of the cancellation of volume fluctuation in net-particle observables at $\mu_B \approx 0$ is obtained in the wounded nucleon model of heavy-ion collisions, where the collision of two ions is modelled as the superposition of multiple binary nucleon-nucleon collisions. From the relation between the particle cumulants and the cumulants of initial wounded nucleons [52],

$$\kappa_2(A) = \kappa_1(N_w)\kappa_2(n_A) + \kappa_2(N_w)[\kappa_1(n_A)]^2, \tag{6.8}$$

$$\kappa_{11}(A,B) = \kappa_1(N_w)\kappa_{11}(n_A,n_B) + \kappa_2(N_w)\kappa_1(n_A)\kappa_1(n_B), \tag{6.9}$$

where N_w is the number of wounded nuclei, while n_A and n_B are the numbers of particles of species A and B produced by a single wounded nucleon source, respectively. Under the assumption that $\kappa_1(n_A) \approx \kappa_1(n_{\bar{A}})$ at the LHC, the second-order fluctuations of N_w cancel out in $\kappa_2(\Delta A)$:

$$\kappa_2(\Delta A) = \kappa_2(N_A) + \kappa_2(N_{\bar{A}}) - 2\kappa_{11}(N_A, N_{\bar{A}}) \tag{6.10}$$
$$\approx \kappa_1(N_w)\left[\kappa_2(n_A) + \kappa_2(n_{\bar{A}}) - 2\kappa_{11}(n_A, n_{\bar{A}})\right] \tag{6.11}$$

A similar result is obtained for $\kappa_{11}(\Delta A, \Delta B)$:

$$\kappa_{11}(\Delta A, \Delta B) = \kappa_{11}(N_A, N_B) + \kappa_{11}(N_{\bar{A}}, N_{\bar{B}}) - \kappa_{11}(N_A, N_{\bar{B}}) - \kappa_{11}(N_{\bar{A}}, N_B) \tag{6.12}$$
$$\approx \kappa_1(N_w)\left[\kappa_{11}(n_A, n_B) + \kappa_{11}(n_{\bar{A}}, n_{\bar{B}}) - \kappa_{11}(n_A, n_{\bar{B}}) - \kappa_{11}(n_{\bar{A}}, n_B)\right] \tag{6.13}$$

Similar cancellation effects are also obtained for $\kappa_2(A)$ when the species A is rarely produced in collisions, i.e., $\kappa_1(A) \ll 1$. In this case, the charge conservation effects are negligible for the species of interest, hence the event-by-event multiplicity distribution approaches the Poissonian limit, where $\kappa_2(n_A) \approx \kappa_1(n_A)$. This effect has been observed by the ALICE Collaboration for $\bar{\mathrm{d}}$ cumulants in Pb–Pb collisions [135]. Consequently, the second term in the right hand side of Eq. (6.8) constitutes a subleading correction that can be neglected compared to the first term, thus determining the cancellation of second order volume fluctuations.

6.2.2 Event-by-event fluctuation observables

The (multi)strange hadron fluctuation observables analysed in this Thesis include the normalised second-order cumulant of net-Ξ number, $\kappa_2(\Delta\Xi)/\langle\Xi^- + \bar{\Xi}^+\rangle$, and the Pearson correlation coefficient between net-K number and net-Ξ number, $\rho_{\Delta\Xi\Delta\mathrm{K}}$. Both of these observables are safe with respect to volume fluctuations, according to the argument of Section 6.2.1. These two quantities are computed as:

$$\frac{\kappa_2(\Delta\Xi)}{\kappa_1(\bar{\Xi}^+ + \Xi^-)} = \frac{\kappa_2(\bar{\Xi}^+) + \kappa_2(\Xi^-) - 2\kappa_{11}(\bar{\Xi}^+, \Xi^-)}{\langle n_{\bar{\Xi}^+} + n_{\Xi^-}\rangle}, \tag{6.14}$$

$$\rho_{\Delta\Xi\Delta\mathrm{K}} = \frac{\kappa_{11}(\bar{\Xi}^+, \mathrm{K}^+) + \kappa_{11}(\Xi^-, \mathrm{K}^-) - \kappa_{11}(\bar{\Xi}^+, \mathrm{K}^-) - \kappa_{11}(\Xi^-, \mathrm{K}^+)}{\sqrt{\kappa_2(\Delta\Xi)\kappa_2(\Delta\mathrm{K})}}. \tag{6.15}$$

The observable defined in Eq. (6.14) is only sensitive to the opposite-strangeness-sign correlation, arising from the covariance term $\kappa_{11}(\bar{\Xi}^+, \Xi^-)$. On the contrary, Eq. (6.15) is sensitive to both the same- and opposite-strangeness-sign correlations,

contained in the covariance terms $\kappa_{11}(\bar{\Xi}^{+}, \mathrm{K}^{+})$ and $\kappa_{11}(\bar{\Xi}^{+}, \mathrm{K}^{-})$, respectively, and the analogous ones for the charge-conjugate states. A similar observable as the one of Eq. (6.14) is also defined for the net-Λ number, namely $\kappa_2(\Delta\Lambda)/\langle\Lambda + \bar{\Lambda}\rangle$. In addition, in the light (anti)nuclei sector, the correlation coefficient between the $\bar{\mathrm{d}}$ number and the net-Λ number, $\rho_{\bar{\mathrm{d}}\Delta\Lambda}$, is also measured. This observable, which is also insensitive to volume fluctuations, is defined as:

$$\rho_{\bar{\mathrm{d}}\Delta\Lambda} = \frac{\kappa_{11}(\bar{\mathrm{d}}, \Lambda) - \kappa_{11}(\bar{\mathrm{d}}, \bar{\Lambda})}{\sqrt{\kappa_2(\bar{\mathrm{d}})\kappa_2(\Delta\Lambda)}}. \tag{6.16}$$

Similarly to Eq. (6.15), this observable is sensitive to both the same-baryon-number and opposite-baryon-number correlations through the two covariance terms in the numerator of Eq. (6.16).

6.3 Candidate identification

Table 6.1: p_{T} intervals set for the different species analysed in this Thesis for event-by-event fluctuation measurements.

Species	p_{T} (GeV/c)
$\mathrm{K}^{\pm}$	[0.2, 1.0]
$\Xi^{\pm}$	[1.0, 3.0]
d	[0.6, 1.8]
$(\bar{\Lambda})\Lambda$	[1.0, 4.0]

The selection of candidates of interest is carried out on a candidate-by-candidate basis by applying the criteria described in Chapter 4. All candidates are selected in the pseudorapidity region $|\eta| < 0.8$. The p_{T} acceptances analysed are reported in for all the species. They include the bulk of hadron production, which is connected to soft hadronisation processes: consequently, the jet fragmentation regime is excluded in this Thesis.

On top of the criteria defined in Chapter 4, a few additional selections are used to mitigate the spurious correlation effects caused by reconstruction artifacts. First, for the hadrons identified via reconstructed decay topologies, multiple candidates can be reconstructed in a single event starting from the same set of tracks, resulting in artificial correlations among the reconstructed candidates. To suppress this effect, which is mostly relevant for high-multiplicity Pb–Pb collisions, all events containing at least two selected decay topologies with at least one shared decay product track are rejected from the data sample. The fraction of rejected events

Table 6.2: Regions of interest (ROI) defined for the identification of species analysed in this Thesis.

Species	p_{T} (GeV/c)	ROI
$\mathrm{K}^{\pm}$	[0.2, 0.4]	$\lvert n\sigma_{\mathrm{ITS}}\rvert < 3.0$ (Pb–Pb) and $\lvert n\sigma_{\mathrm{TPC}}\rvert < 3.0$
	[0.4, 1.0]	$\lvert n\sigma_{\mathrm{TPC}}\rvert < 2.5$ and $\lvert n\sigma_{\mathrm{TOF}}\rvert < 3.0$
$\bar{\mathrm{d}}$	[0.6, 1.0]	$\lvert n\sigma_{\mathrm{TPC}}\rvert < 2.0$
	[1.0, 1.8]	$\lvert n\sigma_{\mathrm{TPC}}\rvert < 2.0$ and $\lvert n\sigma_{\mathrm{TOF}}\rvert < 2.5$
$(\bar{\Lambda})\Lambda$	[1.0, 4.0]	$\lvert M(\mathrm{p}+\pi^{-}) - M_{\Lambda}\rvert < 2\sigma$
$\Xi^{\pm}$	[1.0, 3.0]	$\lvert M(\Lambda+\pi^{-}) - M_{\Xi}\rvert < 3\sigma$

is at most $\approx 0.5\%$ for the 10% most central collisions. In addition, the correlation coefficients measured in this Thesis involve hadrons identified both by tracking and by vertexing. Hence, a single track can be identified as one of the species of interest, as well as being used in the reconstruction of a decay topology of interest. The resulting double counting is an additional source of autocorrelation in the selected candidate sample. It is suppressed by separating the track samples used for the two identification procedures: this is achieved through complementary DCA selections for the tracked species compared to the decay products of the reconstructed decays. In particular, it is required that DCA < 0.1 cm for $\mathrm{K}^{\pm}$ and $\bar{\mathrm{d}}$ candidates, while DCA > 0.1 cm is set for the decay products of $(\bar{\Lambda})\Lambda$ and $\Xi^{\pm}$ candidates.

Finally, for the analysis of fluctuations involving $\bar{\mathrm{d}}$ and net-Λ, a tighter selection on the z coordinate of the reconstructed vertex, V_z, is applied with respect to the nominal one reported in Section 4.1.2. This selection is applied to improve the stability of the reconstruction efficiency with respect to the fluctuation of the vertex position on a collision-by-collision basis. Specifically, it is required that $|V_z| < 8$ cm. A similar procedure was also applied in previous measurements published by the ALICE Collaboration [143].

6.3.1 Purity of the identified candidates

Depending on the reconstruction technique, the selected candidates are finally identified either using the information of the PID detectors or measuring the invariant mass of the decay products. The identification criteria are summarised in Table 6.2. The uncorrected number of candidates is obtained by counting the candidates passing these requirements, for each of the species of interest. As mentioned in Section 6.1, the determination of identified particle multiplicities on an

event-by-event basis requires that the species of interest are identified with a high purity. This is checked by extracting the purity of the selected candidate samples in subintervals of the analysed p_{T} ranges. The purity is computed using the signal and background counts extracted with a fit of either the $n\sigma$ or the invariant mass distributions observed in the data. This computation is performed in each p_{T} bin, for each of the analysed species. The fitting procedure is analogous to the one explained in Section 5.2. Two examples of the fitting performance for K^{+} and Ξ^{-} are shown in Fig. 6.1 in specific p_{T} bins for the 10% most central Pb–Pb collisions.

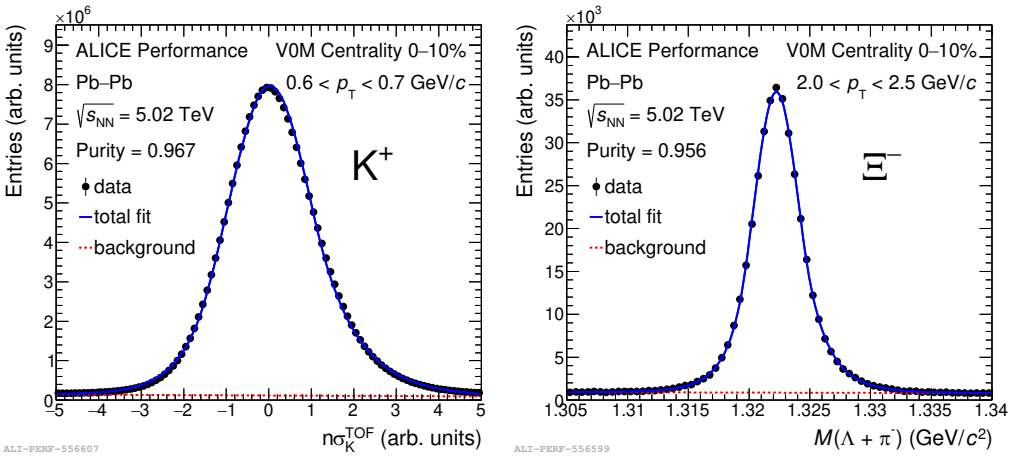

Figure 6.1: Fit performance for the purity determination obtained in this Thesis for K^{+} (left panel) and Ξ^{-} samples (right panel) in the 10% most central Pb–Pb collisions.

The purity obtained as a function of p_{T} in each of the centrality classes used in the Pb–Pb data samples is shown in Fig. 6.2 for K and Ξ, and in Fig. 6.3 for $\bar{\mathrm{d}}$ and Λ, respectively. Overall, for all of the analysed species, the purity is larger than about 92%, hence ensuring a reliable performance of the event-by-event identification of the respective candidates. For the analysis of K and Ξ in pp and p–Pb collisions, the observed purity is larger than 95% in all of the analysed p_{T} bins. The obtained purity shows an increase when going from central to peripheral collisions: this trend is explained by the larger detector occupancy in the most central collisions. For K and $\bar{\mathrm{d}}$, a lower purity is observed at larger p_{T}, where the TOF PID information is also used for the identification of candidates. In those cases, the irreducible effect of mismatch between reconstructed tracks and TOF space points determines a larger contamination than what is present in the low p_{T} region, where the TPC

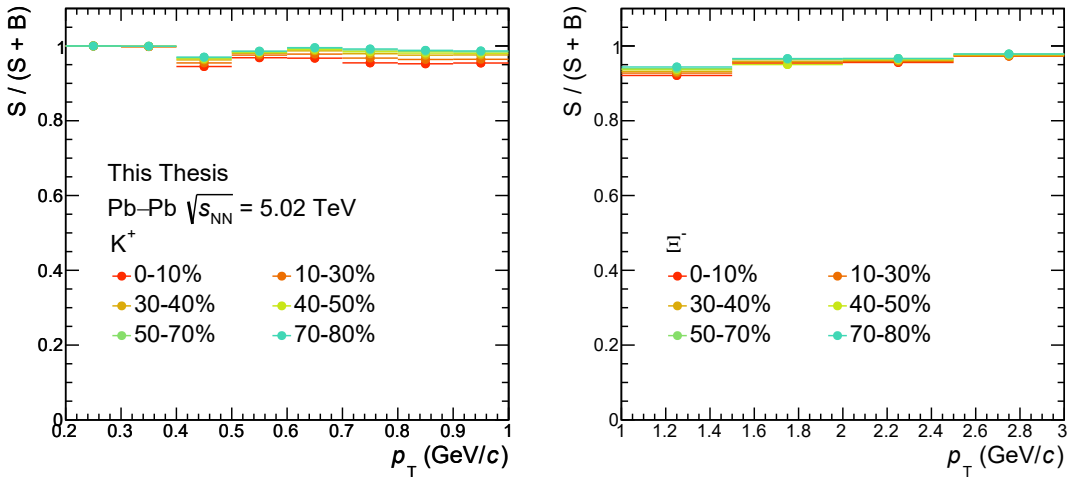

Figure 6.2: Purity of the K^+ (left panel) and Ξ^- samples (right panel) selected in Pb–Pb collisions, for each centrality class.

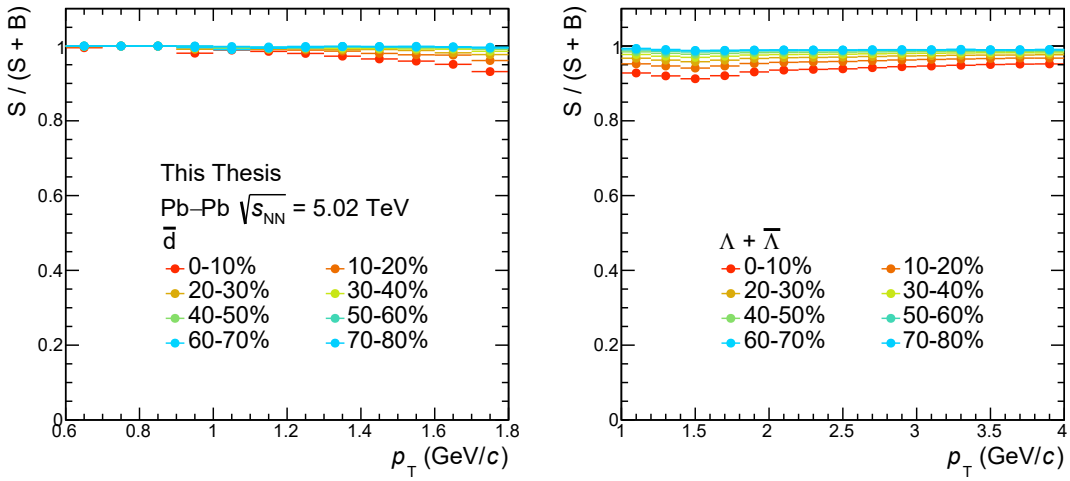

Figure 6.3: Purity of the $\bar{d}$ (left panel) and $\Lambda + \bar{\Lambda}$ samples (right panel) selected in Pb–Pb collisions, for each centrality class.

PID can be performed with an optimal separation among particle species. For both Λ and Ξ, the purity increases with increasing p_T, as a larger residual combinatorial background affects the selected samples in the low p_T region.

The uncorrected event-by-event multiplicity distributions obtained for the analysed species in the 10% most central Pb–Pb events are shown in Fig. 6.4. For each of the hadron species, these histograms are built by determining the frequency

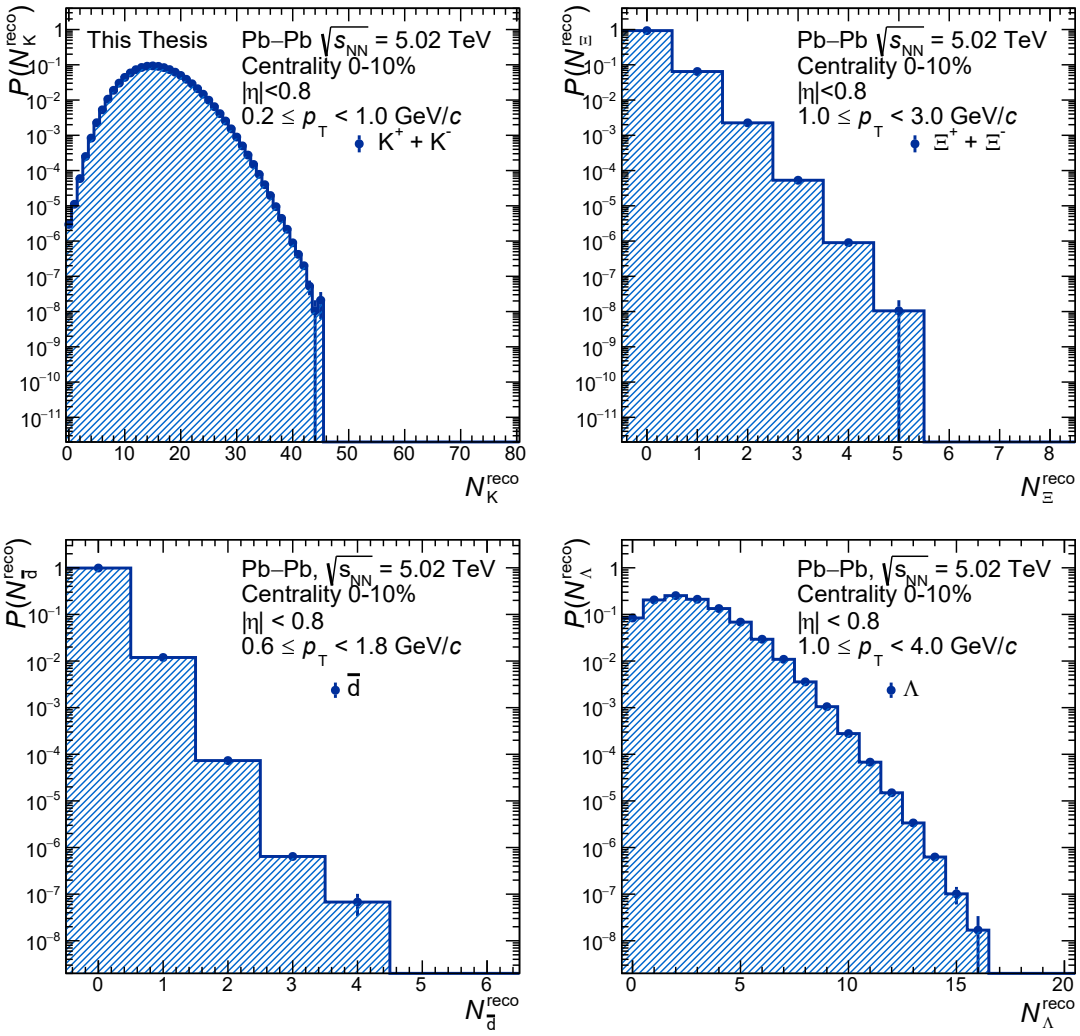

Figure 6.4: Uncorrected event-by-event multiplicity distribution of $K^+ + K^-$, $\bar{\Xi}^+ + \Xi^-$, $\bar{d}$, and Λ observed in the 10% most central Pb–Pb collisions. The distributions are normalised to the total number of events.

of selected events where the number of identified candidates corresponds to the central value of the bin. For all of the analysed species, the obtained distributions show multiple events with more than two reconstructed candidates. This condition is required to extract the second order cumulants of the event-by-event multiplicity distribution. Analogous results are obtained also in the other centrality intervals and for the other collision systems, although with a reduction in the number of events with multple identified candidates due to the reduction of the total event

multiplicity.

6.4 Efficiency correction

The number of candidates extracted in each event with the procedure described in Section 6.3 is affected by the efficiency of the candidate reconstruction and selection criteria. This efficiency is estimated through MC simulations as the fraction of generated particles that are reconstructed and pass the same selection requirements applied in the data. As the event-by-event observables analysed in this Thesis are defined within the experiment geometrical acceptance, both the counts of generated and reconstructed particles are extracted in $|\eta| < 0.8$ for the efficiency calculation:

$$\epsilon = \frac{N_{\mathrm{reco}}(|\eta| < 0.8)}{N_{\mathrm{gen}}(|\eta| < 0.8)} \tag{6.17}$$

As an example, the efficiency obtained from Pb–Pb MC simulations for K^+, $\bar{\mathrm{d}}$, Ξ^-, and Λ is shown in Fig. 6.5, for different p_{T} intervals and centrality classes. The requirement of the matching between tracks and TOF space points determines a descrease in the computed efficiency around 0.4 GeV/c and 1 GeV/c for K^+ and $\bar{\mathrm{d}}$, respectively. In addition, the efficiency shown for Ξ^- is the product of the candidate preliminary selection efficiency and the BDT signal selection efficiency. Similarly to what is observed in Section 5.3.1, the centrality dependence of the efficiency is driven by the increasing detector occupancy going from peripheral to central collisions. This effect is smaller in pp and p–Pb collisions, where the maximum difference is $O(0.01)$.

The efficiency term is included in the observables defined in Section 6.2.2 using a model of the fluctuations in the candidate reconstruction and selection response, as discussed in Reference [213]. To determine the nature of these fluctuations, a response matrix is built for each of the analysed species using MC-simulated data, by correlating the generated-candidate and reconstructed-candidate counts extracted on an event-by-event basis. As an example, the response matrix of K^- is shown in the left panel of Fig. 6.6. The distributions of reconstructed-candidate counts can be determined for fixed values of generated-candidate counts, as it is also shown in the right panel of Fig. 6.6. For each of the analysed species, the obtained distributions are in agreement with the binomial hypothesis, as verified via a binomial fit. Consequently, the measured event-by-event multiplicity distribution, $\tilde{P}(n)$, is

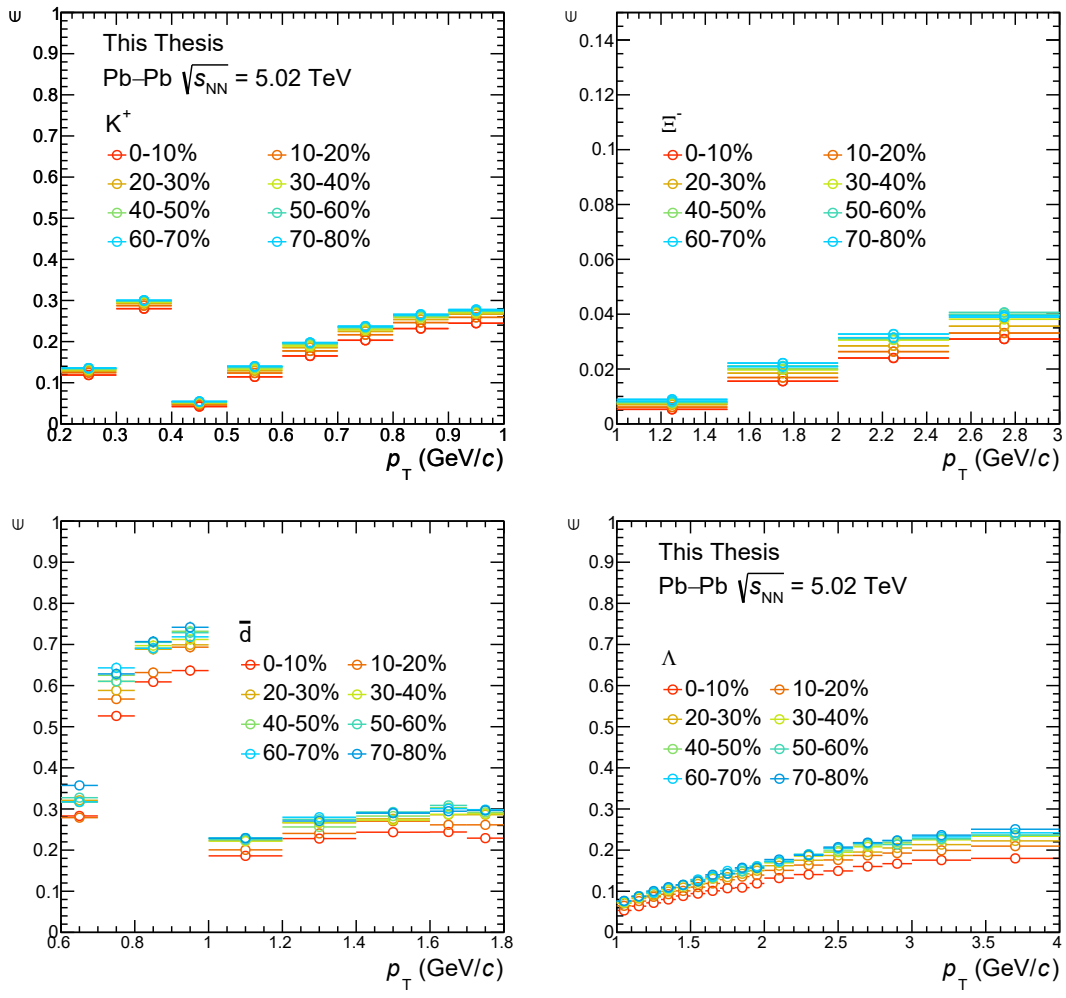

Figure 6.5: Efficiency of the analysed hadron species as a function of p_{T} in Pb–Pb collisions, for different centrality intervals.

connected to the generated one, $P(N)$, by the relation:

$$\tilde{P}(n) = \sum_{N} P(N) B_{\epsilon,N}(n), \tag{6.18}$$

where $B_{\epsilon,N}(n)$, acting as a response matrix, is determined by the binomial law by interpreting the efficiency ϵ as the success probability:

$$B_{\epsilon,N}(N) = \frac{N!}{n!(N-n)!} \epsilon^n (1-\epsilon)^{N-n}. \tag{6.19}$$

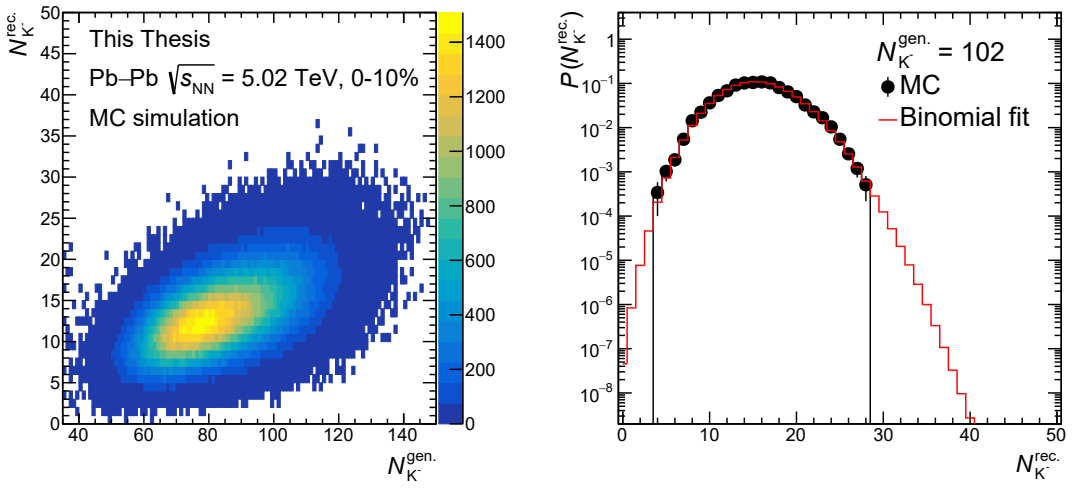

Figure 6.6: Left panel: detector response matrix for K^- in the 10% most central Pb–Pb collisions. Right panel: distribution of the number of reconstructed K^- candidates for a number of generated particles $N^{\text{gen.}}_{K^-} = 102$. The binomial fit to the data is shown in red.

Using Eq. (6.18) to connect the observed counts to the corrected ones, a set of formulas for the efficiency-corrected cumulants can be obtained:

$$\kappa_1(A) = \langle q_1(A) \rangle, \tag{6.20}$$

$$\kappa_2(A) = \langle q_1^2(A) \rangle - \langle q_1(A) \rangle^2 + \langle q_1(A) \rangle - \langle q_2(A) \rangle, \tag{6.21}$$

$$\kappa_{11}(A,B) = \langle q_1(A) q_1(B) \rangle - \langle q_1(A) \rangle \langle q_1(B) \rangle, \tag{6.22}$$

$$\kappa_2(\Delta A) = \langle (q_1(A) - q_1(\bar{A}))^2 \rangle - \langle q_1(A) - q_1(\bar{A}) \rangle^2 + \langle q_1(A) + q_1(\bar{A}) \rangle - \langle q_2(A) + q_2(\bar{A}) \rangle. \tag{6.23}$$

In the formulas of Eq. (6.20), Eq. (6.21), Eq. (6.22), Eq. (6.23), the quantity $q_n(A) = \sum_{i=1}^{M} (N_i(A)/\epsilon_i(A))^n$ is determined from the number of p_{T} bins, M. $N_i(A)$ and $\epsilon_i(A)$ represent the number of reconstructed candidates and the efficiency for the species A in the i-th p_{T} bin, respectively, and $n = 1, 2$. The formulas used in this Thesis are derived under the assumption of p_{T}-binned data. In this way, it is possible to take into account the p_{T} evolution of the efficiency observed in Fig. 6.5. The efficiency-corrected observables are finally computed by expanding the observables defined in Eq. (6.14), Eq. (6.15), and Eq. (6.16) in terms of the efficiency-corrected cumulants, Eq. (6.20), Eq. (6.21), Eq. (6.22), and

Eq. (6.23).

6.5 Statistical uncertainty

In this Thesis, the statistical uncertainty on the event-by-event fluctuation observables, $\mathcal{O}$, is determined via the subensemble method described in Reference [214]. In this procedure, the initial data sample is subdivided into N subsamples of equal size: in each of these samples, the efficiency-corrected observables are determined using the full analysis procedure. The average value, μ, and the standard deviation, σ, of the N estimates are then computed:

$$\mu_{\mathcal{O}} = \frac{\sum_{i=1}^{N} \mathcal{O}_i}{N} \tag{6.24}$$

$$\sigma_{\mathcal{O}} = \sqrt{\frac{\sum_{i=1}^{N} (\mathcal{O}_i - \mu_{\mathcal{O}})^2}{N(N-1)}} \tag{6.25}$$

Consequently, μ is the central value of the observable over the full data sample, while σ is its statistical uncertainty. This method is applied for each of the analysed observables in each centrality and multiplicity interval. For the analysis of the net-K number and net-Ξ number fluctuations, the number of subsamples is $N = 30$, while for the $\bar{\mathrm{d}}$ number and net-Λ number fluctuations $N = 10$ is used. In both cases, the number of subsamples is chosen taking into account both the number of candidates available in each sample and the computational efficiency of the procedure. Nevertheless, to test the stability of the method upon the choice of N, the analysis is also repeated increasing the number of samples by 10: the effect on both the central values and the statistical uncertainties is negligible within the available precision.

6.6 MC closure test

The analysis procedure explained in Section 6.3, Section 6.4, and Section 6.5 is validated through a closure test using MC-simulated data. This check consists in applying the full analysis chain to the reconstructed MC data to extract the fully-corrected observables. The obtained results are then compared with the true MC results, which are extracted using the generated-level information of the simulation: the closure of the analysis is obtained if the two results are compatible.

As an example, the results obtained in the closure tests of $\rho_{\Delta\Xi\Delta\mathrm{K}}$ and $\rho_{\bar{\mathrm{d}}\Delta\Lambda}$ in Pb–Pb collisions are shown in Fig. 6.7. In both cases, the statistical uncertainties

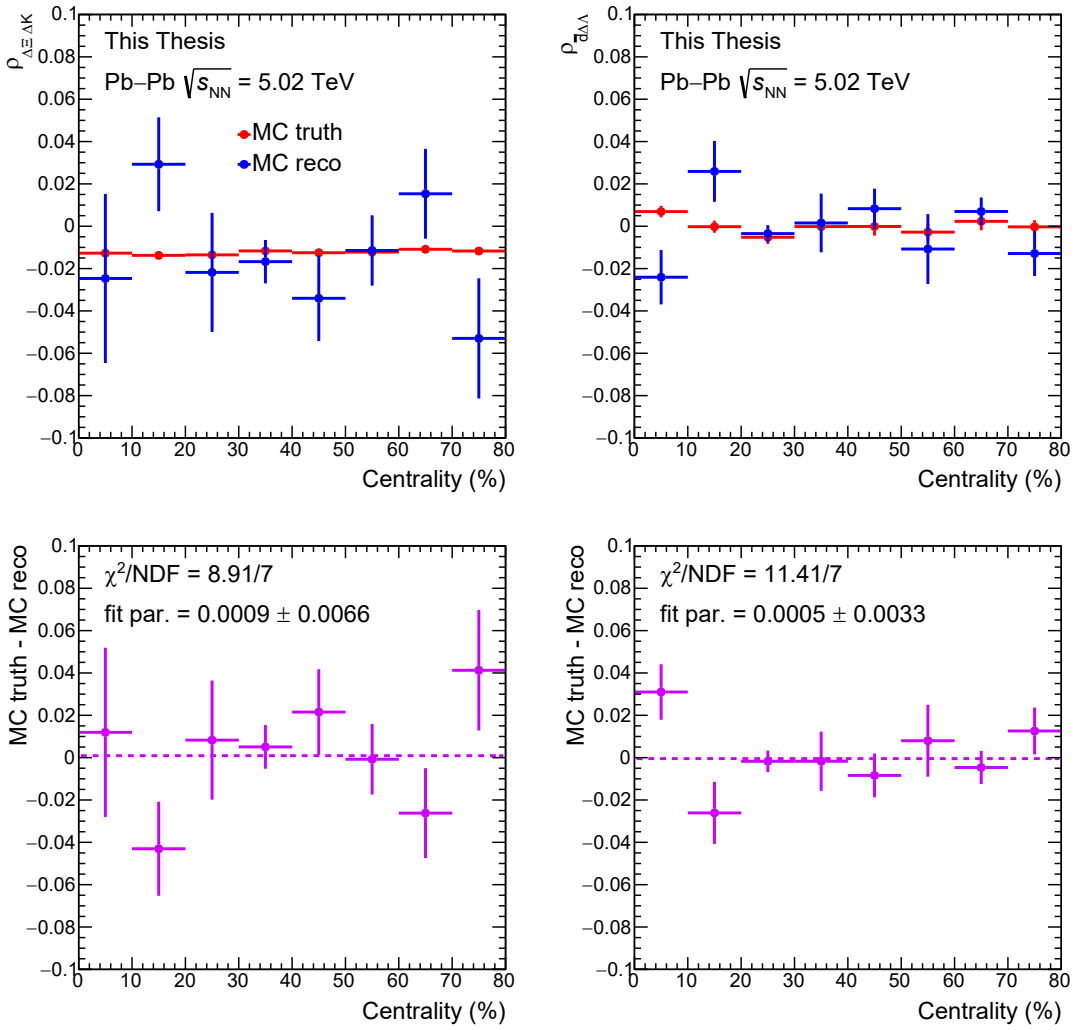

Figure 6.7: MC closure test results for $\rho_{\Delta\Xi\Delta K}$ (left panels) and $\rho_{\bar{d}\Delta\Lambda}$ (right panels), in Pb–Pb collisions. The observables obtained from the MC truth and in the reconstructed MC, using the full analysis chain, are shown in the upper panels. The difference between the MC truth and the observable reconstructed from MC data is shown in the lower panels. The zero-degree polynomial fit on the difference between the two is also shown as a dashed line.

on the observables are determined with the subensemble method described in Section 6.5. For $\rho_{\Delta\Xi\Delta K}$, a small autocorrelation is observed in the simulated data as the employed MC is fully based on the HIJING event generator, where quantum-number conservation effects are simulated through the string-fragmentation hadro-

nisation process. On the contrary, no correlation is obtained for $\rho_{\bar{\mathrm{d}}\Delta\Lambda}$ as the antideuterons produced in the simulation are injected in the HIJING event, hence they are completely uncorrelated with respect to the Λ baryons generated in the underlying event.

In both cases, the MC truth is well reproduced by the reconstructed data analysed with the aforementioned techniques. This is also checked on a quantitative basis by computing the difference between the Mc truth and reconstructed observables and fitting this difference with a polynomial of zero degree. The difference between the MC truth and MC reconstructed levels does not show any dependence on centrality, as verified by the χ^2/NDF of the fits. In addition, the fit parameters obtained in the two cases are compatible with zero within statistical uncertainties, indicating that the analysis procedure correctly reproduces the expected results within the available precision. Similar results are obtained also for the other observable measured in this Thesis, as well as in the other colliding systems analysed.

6.7 Systematic uncertainties

The main source of systematic uncertainty for the fluctuation observables analysed in this Thesis is provided by the MC-to-data matching affecting the accuracy of the efficiency corrections described in Section 6.4. To determine the resulting systematic contributions, the selection criteria described both in Chapter 4 and in Section 6.3 are varied with respect to the nominal ones to assess the effect on the final results. The applied procedures are described in the following, separately for the analysis of net-K and net-Ξ fluctuations and for the one of $\bar{\mathrm{d}}$ and net-Λ fluctuations, due to the different method used in the calculation of the uncertainties.

6.7.1 $\bar{\mathrm{d}}$ number and net-Λ number fluctuations

The variations of the selection criteria used in this analysis are summarised in Table 6.3 and Table 6.4. Besides the variations of the candidate selection and identification criteria, an additional variation is considered for the selection on the V_z. The systematic uncertainties related to each of the sources are obtained by repeating the full analysis with the two varied configurations of the selection. The results obtained for all selection criteria variations are shown in Fig. 6.8 for both $\rho_{\bar{\mathrm{d}}\Delta\Lambda}$ and $\kappa_2(\Delta\Lambda)/\langle\Lambda+\bar{\Lambda}\rangle$.

The uncertainty value is obtained as half of the difference between the two values. This procedure is repeated for each of the analysed centrality classes. The

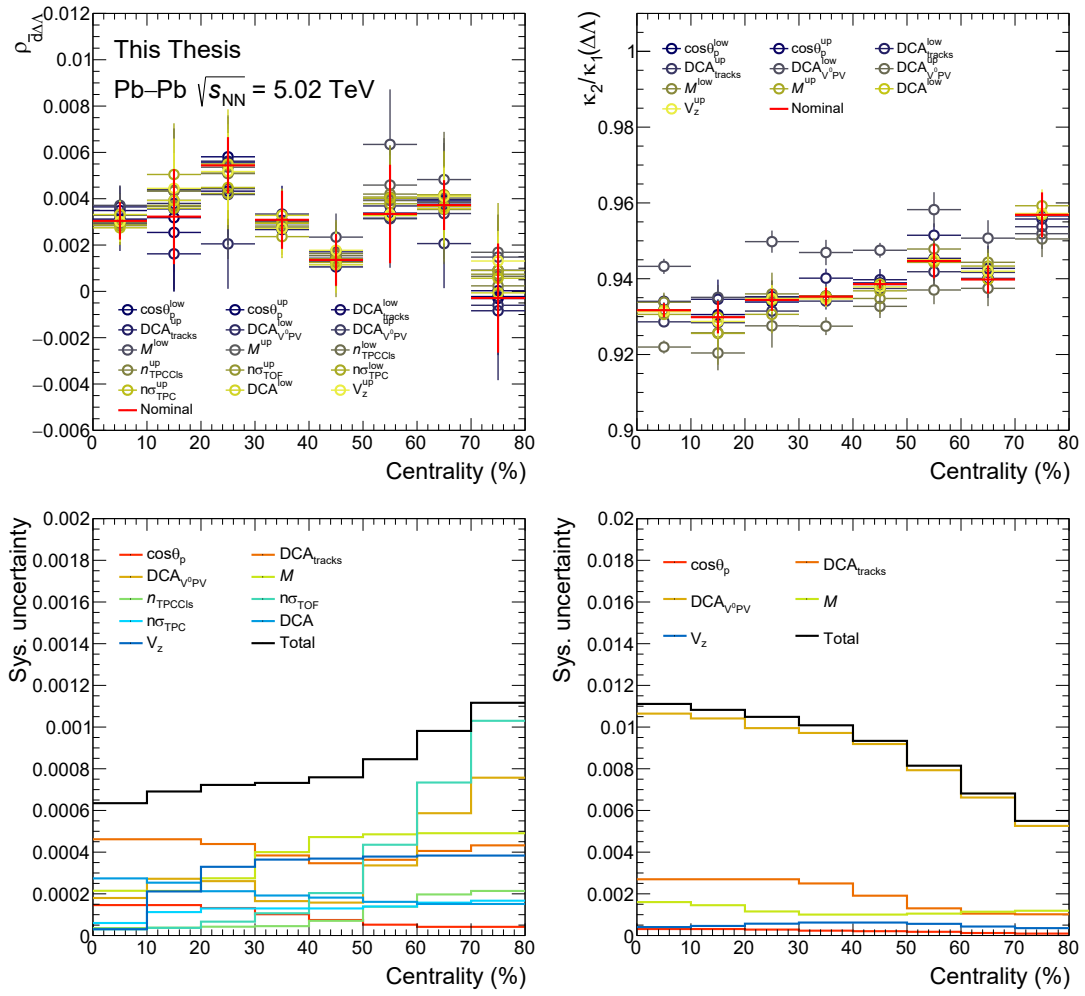

Figure 6.8: Upper panels: results for $\rho_{\bar{\mathrm{d}}\Delta\Lambda}$ (left) and $\kappa_2(\Delta\Lambda)/\langle\Lambda+\bar{\Lambda}\rangle$ (right) obtained with the different variations of the selection criteria. The results obtained with the nominal configuration of selections is also shown. Lower panels: systematic uncertainties on $\rho_{\bar{\mathrm{d}}\Delta\Lambda}$ (left) and $\kappa_2(\Delta\Lambda)/\langle\Lambda+\bar{\Lambda}\rangle$ (right) for both the different systematic sources and the total combination of all sources.

Table 6.3: Variations used for the evaluation of the systematic uncertainties of $\rho_{\bar{\mathrm{d}}\Delta\Lambda}$. The values of the systematic uncertainties assigned to each of the sources are also reported.

Variable	Nominal	Lower var.	Upper var.	Uncertainty
$\cos\theta_p$	0.997	0.995	0.998	0.08×10^{-3}
$\mathrm{DCA}_{V^0,\mathrm{PV}}$	0.5 cm	0.2 cm	1 cm	0.4×10^{-3}
$\mathrm{DCA}_{\mathrm{tracks}}$	0.2 cm	0.1 cm	0.5 cm	0.3×10^{-3}
$\lvert M(p+\pi^-) - M_\Lambda\rvert$	2σ	1σ	3σ	0.4×10^{-3}
DCA	0.1 cm	0.05 cm	–	0.2×10^{-3}
$n_{\mathrm{TPCClusters}}$	70	60	90	0.1×10^{-3}
$n\sigma_{\mathrm{TPC}}$	2	1.5	2.5	0.2×10^{-3}
$n\sigma_{\mathrm{TOF}}$	2.5	–	3	0.4×10^{-3}
$\lvert V_z\rvert$	8 cm	–	10 cm	0.5×10^{-3}

Table 6.4: Variations used for the evaluation of the systematic uncertainties of $\kappa_2(\Delta\Lambda)/\langle\Lambda+\bar{\Lambda}\rangle$. The systematic uncertainties assigned to each source are also reported.

Variable	Nominal	Lower var.	Upper var.	Uncertainty
$\cos\theta_p$	0.997	0.995	0.998	0.2×10^{-3}
$\mathrm{DCA}_{V^0,\mathrm{PV}}$	0.5 cm	0.2 cm	1 cm	8×10^{-3}
$\mathrm{DCA}_{\mathrm{tracks}}$	0.2 cm	0.1 cm	0.5 cm	2×10^{-3}
$\lvert M(p+\pi^-) - M_\Lambda\rvert$	2σ	1σ	3σ	1×10^{-3}
$\lvert V_z\rvert$	8 cm	–	10 cm	0.5×10^{-3}

centrality-averaged uncertainties obtained for each of the selection criteria are also reported in the last column of Table 6.3 and Table 6.4. The final uncertainty is then obtained by adding in quadrature the contributions of all sources, assuming that all sources of systematic uncertainty are fully uncorrelated. The different contributions and the total uncertainties are shown in Fig. 6.8 for each of the centrality intervals analysed. For the $\rho_{\bar{\mathrm{d}}\Delta\Lambda}$, the variations on both $\bar{\mathrm{d}}$ and Λ selection criteria determine similar systematic contributions to the total uncertainty. For $\kappa_2(\Delta\Lambda)/\langle\Lambda+\bar{\Lambda}\rangle$, the main contribution is provided by the variation of the $\mathrm{DCA}_{V^0,\mathrm{PV}}$, which is one of the most powerful selection tools to discriminate between signal and background candidates as discussed in Section 4.3.1.

6.7.2 Net-K number and net-Ξ number fluctuations

In this analysis, the total systematic uncertainty is determined by combining all possible variations of the selection criteria using a multitrial approach similar to that described in Section 5.4.1. For each multiplicity interval, the full analysis is repeated using all possible combinations of the varied selection criteria reported in Table 6.5. The resulting numbers of trials are 1800 and 30 for $\rho_{\Delta\Xi\Delta\mathrm{K}}$ and $\kappa_2(\Delta\Xi)/\langle\Xi^- + \bar{\Xi}^+\rangle$, respectively. The results of $\rho_{\Delta\Xi\Delta\mathrm{K}}$ and $\kappa_2(\Delta\Xi)/\langle\Xi^- + \bar{\Xi}^+\rangle$

Table 6.5: Variations of candidate selections applied for the evaluation of the systematic uncertainties in the analysis of net-Ξ number and net-K number fluctuation.

Variable	variations
$n_{\mathrm{TPCClusters}}$	$\geq 60,\ 70,\ 90$
$\chi^2_{\mathrm{TPC}}/n_{\mathrm{TPCClusters}}$	$< 2,\ 2.5$
|DCA|	< 0.05 (for $p_{\mathrm{T}} > 0.5$ GeV/c), 0.1 cm
$\lvert n\sigma_{\mathrm{TPC,TOF}}\rvert$	$< 2,\ 2.5,\ 3,\ 3.5,\ 4$
BDT efficiency	nominal $\pm 5\%$ ($\Delta\epsilon_{\mathrm{BDT}} = 1\%$, 10 variations)
$\lvert M(\Lambda + \pi^- + \text{c.c.}) - M_\Xi\rvert$	$< 2\sigma,\ 3\sigma,\ 4\sigma$

are obtained for each of the trials and the distribution of the results is built. The systematic uncertainty is then obtained as the standard deviation of the distribution. The mean value of the distribution is assigned as the central value of the observable. The statistical uncertainty, estimated in each trial with the subensemble method, for the combination of selections that is closest to the obtained central value, is assigned as statistical uncertainty of the final result. The multitrial distributions obtained from the analysis of the Pb–Pb data sample in each of the analysed centrality intervals are shown in Fig. 6.9 and Fig. 6.10. The central value and standard deviation of each of the distributions are reported in the text of the figure. As discussed above, the results obtained with the nominal selection are not reported in the final results. Nevertheless, they are shown in the Fig. 6.9 and Fig. 6.10: in all cases, they agree with the central value of the distributions. Similar results are also obtained from the analysis of the pp and p–Pb data samples.

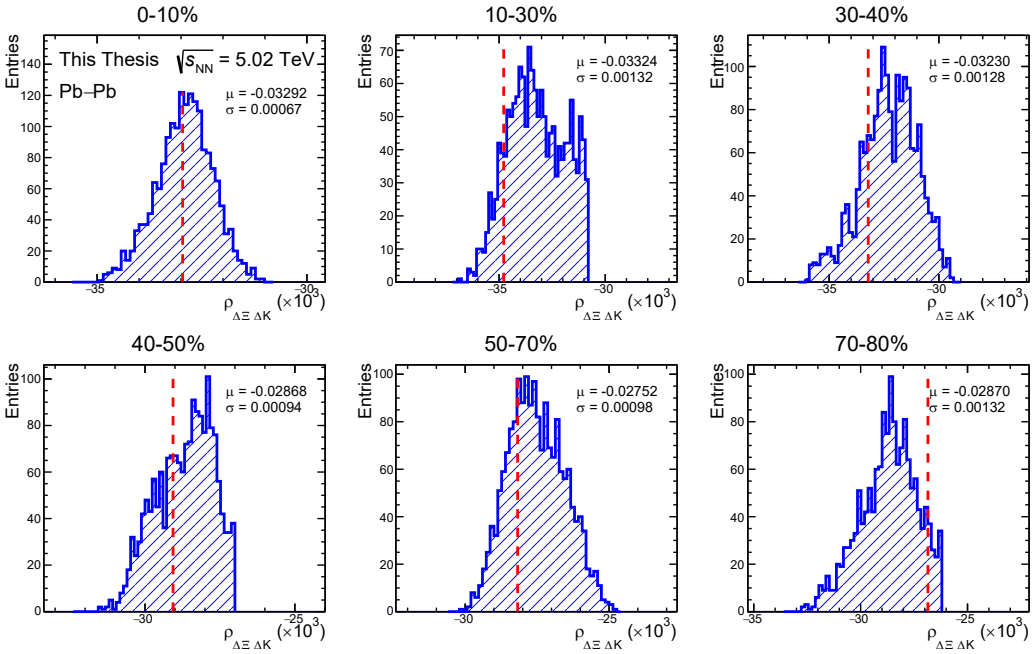

Figure 6.9: Multitrial distributions of $\rho_{\Delta\Xi\Delta K}$ in Pb–Pb collisions, for each analysed centrality interval. The results obtained with nominal selections are shown with red dotted lines.

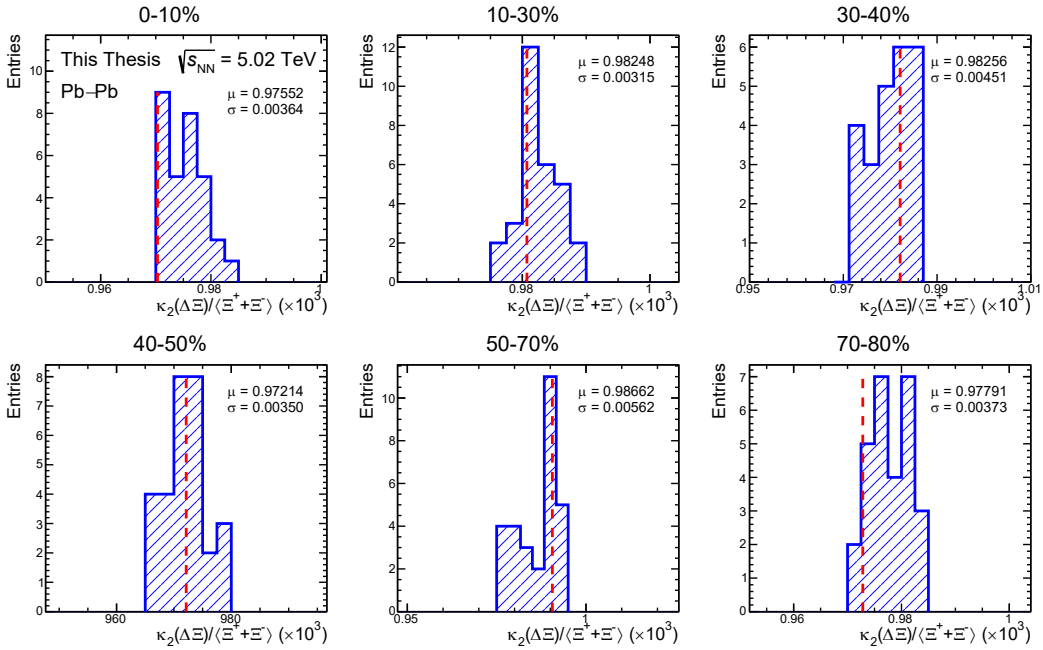

Figure 6.10: Multitrial distributions of $\kappa_2(\Delta\Xi)/\langle\Xi^- + \bar{\Xi}^+\rangle$ in Pb–Pb collisions, for each analysed centrality interval. The results obtained with nominal selections are shown with red dotted lines.

6.8 Results

In this section, the results obtained in this Thesis for event-by-event observables are presented. The results are separately presented and discussed based on the physics processes studied with these observables: namely strangeness hadronisation mechanisms on the one hand, and light nuclei formation process on the other.

6.8.1 Net-K number and net-Ξ number fluctuations

The results obtained for $\kappa_2(\Delta\Xi)/\langle\Xi^- + \bar{\Xi}^+\rangle$ and $\rho_{\Delta\Xi\Delta\mathrm{K}}$ in pp, p–Pb, and Pb–Pb collisions at $\sqrt{s_{\mathrm{NN}}} = 5.02$ TeV as a function of the average charged particle multiplicity, $\langle \mathrm{d}N_{\mathrm{ch}}/\mathrm{d}\eta\rangle$, are shown in Fig. 6.11. The charged particle multiplicity was previously measured by the ALICE Collaboration for each of the analysed colliding systems [215–217].

For both observables, the experimental results are compared with the baseline values obtained under the hypothesis of fully uncorrelated particle production. In this case, the net-particle number is the difference between two independent Poissonian random variables. The probability density function of the difference is described by the Skellam distribution. The normalized second-order cumulant of the Skellam distribution is equal to one, while the Pearson correlation coefficient of the two-dimensional distribution is zero. These baseline values are represented by black dashed lines in Fig. 6.11. In both cases, a deviation from this baseline is observed across colliding systems: this is interpreted as the effect of correlated particle production arising from quantum number conservation in the hadronisation process.

In addition, the experimental results show a continuous evolution from low-multiplicity to high-multiplicity events, across the different colliding systems. This observation suggests that strangeness hadronisation is driven by a common production mechanism going from hadronic to heavy-ion collisions. The measured observables show a decreasing trend for increasing charged-particle multiplicity, with a saturation towards semicentral Pb–Pb collisions. This is understood as an effect of the evolution of the K and Ξ p_{T} spectra, induced by dynamical multiparticle correlations, across the explored multiplicity range [21, 120–122]. This results in a shift of the average tranverse momentum, $\langle p_{\mathrm{T}}\rangle$, and hence of the bulk of the production, within the analysed p_{T} acceptance. For very low multiplicity collisions, this trend is also affected by the limited size of the produced system, resulting in a reduction

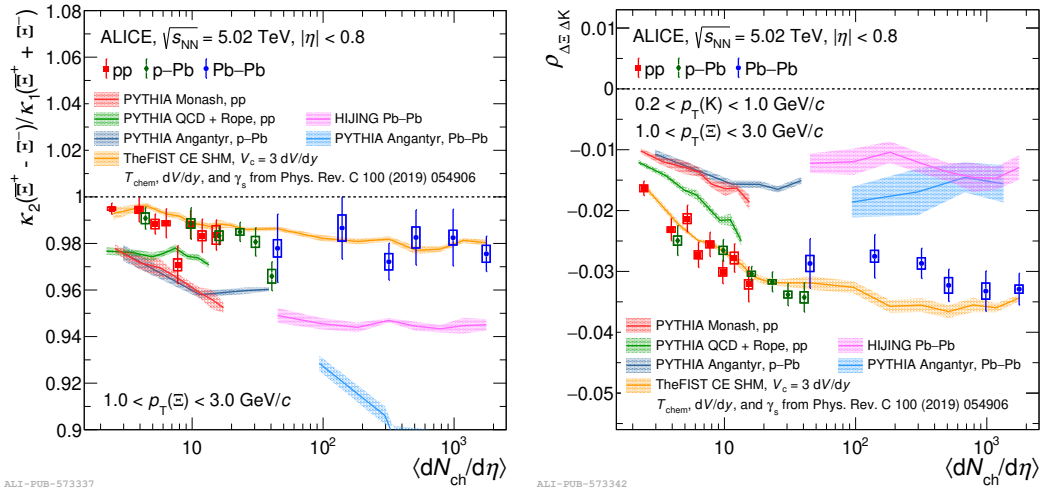

Figure 6.11: Results obtained in this Thesis for $\kappa_2(\Delta\Xi)/\langle\Xi^- + \bar{\Xi}^+\rangle$ (left) and $\rho_{\Delta\Xi\Delta K}$ (right) in pp, p–Pb, and Pb–Pb collisions, as a function of the average charged particle multiplicity. The error bars show the statistical uncertainties, while systematic uncertainties are shown as boxes. The calculations of various phenomenological models are shown as bands. The width of the band depicts the statistical uncertainty in the model calculations.

of the candidates available in the analysed phase space.

Model-to-data comparison

The experimental points are compared with the predictions of various hadronisation models. All of the models used in this Thesis are implemented as MC event generators: consequently, statistical uncertainties are assigned to the calculations shown in Fig. 6.11. A subset of these models implements the Lund string fragmentation mechanism as the underlying hadronisation process. These include different tunes and versions of PYTHIA 8 [57], depending on the colliding system analysed. For pp collisions, both the Monash tune [123] and the state-of-the-art implementation of QCD-based colour reconnection (CR) and rope hadronisation are used [63]. In the former, the model parameters are tuned on sets of measurements carried out at e^+e^- facilities; the latter includes both the rearrangement of final-state colour configurations (colour reconnection) based on the SU(3) colour algebra and the interaction among strings. This interaction leads to colour ropes formation, where the increased tension determines an enhanced production of strangeness in high-multiplicity pp collisions. For p–Pb and Pb–Pb collisions, the PYTHIA ANGANTYR model [58] is used, consisting of an extrapolation of the

string-fragmentation hadronisation to heavy-ion reactions. In addition, the HIJING generator [59], which is also based on string-fragmentation hadronisation is used for Pb–Pb collisions.

Finally, the expectations from the statistical hadronisation model (SHM) are computed using the THERMAL-FIST code [54]. The canonical ensemble (CE) SHM implementation is used, where quantum numbers are conserved exactly. In THERMAL-FIST, this is achieved by imposing global quantum number conservation across a static canonical volume, V_c, centred around midrapidity. The canonical volume is expressed in terms of the unitary volume corresponding to one rapidity unit, $\mathrm{d}V/\mathrm{d}y$. This model also includes a strangeness saturation parameter, γ_s, enabling the description of (multi)strange hadron yields in small collision systems [127]. The thermal parameters, T_{chem}, $\mathrm{d}V/\mathrm{d}y$, and γ_s, are tuned on the measurements of hadron yields as a function of $\langle \mathrm{d}N_{\mathrm{ch}}/\mathrm{d}\eta \rangle$ published by the ALICE Collaboration [127]. The MC event generator implemented in THERMAL-FIST also includes a sampling of the hadron momenta based on the Blast-Wave model [177]. The Blast-Wave parameters used in this Thesis were extracted by the ALICE Collaboration via combined fits to the light-flavour hadron p_{T} spectra measured in pp and Pb–Pb collisions [21, 218].

From the model-to-data comparison of $\kappa_2(\Delta\Xi)/\langle \Xi^- + \bar{\Xi}^+ \rangle$, shown in the left panel of Fig. 6.11, it is observed that all models that implement the Lund string fragmentation mechanism overestimate the deviation of the observable from the Skellam baseline. On the contrary, THERMAL-FIST calculation well describes the data by setting the canonical volume $V_c = 3\ \mathrm{d}V/\mathrm{d}y$. This quantity is only affected by the correlation between hadrons carrying opposite-strangeness-sign, which is present in Eq. (6.14) via the two-particle cumulant $\kappa_{11}(\bar{\Xi}^+, \Xi^-)$. Thus, a larger deviation from the uncorrelated baseline implies a stronger strange-antistrange hadron correlation, which in turn hints to a shorter-rapidity-range correlation. Consequently, the experimental observations are consistent with the hypothesis of strangeness correlations over a large rapidity range, from low-multiplicity pp to the most central Pb–Pb collisions.

By analysing $\rho_{\Delta\Xi\Delta\mathrm{K}}$, it is observed that the models relying on string fragmentation underestimate the anticorrelation observed in the data across different colliding systems, while the CE SHM calculations are in agreement with the data. Contrarily to the normalised second-order cumulant, the Pearson correlation coefficient of net-particle numbers is also sensitive to the same-strangeness-sign correlation,

which is introduced by the two-particle cumulant terms in Eq. (6.15). Hence, the observed discrepancy between the string-fragmentation expectation and the data hints to the existence of a same-strangeness-sign correlation in the data. This effect is intrinsically included in the CE SHM implementation of THERMAL-FIST by the requirement of the exact quantum number conservation over a large finite volume.

The deviation between the state-of-the-art PYTHIA 8 calculations in pp collisions and the experimental results is also quantified by a χ^2 test. The test is carried out computing a combined χ^2 for the two observables analysed, i.e., $\chi^2 = \chi^2_\rho + \chi^2_{\kappa_2/\kappa_1}$. For the χ^2 calculation, the systematic uncertainties are treated as fully correlated with the charged-particle multiplicity, using a conservative approach. The separation between the model calculations and the experimental data is then experessed in terms of standard deviations. A discrepancy of 7.5σ is obtained with this procedure. This observation hints to a shortcoming of the PYTHIA 8 to describe the correlations observed in the data. This effect was also observed, limited to opposite-strangeness-sign correlations, in previous studies of angular correlations between identified (multi)strange hadrons [219].

Estimation of the canonical volume

The V_c parameter of THERMAL-FIST is extracted from the experimental results obtained in Pb–Pb collisions by a combined fit of the $\kappa_2(\Delta\Xi)/\langle\Xi^- + \bar{\Xi}^+\rangle$ and $\rho_{\Delta\Xi\Delta\mathrm{K}}$ data with the model calculations. The THERMAL-FIST calculations are repeated for several values of V_c in the range $\mathrm{d}V/\mathrm{d}y \leq V_c \leq 4\ \mathrm{d}V/\mathrm{d}y$. For this fit, the temperature is fixed for all multplicities to $T_{\mathrm{chem}} = 155$ TeV and the strangeness saturation parameter is fixed to $\gamma_s = 1$. These parameters provide a good description of the hadron yields observed in Pb–Pb collisions at the LHC [127]. A combined χ^2 is determined for each of V_c value by comparing the data and model calculations for both of the analysed observables. The resulting χ^2 profile is shown in Fig. 6.12. For the χ^2 calculation, only statistical uncertainties are used: the best V_c is determined by minimising the χ^2 obtained. The systematic uncertainties are treated as fully-correlated with multiplicity. The effect on the extracted V_c is assessed by reapplying the fit procedure to the data points coherently shifted both upwards and downwards by the systematic uncertainty value. The half-difference between the two values extracted is assigned as systematic uncertainty of V_c.

The obtained result, $V_c = 3.19 \pm 0.14\ \mathrm{d}V/\mathrm{d}y$, is reported with the full uncertainty, computed as the sum in quadrature of the statistical and systematic uncertainties.

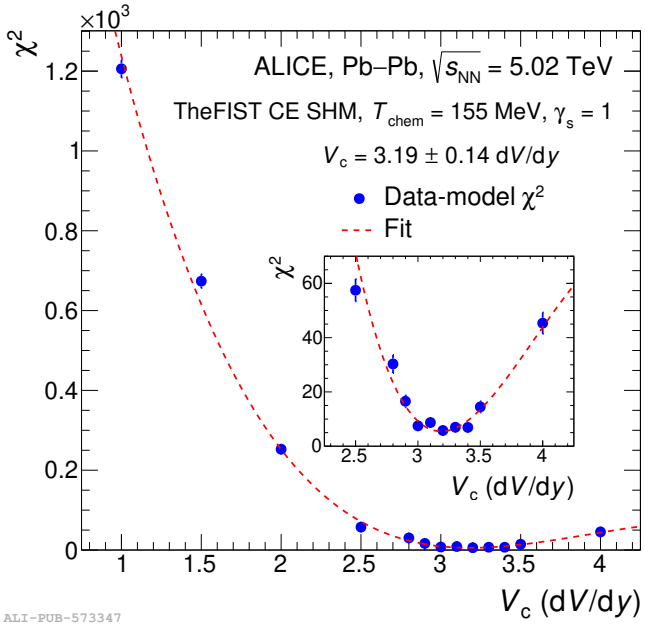

Figure 6.12: χ^2 profile obtained from the combined fit of $\kappa_2(\Delta\Xi)/\langle\Xi^- + \bar{\Xi}^+\rangle$ and $\rho_{\Delta\Xi\Delta K}$ with THREMAL-FIST calculations, in Pb–Pb collisions. The error bars on the χ^2 estimates is obtained from the propagation of the model uncertainties. The χ^2 values obtained from the V_c scan are fitted with a quartic function, shown as a dashed red line. The inset shows a close up of the χ^2 profile in the minimum region.

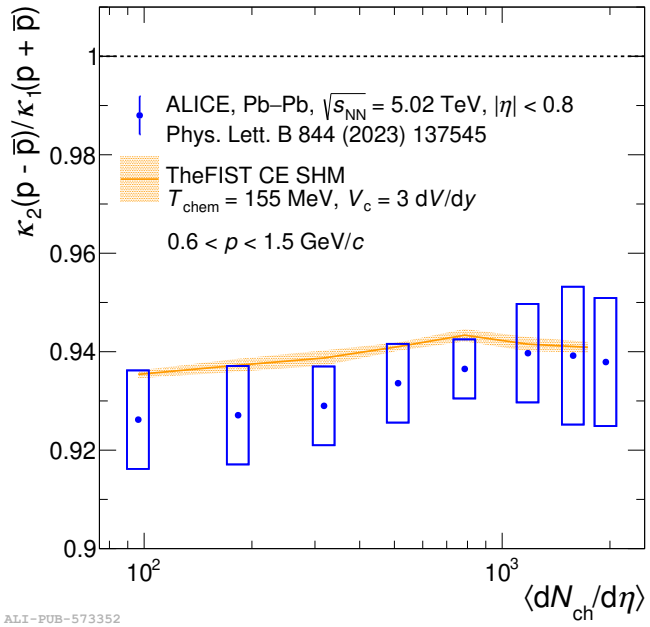

Figure 6.13: Comparison between the $\kappa_2(\Delta \mathrm{p})/\langle \mathrm{p} + \bar{\mathrm{p}} \rangle$ measured by the ALICE Collaboration [143] and the expectations of THERMAL-FIST obtained in this Thesis setting $V_c = 3$ dV/dy.

This result is in agreement with CE SHM analyses of the Ξ/π yield ratio measured in different colliding system by the ALICE Collaboration [127]. In addition, the obtained volume is consistent with the event-by-event fluctuation observations made for the net-proton number in Pb–Pb collisions by the ALICE Collaboration [143]. The comparison between the experimental data and the THERMAL-FIST expectations for $\kappa_2(\Delta \mathrm{p})/\langle \mathrm{p} + \bar{\mathrm{p}} \rangle$ are shown in Fig. 6.13. The model calculations are obtained using $V_c = 3$ dV/dy for the conservation of the baryon quantum number. This observation hints to a common hadronisation mechanism for light and strange hadrons, where the conservation of quantum numbers takes place across a large volume of about 3 units of rapidity. These conclusions are also extended to the event-by-event fluctuations of net-Λ number, as it is discussed in Section 6.8.2.

6.8.2 $\bar{\mathrm{d}}$ number and net-Λ number fluctuations

The results obtained in this Thesis for $\kappa_2(\Delta\Lambda)/\langle \Lambda + \bar{\Lambda} \rangle$ and $\rho_{\bar{\mathrm{d}}\Delta\Lambda}$ in Pb–Pb collisions at $\sqrt{s_{\mathrm{NN}}} = 5.02$ TeV as a function of centrality are shown in Fig. 6.14. As expected from quantum number conservation, the two measured observables deviate from

the Skellam baseline. The size of the deviation is related to the strength of the correlation, as it can be obtained from Eq. (6.16) and Eq. (6.14) (modified for the net-Λ case).

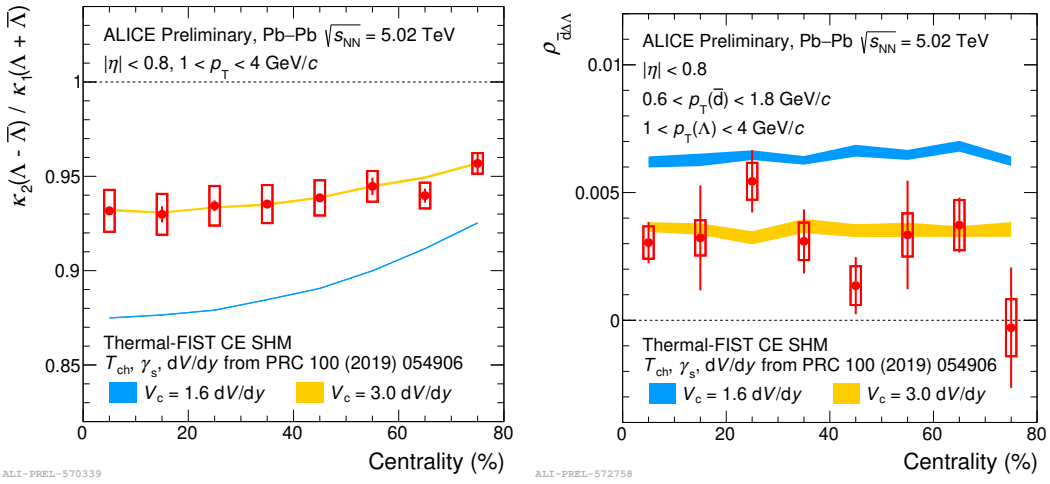

Figure 6.14: Trend of the values of $\kappa_2(\Delta\Lambda)/\langle\Lambda+\bar{\Lambda}\rangle$ (left) and $\rho_{\bar{\mathrm{d}}\Delta\Lambda}$ (right) in Pb–Pb collisions, for different centrality classes. The error bars show the statistical uncertainties, while systematic uncertainties are shown as boxes. The expectations of the Thermal-FIST SHM for different canonical volumes are depicted as bands.

Model-to-data comparison

Similarly to what is presented in Section 6.8.1, the experimental results are compared with different model calculations. In this case, the THERMAL-FIST model is used with two configurations of V_c: namely, 1.6 dV/dy and 3 dV/dy. The value $V_c = 1.6$ dV/dy was obtained from the analysis of the Pearson correlation coefficient of the $\bar{\mathrm{d}}$ number and $\bar{\mathrm{d}}$ number, $\rho_{\bar{\mathrm{d}}\bar{\mathrm{p}}}$ [135]. On the other hand, the $V_c = 3$ dV/dy value is the reference one obtained from the analysis of light-flavour hadron fluctuation observables, as shown in Section 6.8.1. The chemical freeze-out temperature is set to $T_{\mathrm{chem}} = 155$ MeV, while the dV/dy and γ_s parameterisations are extracted from Reference [127].

The ratio $\kappa_2(\Delta\Lambda)/\langle\Lambda+\bar{\Lambda}\rangle$, reported on the left of Fig. 6.14, is well described by the THERMAL-FIST calculations using a canonical volume of 3 dV/dy. This observation is in agreement with the other measurements carried out for net-p, net-K, and Ξ discussed in Section 6.8.1. This confirms that quantum numbers associated to light-flavour hadrons are conserved over a large volume in Pb–Pb collisions. The evolution of the cumulant ratio as a function of centrality is in agreement with

the change of the $\langle p_{\mathrm{T}} \rangle$ of produced Λ within the studied p_{T} acceptance across the analysed centrality range.

The experimental results of $\rho_{\bar{\mathrm{d}}\Delta\Lambda}$, reported on the right of Fig. 6.14,are well described by the larger V_c setting, while the calculations carried out for $V_c = 1.6\ \mathrm{d}V/\mathrm{d}y$ show a deviation from the data. This discrepancy is quantified by a χ^2 test, assuming that systematic uncertainties are fully correlated with centrality. The discrepancy, expressed in terms of standard deviations, is found to be 2.94σ. On the contrary, the computations obtained with $V_c = 3\ \mathrm{d}V/\mathrm{d}y$ are compatible with the data within 1σ. As discussed in Section 6.1, this observable is sensitive to the hadron production mechanisms underlying the nuclear formation process, i.e., it probes the effects of baryon number conservation in the production of the constituents of light nuclei. Consequently, the measurement presented in this Thesis suggests that a common hadronisation mechanism determines the production of light flavour particles, including the antideuteron constituents. This implies that the stronger correlation observed in $\rho_{\bar{\mathrm{d}}\bar{\mathrm{p}}}$ compared to $\rho_{\bar{\mathrm{d}}\Delta\Lambda}$, corresponding to a smaller V_c value in the THERMAL-FIST model, is induced by the nuclear formation process acting on top of the nucleon production. For instance, this could hint to the presence of nuclear coalescence effects inducing local correlations among nucleons on top of the correlations due to the quantum number conservation in the nucleon production itself.

Chapter 7

Conclusions

This Thesis aims at exploring two aspects of light-flavour hadron production in hadronic and heavy-ion collisions at the LHC. On the one hand, the antimatter-to-matter balance of the system formed in Pb–Pb collisions was characterised by extracting chemical potentials from measurements of antiparticle-to-particle yield ratios of different hadron species. On the other, the hadronisation mechanism leading to the formation of (multi)strange hadrons and light antinuclei was investigated through measurements of event-by-event hadron multiplicity fluctuations. On a more fundamental level, these studies probe the underlying quantum-number conservation mechanism in both the collision and the hadronisation processes. A summary of the main results obtained in this Thesis is presented in the following.

The baryon-number and electric-charge chemical potentials, μ_B and μ_Q, were extracted from yield ratios of antiparticles and respective particles measured in Pb–Pb collisions at $\sqrt{s_{\rm NN}} = 5.02$ TeV. The measurement was carried out in classes of centrality across the range 0-90%. The values of μ_B and μ_Q extracted with fits based on the GCE SHM are compatible with zero across centrality, indicating that the medium formed in such collisions is baryon-symmetric and electrically neutral independently of the collision geometry. The centrality-averaged values obtained are $\mu_B = 0.71 \pm 0.45$ MeV and $\mu_Q = -0.18 \pm 0.90$ MeV. These results pose tight constraints on baryon-number transport mechanisms, such as the baryon-junction model, in the TeV energy scale. In Fig. 7.1, the μ_B estimate determined in this Thesis is shown in red along with the results obtained in previous works. The measurements presented in this Thesis confirm the decreasing trend of μ_B, and

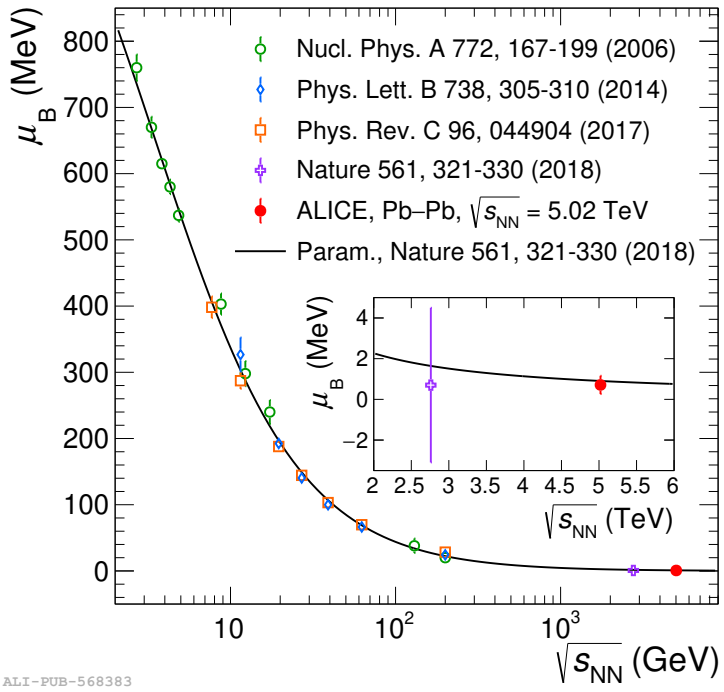

Figure 7.1: Baryon chemical potential, μ_B, extracted as a function of the centre-of-mass energy per nucleon pair, $\sqrt{s_{\rm NN}}$, from the SHM analysis of hadron yields and yield ratios measured in Au–Au and Pb–Pb collisions at the AGS (E802, E866, E877, E895, E896, E917 Collaborations), SPS (NA44, NA49, NA47 Collaborations), RHIC (BRAHMS, PHENIX, STAR Collaboration), and LHC (ALICE Collaboration) facilities [111, 113, 114]. The phenomenological parameterization of $\mu_B(\sqrt{s_{\rm NN}})$ is shown in black [19]. The comparison between the two results obtained at the LHC is shown in the inset of the figure [19]

hence of baryon-antibaryon number imbalance, with increasing centre-of-mass energy. Moreover, the results extracted in this Thesis improve by more than a factor of eight the precision of the measurement when compared to the previous estimate at the LHC. This is due to the full treatment of correlated and uncorrelated systematic uncertainties in the present measurement. The observation of nuclear transparency up to central Pb–Pb collisions enables the measurement of event-by-event fluctuation observables, as the matter-antimatter balance is a condition required to decouple the fluctuations originating in the hadronisation dynamics from those arising in the event multiplicity variations within the fixed multiplicity intervals employed in the analysis.

In this Thesis, the normalised second order cumulants of both the net-Ξ number

and net-Λ number were determined. In addition, the Pearson correlation coefficient between the net-K and net-Ξ numbers and the one between the net-Λ and antideuteron numbers were measured. The analyses were carried out in Pb–Pb collisions at $\sqrt{s_{\rm NN}} = 5.02$ TeV for all the species. For kaons and Ξ, the measurements were also extended to pp and p–Pb collisions. The results are shown in Fig. 7.2, as a function of either the centrality or charged-particle multiplicity of the collision. All of the obtained results exhibit deviations from the uncorrelated-particle-production baseline: this is understood as an effect of global quantum-number conservation in the system. By comparing the experimental results with different model calculations, it is observed that the data are consistent with the expectations of the canonical ensemble statistical hadronisation model (CE SHM) as implemented in THERMAL-FIST [54], suggesting that both baryon-number and strangeness are correlated over a conservation volume extending over about three rapidity units. This picture consistently holds both for small and large colliding systems. For the strangeness sector in small systems, the state-of-the-art string fragmentation implementation of PYTHIA 8 deviates from the data, suggesting both that the correlation range of strangeness is larger than predicted by the string breaking mechanism and that a strange-strange correlation, as predicted by the CE SHM approach, might exist in nature.

The studies presented in this Thesis will be further expanded with the data collected by the ALICE Collaboration in the ongoing physics data taking run (Run 3) of the LHC. Specifically, the large data sample of Pb–Pb collisions to be collected over the whole Run 3, amounting to an integrated luminosity of $L_{\rm int} \approx 5$ nb^{-1}, will enable a more precise determination of the antiparticle-to-particle imbalance of light nuclei. This will imply an improved constraint on the baryon-number asymmetry of the system using baryon-rich species. Concerning event-by-event fluctuation measurements, the next frontier is measuring observables that, unlike those presented in this work, could separately probe same- and opposite-quantum-number correlations. This would provide a direct probe for the existence of canonical-like quantum-number conservation in small collision systems. The major limitation for these measurements is posed by volume fluctuation effects convoluted with the correlations arising from the hadronisation process. The new larger minimum-bias data samples collected with proton beams, corresponding to $L_{\rm int} \approx O(5$ pb$^{-1})$, could be used to investigate quantum-number fluctuations via rarer probes, such as $\Omega^{\pm}$ baryons, as they are less affected by volume fluctuations.

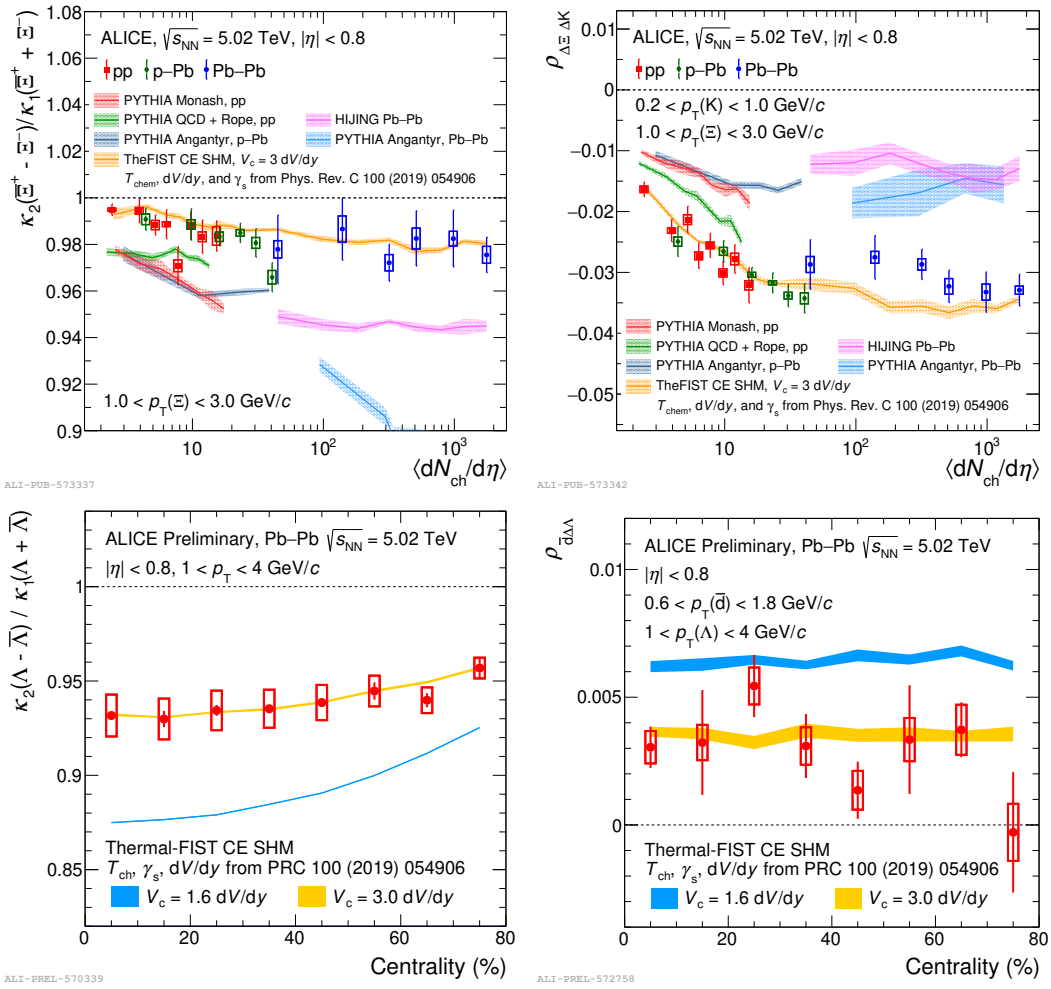

Figure 7.2: First row: results obtained in this Thesis for $\kappa_2(\Delta\Xi)/\langle\Xi^- + \bar{\Xi}^+\rangle$ (left) and $\rho_{\Delta\Xi\Delta\mathrm{K}}$ (right) in pp, p–Pb, and Pb–Pb collisions, as a function of the average charged particle multiplicity. Second row: results obtained in this Thesis for $\kappa_2(\Delta\Lambda)/\langle\Lambda + \bar{\Lambda}\rangle$ (left) and $\rho_{\bar{\mathrm{d}}\Delta\Lambda}$ (right) in Pb–Pb collisions, for different centrality classes. The error bars show the statistical uncertainties, while systematic uncertainties are shown as boxes. The calculations of various phenomenological models are shown as bands. The width of the band depicts the statistical uncertainty in the model calculations.

List of Figures

List of Tables

Bibliography

[1] Shreyasi Acharya et al. "Measurements of Chemical Potentials in Pb-Pb Collisions at sNN=5.02 TeV". In: *Phys. Rev. Lett.* 133.9 (2024), p. 092301. DOI: 10.1103/PhysRevLett.133.092301. arXiv: 2311.13332 [nucl-ex].

[2] Shreyasi Acharya et al. "Probing Strangeness Hadronization with Event-by-Event Production of Multistrange Hadrons". In: *Phys. Rev. Lett.* 134.2 (2025), p. 022303. DOI: 10.1103/PhysRevLett.134.022303. arXiv: 2405.19890 [nucl-ex].

[3] T. Nakano and K. Nishijima. "Charge Independence for V-particles". In: *Prog. Theor. Phys.* 10 (1953), pp. 581–582. DOI: 10.1143/PTP.10.581.

[4] Murray Gell-Mann. "A Schematic Model of Baryons and Mesons". In: *Phys. Lett.* 8 (1964), pp. 214–215. DOI: 10.1016/S0031-9163(64)92001-3.

[5] H. David Politzer. "Reliable Perturbative Results for Strong Interactions?" In: *Phys. Rev. Lett.* 30 (1973). Ed. by J. C. Taylor, pp. 1346–1349. DOI: 10.1103/PhysRevLett.30.1346.

[6] David J. Gross and Frank Wilczek. "Ultraviolet Behavior of Nonabelian Gauge Theories". In: *Phys. Rev. Lett.* 30 (1973). Ed. by J. C. Taylor, pp. 1343–1346. DOI: 10.1103/PhysRevLett.30.1343.

[7] Steven Weinberg. "A Model of Leptons". In: *Phys. Rev. Lett.* 19 (1967), pp. 1264–1266. DOI: 10.1103/PhysRevLett.19.1264.

[8] Chen-Ning Yang and Robert L. Mills. "Conservation of Isotopic Spin and Isotopic Gauge Invariance". In: *Phys. Rev.* 96 (1954). Ed. by Jong-Ping Hsu and D. Fine, pp. 191–195. DOI: 10.1103/PhysRev.96.191.

[9] S. Navas et al. "Review of particle physics". In: *Phys. Rev. D* 110.3 (2024), p. 030001. DOI: 10.1103/PhysRevD.110.030001.

[10] Ulrich W. Heinz. "Concepts of Heavy-Ion Physics". In: (2004). arXiv: hep-ph/0407360.

[11] Cheuk-Yin Wong. *Introduction to High-Energy Heavy Ion Collisions*. Singapore: World Scientific, 1994.

[12] Y. Aoki et al. "The Order of the quantum chromodynamics transition predicted by the standard model of particle physics". In: *Nature* 443 (2006), pp. 675–678. DOI: 10.1038/nature05120. arXiv: hep-lat/0611014.

[13] A. Bazavov et al. "Equation of state in (2+1)-flavor QCD". In: *Phys. Rev. D* 90 (2014), p. 094503. DOI: 10.1103/PhysRevD.90.094503. arXiv: 1407.6387 [hep-lat].

[14] Claudia Ratti. "Equation of state for QCD from lattice simulations". In: *Prog. Part. Nucl. Phys.* 129 (2023), p. 104007. DOI: 10.1016/j.ppnp.2022.104007.

[15] M. S. Abdallah et al. "Measurements of Proton High Order Cumulants in $\sqrt{s_{\rm NN}} = 3$ GeV Au+Au Collisions and Implications for the QCD Critical Point". In: *Phys. Rev. Lett.* 128.20 (2022), p. 202303. DOI: 10.1103/PhysRevLett.128.202303. arXiv: 2112.00240 [nucl-ex].

[16] Rajeev S. Bhalerao. "Relativistic Heavy-Ion Collisions". In: (2014). arXiv: 1404.3294.

[17] Michael L. Miller et al. "Glauber Modeling in High-Energy Nuclear Collisions". In: *Annual Review of Nuclear and Particle Science* 57 (2007), pp. 205–243.

[18] Peter Braun-Munzinger and Benjamin Dönigus. "Loosely-bound objects produced in nuclear collisions at the LHC". In: *Nuclear Physics A* 987 (2019).

[19] Anton Andronic et al. "Decoding the phase structure of QCD via particle production at high energy". In: *Nature* 561.7723 (2018), pp. 321–330. DOI: 10.1038/s41586-018-0491-6. arXiv: 1710.09425 [nucl-th].

[20] ALICE Collaboration. "Centrality dependence of π, K, and p production in Pb-Pb collisions at $\sqrt{s_{\rm NN}} = 2.76$ TeV". In: *Phys. Rev. C* 88 (2013), p. 044910.

[21] Shreyasi Acharya et al. "Production of charged pions, kaons, and (anti-)protons in Pb-Pb and inelastic *pp* collisions at $\sqrt{s_{\mathrm{NN}}} = 5.02$ TeV". In: *Phys. Rev. C* 101.4 (2020), p. 044907. DOI: 10.1103/PhysRevC.101.044907. arXiv: 1910.07678 [nucl-ex].

[22] ALICE Collaboration. "Transverse Momentum Distribution and Nuclear Modification Factor of Charged Particles in p+Pb Collisions at $\sqrt{s_{\mathrm{NN}}}$=5.02 TeV". In: *Phys. Rev. Lett.* 110 (2013), p. 082302.

[23] S. Acharya et al. "Transverse momentum spectra and nuclear modification factors of charged particles in pp, p-Pb and Pb-Pb collisions at the LHC". In: *JHEP* 11 (2018), p. 013. DOI: 10.1007/JHEP11(2018)013. arXiv: 1802.09145 [nucl-ex].

[24] Panagiota Foka and Małgorzata Janik. "An overview of experimental results from ultra-relativistic heavy-ion collisions at the CERN LHC: Hard probes". In: *Reviews in Physics* 1 (2016).

[25] J. W. Cronin et al. "Production of hadrons at large transverse momentum at 200, 300, and 400 GeV". In: *Phys. Rev. D* 11 (1975), pp. 3105–3123.

[26] ALICE Collaboration. "Measurement of D^0, D^+, D^{*+} and D_s^+ production in Pb-Pb collisions at $\sqrt{s_{\mathrm{NN}}} = 5.02$ TeV". In: *JHEP* 10 (2018), p. 174. arXiv: 1804.09083 [nucl-ex].

[27] CMS Collaboration. "Observation and studies of jet quenching in PbPb collisions at $\sqrt{s_{\mathrm{NN}}} = 2.76$ TeV". In: *Phys. Rev. C* 84 (2011), p. 024906.

[28] T. Matsui and H. Satz. "J/ψ Suppression by Quark-Gluon Plasma Formation". In: *Phys. Lett. B* 178 (1986), pp. 416–422.

[29] Armen Tumasyan et al. "Observation of the $\Upsilon(3S)$ Meson and Suppression of Υ States in Pb-Pb Collisions at $\sqrt{s_{\mathrm{NN}}} = 5.02$ TeV." In: *Phys. Rev. Lett.* 133.2 (2024), p. 022302. DOI: 10.1103/PhysRevLett.133.022302. arXiv: 2303.17026 [hep-ex].

[30] Shreyasi Acharya et al. "ψ(2S) Suppression in Pb-Pb Collisions at the LHC". In: *Phys. Rev. Lett.* 132.4 (2024), p. 042301. DOI: 10.1103/PhysRevLett.132.042301. arXiv: 2210.08893 [nucl-ex].

[31] Fred Cooper and Graham Frye. "Single-particle distribution in the hydrodynamic and statistical thermodynamic models of multiparticle production". In: *Phys. Rev. D* 10 (1974), pp. 186–189.

[32] K. Werner et al. "Analysing radial flow features in p-Pb and p-p collisions at several TeV by studying identified particle production in EPOS3". In: *Phys. Rev. C* 89.6 (2014), p. 064903. DOI: 10.1103/PhysRevC.89.064903. arXiv: 1312.1233 [nucl-th].

[33] ALICE Collaboration. "Anisotropic Flow of Charged Particles in Pb-Pb Collisions at $\sqrt{s_{\mathrm{NN}}} = 5.02$ TeV". In: *Phys. Rev. Lett.* 116 (2016), p. 132302.

[34] Ulrich Heinz, Chun Shen, and Huichao Song. "The viscosity of quark-gluon plasma at RHIC and the LHC". In: *AIP Conf. Proc.* 1441.1 (2012). Ed. by Stephen G. Steadman and George S. F. Stephans, pp. 766–770. DOI: 10.1063/1.3700674. arXiv: 1108.5323 [nucl-th].

[35] P. F. Kolb et al. "Elliptic flow at SPS and RHIC: From kinetic transport to hydrodynamics". In: *Phys. Lett. B* 500 (2001), pp. 232–240. DOI: 10.1016/S0370-2693(01)00079-X. arXiv: hep-ph/0012137.

[36] Fermi, Enrico. "High Energy Nuclear Events". In: *Progress of Theoretical Physics* 5 (1950), pp. 570–583.

[37] Rolf Hagedorn. "Statistical Thermodynamics of Strong Interactions at High Energies". In: *Nuovo Cimento, Suppl.* 3 (1965), pp. 147–186.

[38] Francesco Becattini and R. Fries. "The QCD confinement transition: Hadron formation". In: *Landolt-Bornstein* 23 (2010). Ed. by R. Stock, p. 208. DOI: 10.1007/978-3-642-01539-7_8. arXiv: 0907.1031 [nucl-th].

[39] Peter Braun-Munzinger and Johanna Stachel. "Dynamics of ultrarelativistic nuclear collisions with heavy beams: An Experimental overview". In: *Nucl. Phys. A* 638 (1998). Ed. by T. Hatsuda et al., pp. 3–18. DOI: 10.1016/S0375-9474(98)00342-X. arXiv: nucl-ex/9803015.

[40] J. Cleymans and K. Redlich. "Unified description of freezeout parameters in relativistic heavy ion collisions". In: *Phys. Rev. Lett.* 81 (1998), pp. 5284–5286. DOI: 10.1103/PhysRevLett.81.5284. arXiv: nucl-th/9808030.

[41] Peter Braun-Munzinger, Krzysztof Redlich, and Johanna Stachel. "Particle production in heavy ion collisions". In: *Quark–Gluon Plasma 3*. World Scientific, 2004, pp. 491–599. DOI: 10.1142/9789812795533_0008. arXiv: nucl-th/0304013.

[42] J. Cleymans et al. "Comparison of chemical freeze-out criteria in heavy-ion collisions". In: *Phys. Rev. C* 73 (2006), p. 034905. DOI: 10.1103/PhysRevC.73.034905. arXiv: hep-ph/0511094.

[43] P. Braun-Munzinger and J. Wambach. "The Phase Diagram of Strongly-Interacting Matter". In: *Rev. Mod. Phys.* 81 (2009), pp. 1031–1050. DOI: 10.1103/RevModPhys.81.1031. arXiv: 0801.4256 [hep-ph].

[44] Volodymyr Vovchenko and Horst Stoecker. "Examination of the sensitivity of the thermal fits to heavy-ion hadron yield data to the modeling of the eigenvolume interactions". In: *Phys. Rev. C* 95.4 (2017), p. 044904. DOI: 10.1103/PhysRevC.95.044904. arXiv: 1606.06218 [hep-ph].

[45] Peter Braun-Munzinger et al. "Properties of hot and dense matter from relativistic heavy ion collisions". In: *Phys. Rept.* 621 (2016), pp. 76–126. DOI: 10.1016/j.physrep.2015.12.003. arXiv: 1510.00442 [nucl-th].

[46] M. Hauer, V. V. Begun, and M. I. Gorenstein. "Multiplicity Distributions in Canonical and Microcanonical Statistical Ensembles". In: *Eur. Phys. J. C* 58 (2008), pp. 83–110. DOI: 10.1140/epjc/s10052-008-0724-1. arXiv: 0706.3290 [nucl-th].

[47] R. Hagedorn and K. Redlich. "Statistical Thermodynamics in Relativistic Particle and Ion Physics: Canonical or Grand Canonical?" In: *Z. Phys. C* 27 (1985), p. 541. DOI: 10.1007/BF01436508.

[48] K. Redlich et al. "Conservation laws and particle production in heavy ion collisions". In: *AIP Conf. Proc.* 594.1 (2002). Ed. by I. T. Cheon et al., pp. 318–329. DOI: 10.1063/1.1425518. arXiv: hep-ph/0110337.

[49] Granddon D. Yen et al. "Excluded volume hadron gas model for particle number ratios in A+A collisions". In: *Phys. Rev. C* 56 (1997), pp. 2210–2218. DOI: 10.1103/PhysRevC.56.2210. arXiv: nucl-th/9711062.

[50] Anton Andronic et al. "The thermal proton yield anomaly in Pb-Pb collisions at the LHC and its resolution". In: *Phys. Lett. B* 792 (2019), pp. 304–309. DOI: 10.1016/j.physletb.2019.03.052. arXiv: 1808.03102 [hep-ph].

[51] Volodymyr Vovchenko et al. "Connecting fluctuation measurements in heavy-ion collisions with the grand-canonical susceptibilities". In: *Phys. Lett. B* 811 (2020), p. 135868. DOI: 10.1016/j.physletb.2020.135868. arXiv: 2003.13905 [hep-ph].

[52] P. Braun-Munzinger, A. Rustamov, and J. Stachel. "Bridging the gap between event-by-event fluctuation measurements and theory predictions in relativistic nuclear collisions". In: *Nucl. Phys. A* 960 (2017), pp. 114–130. DOI: 10.1016/j.nuclphysa.2017.01.011. arXiv: 1612.00702 [nucl-th].

[53] Volodymyr Vovchenko, Roman V. Poberezhnyuk, and Volker Koch. "Cumulants of multiple conserved charges and global conservation laws". In: *JHEP* 10 (2020), p. 089. DOI: 10.1007/JHEP10(2020)089. arXiv: 2007.03850 [hep-ph].

[54] Volodymyr Vovchenko and Horst Stoecker. "Thermal-FIST: A package for heavy-ion collisions and hadronic equation of state". In: *Comput. Phys. Commun.* 244 (2019), pp. 295–310. DOI: 10.1016/j.cpc.2019.06.024. arXiv: 1901.05249 [nucl-th].

[55] Peter Braun-Munzinger et al. "The imprint of conservation laws on correlated particle production". In: (Dec. 2023). arXiv: 2312.15534 [nucl-th].

[56] Bo Andersson, G. Gustafson, and B. Soderberg. "A General Model for Jet Fragmentation". In: *Z. Phys. C* 20 (1983), p. 317. DOI: 10.1007/BF01407824.

[57] Christian Bierlich et al. "A comprehensive guide to the physics and usage of PYTHIA 8.3". In: (Mar. 2022). DOI: 10.21468/SciPostPhysCodeb.8. arXiv: 2203.11601 [hep-ph].

[58] Christian Bierlich et al. "The Angantyr model for Heavy-Ion Collisions in PYTHIA8". In: *JHEP* 10 (2018), p. 134. DOI: 10.1007/JHEP10(2018)134. arXiv: 1806.10820 [hep-ph].

[59] Xin-Nian Wang and Miklos Gyulassy. "HIJING: A Monte Carlo model for multiple jet production in p p, p A and A A collisions". In: *Phys. Rev. D* 44 (1991), pp. 3501–3516. DOI: 10.1103/PhysRevD.44.3501.

[60] E. Eichten et al. "Charmonium: The Model". In: *Phys. Rev. D* 17 (1978). [Erratum: Phys.Rev.D 21, 313 (1980)], p. 3090. DOI: 10.1103/PhysRevD.17.3090.

[61] Christian Bierlich. "Soft modifications to jet fragmentation in high energy proton–proton collisions". In: *Phys. Lett. B* 795 (2019), pp. 194–199. DOI: 10.1016/j.physletb.2019.06.018. arXiv: 1901.07447 [hep-ph].

[62] Christian Bierlich et al. "Effects of Overlapping Strings in pp Collisions". In: *JHEP* 03 (2015), p. 148. DOI: 10.1007/JHEP03(2015)148. arXiv: 1412.6259 [hep-ph].

[63] Jesper Christiansen and Peter Skands. "String Formation Beyond Leading Colour". In: *JHEP* 08 (2015), p. 003. DOI: 10.1007/JHEP08(2015)003. arXiv: 1505.01681 [hep-ph].

[64] G. C. Rossi and G. Veneziano. "A Possible Description of Baryon Dynamics in Dual and Gauge Theories". In: *Nucl. Phys. B* 123 (1977), pp. 507–545. DOI: 10.1016/0550-3213(77)90178-X.

[65] S. Wheaton and J. Cleymans. "THERMUS: A Thermal model package for ROOT". In: *Comput. Phys. Commun.* 180 (2009), pp. 84–106. DOI: 10.1016/j.cpc.2008.08.001. arXiv: hep-ph/0407174.

[66] Giorgio Torrieri et al. "SHARE: Statistical hadronization with resonances". In: *Comput. Phys. Commun.* 167 (2005), pp. 229–251. DOI: 10.1016/j.cpc.2005.01.004. arXiv: nucl-th/0404083.

[67] "The ALICE experiment – A journey through QCD". In: (Nov. 2022). arXiv: 2211.04384 [nucl-ex].

[68] Rene Brun and Fons Rademakers. "ROOT — An object oriented data analysis framework". In: *Nuclear Instruments and Methods in Physics Research Section A: Accelerators, Spectrometers, Detectors and Associated Equipment* 389 (1997), pp. 81–86.

[69] Yacine Mehtar-Tani and Georg Wolschin. "Baryon stopping and saturation physics in relativistic collisions". In: *Phys. Rev. C* 80 (2009), p. 054905. DOI: 10.1103/PhysRevC.80.054905. arXiv: 0907.5444 [hep-ph].

[70] A. Capella and B. Z. Kopeliovich. "Novel mechanism of nucleon stopping in heavy ion collisions". In: *Phys. Lett. B* 381 (1996), pp. 325–330. DOI: 10.1016/0370-2693(96)00533-3. arXiv: hep-ph/9603279.

[71] S. E. Vance, M. Gyulassy, and X. N. Wang. "Baryon junction stopping at the SPS and RHIC via HIJING/B". In: *Nucl. Phys. A* 638 (1998). Ed. by Wolfgang Bauer and Hans-Georg Ritter, pp. 395C–398C. DOI: 10.1016/S0375-9474(98)00394-7. arXiv: nucl-th/9802036.

[72] V. Topor Pop et al. "Stopping power from SPS to LHC energies". In: *J. Phys. G* 35.5 (2008). Ed. by N. Armesto et al., p. 054001.15. DOI: 10.1088/0954-3899/35/5/054001. arXiv: 0705.2759 [hep-ph].

[73] Johannes Hoelck and Georg Wolschin. "Baryon stopping as a relativistic Markov process in phase space". In: *Phys. Rev. Res.* 2.3 (2020), p. 033409. DOI: 10.1103/PhysRevResearch.2.033409. arXiv: 2009.08913 [nucl-th].

[74] H. Appelshäuser et al. "Xi and anti-xi production in 158-GeV / nucleon Pb + Pb collisions". In: *Phys. Lett. B* 444 (1998), pp. 523–530. DOI: 10.1016/S0370-2693(98)01399-9. arXiv: nucl-ex/9810005.

[75] L. Ahle et al. "Kaon production in Au+Au collisions at 11.6AGeV/c". In: *Phys. Rev. C* 58 (6 Dec. 1998), pp. 3523–3538. DOI: 10.1103/PhysRevC.58.3523.

[76] L. Ahle et al. "Proton and deuteron production in Au + Au reactions at 11.6/A-GeV/c". In: *Phys. Rev. C* 60 (1999), p. 064901. DOI: 10.1103/PhysRevC.60.064901.

[77] L. Ahle et al. "Excitation function of K+ and pi+ production in Au + Au reactions at 2/A-GeV to 10/A-GeV". In: *Phys. Lett. B* 476 (2000), pp. 1–8. DOI: 10.1016/S0370-2693(00)00037-X. arXiv: nucl-ex/9910008.

[78] J. Barrette et al. "Proton and pion production in Au + Au collisions at 10.8A-GeV/c". In: *Phys. Rev. C* 62 (2000), p. 024901. DOI: 10.1103/PhysRevC.62.024901. arXiv: nucl-ex/9910004.

[79] S.V. Afanasiev et al. "Production of phi-mesons in p+p, p+Pb and central Pb+Pb collisions at Ebeam=158AGeV". In: *Physics Letters B* 491.1 (2000), pp. 59–66. ISSN: 0370-2693. DOI: https://doi.org/10.1016/S0370-2693(00)01023-6.

[80] L Ahle et al. "An Excitation function of K- and K+ production in Au + Au reactions at the AGS". In: *Phys. Lett. B* 490 (2000), pp. 53–60. DOI: 10.1016/S0370-2693(00)00916-3. arXiv: nucl-ex/0008010.

[81] B. B. Back et al. "Baryon rapidity loss in relativistic Au+Au collisions". In: *Phys. Rev. Lett.* 86 (2001), pp. 1970–1973. DOI: 10.1103/PhysRevLett.86.1970. arXiv: nucl-ex/0003007.

[82] C. Pinkenburg et al. "Production and collective behavior of strange particles in Au + Au collisions at 2-AGeV - 8-AGeV". In: *Nucl. Phys. A* 698 (2002). Ed. by T. J. Hallman et al., pp. 495–498. DOI: 10.1016/S0375-9474(01)01412-9. arXiv: nucl-ex/0104025.

[83] J. L. Klay et al. "Longitudinal flow from 2-A-GeV to 8-A-GeV Au+Au collisions at the Brookhaven AGS". In: *Phys. Rev. Lett.* 88 (2002), p. 102301. DOI: 10.1103/PhysRevLett.88.102301. arXiv: nucl-ex/0111006.

[84] S. Albergo et al. "Λ Spectra in 11.6$AGeV/c$ Au-Au Collisions". In: *Phys. Rev. Lett.* 88 (6 Jan. 2002), p. 062301. DOI: 10.1103/PhysRevLett.88.062301.

[85] C. Adler et al. "Kaon production and kaon to pion ratio in Au+Au collisions at s(NN)**1/2 = 130-GeV". In: *Phys. Lett. B* 595 (2004), pp. 143–150. DOI: 10.1016/j.physletb.2004.06.044. arXiv: nucl-ex/0206008.

[86] C. Adler et al. "K*(892)0 production in relativistic heavy ion collisions at S(NN)**(1/2) = 130-GeV". In: *Phys. Rev. C* 66 (2002), p. 061901. DOI: 10.1103/PhysRevC.66.061901. arXiv: nucl-ex/0205015.

[87] S. V. Afanasiev et al. "Energy dependence of pion and kaon production in central Pb + Pb collisions". In: *Phys. Rev. C* 66 (2002), p. 054902. DOI: 10.1103/PhysRevC.66.054902. arXiv: nucl-ex/0205002.

[88] K. Adcox et al. "Measurement of the Lambda and anti-Lambda particles in Au+Au collisions at s(NN)**(1/2) = 130-GeV". In: *Phys. Rev. Lett.* 89 (2002), p. 092302. DOI: 10.1103/PhysRevLett.89.092302. arXiv: nucl-ex/0204007.

[89] C. Adler et al. "Midrapidity phi production in Au + Au collisions at s N N = 130-GeV". In: *Phys. Rev. C* 65 (2002), p. 041901. DOI: 10.1103/PhysRevC.65.041901.

[90] I. G. Bearden et al. "Particle production in central Pb + Pb collisions at 158-A-GeV/c". In: *Phys. Rev. C* 66 (2002), p. 044907. DOI: 10.1103/PhysRevC.66.044907. arXiv: nucl-ex/0202019.

[91] B. B. Back et al. "Production of phi mesons in Au+Au collisions at 11.7-A-GeV/c". In: *Phys. Rev. C* 69 (2004), p. 054901. DOI: 10.1103/PhysRevC.69.054901. arXiv: nucl-ex/0304017.

[92] J. L. Klay et al. "Charged pion production in 2 to 8 agev central au+au collisions". In: *Phys. Rev. C* 68 (2003), p. 054905. DOI: 10.1103/PhysRevC.68.054905. arXiv: nucl-ex/0306033.

[93] P. Chung et al. "Near threshold production of the multistrange xi- hyperon". In: *Phys. Rev. Lett.* 91 (2003), p. 202301. DOI: 10.1103/PhysRevLett.91.202301. arXiv: nucl-ex/0302021.

[94] K. Adcox et al. "Single identified hadron spectra from s(NN)**(1/2) = 130-GeV Au+Au collisions". In: *Phys. Rev. C* 69 (2004), p. 024904. DOI: 10.1103/PhysRevC.69.024904. arXiv: nucl-ex/0307010.

[95] T. Anticic et al. "Energy and centrality dependence of deuteron and proton production in Pb + Pb collisions at relativistic energies". In: *Phys. Rev. C* 69 (2 Feb. 2004), p. 024902. DOI: 10.1103/PhysRevC.69.024902.

[96] T. Anticic et al. "Lambda and anti-Lambda production in central Pb - Pb collisions at 40-A-GeV, 80-A-GeV and 158-A-GeV". In: *Phys. Rev. Lett.* 93 (2004), p. 022302. DOI: 10.1103/PhysRevLett.93.022302. arXiv: nucl-ex/0311024.

[97] S. S. Adler et al. "Identified charged particle spectra and yields in Au+Au collisions at S(NN)**1/2 = 200-GeV". In: *Phys. Rev. C* 69 (2004), p. 034909. DOI: 10.1103/PhysRevC.69.034909. arXiv: nucl-ex/0307022.

[98] J. Adams et al. "Multistrange baryon production in Au-Au collisions at S(NN)**1/2 = 130 GeV". In: *Phys. Rev. Lett.* 92 (2004), p. 182301. DOI: 10.1103/PhysRevLett.92.182301. arXiv: nucl-ex/0307024.

[99] J. Adams et al. "Identified particle distributions in pp and Au+Au collisions at s(NN)**(1/2) = 200 GeV". In: *Phys. Rev. Lett.* 92 (2004), p. 112301. DOI: 10.1103/PhysRevLett.92.112301. arXiv: nucl-ex/0310004.

[100] C. Alt et al. "Omega- and anti-Omega+ production in central Pb + Pb collisions at 40-AGeV and 158-AGeV". In: *Phys. Rev. Lett.* 94 (2005), p. 192301. DOI: 10.1103/PhysRevLett.94.192301. arXiv: nucl-ex/0409004.

[101] F. Antinori et al. "Energy dependence of hyperon production in nucleus nucleus collisions at SPS". In: *Phys. Lett. B* 595 (2004), pp. 68–74. DOI: 10.1016/j.physletb.2004.05.025. arXiv: nucl-ex/0403022.

[102] J. Adams et al. "K(892)* resonance production in Au+Au and p+p collisions at s(NN)**(1/2) = 200-GeV at STAR". In: *Phys. Rev. C* 71 (2005), p. 064902. DOI: 10.1103/PhysRevC.71.064902. arXiv: nucl-ex/0412019.

[103] S. S. Adler et al. "Production of phi mesons at mid-rapidity in s(NN)**(1/2) = 200- GeV Au+Au collisions at RHIC". In: *Phys. Rev. C* 72 (2005), p. 014903. DOI: 10.1103/PhysRevC.72.014903. arXiv: nucl-ex/0410012.

[104] S. S. Adler et al. "Deuteron and antideuteron production in Au + Au collisions at s(NN)**(1/2) = 200-GeV". In: *Phys. Rev. Lett.* 94 (2005), p. 122302. DOI: 10.1103/PhysRevLett.94.122302. arXiv: nucl-ex/0406004.

[105] John Adams et al. "phi meson production in Au + Au and p+p collisions at s(NN)**(1/2) = 200-GeV". In: *Phys. Lett. B* 612 (2005), pp. 181–189. DOI: 10.1016/j.physletb.2004.12.082. arXiv: nucl-ex/0406003.

[106] Anja E M Billmeier and (for the STAR Collaboration). "Strange and multi-strange particle ratios in p + p reactions at GeV at RHIC". In: *Journal of Physics G: Nuclear and Particle Physics* 30.1 (Dec. 2003), S363. DOI: 10.1088/0954-3899/30/1/043.

[107] Hai-bin Zhang. "Delta, K* and rho resonance production and their probing of freezeout dynamics at RHIC". In: *17th International Conference on Ultra Relativistic Nucleus-Nucleus Collisions (Quark Matter 2004)*. Mar. 2004. arXiv: nucl-ex/0403010.

[108] Olga Yu. Barannikova. "Probing collision dynamics at RHIC". In: *17th International Conference on Ultra Relativistic Nucleus-Nucleus Collisions (Quark Matter 2004)*. Mar. 2004. arXiv: nucl-ex/0403014.

[109] F. Antinori et al. "Rapidity distributions around mid-rapidity of strange particles in Pb-Pb collisions at 158-A-GeV/c". In: *J. Phys. G* 31 (2005), pp. 1345–1357. DOI: 10.1088/0954-3899/31/11/015. arXiv: nucl-ex/0509009.

[110] I. Arsene et al. "Centrality dependent particle production at y=0 and y ˜ 1 in Au + Au collisions at s(NN)**(1/2) = 200-GeV". In: *Phys. Rev. C* 72 (2005), p. 014908. DOI: 10.1103/PhysRevC.72.014908. arXiv: nucl-ex/0503010.

[111] A. Andronic, P. Braun-Munzinger, and J. Stachel. "Hadron production in central nucleus-nucleus collisions at chemical freeze-out". In: *Nucl. Phys. A* 772 (2006), pp. 167–199. DOI: 10.1016/j.nuclphysa.2006.03.012. arXiv: nucl-th/0511071.

[112] A. Andronic, P. Braun-Munzinger, and J. Stachel. "Thermal hadron production in relativistic nuclear collisions: The Hadron mass spectrum, the horn, and the QCD phase transition". In: *Phys. Lett. B* 673 (2009). [Erratum: Phys.Lett.B 678, 516 (2009)], pp. 142–145. DOI: 10.1016/j.physletb.2009.06.021. arXiv: 0812.1186 [nucl-th].

[113] Paolo Alba et al. "Freeze-out conditions from net-proton and net-charge fluctuations at RHIC". In: *Phys. Lett. B* 738 (2014), pp. 305–310. DOI: 10.1016/j.physletb.2014.09.052. arXiv: 1403.4903 [hep-ph].

[114] L. Adamczyk et al. "Bulk Properties of the Medium Produced in Relativistic Heavy-Ion Collisions from the Beam Energy Scan Program". In: *Phys. Rev. C* 96.4 (2017), p. 044904. DOI: 10.1103/PhysRevC.96.044904. arXiv: 1701.07065 [nucl-ex].

[115] A. Andronic et al. "Hadron yields in central nucleus-nucleus collisions, the statistical hadronization model and the QCD phase diagram". In: *Criticality in QCD and the Hadron Resonance Gas*. Jan. 2021. DOI: 10.5506/APhysPolBSupp.14.341. arXiv: 2101.05747 [nucl-th].

[116] E. Andersen et al. "Strangeness enhancement at mid-rapidity in Pb Pb collisions at 158-A-GeV/c". In: *Phys. Lett. B* 449 (1999), pp. 401–406. DOI: 10.1016/S0370-2693(99)00140-9.

[117] S. V Afanasiev et al. "Cascade and anti-Cascade+ production in central Pb + Pb collisions at 158-GeV/c per nucleon". In: *Phys. Lett. B* 538 (2002), pp. 275–281. DOI: 10.1016/S0370-2693(02)01970-6. arXiv: hep-ex/0202037.

[118] Johann Rafelski and Berndt Muller. "Strangeness Production in the Quark - Gluon Plasma". In: *Phys. Rev. Lett.* 48 (1982). [Erratum: Phys.Rev.Lett. 56, 2334 (1986)], p. 1066. DOI: 10.1103/PhysRevLett.48.1066.

[119] Ahmed Tounsi and Krzysztof Redlich. "Strangeness enhancement and canonical suppression". In: (Nov. 2001). arXiv: hep-ph/0111159.

[120] Jaroslav Adam et al. "Enhanced production of multi-strange hadrons in high-multiplicity proton-proton collisions". In: *Nature Phys.* 13 (2017), pp. 535–539. DOI: 10.1038/nphys4111. arXiv: 1606.07424 [nucl-ex].

[121] Jaroslav Adam et al. "Multi-strange baryon production in p-Pb collisions at $\sqrt{s_{\mathrm{NN}}} = 5.02$ TeV". In: *Phys. Lett. B* 758 (2016), pp. 389–401. DOI: 10.1016/j.physletb.2016.05.027. arXiv: 1512.07227 [nucl-ex].

[122] Betty Bezverkhny Abelev et al. "Multi-strange baryon production at mid-rapidity in Pb-Pb collisions at $\sqrt{s_{\mathrm{NN}}} = 2.76$ TeV". In: *Phys. Lett. B* 728 (2014). [Erratum: Phys.Lett.B 734, 409–410 (2014)], pp. 216–227. DOI: 10.1016/j.physletb.2014.05.052. arXiv: 1307.5543 [nucl-ex].

[123] Peter Skands, Stefano Carrazza, and Juan Rojo. "Tuning PYTHIA 8.1: the Monash 2013 Tune". In: *Eur. Phys. J. C* 74.8 (2014), p. 3024. DOI: 10.1140/epjc/s10052-014-3024-y. arXiv: 1404.5630 [hep-ph].

[124] T. Pierog et al. "EPOS LHC: Test of collective hadronization with data measured at the CERN Large Hadron Collider". In: *Phys. Rev. C* 92.3 (2015), p. 034906. DOI: 10.1103/PhysRevC.92.034906. arXiv: 1306.0121 [hep-ph].

[125] Christian Bierlich and Jesper Roy Christiansen. "Effects of color reconnection on hadron flavor observables". In: *Phys. Rev. D* 92.9 (2015), p. 094010. DOI: 10.1103/PhysRevD.92.094010. arXiv: 1507.02091 [hep-ph].

[126] Ranjit Nayak, Subhadip Pal, and Sadhana Dash. "Effect of rope hadronization on strangeness enhancement in p−p collisions at LHC energies". In: *Phys. Rev. D* 100.7 (2019), p. 074023. DOI: 10.1103/PhysRevD.100.074023. arXiv: 1812.07718 [hep-ph].

[127] Volodymyr Vovchenko, Benjamin Dönigus, and Horst Stoecker. "Canonical statistical model analysis of p-p , p -Pb, and Pb-Pb collisions at energies available at the CERN Large Hadron Collider". In: *Phys. Rev. C* 100.5 (2019), p. 054906. DOI: 10.1103/PhysRevC.100.054906. arXiv: 1906.03145 [hep-ph].

[128] Jean Cleymans et al. "Multiplicity dependence of (multi)strange baryons in the canonical ensemble with phase shift corrections". In: *Phys. Rev. C* 103.1 (2021), p. 014904. DOI: 10.1103/PhysRevC.103.014904. arXiv: 2009.04844 [hep-ph].

[129] Kapusta, J. I. "Mechanisms for deuteron production in relativistic nuclear collisions". In: *Physical Review C* 21 (1980), 1301–1310.

[130] Francesca Bellini and Alexander Philipp Kalweit. "Testing production scenarios for (anti-)(hyper-)nuclei and exotica at energies available at the CERN Large Hadron Collider". In: *Phys. Rev. C* 99.5 (2019), p. 054905. DOI: 10.1103/PhysRevC.99.054905. arXiv: 1807.05894 [hep-ph].

[131] Francesca Bellini et al. "Examination of coalescence as the origin of nuclei in hadronic collisions". In: *Phys. Rev. C* 103.1 (2021), p. 014907. DOI: 10.1103/PhysRevC.103.014907. arXiv: 2007.01750 [nucl-th].

[132] Maximilian Mahlein et al. "A realistic coalescence model for deuteron production". In: *Eur. Phys. J. C* 83.9 (2023), p. 804. DOI: 10.1140/epjc/s10052-023-11972-3. arXiv: 2302.12696 [hep-ex].

[133] Shreyasi Acharya et al. "Measurement of ${}^{3}_{\Lambda}$H production in Pb-Pb collisions at $\sqrt{s_{\mathrm{NN}}} = 5.02$ TeV". In: (May 2024). arXiv: 2405.19839 [nucl-ex].

[134] S. Acharya et al. "Measurement of the Lifetime and Λ Separation Energy of ${}^{3}_{\Lambda}$H". In: *Phys. Rev. Lett.* 131.10 (2023), p. 102302. DOI: 10.1103/PhysRevLett.131.102302. arXiv: 2209.07360 [nucl-ex].

[135] Shreyasi Acharya et al. "First Measurement of Antideuteron Number Fluctuations at Energies Available at the Large Hadron Collider". In: *Phys. Rev. Lett.* 131.4 (2023), p. 041901. DOI: 10.1103/PhysRevLett.131.041901. arXiv: 2204.10166 [nucl-ex].

[136] Zuzana Fecková et al. "Formation of deuterons by coalescence: Consequences for deuteron number fluctuations". In: *Phys. Rev. C* 93.5 (2016), p. 054906. DOI: 10.1103/PhysRevC.93.054906. arXiv: 1603.05854 [nucl-th].

[137] Bjoern Schenke, Sangyong Jeon, and Charles Gale. "(3+1)D hydrodynamic simulation of relativistic heavy-ion collisions". In: *Phys. Rev. C* 82 (2010), p. 014903. DOI: 10.1103/PhysRevC.82.014903. arXiv: 1004.1408 [hep-ph].

[138] Bjorn Schenke, Sangyong Jeon, and Charles Gale. "Elliptic and triangular flow in event-by-event (3+1)D viscous hydrodynamics". In: *Phys. Rev. Lett.* 106 (2011), p. 042301. DOI: 10.1103/PhysRevLett.106.042301. arXiv: 1009.3244 [hep-ph].

[139] Jean-François Paquet et al. "Production of photons in relativistic heavy-ion collisions". In: *Phys. Rev. C* 93.4 (2016), p. 044906. DOI: 10.1103/PhysRevC.93.044906. arXiv: 1509.06738 [hep-ph].

[140] S. A. Bass et al. "Microscopic models for ultrarelativistic heavy ion collisions". In: *Prog. Part. Nucl. Phys.* 41 (1998), pp. 255–369. DOI: 10.1016/S0146-6410(98)00058-1. arXiv: nucl-th/9803035.

[141] M. Bleicher et al. "Relativistic hadron hadron collisions in the ultrarelativistic quantum molecular dynamics model". In: *J. Phys. G* 25 (1999), pp. 1859–1896. DOI: 10.1088/0954-3899/25/9/308. arXiv: hep-ph/9909407.

[142] Kai-Jia Sun and Che Ming Ko. "Event-by-event antideuteron multiplicity fluctuation in Pb+Pb collisions at $\sqrt{s_{\rm NN}} = 5.02$ TeV". In: *Phys. Lett. B* 840 (2023), p. 137864. DOI: 10.1016/j.physletb.2023.137864. arXiv: 2204.10879 [nucl-th].

[143] Shreyasi Acharya et al. "Closing in on critical net-baryon fluctuations at LHC energies: Cumulants up to third order in Pb–Pb collisions". In: *Phys. Lett. B* 844 (2023), p. 137545. DOI: 10.1016/j.physletb.2022.137545. arXiv: 2206.03343 [nucl-ex].

[144] The ALICE Collaboration et al. "The ALICE experiment at the CERN LHC". In: *JINST* 3 (2008), S08002.

[145] Esma Mobs. "The CERN accelerator complex - 2018". In: *CERN graphics* (2018).

[146] "LHC Design Report. 3. The LHC injector chain". In: (2004). Ed. by M. Benedikt et al.

[147] H. Bartosik et al. "Performance of the CERN Heavy Ion Production Complex". In: *Conf. Proc. C* 1205201 (2012). Ed. by Vic Suller, pp. 3752–3754.

[148] S. van der Meer. "Calibration of the Effective Beam Height in the ISR". In: (June 1968).

[149] P Cortese et al. "ALICE: Physics performance report, volume I". In: *J. Phys. G* 30 (2004). Ed. by F Carminati et al., pp. 1517–1763.

[150] Christian Wolfgang Fabjan et al. "ALICE: Physics performance report, volume II". In: *J. Phys. G* 32 (2006). Ed. by B Alessandro et al., pp. 1295–2040.

[151] G. Dellacasa et al. "ALICE technical design report of the inner tracking system (ITS)". In: (1999).

[152] J. Alme et al. "The ALICE TPC, a large 3-dimensional tracking device with fast readout for ultra-high multiplicity events". In: *Nuclear Instruments and Methods in Physics Research Section A: Accelerators, Spectrometers, Detectors and Associated Equipment* 622 (2010), pp. 316–367.

[153] G. Dellacasa et al. "ALICE technical design report of the time-of-flight system (TOF)". In: (Feb. 2000).

[154] ALICE Collaboration. "Determination of the event collision time with the ALICE detector at the LHC". In: 132 (2017), p. 99. arXiv: `1610.03055 [physics.ins-det]`.

[155] F. Carnesecchi. "Performance of the ALICE Time-Of-Flight detector at the LHC". In: *Journal of Instrumentation* 14 (2019), pp. C06023–C06023.

[156] ALICE Collaboration. "Technical Design Report on the Trigger, Data Acquisition, High Level Trigger and Control System". In: *CERN* (2004).

[157] F. Carena et al. "The ALICE data acquisition system". In: *Nuclear Instruments and Methods in Physics Research Section A: Accelerators, Spectrometers, Detectors and Associated Equipment* 741 (2014), pp. 130–162.

[158] Mikolaj Krzewicki et al. "The ALICE High Level Trigger: status and plans". In: *J. Phys. Conf. Ser.* 664 (2015), p. 082023.

[159] Jamie Shiers. "The Worldwide LHC Computing Grid (worldwide LCG)". In: *Computer Physics Communications* 177 (2007), pp. 219–223.

[160] ALICE Collaboration. "Performance of the ALICE experiment at the CERN LHC". In: *International Journal of Modern Physics A* 29 (2014), p. 1430044.

[161] Rudolph Emil Kalman. "A New Approach to Linear Filtering and Prediction Problems". In: *Transactions of the ASME–Journal of Basic Engineering* 82.Series D (1960), pp. 35–45.

[162] Marain Ivanov et al. "Track reconstruction in high density environment". In: *Nuclear Instruments & Methods in Physics Research Section A-accelerators Spectrometers Detectors and Associated Equipment - NUCL INSTRUM METH PHYS RES A* 566 (2006), pp. 70–74.

[163] René Brun et al. "GEANT Detector Description and Simulation Tool". In: *CERN* (1994).

[164] S. Agostinelli et al. "Geant4—a simulation toolkit". In: *Nuclear Instruments and Methods in Physics Research Section A: Accelerators, Spectrometers, Detectors and Associated Equipment* 506 (2003), pp. 250–303.

[165] Alfredo Ferrari et al. "FLUKA: A multi-particle transport code (Program version 2005)". In: *CERN* (Oct. 2005).

[166] Luigi Rolandi, Werner Riegler, and Walter Blum. *Particle Detection with Drift Chambers*. 2008.

[167] ALEPH Collaboration. "Performance of the ALEPH detector at LEP". In: *Nuclear Instruments and Methods in Physics Research Section A: Accelerators, Spectrometers, Detectors and Associated Equipment* 360.3 (1995), pp. 481–506.

[168] ALICE Collaboration. "Centrality determination of Pb-Pb collisions at $\sqrt{s_{\mathrm{NN}}} = 2.76$ TeV with ALICE". In: *Physical Review C* 88.4 (2013).

[169] S. Agostinelli et al. "GEANT4–a simulation toolkit". In: *Nucl. Instrum. Meth. A* 506 (2003), pp. 250–303. DOI: 10.1016/S0168-9002(03)01368-8.

[170] Shreyasi Acharya et al. "Hypertriton Production in p-Pb Collisions at $\sqrt{s_{\mathrm{NN}}}$=5.02 TeV". In: *Phys. Rev. Lett.* 128.25 (2022), p. 252003. DOI: 10.1103/PhysRevLett.128.252003. arXiv: 2107.10627 [nucl-ex].

[171] J. Podolanski and R. Armenteros. "III. Analysis of V-events". In: *The London, Edinburgh, and Dublin Philosophical Magazine and Journal of Science* 45.360 (1954), pp. 13–30. DOI: 10.1080/14786440108520416. eprint: https://doi.org/10.1080/14786440108520416. URL: https://doi.org/10.1080/14786440108520416.

[172] Tianqi Chen and Carlos Guestrin. "XGBoost: A Scalable Tree Boosting System". In: *Proceedings of the 22nd ACM SIGKDD International Conference on Knowledge Discovery and Data Mining*. KDD '16. San Francisco, California, USA: Association for Computing Machinery, 2016, pp. 785–794. ISBN: 9781450342322. DOI: 10.1145/2939672.2939785.

[173] Luca Barioglio et al. *hipe4ml/hipe4ml*. Version v0.0.14. July 2024. DOI: 10.5281/zenodo.7014886. URL: https://doi.org/10.5281/zenodo.7014886.

[174] Fernando Nogueira. *Bayesian Optimization: Open source constrained global optimization tool for Python*. 2014–. URL: https://github.com/bayesian-optimization/BayesianOptimization.

[175] George Casella, Christian P. Robert, and Martin T. Wells. "Generalized Accept-Reject Sampling Schemes". In: *Lecture Notes-Monograph Series* 45 (2004), pp. 342–347. ISSN: 07492170. URL: http://www.jstor.org/stable/4356322 (visited on 12/23/2024).

[176] Shreyasi Acharya et al. "Light (anti)nuclei production in Pb-Pb collisions at $\sqrt{s_{\mathrm{NN}}} = 5.02$ TeV". In: *Phys. Rev. C* 107.6 (2023), p. 064904. DOI: 10.1103/PhysRevC.107.064904. arXiv: 2211.14015 [nucl-ex].

[177] Philip J. Siemens and John O. Rasmussen. "Evidence for a blast wave from compress nuclear matter". In: *Phys. Rev. Lett.* 42 (1979), pp. 880–887. DOI: 10.1103/PhysRevLett.42.880.

[178] J. Cleymans et al. "Statistical model predictions for particle ratios at $\sqrt{s_{\mathrm{NN}}} =$ 5.5 TeV". In: *Phys. Rev. C* 74 (2006), p. 034903.

[179] Shreyasi Acharya et al. "Measurement of the low-energy antideuteron inelastic cross section". In: *Phys. Rev. Lett.* 125.16 (2020), p. 162001. DOI: 10.1103/PhysRevLett.125.162001. arXiv: 2005.11122 [nucl-ex].

[180] Kyle S. Cranmer. "Kernel estimation in high-energy physics". In: *Comput. Phys. Commun.* 136 (2001), pp. 198–207. DOI: 10.1016/S0010-4655(00)00243-5. arXiv: hep-ex/0011057.

[181] Wouter Verkerke and David P. Kirkby. "The RooFit toolkit for data modeling". In: *eConf* C0303241 (2003). Ed. by L. Lyons and Muge Karagoz, MOLT007. DOI: 10.1142/9781860948985_0039. arXiv: physics/0306116.

[182] Jaroslav Adam et al. "Quarkonium signal extraction in ALICE". In: *ALICE-PUBLIC-2015-006* (2015). URL: https://cds.cern.ch/record/2060096/.

[183] Shreyasi Acharya et al. "Measurement of anti-^{3}He nuclei absorption in matter and impact on their propagation in the Galaxy". In: *Nature Phys.* 19.1 (2023), pp. 61–71. DOI: 10.1038/s41567-022-01804-8. arXiv: 2202.01549 [nucl-ex].

[184] Shreyasi Acharya et al. "Measurement of the low-energy antitriton inelastic cross section". In: (July 2023). arXiv: 2307.03603 [nucl-ex].

[185] M.V. Evlanov et al. "Interaction of hypertritons with nuclei at high energies". In: *Nuclear Physics A* 632.4 (1998), pp. 624–632. ISSN: 0375-9474. DOI: https://doi.org/10.1016/S0375-9474(98)00116-X. URL: https://www.sciencedirect.com/science/article/pii/S037594749800116X.

[186] Roger Barlow. "Systematic errors: Facts and fictions". In: *Conference on Advanced Statistical Techniques in Particle Physics*. July 2002, pp. 134–144. arXiv: hep-ex/0207026.

[187] F. F. Chen, C. P. Leavitt, and A. M. Shapiro. "Attenuation Cross Sections for 860-Mev Protons". In: *Physical Review* 99 (1955), p. 857. DOI: 10.1103/PhysRev.99.857.

[188] N. E. Booth et al. "Nuclear cross sections for 900 MeV protons." In: *Proc.Physical Society (London), Section A* 70 (1957), p. 209. DOI: 10.1088/0370-1298/70/3/306.

[189] N. T. Porile. "Simple Nuclear Reactions of Indium with 30 and 2.9 GeV Protons". In: *Physical Review* 128 (1962), p. 1916. DOI: 10.1103/PhysRev.128.1916.

[190] O. Artun et al. "Multinucleon Removal Induced by High-Energy Protons". In: *Phys. Rev. Lett.* 35 (1975), p. 773. DOI: 10.1103/PhysRevLett.35.773.

[191] M. E. Sadler et al. "Interaction of 80-164 MeV Protons with Nickel Isotopes". In: *Phys. Rev. C* 21 (1980), p. 2303. DOI: 10.1103/PhysRevC.21.2303.

[192] D. Ashery et al. "True Absorption and Scattering of Pions on Nuclei". In: *Phys. Rev. C* 23 (1981), pp. 2173–2185. DOI: 10.1103/PhysRevC.23.2173.

[193] K. Nakamura et al. “Absorption and Forward Scattering of Antiprotons by C, Al, and Cu Nuclei in the Region 470-880 MeV/c”. In: *Phys. Rev. Lett.* 52 (1984), pp. 731–734. DOI: 10.1103/PhysRevLett.52.731.

[194] J. A. McGill et al. “Proton + Nucleus Inclusive (p,p‘) Scattering at 800 MeV”. In: *Phys. Rev. C* 29 (1984), p. 204. DOI: 10.1103/PhysRevC.29.204.

[195] N. G. Zaitseva et al. “Excitation Function and Yield for ^{97}Ru Production in ^{99}Tc(p,3n)^{97}Ru Reaction in 20-100 MeV Proton Energy Range”. In: *Radiochimica Acta* 56 (1992), p. 59. DOI: 10.1524/ract.1992.56.2.59.

[196] V. F. Kuzichev, Yu. B. Lepikhin, and V. A. Smirnitsky. “The Anti-proton - nuclei annihilation cross-section at the momentum range from 0.70 GeV/c to 2.5 GeV/c”. In: *Nucl. Phys. A* 576 (1994), pp. 581–602. DOI: 10.1016/0375-9474(94)90745-5.

[197] C. -M. Herbach et al. “Systematic investigation of 1.2 GeV proton-induced spallation reactions on targets between Al and U”. In: *Nucl. Instrum. Methods in Physics Res., Sect.A* 562 (2006), p. 729. DOI: 10.1016/j.nima.2006.02.033.

[198] M. Zamani et al. “Indirect measurement of inelastic cross section of relativistic protons in Pb target”. In: *Annals of Nuclear Energy* 37 (2010), p. 923. DOI: 10.1016/j.anucene.2010.03.015.

[199] D. W. Bardayan et al. “Inelastic ^{17}F(p,p)^{17}F scattering at $E_{c.m.}$=3 MeV and the ^{14}O(—a,p)^{17}F reaction rate”. In: *Phys. Rev. C* 81 (2010), p. 065802. DOI: 10.1103/PhysRevC.81.065802.

[200] Betty Bezverkhny Abelev et al. “Performance of the ALICE Experiment at the CERN LHC”. In: *Int. J. Mod. Phys. A* 29 (2014), p. 1430044. DOI: 10.1142/S0217751X14300440. arXiv: 1402.4476 [nucl-ex].

[201] Volodymyr Vovchenko, Mark I. Gorenstein, and Horst Stoecker. “Finite resonance widths influence the thermal-model description of hadron yields”. In: *Phys. Rev. C* 98.3 (2018), p. 034906. DOI: 10.1103/PhysRevC.98.034906. arXiv: 1807.02079 [nucl-th].

[202] B. I. Abelev et al. “Systematic Measurements of Identified Particle Spectra in pp, d^+ Au and Au+Au Collisions from STAR”. In: *Phys. Rev. C* 79 (2009), p. 034909. DOI: 10.1103/PhysRevC.79.034909. arXiv: 0808.2041 [nucl-ex].

[203] Betty Abelev et al. "Centrality dependence of π, K, p production in Pb-Pb collisions at $\sqrt{s_{\mathrm{NN}}} = 2.76$ TeV". In: *Phys. Rev. C* 88 (2013), p. 044910. DOI: 10.1103/PhysRevC.88.044910. arXiv: 1303.0737 [hep-ex].

[204] J. Cleymans, H. Oeschler, and K. Redlich. "Statistical model description of K+ and K- production between 1-GeV/A to 10-GeV/A". In: *Phys. Lett. B* 485 (2000), pp. 27–31. DOI: 10.1016/S0370-2693(00)00674-2. arXiv: nucl-th/0004025.

[205] A. Bazavov et al. "Freeze-out Conditions in Heavy Ion Collisions from QCD Thermodynamics". In: *Phys. Rev. Lett.* 109 (2012), p. 192302. DOI: 10.1103/PhysRevLett.109.192302. arXiv: 1208.1220 [hep-lat].

[206] James Daniel Brandenburg et al. "Search for baryon junctions in photonuclear processes and isobar collisions at RHIC". In: (May 2022). arXiv: 2205.05685 [hep-ph].

[207] D. Kharzeev. "Can gluons trace baryon number?" In: *Phys. Lett. B* 378 (1996), pp. 238–246. DOI: 10.1016/0370-2693(96)00435-2. arXiv: nucl-th/9602027.

[208] "Centrality determination in heavy ion collisions". In: *ALICE-PUBLIC-2018-011* (2018). URL: https://cds.cern.ch/record/2636623.

[209] K. Aamodt et al. "Midrapidity antiproton-to-proton ratio in pp collisions at $\sqrt{s} = 0.9$ and 7 TeV measured by the ALICE experiment". In: *Phys. Rev. Lett.* 105 (2010), p. 072002. DOI: 10.1103/PhysRevLett.105.072002. arXiv: 1006.5432 [hep-ex].

[210] E. Abbas et al. "Mid-rapidity anti-baryon to baryon ratios in pp collisions at $\sqrt{s} = 0.9$, 2.76 and 7 TeV measured by ALICE". In: *Eur. Phys. J. C* 73 (2013), p. 2496. DOI: 10.1140/epjc/s10052-013-2496-5. arXiv: 1305.1562 [nucl-ex].

[211] Shreyasi Acharya et al. "Multiplicity dependence of light (anti-)nuclei production in p-Pb collisions at $\sqrt{s_{\mathrm{NN}}} = 5.02$ TeV". In: *Phys. Lett. B* 800 (2020), p. 135043. DOI: 10.1016/j.physletb.2019.135043. arXiv: 1906.03136 [nucl-ex].

[212] Shreyasi Acharya et al. "Production of (anti-)^{3}He and (anti-)^{3}H in p-Pb collisions at $\sqrt{s_{\mathrm{NN}}} = 5.02$ TeV". In: *Phys. Rev. C* 101.4 (2020), p. 044906. DOI: 10.1103/PhysRevC.101.044906. arXiv: 1910.14401 [nucl-ex].

[213] Toshihiro Nonaka, Masakiyo Kitazawa, and ShinIchi Esumi. "More efficient formulas for efficiency correction of cumulants and effect of using averaged efficiency". In: *Phys. Rev. C* 95.6 (2017). [Erratum: Phys.Rev.C 103, 029901 (2021)], p. 064912. DOI: 10.1103/PhysRevC.95.064912. arXiv: 1702.07106 [physics.data-an].

[214] Ashish Pandav, Debasish Mallick, and Bedangadas Mohanty. "Effect of limited statistics on higher order cumulants measurement in heavy-ion collision experiments". In: *Nucl. Phys. A* 991 (2019), p. 121608. DOI: 10.1016/j.nuclphysa.2019.08.002. arXiv: 1809.08892 [nucl-ex].

[215] Betty Abelev et al. "Multiplicity Dependence of Pion, Kaon, Proton and Lambda Production in p–Pb Collisions at $\sqrt{s_{\mathrm{NN}}} = 5.02$ TeV". In: *Phys. Lett. B* 728 (2014), pp. 25–38. DOI: 10.1016/j.physletb.2013.11.020. arXiv: 1307.6796 [nucl-ex].

[216] Jaroslav Adam et al. "Centrality Dependence of the Charged-Particle Multiplicity Density at Midrapidity in Pb-Pb Collisions at $\sqrt{s_{\mathrm{NN}}} = 5.02$ TeV". In: *Phys. Rev. Lett.* 116.22 (2016), p. 222302. DOI: 10.1103/PhysRevLett.116.222302. arXiv: 1512.06104 [nucl-ex].

[217] Shreyasi Acharya et al. "Production of light (anti)nuclei in pp collisions at $\sqrt{s} = 5.02$ TeV". In: *Eur. Phys. J. C* 82.4 (2022), p. 289. DOI: 10.1140/epjc/s10052-022-10241-z. arXiv: 2112.00610 [nucl-ex].

[218] Shreyasi Acharya et al. "Multiplicity dependence of π, K, and p production in pp collisions at $\sqrt{s} = 13$ TeV". In: *Eur. Phys. J. C* 80.8 (2020), p. 693. DOI: 10.1140/epjc/s10052-020-8125-1. arXiv: 2003.02394 [nucl-ex].

[219] Shreyasi Acharya et al. "Studying strangeness and baryon production mechanisms through angular correlations between charged Ξ baryons and identified hadrons in pp collisions at $\sqrt{s} = 13$ TeV". In: *JHEP* 09 (2024), p. 102. DOI: 10.1007/JHEP09(2024)102. arXiv: 2308.16706 [hep-ex].

Acknowledgments

I would like to thank Stefania Bufalino and Massimo Masera for their incredible support in all my activities and for their useful suggestions over the past three years. I want to acknowledge Maximiliano Puccio and Sourav Kundu for providing invaluable insights on heavy-ion physics and data analysis techniques, and for answering all my questions. I also want to express my gratitude to all my colleagues in Torino and at CERN for the fruitful discussions and for the great time spent together. Finally, I would like to thank my family for their support and patience during my academic studies.